# Low Energy Background in the NCD Phase of the Sudbury Neutrino Observatory

Helen Mary O'Keeffe
Lincoln College, Oxford

Thesis submitted in partial fulfilment of the requirements for the degree of Doctor of Philosophy at the University of Oxford

Hilary Term 2008

# Low Energy Background in the NCD Phase of the Sudbury Neutrino Observatory

Helen Mary O'Keeffe
Lincoln College, Oxford

Thesis submitted in partial fulfilment of the requirements for the degree of Doctor of Philosophy at the University of Oxford
Hilary Term 2008

**Abstract**

The Sudbury Neutrino Observatory (SNO) was a 1 kilotonne heavy water Čerenkov detector. Evidence for flavour changing neutrino oscillations was found by comparing the rate of Charged Current interactions with that of Neutral Current (NC) interactions.

This thesis is concerned with the accurate determination of the NC flux in the Neutral Current Detector (NCD) phase of SNO. The measurement and understanding of radioactive backgrounds arising from decays of naturally occurring $^{232}$Th and $^{238}$U chain nuclei is crucial. This is because their daughter nuclei can produce neutrons via photodisintegration of deuterium. These would be indistinguishable from those produced by NC neutrino interactions. As the probability of neutron production was dependent upon the nature and location of activity, each contribution had to be determined separately. Of particular concern were $^{232}$Th and $^{238}$U in the $D_2O$ and Neutral Current Detectors (NCDs). A maximum likelihood method was developed that exploited differences in the event isotropy and radial profile of each event class. These results were in agreement with water assay results and pre-deployment radioassays of the NCDs.

An independent measurement of the $^{232}$Th content in the $D_2O$ and $H_2O$ was made by regularly assaying the water using filters loaded with hydrous titanium oxide. The concentration of $^{232}$Th in the water was determined by coincidence counting of the final assay sample. A new counter system was designed and built and the calibration and use of this system are presented.

Two areas of increased activity were discovered on two of the NCDs deployed in the detector which would have prevented an accurate measurement of the NC flux. A method was devised to determine the composition and activity of one of these hotspots. The results were in good agreement with two independent methods and the uncertainty on the NC flux was reduced from $> 7\%$ to $< 1\%$.

The total number of neutrons produced per day by photodisintegration for $^{232}$Th and $^{238}$U in the $D_2O$ and NCDs was measured to be $0.66^{+0.08}_{-0.07}$. This was significantly less than the expected 12.6 NC neutrino interactions per day.

In the third phase, two independent data streams existed: PMT and NCD. A Monte Carlo study was undertaken to determine whether an accurate measure of the NC flux could be obtained using only PMT data. Results showed that no improvement could be made upon results from previous phases and the best measurement of the NC flux in the final phase would be made using PMT and NCD data.

To my Mam and Dad

## Acknowledgements

First I would like to thank my supervisor, Professor Nick Jelley, for his guidance, advice and encouragement during my time at Oxford. It has been a privilege to work with him. His interest in this work was always greatly appreciated and valued. Above all, thanks for being a fantastic supervisor.

It has been a pleasure to work with the Oxford SNO group; Steve Biller, George Doucas, Hadi Fergani, Nick Jelley, James Loach, Sherry Majerus, Gabriel Orebi Gann, Simon Peeters, Wan Tseung, Nick West and Jeanne Wilson. I would especially like to thank Sherry Majerus for her help and advice during the development of the NCD elution method and for performing extra assays during the commissioning of the beta-alpha counters. Thank you also to Gabriel Orebi Gann for being a great office mate and friend.

Thank you to Beverly Roger and Kim Proudfoot for organising my many trips to Sudbury which always went smoothly. Thanks to Colin Perry, Ron Morton and the Central Electronics group for their help with the modifications to the beta-alpha counter system. I am thankful to all of the staff and students of the sub-department of particle physics for making the Denys Wilkinson Building a great place to work. I would also like to thank the staff and students of Lincoln College, my Oxford home for the past eight years.

During my trips to Sudbury, I was always made to feel welcome by the on-site SNO collaborators. I would particularly like to thank Lina Anselmo, Pat Brouse, Nancy Brown, Melin Huang, Kim Keen, Shari Moss and Carol Woodliffe for making my trips so enjoyable. I am thankful for the advice and interest from the whole SNO collaboration.

Thank you to Mr Gerard McCabe, former physics teacher at St. Joseph's R.C. Comprehensive School, Hebburn, who took my interest in physics seriously and encouraged me along this path many years ago. I also acknowledge with thanks the STFC (formerly PPARC) for funding this research.

Finally, the most important people, who deserve most thanks, are my Mam (Marilyn), Dad (George) and brothers (John, Aidan and Stephen). Thank you for all of your love, encouragement and support during the completion of this thesis and all that went before it. I really couldn't have done it without you all.

Deo gratias.

*I love the Sun.*
*It shines on me.*
*God made the Sun*
*And God made me.*

Gwen F. Smith

My favourite infant school hymn... Miss McBride's class.

# Contents


**1 Neutrino Physics** **1**

1.1 Neutrinos . . . 1
1.2 Standard Model of Particle Physics . . . 2
1.3 The Standard Solar Model . . . 3
1.4 Solar Neutrino Experiments . . . 6
1.4.1 Chlorine . . . 6
1.4.2 Water Čerenkov . . . 7
1.4.3 Gallium . . . 8
1.5 The Solar Neutrino Problem . . . 9
1.6 Neutrino Oscillations . . . 9
1.6.1 Two flavour vacuum oscillations . . . 10
1.6.2 Matter Enhanced Oscillations . . . 12
1.7 Results from the Sudbury Neutrino Observatory . . . 14
1.8 Results from KamLAND . . . 15
1.9 Large Mixing Angle solution . . . 15
1.10 Other Neutrino Experiments . . . 17
1.10.1 Atmospheric neutrino experiments . . . 17
1.10.2 Solar Neutrino detection with scintillator . . . 18
1.10.3 Accelerator neutrino experiments . . . 18
1.10.4 Reactor neutrino experiments . . . 19
1.11 Summary of Neutrino Physics . . . 20
1.12 Thesis Outline . . . 21

**2 The SNO detector** **23**

2.1 Čerenkov Radiation . . . 24
2.1.1 Charged Current . . . 25
2.1.2 Elastic Scattering . . . 25
2.1.3 Neutral Current . . . 26
2.2 Photomultiplier Tubes . . . 27
2.3 Neutral Current Detectors . . . 29
2.4 Calibration . . . 33
2.4.1 Electronics Calibration . . . 34

2.4.2 PMT Calibration . . . 35
2.4.3 Energy Calibration . . . 35
2.4.4 Neutron Calibration . . . 35
2.4.5 Distributed sources . . . 36
2.5 Data Quality . . . 37
2.5.1 First pass selection . . . 37
2.5.2 Second pass selection . . . 38
2.6 SNOMAN . . . 38
2.7 Water Systems . . . 38
2.7.1 Light Water . . . 39
2.7.2 Heavy Water . . . 39
2.7.3 Assays . . . 39

**3 Backgrounds** **44**
3.1 Instrumental backgrounds . . . 44
3.2 Physical backgrounds . . . 45
3.2.1 Muons and muon followers . . . 45
3.2.2 Neutral Current induced reactions . . . 46
3.2.3 Radioactive backgrounds . . . 47
3.2.4 Photodisintegration . . . 50
3.3 Sources of radioactivity in SNO . . . 51
3.4 Measurement of radioactivity . . . 55

**4 *In-situ* analysis of radioactive backgrounds** **57**
4.1 Backgrounds in the $D_2O$ region . . . 59
4.1.1 Analysis cuts . . . 59
4.1.2 Energy Separation . . . 62
4.1.3 Isotropy Separation . . . 62
4.1.4 Isotropy distribution verification . . . 64
4.1.5 $\beta_{14}$ Radial profile . . . 67
4.1.6 Radial separation . . . 67
4.1.7 Verification of radial distributions . . . 68
4.1.8 Maximum likelihood fit to the data . . . 69
4.1.9 Calculation of the concentrations . . . 71
4.1.10 Systematic Errors . . . 73
4.1.11 Uniformity of NCD bulk backgrounds . . . 77
4.1.12 Recommended $D_2O$ and NCD concentrations . . . 78
4.2 NCD Hotspots . . . 79
4.2.1 K5 . . . 80
4.2.2 Composition and strength of the K5 hotspot . . . 83
4.2.3 Error Analysis . . . 84
4.2.4 K2 . . . 85

4.2.5 An upper limit of the K2 hotspot mass . . . 85
4.2.6 *Ex-situ* hotspot measurements . . . 87
4.3 PSUP $H_2O$ . . . 87
4.3.1 Error analysis . . . 89
4.3.2 Analysis of the $H_2O$ Rn spike . . . 92
4.3.3 Recommended $H_2O$ concentrations . . . 95
4.4 Summary of photodisintegration backgrounds . . . 95

**5 The Hydrous Titanium Oxide assay 97**
5.1 Properties of HTiO . . . 98
5.2 Preparation of HTiO . . . 98
5.3 The HTiO assay . . . 99
5.3.1 Deposition . . . 99
5.3.2 Extraction . . . 99
5.3.3 Elution . . . 100
5.3.4 Secondary concentration . . . 101
5.3.5 Counting . . . 102
5.4 Analysis of NCD phase HTiO assays . . . 103
5.4.1 Data Analysis . . . 104
5.4.2 Equipment and Reagent background . . . 109
5.4.3 Accounting for fluctuating rig backgrounds . . . 110
5.4.4 Extraction efficiency . . . 112
5.5 Flow rates for PSUP assays . . . 115
5.6 HTiO assay efficiency . . . 115
5.7 Systematic errors . . . 116
5.7.1 Processed mass . . . 117
5.7.2 Re-sampling correction . . . 117
5.7.3 Feedback correction . . . 118
5.7.4 Extraction and elution . . . 119
5.7.5 Secondary concentration . . . 119
5.7.6 Counting efficiency . . . 120
5.7.7 Alpha peak drift . . . 120
5.7.8 Sample cloudiness . . . 120
5.7.9 Software cuts . . . 121
5.7.10 Fitting . . . 121
5.7.11 Background subtraction . . . 121
5.8 Assay results . . . 122

**6 The Oxford Beta-Alpha coincidence counters 124**
6.1 Beta-alpha coincidence counting . . . 124
6.2 System Overview . . . 126
6.3 Pulse handling . . . 128

6.3.1 RUN threshold . . . 128
6.3.2 ALPHA threshold . . . 128
6.3.3 MU threshold . . . 129
6.3.4 FIRST time interval . . . 129
6.3.5 SHORT time interval . . . 129
6.3.6 LONG time interval . . . 130
6.4 An example coincidence . . . 130
6.5 Read out of the system . . . 132
6.6 Setting up and testing the system . . . 132
6.6.1 Setting the thresholds . . . 133
6.6.2 Setting the timings . . . 134
6.6.3 Setting the PMT HV . . . 135
6.7 System calibration . . . 135
6.8 Assay results using the new counter system . . . 137
6.8.1 Light water assay 71 . . . 137
6.8.2 Light water assay 80 . . . 138
6.9 Conclusions . . . 139

**7 Measurements of NCD hotspots** **140**
7.1 *In-situ* analysis . . . 141
7.1.1 K5 hotspot . . . 141
7.1.2 K2 hotspot . . . 143
7.2 Hotspot searches . . . 143
7.3 The need for *ex-situ* measurements . . . 143
7.4 Acid elution of an NCD . . . 144
7.4.1 ICP-MS analysis of Ni concentration in the HCl eluate . . . 145
7.5 Spike experiments . . . 145
7.5.1 Soak solution concentration . . . 147
7.5.2 HTiO co-precipitation efficiency . . . 148
7.5.3 $^{228}$Th plating onto polypropylene . . . 148
7.6 Results from the spike experiments . . . 149
7.6.1 Background . . . 149
7.6.2 Spike 1 . . . 149
7.6.3 Spike 2 . . . 150
7.6.4 Spike 3 . . . 151
7.6.5 Spike 4 . . . 152
7.6.6 Spike 5 . . . 152
7.6.7 Spike 6 . . . 153
7.6.8 Spike 7 . . . 153
7.6.9 Overall conclusions from the spike tests . . . 153
7.7 Sensitivity . . . 154

7.8 Elution of K5 . . . 154
7.8.1 Testing for Ni interference . . . 157
7.9 Elution results . . . 157
7.10 External Alpha Counting of K5 . . . 158
7.10.1 Location of the K5 hotspot(s) . . . 158
7.10.2 Measurement of composition . . . 159
7.10.3 Coincidence analysis . . . 161
7.11 Measurements of K2 . . . 162
7.12 Results and conclusions . . . 162

**8 Signal Extraction** **165**
8.1 Event selection . . . 165
8.2 Extended maximum likelihood . . . 166
8.3 Extracting the signals . . . 166
8.4 Fits to fake data . . . 168
8.5 Systematic Errors . . . 169
8.6 Conclusions . . . 170

**9 Conclusions** **171**

**A Neutral Current induced backgrounds in salt** **175**
A.1 Theoretical estimate . . . 176
A.1.1 The probability of photodisintegration . . . 177

**B NCD names and numbers** **181**

**C The Oxford Elution Rig** **182**

**Bibliography** **183**

# List of Figures


1.1 Neutrino producing reactions in the Sun. . . . . 5
1.2 Solar neutrino energy spectra for each branch of the pp chain . . . . . 6
1.3 MSW contour plots for the salt phase of SNO. . . . . 16
1.4 Schematic representation of electron neutrino survival probability as a function of energy for an LMA solution. . . . . 17

2.1 Schematic of the SNO detector. . . . . 24
2.2 Schematic diagram of the NCD array in SNO. . . . . 29
2.3 Schematic diagram of an NCD. . . . . 31
2.4 NCD array neutron capture spectrum from a uniformly distributed $^{24}$Na calibration. . . . . 32
2.5 Overview of the $H_2O$ systems. Figure provided by J. Farine. . . . . 40
2.6 Overview of the $D_2O$ systems. Figure provided by J. Farine. . . . . 41

3.1 The decay chain of $^{232}$Th. . . . . 48
3.2 The decay chain of $^{238}$U. . . . . 49
3.3 $^{208}$Tl decay scheme . . . . . 52
3.4 Simplified $^{214}$Bi decay scheme. . . . . 53

4.1 Schematic of the NCD array . . . . . 58
4.2 Definition of $\theta_{ij}$ . . . . . 60
4.3 Exclusion cuts for the K5 and K2 hotspots. . . . . 62
4.4 Energy distributions for $D_2O$ and NCD MC events in the *in-situ* monitoring window. . . . . 63
4.5 Isotropy distributions for $D_2O$ and NCD MC events in the *in-situ* monitoring window. . . . . 64
4.6 Isotropy distributions for $^{222}$Rn source data and MC. . . . . 65
4.7 Data and MC isotropy distributions for the 2005 $^{24}$Na spike. . . . . 66
4.8 Gaussian mean $\beta_{14}$ value versus radius for $D_2O$ $^{16}$N runs. . . . . 68
4.9 Radial distributions for NCD and $D_2O$ backgrounds in the *in-situ* monitoring window. . . . . 69
4.10 Radial distributions for Bi $D_2O$, Tl $D_2O$ and Na 2005 data . . . . . 70

4.11 Radial distributions for Bi+Tl surface, Tl $D_2O$ and K5 hotspot data. In this plot, $R^2_{NCD} = (x_{EVENT} - x_{NCD})^2 + (y_{EVENT} - y_{NCD})^2$, where $x_{NCD} = x$ coordinate of the NCD, $x_{EVENT} = x$ coordinate of the event vertex and similarly for $y$. . . . . 70
4.12 Fitted fraction of events for different exclusion volumes around K5. . . . . 78
4.13 Excluded radius versus concentration for Tl and Bi $D_2O$ backgrounds. . . . 79
4.14 $z$ distribution of events on K2 (string 31) and K5 (string 18). . . . . 81
4.15 The endcap region of two joined NCDs. . . . . 82
4.16 $\beta_{14}$ distribution of events originating from K5 (string 18). . . . . 83
4.17 142 hours of commissioning data compared to 142 hours of open month data. 84
4.18 $\beta_{14}$ distribution of events originating from K2 (string 31). . . . . 86
4.19 Diagram of $\mathbf{u}.\mathbf{r}$ for an outward going event. . . . . 89
4.20 (Data-MC)/Data for $\beta_{14}$ versus radius for $H_2O$ $^{16}N$ scans in the NCD phase. 91
4.21 $N_{corr}$ versus radius for $H_2O$ N16 scans in the NCD phase. . . . . 92
4.22 $\mathbf{u}.\mathbf{r}$ distributions for selected data, Bi MC and Tl MC in the $H_2O$ region. . 93
4.23 Number of events passing the *in-situ* analysis cuts as a function of time. . 94

5.1 Schematic diagram of an HTiO loaded filter in a polypropylene column. . . 100
5.2 An example of data taken by the beta-alpha coincidence counters. . . . . 105
5.3 A schematic representation of the the diagonal cutting method. . . . . 106
5.4 The fitting of true beta-alpha coincidences binned per hour for LWA75 for Th chain activity. . . . . 108
5.5 NCD phase HTiO assay results for the PSUP region. . . . . 110
5.6 Comparison between results with and without the additional background error. There is no additional error for the last 5 points as those assays were performed using the $D_2O$ rig. . . . . 113
5.7 The variation of thorium concentration for different flow rates in PSUP assays. There was no obvious dependence of concentration on flow rate. . 116
5.8 A diagram of the feedback loop used in PSUP and cavity assays. . . . . 119

6.1 Plot of average pulse shape for betas and alphas . . . . . 125
6.2 Schematic diagram of the source, PMT and copper housing. . . . . 127
6.3 Circuit diagram of the smoother unit. . . . . 128
6.4 An example coincidence, with pulses separated by 100 ns. . . . . 131
6.5 Thorium chain results from a typical run using a 5 mBq $^{228}Th$ source. . . . 138
6.6 Results from NCD phase cavity assays. . . . . 139

7.1 Plots of the (x,y), (x,z), (y,z) and (x,y,z) distributions of reconstructed events.142
7.2 Location of cuts and approximate locations of the two K5 hotspots. The red bands are where the EAC localised the hotspot. . . . . 155
7.3 Schematic comparison of EAC and *in-situ* results for the K5 distribution. . 160
7.4 The $\alpha$-energy spectra of the K5 hotspots. . . . . 161

8.1 Histograms of $E$, $R$ and $\cos\theta_\odot$ for CC (red), NC (blue) and ES (green) events. . . . . 167

A.1 A schematic representation of a double event. . . . . 176
A.2 Energy dependence of photodisintegration cross section. . . . . 177

C.1 A schematic diagram of the Oxford elution rig . . . . . 182

# List of Tables


1.1 Particles of the Standard Model of Particle Physics. . . . . 3
1.2 Measured neutrino fluxes from solar neutrino experiments. The SNO results are not included. The Borexino experiment is discussed later in this chapter. . . . . 9
1.3 Summary of results from the first two phases of the SNO experiment . . . 14
1.4 Summary of neutrino mixing parameters to date . . . . . 20

2.1 Distributed sources deployed during the NCD phase. . . . . 36

3.1 Target radiopurity levels for the $D_2O$ and $H_2O$ (PSUP) regions. . . . . 54

4.1 Results from the analysis of source data and MC for specified calibration sources . . . . . 65
4.2 Results for $\beta_{14}$ from simulations of 5 MeV (kinetic) energy electrons and $^{208}$Tl decays with normal and increased NCD reflectivity. . . . . 67
4.3 Results from preliminary fake data tests of the two 2D likelihood fitting routines. Prototype is the code written by the author and ROOT is the TFractionFitter code. . . . . 72
4.4 Generated rates and concentrations for each background MC in the $D_2O$ region of the detector. A mass of 1000 tonnes of $D_2O$ and 189 kg of Ni were used. . . . . 73
4.5 Number of events obtained from the maximum likelihood fit to the data in the $D_2O$ region. . . . . 74
4.6 Summary of systematic errors for the *in-situ* analysis of Th and U $D_2O$ backgrounds. . . . . 74
4.7 Summary of systematic errors for the *in-situ* analysis of Th and U bulk NCD backgrounds. . . . . 75
4.8 Summary of results from the *in-situ* analysis of the three distributed sources deployed in the $D_2O$ region during the NCD phase. . . . . 75
4.9 Correlation matrix for the 2D fit. . . . . 80
4.10 Rates and masses (of parent nuclei) for the K5 Monte Carlo. . . . . 85
4.11 Number of events obtained from the maximum likelihood fit to the K5 data. 85
4.12 Summary of systematic errors for the *in-situ* analysis of the K5 hotspot. . 86

4.13 Summary of systematic errors for the *in-situ* analysis of the K2 hotspot. . 87
4.14 Number of events obtained from the maximum likelihood fit to the data. The number of events passing each cut in the corresponding MC are given, along with the resulting concentrations. . . . . 89
4.15 Summary of errors for the *in-situ* analysis in the $H_2O$ PSUP region. . . . . 90
4.16 Correlation matrix for the $H_2O$ fit. . . . . 95
4.17 Summary of neutron production via photodisintegration in the NCD phase. 95

5.1 Central values of Th concentration and absolute systematic error due to uncertainty in the rig background measurements for PSUP and cavity HTiO assays in the NCD phase. Values given are $gTh/gH_2O \times 10^{-15}$. . . . . 112
5.2 Results from the $D_2O$ efficiency check assays. . . . . 114
5.3 Results from the cavity efficiency check assays. . . . . 114
5.4 Summary of efficiencies for the new HTiO procedure. . . . . 116
5.5 Systematic errors for $D_2O$ and $H_2O$ assays. All errors are percentages. . . . 117
5.6 Error weighted mean $^{232}$Th concentrations for each region from the HTiO assays. . . . . 122
5.7 Comparison of *ex-situ* and *in-situ* Th chain results. . . . . 122

6.1 Default values for all thresholds and timings as set on the Sudbury and Oxford boards, August 2007. . . . . 130
6.2 Probe points and thresholds . . . . . 133

7.1 Results from the *in-situ* analysis of the K5 hotspot. . . . . 141
7.2 Start and end dates for the NCD spike samples. . . . . 147
7.3 Results from the elution of the K5 hotspots. . . . . 158
7.4 Efficiencies for each stage of the acid elution technique. . . . . 158
7.5 Masses of uranium and thorium measured by acid elution. . . . . 159
7.6 The hotspot strengths which best describe the EAC data. . . . . 161
7.7 Results from the coincidence analysis of the EAC data. . . . . 162
7.8 Masses of uranium and thorium measured by each technique for the K5 and K2 hotspots. . . . . 163
7.9 Neutrons produced per day by each hotspot. . . . . 163

8.1 Average results from Fake data fits. Statistical errors only are given. . . . . 168
8.2 Summary of systematic errors for the fake data trials. . . . . 169

A.1 Principle decay modes for 2 and 3 gamma decays involved in this calculation. 178

B.1 Name and numbering convention for NCDs . . . . . 181

# Glossary

**ADC** Analogue to Digital Convertor

**AV** Acrylic Vessel

**CAMAC** Computer Automated Measurement and Control

**CC** Charged Current interaction

**cph** Counts Per Hour

**CPT** Charge, Parity and Time

**DAMN** Data Analysis Mask Number

**DAQ** Data Acquisition System

**EAC** External Alpha Counter

**EDTA** EthyleneDiamineTetraacetic Acid

**ES** Elastic Scattering

**FIFO** First In, First Out

**FPGA** Field Programmable Gate Array

**HTiO** Hydrous Titanium Oxide

**HV** High Voltage

**INCO** International Nickel Company

**ITR** In Time Ratio

**LED** Light Emitting Diode

**LMA** Large Mixing Angle

**LWA** Light Water Assay

**MAC** Mass Attenuation Coefficient

**MC** Monte Carlo

**MnOx** Manganese Oxide

**MSW** Mikheyev, Smirnov and Wolfenstein

**MXF** Maximum Likelihood Fitter

**NC** Neutral Current interaction

**NCD** Neutral Current Detector

**NIM** Nuclear Instrument Module

**OFHC** Oxygen Free High Conductivity (Copper)

**pdf** Probability Density Function

**psd** Pulse Shape Discrimination

**PMT** Photomultiplier Tube

**PSUP** Photomultiplier Support Structure

**PTFE** PolytetraFluoroEthene

**RDA** Radium $D_2O$ Assay

**RO** Reverse Osmosis

**RSP** Calibrated Energy Response

**SNO** Sudbury Neutrino Observatory

**SNOMAN** SNO Monte Carlo Analysis program

**TDC** Time to Digital Convertor

**UPW** Ultra Pure Water

# Chapter 1

# Neutrino Physics

## 1.1 Neutrinos

The neutrino was first postulated by Wolfgang Pauli in 1930 to explain the experimentally observed continuous energy spectrum of electrons emitted by beta decay of nuclei [1]. With the inclusion of what is now known to be an anti-neutrino*, the beta decay of a nucleus may be represented by

$$(N, Z) \rightarrow (N - 1, Z + 1) + e^- + \bar{\nu}_e \tag{1.1}$$

where $\bar{\nu}_e$ is the anti-neutrino, $e^-$ is an electron, $N$ is the atomic mass number of the nucleus and $Z$ is the proton number of the nucleus. The inclusion of the anti-neutrino allows the final state energy to be shared between it and the emitted electron, the only constraints being that the sum of their energies is equal to the $Q$-value of the reaction, and the small nuclear recoil energy is neglected. This explained the experimentally observed electron energy spectrum. In addition, Pauli's neutrino allowed angular momentum to be conserved. It was observed in beta decays that if the parent nuclei carries integer (fractional) spin, the daughter nuclei also has integer (fractional) spin. This could not be explained by the emission of a single spin-half electron. Pauli's neutrino would explain this observation if it too was spin-half. Higher values of neutrino spin were ruled out by the observation of spin-zero to spin-zero transitions in nuclear beta decay that occurred at a similar rate to other allowed ($l = 0$) transitions.

The discovery of the neutron by Chadwick in 1932, [2] led Fermi to develop a theoretical description of $\beta$ decay [3]. Fermi treated beta decay as a transition, dependent upon the strength of coupling between the initial and final states, that was mediated by an interaction of zero range. Fermi's theory provided a theoretical framework for Pauli's postulate.

*This is to ensure lepton number is conserved

In 1953, a small scale reactor experiment performed by Reines and Cowan provided possible evidence for the neutrino [4]. They then constructed a larger scale experiment, with better background shielding at the Savannah River nuclear power plant [5]. The reactor provided a source of neutrinos and the detector consisted of a tank of aqueous cadmium chloride, surrounded by two tanks of scintillator. Neutrinos were detected via the following inverse beta decay reaction

$$\bar{\nu}_e + \mathrm{p} \rightarrow e^+ + \mathrm{n}$$

where $\bar{\nu}$ is the anti-neutrino, p is a proton, $e^+$ is an positron and n is a neutron. The positron annihilates, producing 0.511 MeV gammas which are detected in delayed coincidence with a neutron capture approximately 5 $\mu$s later. In 1956 this improved experiment provided the first conclusive proof of the neutrino [5].

In 1957, Feynman and Gell-Mann proposed a theory of weak interactions that acts on left handed particles and right handed anti-particles. This theory is known as the V-A (vector minus axial) theory of weak interactions. The observation that the neutrino helicity[†] was consistent with a -1 state led to the assumption that the neutrino was massless and this was incorporated into the Standard Model of Particle Physics.

The neutrino helicity was measured in 1958 in an experiment performed by Goldhaber *et al* [6]. This demonstrated that the neutrino exists only in a left hand state, consistent with a helicity of -1. In this experiment, gammas produced by the decay of $^{152}$Sm underwent resonant scattering in a ring of $Sm_2O_3$. The subsequent gammas produced by this scattering were recorded by a sodium iodide scintillator and photomultiplier tube. The transmission of the initial gammas from the $^{152}$Sm decay depends on the helicity and the direction of an applied magnetic field. By reversing the direction of the applied magnetic field, the polarisation of the neutrino could be determined from the change in count rate.

## 1.2 Standard Model of Particle Physics

The Standard Model of Particle Physics describes the fundamental particles of nature and their interactions. All matter is composed of fundamental spin-half particles, which may be split into two sub-groups, namely quarks and leptons. The quarks and leptons have corresponding anti-particles. Charges of the quarks and leptons are given in Table 1.1. Quarks and leptons are grouped into three generations according to their mass, with the first generation being the lightest and only stable particles.

[†]Helicity is the projection of spin onto the direction of momentum.

| | Particle | Charge | Symbol | Generation |
|---|---|---|---|---|
| Quarks | Up | $+\frac{2}{3}$ | u | First |
| | Down | $-\frac{1}{3}$ | d | First |
| | Strange | $-\frac{1}{3}$ | s | Second |
| | Charm | $+\frac{2}{3}$ | c | Second |
| | Bottom | $-\frac{1}{3}$ | b | Third |
| | Top | $+\frac{2}{3}$ | t | Third |
| Leptons | Electron | $-1$ | e | First |
| | Electron neutrino | 0 | $\nu_e$ | First |
| | Muon | $-1$ | $\mu$ | Second |
| | Muon neutrino | 0 | $\nu_\mu$ | Second |
| | Tau | $-1$ | $\tau$ | Third |
| | Tau neutrino | 0 | $\nu_\tau$ | Third |

Table 1.1: Particles of the Standard Model of Particle Physics.

Quarks and leptons interact with each other by the exchange of integer spin particles known as Bosons. Such Bosons are the *force carriers* of the Standard Model and are responsible for the three fundamental forces that exist in the Standard Model; electromagnetic, strong and weak. Gravitational force is not included in the Standard Model. Electromagnetic force leads to bound states of atoms and molecules. It is mediated by the massless photon ($\gamma$) and only exists between charged particles or neutral particles with non-zero magnetic moments such as the neutron. Weak interactions are charge independent and involve the exchange of one of three (massive) weak bosons, $W^+$, $W^-$ or $Z^0$. The weak force involving $W^+$ and $W^-$ exchange is responsible for beta decay in nuclei. Strong interactions only occur between quarks and proceed by exchange of massless gluons ($g$). The strong force binds quarks into hadrons and neutrons and protons into atomic nuclei, via the exchange of mesons[‡].

To date, the Standard Model of Particle Physics has successfully described the majority of experimental observations. Evidence of physics beyond the Standard Model has been observed in solar and atmospheric neutrino experiments. These observations will now be discussed further, beginning with a description of the Standard Solar Model.

## 1.3 The Standard Solar Model

The energy radiated by the Sun is produced by a series of fusion reactions occurring within its core. Most of this energy is produced by the proton-proton (pp) chain. Detailed models of the Sun have been developed and refined over many years. Such models assume that

[‡]A meson is a bound quark and anti-quark

the pressure generated by fusion within the Sun exactly balances its gravitational force to prevent collapse. They also assume that the energy released by the nuclear processes is the dominant source of energy produced. Under these assumptions, detailed models have been developed that reproduce many features of the Sun. One such Standard Solar Model was devised by John Bahcall [7] and it has successfully predicted a number of properties.

The Standard Solar Model has been used to predict the speed with which sound travels in the Sun. The speed of sound is dependent upon the temperature and helium abundance in the Sun. A prediction of its speed may be made by calculating the frequency of the surface vibrational modes of the Sun using the Standard Solar Model. This prediction can be compared with helioseismological observations which measure the frequency spectrum of pressure oscillations on the Sun's surface. Good agreement between the observed and predicted values of parameters such as core temperature, radius and luminosity has been found [8]. This suggests that the Standard Solar Model correctly models the dynamic behaviour of the Sun.

Of particular interest to this thesis is that the Standard Solar Model can be used to predict the number of neutrinos produced by the Sun. As luminosity is determined by the energy released by nuclear processes in the Sun, it provides a strong constraint on the number of neutrinos produced. Neutrinos are produced in abundance by a number of reactions in the Sun. These are shown in Figure 1.1. The neutrino energy spectra for each process in the pp chain are well understood and can be explained using existing nuclear physics. The Standard Solar Model may be used to predict the relative contributions from each branch of the chain to the total flux of solar neutrinos. The branches are shown in Figure 1.2.

The total solar neutrino spectrum is dominated by neutrinos produced by the initial pp reaction. Despite the flux[§] being much less than that of the pp reaction, the $^8$B process (shown in Figure 1.1) presented the best possibility of detection for early neutrino experiments. This is partially offset as the cross sections of neutrino interactions are proportional to $E^2$, at low energies, making higher energy solar neutrinos easier to detect.

The current theoretical estimate of the solar neutrino fluxes is from the 2004 Bahcall-Pinsonneault model [10]. From this model, the predicted total flux of $^8$B solar neutrinos ($\Phi(^8B)$) is

$$\Phi(^8B) = 5.79 \times (1 \pm 0.23) \times 10^6 \mathrm{cm}^{-2}\mathrm{s}^{-1}. \tag{1.2}$$

The quoted uncertainty is dominated by uncertainty on the abundance of heavy elements on the surface of the Sun and uncertainty in the cross section of the following process

$$^3\mathrm{He} + {}^4\mathrm{He} \rightarrow {}^7\mathrm{Be} + \gamma.$$

[§]flux = number of particles per square cm per second

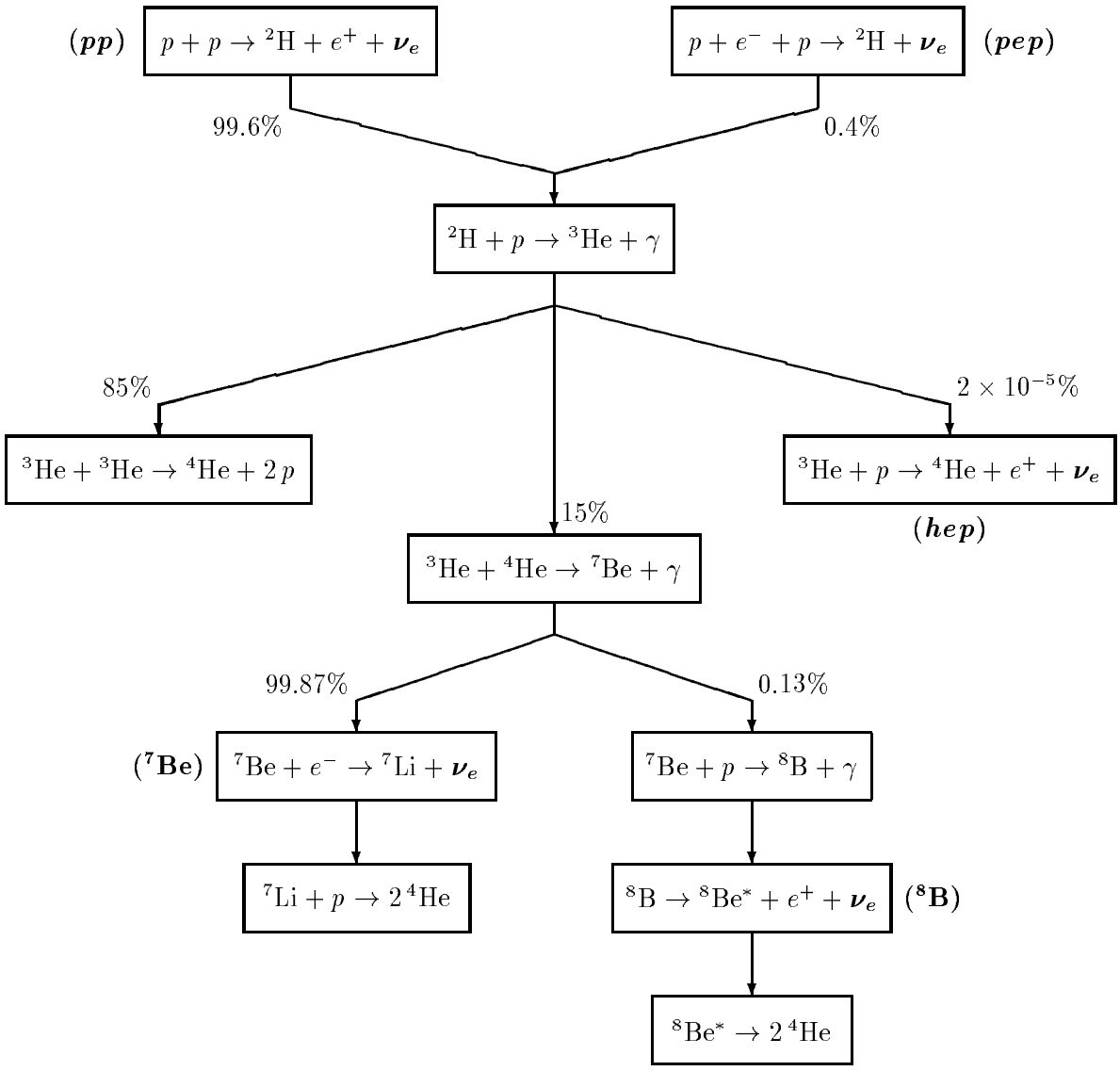


Figure 1.1: Neutrino producing reactions in the Sun [9].

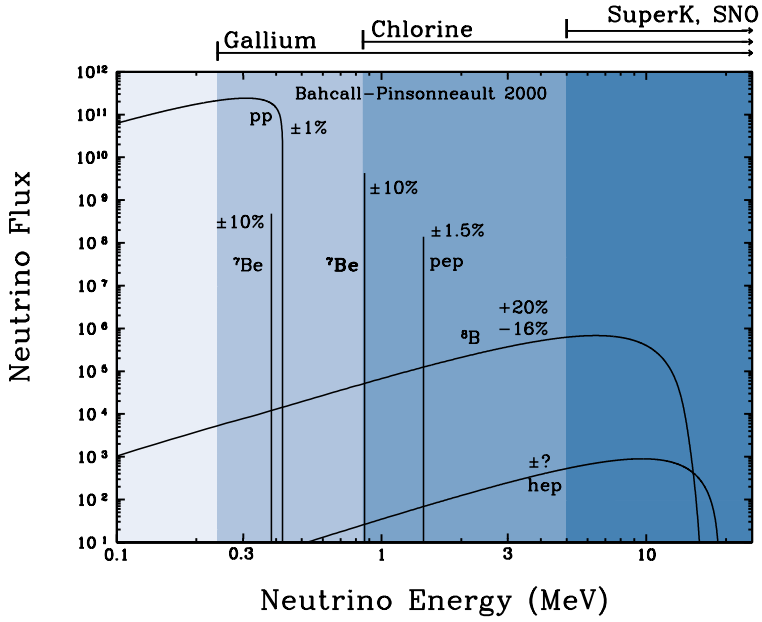


Figure 1.2: Solar neutrino energy spectra for each branch of the pp chain. The approximate thresholds of current solar neutrino experiments are shown for comparison.

These theoretical results may be compared with results observed in various solar neutrino experiments which are now described.

## 1.4 Solar Neutrino Experiments

### 1.4.1 Chlorine

The first solar neutrino detector was built by Ray Davis and collaborators from Brookhaven National Laboratory, New York, USA in 1967 [11]. Located approximately 4800 feet underground in the Homestake gold mine in South Dakota, the detector consisted of 615 tonnes of perchloroethylene $C_2Cl_4$, held in a tank and surrounded by water. Solar neutrinos interacted with chlorine ($^{37}$Cl), producing a radioactive isotope of argon ($^{37}$Ar) via the following interaction

$$\nu_e + {}^{37}\mathrm{Cl} \rightarrow {}^{37}\mathrm{Ar} + e^-.$$

The number of $^{37}$Ar atoms produced was directly proportional to the integrated solar neutrino flux above this threshold making it sensitive to neutrinos produced by several different branches of the pp chain. The dominant contribution to $^{37}$Ar production was from $^8$B neutrinos.

Approximately 5% of the tank volume was made up of helium (He) gas which was

used to flush out $^{37}$Ar at the end of a run. At the end of each two month run, helium was bubbled through the tank to remove any $^{37}$Ar produced and collect it in a charcoal trap. Once the entire tank had been processed, the $^{37}$Ar was removed from the trap, purified using gas chromatography, mixed with methane and counted in a small proportional counter for a year. After a year, decay spectra were fitted to the counting (rate) data and the number of $^{37}$Ar calculated.

Results from the Homestake experiment were announced in 1968 and the number of observed $^{37}$Ar decays was significantly lower than that predicted using the Standard Solar Model. The experiment continued for approximately 30 years and the final results found that the measured flux of electron neutrinos from the Sun was $0.34 \pm 0.03$ times the expected solar neutrino flux [12].

As the difference was so large, many checks were made on the radiochemistry involved. Of particular importance was the need to determine whether or not the Homestake experiment accurately measured the amount of $^{37}$Ar produced. Argon atoms could have become trapped in the parent molecules of $C_2Cl_4$. To determine the detection efficiency, $^{36}$Cl was added to the detector. $^{36}$Cl beta decays to $^{36}$Ar. During the test, $^{36}$Ar was extracted using the same methods as those used at the end of each run. This test proved that Ar was not trapped in the parent molecule and confirmed a genuine discrepancy between theory and experiment.

### 1.4.2 Water Čerenkov

The Kamiokande (Kamioka Nucleon Decay Experiment) detector was constructed in the early 1980s to search for nucleon decay [13]. After an upgrade in 1985, the detector was used to detect low energy neutrino events. The detector consisted of a cylindrical tank containing 2140 tonnes of pure $H_2O$. Neutrinos interacted in the water via the following reaction

$$\nu_x + e^- \rightarrow \nu_x + e^-$$

where $x$ is any flavour of neutrino. The electrons produced by this elastic scattering reaction radiate Čerenkov light that was detected by 1000 20 inch photomultiplier tubes surrounding the detector. The experiment was sensitive to all three active flavours of neutrino, but was approximately 6 times more sensitive to electron type neutrinos. Because of its threshold, the Kamiokande experiment could only detect $^8$B neutrinos and approximately 50% of the predicted neutrino flux was seen.

In 1991, a larger and improved version of the Kamiokande experiment was constructed. The Super-Kamiokande experiment (Super-K) began taking data in 1996. The Super-K detector is a cylindrical tank, 41.4 m tall, 39.3 m in diameter and holds 50,000 tons of ultra pure water. The tank is surrounded by 11,146 20 inch photomultiplier

tubes. The measured flux from 1258 days of data was $0.451 \pm 0.005(\text{stat})^{+0.016}_{-0.014}(\text{syst})$ of the expected neutrino flux [13]. Like the Homestake experiment, this was less than that predicted by the Standard Solar Model.

### 1.4.3 Gallium

Following the Homestake experiment, two radiochemical experiments using gallium (Ga) were devised to detect neutrinos via

$$\nu_e + {}^{71}\text{Ga} \rightarrow {}^{71}\text{Ge} + e^-$$

which has a threshold of 0.233 MeV. This threshold value allows pp neutrinos to be detected. As the half life of $^{71}$Ge is around 11.4 days, the experiment could be run for several weeks before attempting to extract the Ge. Two Ga experiments have been carried out, SAGE (Soviet-American Gallium Experiment) [14] and GALLEX (Gallium Experiment). Later, GNO (Gallium Neutrino Observatory) [15], was designed and built as an upgrade to GALLEX.

The SAGE experiment consisted of 8 Teflon lined tanks, each containing 7 tonnes of (pure) liquid Ga at a temperature of 30°C. The experiment was located underground at an equivalent depth of 4.27 km of water. At the end of each run, which typically lasted one month, liquid Ga from the detector was treated with various solvents to remove Ge. Following concentration and synthesis to produce gaseous germane ($GeH_4$), the amount of Ge was inferred by counting the rate of beta decays of $^{71}$Ge to $^{71}$Ga using a proportional chamber.

The GALLEX detector used a single 70 m$^3$ tank containing an aqueous solution of 8 mol/$l$ gallium chloride ($GaCl_3$) and hydrochloric acid (HCl). The detector was located in the Grand Sasso Laboratory (Italy) with a rock overburden equivalent to 3.3 km of water. The Ge produced by neutrino interactions formed $GeCl_4$ which was removed at the end of a run by forcing nitrogen gas through the detector. The $GeCl_4$ was then converted into $GeH_4$ and counted using a proportional counter. The GNO experiment used a larger target mass and an improved data analysis technique.

Combination of results from these three gallium experiments gave a measurement of $0.579 \pm 0.050$ of the expected neutrino flux [16]. Like the Homestake and water Čerenkov experiments, the number of observed solar neutrinos was significantly below theoretical predictions.

| Experiment | Energy Threshold | Measured/SSM flux |
|---|---|---|
| Homestake | 0.814 MeV | 0.34 |
| SAGE/GALLEX/GNO | 0.233 MeV | 0.58 |
| Super-Kamiokande | 5-20 MeV | 0.45 |
| Borexino | 0.270 MeV | 0.65 |

Table 1.2: Measured neutrino fluxes from solar neutrino experiments. The SNO results are not included. The Borexino experiment is discussed later in this chapter.

## 1.5 The Solar Neutrino Problem

Fluxes measured by the solar neutrino experiments discussed above are given in Table 1.2. In each case, there is significant disagreement between the experimental results and the values predicted by the Standard Solar Model. Solar observations suggested that the Standard Solar Model correctly modelled the Sun's behaviour. However, particle physics observations consistently contradicted this. This disagreement became generally known as the Solar Neutrino Problem, the solution to which is now discussed.

## 1.6 Neutrino Oscillations

The experiments presented so far in this chapter were primarily sensitive only to electron type neutrinos. If other flavours of neutrino were emitted from the Sun, they would not be recorded by these experiments. As a result, the measured flux of solar neutrinos would be less than that predicted by the Standard Solar Model. The Solar Neutrino Problem would be solved if the electron type neutrinos produced by the Sun changed into one of the other two flavours of neutrino before they were detected on the Earth. In 1969 Gribov and Pontecorvo correctly proposed that the solar neutrino problem could be due to neutrino oscillation [17], but incorrectly suggested that they oscillate into anti-neutrinos and not to other flavours.

Neutrinos interact with matter via the weak interaction and are always produced along with their corresponding charged lepton partner. Neutrinos may also be expressed in terms of mass states $\nu_1$, $\nu_2$, $\nu_3$. If lepton number is not absolutely conserved and the neutrino has a finite mass, the mass eigenstates do not correspond exactly to the flavour eigenstates, allowing the possibility of mixing between flavour states. In this scenario, flavour eigenstates would be formed from linear combinations of mass eigenstates as shown below in (1.3)

$$|\nu_x\rangle = U_{PMNS}|\nu_i\rangle \tag{1.3}$$

where $U_{PMS}$ is the Pontecorvo-Maki-Nakagawa-Sakata (PMNS) matrix, $x = e, \mu, \tau$ and

$i = 1, 2, 3$. The PMNS matrix is

$$\begin{pmatrix} U_{e1} & U_{e2} & U_{e3} \\ U_{\mu 1} & U_{\mu 2} & U_{\mu 3} \\ U_{\tau 1} & U_{\tau 2} & U_{\tau 3} \end{pmatrix} = \begin{pmatrix} c_{12}c_{13} & s_{12}c_{12} & s_{13}e^{-i\delta} \\ -s_{12}c_{23} - c_{12}s_{23}s_{13}e^{-i\delta} & c_{12}c_{23} - c_{12}s_{23}s_{13}e^{-i\delta} & s_{23}c_{13} \\ s_{12}s_{23} - c_{12}s_{13}e^{-i\delta} & -c_{12}s_{23} - s_{12}c_{23}s_{13}e^{-i\delta} & c_{23}c_{13} \end{pmatrix} \quad (1.4)$$

where $s$ and $c$ represent sine and cosine of the mixing angles between the mass states and $\delta$ is a phase factor which is only non-zero if neutrino oscillations violate CP conservation.

The Chooz reactor experiment [18] has demonstrated that $U_{e3}$ is small and close to zero. This allows the mixing matrix to be simplified to a good approximation, thus (1.4) becomes

$$\begin{pmatrix} \cos\theta_\nu & \sin\theta_\nu \\ -\sin\theta_\nu & \cos\theta_\nu \end{pmatrix} \quad (1.5)$$

and the interference is between two neutrino states: $\nu_e$ and $\nu_\chi$ where $\nu_\chi$ is a linear combination of $\nu_\mu$ and $\nu_\tau$ states, namely

$$\nu_\chi = \frac{1}{\sqrt{2}}(\nu_\mu - \nu_\tau).$$

The simplest case will now be presented mathematically.

### 1.6.1 Two flavour vacuum oscillations

In this case, the flavour eigenstates are related to the mass eigenstates as follows

$$\begin{pmatrix} |\nu_e\rangle \\ |\nu_\chi\rangle \end{pmatrix} = \begin{pmatrix} \cos\theta_\nu & \sin\theta_\nu \\ -\sin\theta_\nu & \cos\theta_\nu \end{pmatrix} \begin{pmatrix} |\nu_1\rangle \\ |\nu_2\rangle \end{pmatrix}$$

where $\theta_\nu$ is the vacuum mixing angle between the states. Neutrinos are produced and measured as flavour eigenstates, but propagate through spacetime as mass eigenstates. As the masses corresponding to the mass eigenstates are not equal, i.e. $m_1 \neq m_2$ the mass eigenstates propagate at different speeds. Therefore, the wavefunction of the neutrino is given by the superposition of two mass states

$$\begin{aligned} |\nu_e\rangle &= \cos\theta_\nu|\nu_1\rangle + \sin\theta_\nu|\nu_2\rangle \\ |\nu_\chi\rangle &= -\sin\theta_\nu|\nu_1\rangle + \cos\theta_\nu|\nu_2\rangle. \end{aligned} \quad (1.6)$$

By rearranging (1.6), the mass eigenstates may be expressed in terms of flavour eigenstates

$$\begin{aligned} |\nu_1\rangle &= \cos\theta_\nu|\nu_e\rangle - \sin\theta_\nu|\nu_\chi\rangle \\ |\nu_2\rangle &= \sin\theta_\nu|\nu_e\rangle + \cos\theta_\nu|\nu_\chi\rangle. \end{aligned} \quad (1.7)$$

The mass eigenstates in (1.7) satisfy the time dependent relativistic Schrödinger equation with solutions

$$\begin{aligned} |\nu_1(t)\rangle &= e^{iE_1t-ik_1l}|\nu_1(0)\rangle \\ |\nu_2(t)\rangle &= e^{iE_2t-ik_2l}|\nu_2(0)\rangle \end{aligned} \tag{1.8}$$

where $|\nu_1(0)\rangle$ and $|\nu_2(0)\rangle$ are the eigenstates at $t = 0$. It has been assumed that the two mass eigenstates have equal energy ($E_1$ and $E_2$) but different masses ($m_1$ and $m_2$) and momenta ($k_1$ and $k_2$). As mentioned above, if $m_1 \neq m_2$ the mass eigenstates will propagate at different speeds which allows the possibility that a state produced as $\nu_e$ at $t = 0$ may be detected as $\nu_\chi$ at $t > 0$. $P(\nu_e \to \nu_e)$, the probability of producing an electron type neutrino at $t = 0$ and detecting it as an electron type neutrino at $t > 0$ may be calculated as follows.

The following expressions are obtained by substituting (1.8) into (1.6)

$$\begin{aligned} |\nu_e(t)\rangle =& e^{iE_1t-ik_1l}\cos\theta_\nu|\nu_1(0)\rangle + e^{iE_1t-k_2l}\sin\theta_\nu|\nu_2(0)\rangle \\ =& e^{iE_1t-ik_1l}\big(\cos\theta_\nu|\nu_1(0)\rangle + e^{i(k_1-k_2)l}\sin\theta_\nu|\nu_2(0)\rangle\big), \end{aligned} \tag{1.9}$$

where $\theta_\nu$ is the mixing angle between the flavour and mass eigenstates. As the neutrino is relativistic, $E \approx p + \frac{m^2}{2p}$ and $E_1 = E_2$, the difference between the momenta $k_1$ and $k_2$ can be written as

$$k_1 - k_2 \approx \frac{m_1^2}{2k_1} - \frac{m_2^2}{2k_2} \approx \frac{m_1^2 - m_2^2}{2E_\nu} \equiv \frac{\Delta m^2}{2E_\nu}$$

where $E_\nu$ is the energy of the neutrino and $\Delta m^2$ is the difference between the square of the mass eigenstates of neutrino propagation. Substituting this into (1.9) gives

$$|\nu_e(t)\rangle = e^{iE_1t}\big(\cos\theta_\nu|\nu_1(0)\rangle + e^{\frac{i\Delta m^2t}{2E_\nu}}\sin\theta_\nu|\nu_2(0)\rangle\big).$$

The probability amplitude of detecting an electron neutrino at $t > 0$ is

$$\langle\nu_e|\nu_e\rangle = e^{iE_1t}\big(\cos\theta_\nu\langle\nu_e|\nu_1(0)\rangle + e^{\frac{i\Delta m^2t}{2E_\nu}}\sin\theta_\nu\langle\nu_e|\nu_2(0)\rangle\big).$$

Using this and the relation $\langle\nu_i|\nu_j\rangle = \delta_{ij}$, the probability that the neutrino flavour remains unchanged is given by

$$\begin{aligned} P(\nu_e \to \nu_e) =& |\langle\nu_e|\nu_e\rangle|^2 \\ =& |\cos^2\theta_\nu + e^{\frac{i\Delta m^2t}{2E_\nu}}\sin^2\theta_\nu|^2 \\ =& \cos^4\theta_\nu + 2\big(e^{\frac{i\Delta m^2t}{2E_\nu}} + e^{\frac{-i\Delta m^2t}{2E_\nu}}\big)\sin^2\theta_\nu\cos^2\theta_\nu + \sin^4\theta_\nu. \end{aligned} \tag{1.10}$$

As neutrinos travel close to the speed of light, $t$ may be replaced by $L$, where $L$ is the distance between the source of neutrinos and the point of detection. By use of the

identities, $\cos x \equiv \frac{e^{ix}+e^{-ix}}{2}$, $\sin^2 x \equiv \frac{1-\cos 2x}{2}$ and $\cos x \equiv \frac{1+\cos 2x}{2}$, (1.10) may be simplified to

$$\begin{aligned} P(\nu_e \to \nu_e) =& 1 - \sin^2 2\theta_\nu \sin^2\left(\frac{\Delta m^2 L}{4E_\nu}\right) \\ =& 1 - P(\nu_e \to \nu_\chi). \end{aligned} \tag{1.11}$$

The probability of the neutrino flavour remaining unchanged is a function of distance. After a given distance, the neutrino will return to its initial state. This distance is referred to as the *vacuum oscillation length*. Defining the vacuum oscillation length to be $L_\nu = \frac{4\pi E}{\Delta m^2}$, (1.11) may be written as

$$P(\nu_e \to \nu_e) = 1 - \sin^2 2\theta_\nu \sin^2\left(\frac{\pi L}{L_\nu}\right).$$

In the case of solar neutrinos, the variation in distance between creation and detection is much larger than $L_\nu$. Therefore, the mean observed value of $P(\nu_e \to \nu_e)$, i.e. $\overline{P(\nu_e \to \nu_e)}$, is given by

$$\overline{P(\nu_e \to \nu_e)} = 1 - \frac{\sin^2\theta_\nu}{2} = \frac{1}{2}\big(1 + \cos^2 2\theta_\nu\big),$$

as the average value of $\sin^2\left(\frac{\pi L}{L_\nu}\right)$ is $\frac{1}{2}$. This probability can never be less than $\frac{1}{2}$. The majority of solar neutrino experiments have found the probability of survival to be less than $\frac{1}{2}$, implying that the simple case of vacuum oscillations does not apply to solar neutrinos.

### 1.6.2 Matter Enhanced Oscillations

When electron neutrinos travel through matter they can interact with electrons via charge current reactions. Muon and tau neutrinos cannot interact via charged current processes as there are no naturally occurring muons or taus and these neutrinos do not have sufficient energy to produce them. The possibility that an electron neutrino could participate in a charge current interaction introduces an additional potential in the Hamiltonian that only electron neutrinos experience. This idea was first proposed by Wolfenstein [19] and extended by Mikheyev and Smirnov [20]. The difference between the potential experienced by the electron and other flavours ($\chi$) of neutrino is

$$\Delta V = V_e - V_\chi = \sqrt{2} G_F n_e$$

where $G_F$ is the Fermi constant and $n_e$ is the density of electrons in the media through which the neutrino travel. As the mass differences between neutrino states are small and

the mass equivalent of the potential given above can be comparable, matter effects can significantly affect the oscillation.

The vacuum oscillation eigenstates given in (1.6) can be re-written for neutrinos travelling through matter as follows:

$$|\nu_{1m}\rangle = \cos\theta_m|\nu_e\rangle + \sin\theta_m|\nu_\chi\rangle$$
$$|\nu_{2m}\rangle = -\sin\theta_m|\nu_e\rangle + \cos\theta_m|\nu_\chi\rangle$$

where $|\nu_{1m,2m}\rangle$ are the mass eigenstates and $\theta_m$ is the matter mixing angle, defined by

$$\tan 2\theta_m = \frac{\sin 2\theta_\nu}{\cos 2\theta_\nu - \sqrt{2}G_F n_e \frac{E}{\Delta m^2}}. \tag{1.12}$$

If the density of the medium and energy of the neutrino are such that $\sqrt{2}G_F n_e \frac{E}{\Delta m^2} = \cos 2\theta_\nu$ then resonance occurs and $\theta_m = 45°$. As the density of the Sun is not constant, resonance can occur at different points in time as the density of material is effectively time dependent. At the centre of the Sun, $\sqrt{2}G_F n_e$ is large and $\tan 2\theta_m \to 0$, so $\theta_m \to \frac{\pi}{2}$, $\sin\theta_m \to 1$ and $\cos 2\theta_m \to -1$. In this limit, the neutrino mass state $\nu_{2m}$ is identical to the flavour eigenstate $\nu_e$ as the additional potential "raises" the mass of the $\nu_e$. If the density changes adiabatically, the neutrino will remain in the upper energy state, emerge from the Sun as $\nu_2$ and the survival probability, $P(\nu_e \to \nu_e) = \sin^2\theta_\nu$. In general, if the adiabatic condition holds, oscillations between matter eigenstates may be neglected and the neutrino emerges from the Sun as

$$|\nu_e\rangle = -\sin\theta_m|\nu_2\rangle + \cos\theta_m|\nu_1\rangle e^{i\phi}$$

where $\phi = \frac{\Delta m^2 t}{2E_\nu}$. Therefore, in the adiabatic case, the survival probability of electron neutrinos is given by

$$P(\nu_e \to \nu_e) = \sin^2\theta_m \sin^2\theta_\nu + \cos^2\theta_m \cos^2\theta_\nu - 2\sin\theta_\nu \sin\theta_m \cos\theta_\nu \cos\theta_m \cos\phi.$$

Upon reaching the Earth, the average value of the phase factor, $\cos\phi$, is 0. Therefore, the average survival probability is

$$\overline{P(\nu_e \to \nu_e)} = \frac{1}{2}\big(1 + \cos 2\theta_m \cos 2\theta_\nu\big).$$

At low energies, $\theta_m = \theta_\nu$ and the vacuum oscillation case is recovered, while at high energies it is less than $\frac{1}{2}$ and equal to $\sin^2\theta_\nu$. In the Sun, the scale of density variation is large compared with the oscillation length and the adiabacity condition holds true. As a result, the survival probability can be less than $\frac{1}{2}$, as observed by solar neutrino experiments. To further investigate the solar neutrino problem another experiment, SNO, was devised and this is now discussed.

| Phase | Signal | Flux ($\times 10^6$ cm$^{-2}$s$^{-1}$) |
|---|---|---|
| $D_2O$ | CC | $1.76^{+0.11}_{-0.10}$ |
| | NC | $5.13^{+0.64}_{-0.61}$ |
| | ES | $2.39^{+0.26}_{-0.26}$ |
| Salt | CC | $1.68^{+0.10}_{-0.11}$ |
| | NC | $4.94^{+0.43}_{-0.40}$ |
| | ES | $2.35^{+0.27}_{-0.27}$ |

Table 1.3: Summary of results from the first two phases of the SNO experiment

## 1.7 Results from the Sudbury Neutrino Observatory

Before the Sudbury Neutrino Observatory (SNO) experiment, all previous solar neutrino experiments had measured a deficit in the flux of $\nu_e$ from the Sun. Although it was thought that neutrino oscillations explained the observed discrepancy, an experiment capable of measuring all three flavours of neutrino was required to validate this theory. SNO was built to measure independently the flux of $\nu_e$ and the flux of all active neutrino flavours from the Sun. The SNO experiment is described in detail in Chapter 2. It used pure heavy water ($D_2O$) as a target for $^8$B neutrinos which could interact in one of the following three ways:

1. Charged current (CC) which provides a measure of the $\nu_e$ flux.

2. Neutral current (NC) providing a measure of the total flux of solar neutrinos, independent of flavour.

3. Elastic scattering (ES) which measures all three active flavours of neutrino and is 6.5 times more sensitive to $\nu_e$.

If the flux measured by the CC reaction disagrees with that measured by the NC reaction, it confirms that the discrepancy between the measured and predicted flux of solar neutrinos is explained by flavour changing neutrino oscillations.

The first phase of the SNO experiment ran from November 1999 to April 2002 and used pure $D_2O$ as a target. Following the addition of 2 tonnes of sodium chloride (NaCl), to enhance sensitivity to the NC process, the second phase ran from May 2002 to September 2004. Results from both these phases are given in Table 1.3.

Results from the first two phases of the SNO experiment [21, 22, 23] show a clear difference between the fluxes of $\nu_e$ and all neutrinos. The measured flux of all active

flavours (from the NC process) is in good agreement with that predicted by the Standard Solar Model.

Figure 1.3 shows contour plots of the two mixing parameters for the salt phase data [22]. By combining the SNO salt phase results with those obtained by the KamLAND experiment, the best fit values for the mixing parameters are $\Delta m^2_{12} = 8.0^{+0.6}_{-0.4} \times 10^{-5}$ eV$^2$ and $\theta_{12} = 33.9^{+2.4}_{-2.2}$ degrees. The SNO results strongly favour the Large Mixing Angle (LMA) hypothesis of mixing.

## 1.8 Results from KamLAND

The Kamioka Liquid scintillator ANti-neutrino Detector (KamLAND) is located in Japan next to the Super-K experiment (discussed later). KamLAND detects anti-neutrinos produced by 53 nuclear reactors in Japan and it is located at an average distance of 180 km from each reactor. Anti-neutrinos are detected via the following interaction

$$\bar{\nu}_e + \mathrm{p} \rightarrow e^+ + \mathrm{n}$$

which is an inverse beta decay process. The reaction is detected using a delayed coincidence counting method, where the signal is a scintillation light signal from the prompt $e^+$ followed around 220 $\mu$s later by a signal from neutron capture on a proton. The coincidence counting method significantly reduces the number of background signals in the data set. The first results from KamLAND [24] found $0.611 \pm 0.085$ (stat) $\pm 0.041$ (syst) of the expected flux. Assuming charge-parity-time (CPT) conservation and two neutrino mixing, the results excluded all oscillation solutions except the large mixing angle (LMA) solution. The LMA solution will now be discussed.

## 1.9 Large Mixing Angle solution

Results from the SNO and KamLAND experiments strongly favour the Large Mixing Angle (LMA) region of mixing parameter space. The LMA solution assumes that the adiabacity condition holds and neutrinos travel many oscillation lengths during their propagation through the Sun. The survival probability when $\theta_{13}$ is small but non-zero is therefore given by

$$P(\nu_e \rightarrow \nu_e) = \frac{1}{2}(1 + \cos 2\theta_m \cos 2\theta_{12}) \cos^4 \theta_{13}$$

and $\theta_m$ is that given in Equation (1.12). At energies greater than 10 MeV, the density dependent term is greater than 1 and the survival probability reduces to $\sin^2 \theta_{12}$, where $\theta_{12}$ is the vacuum mixing angle. For energies below 2 MeV, resonance is not possible and the

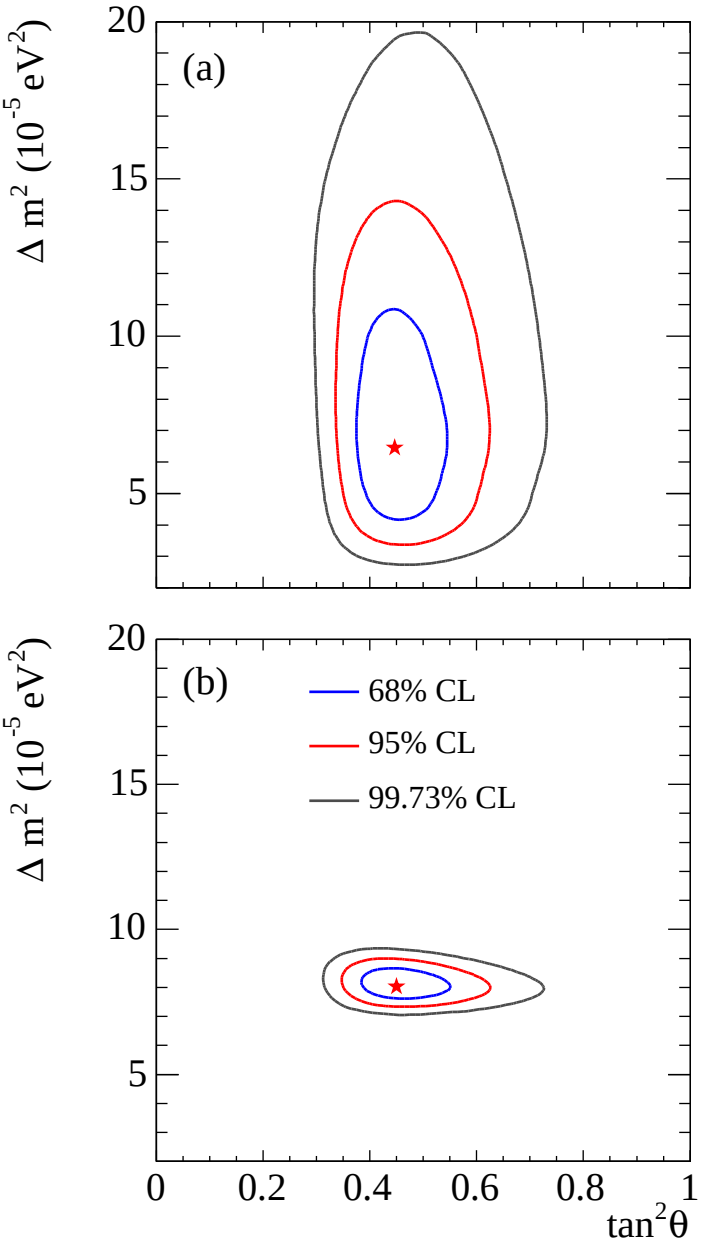


Figure 1.3: MSW contour plots for the salt phase of SNO. (a) is for solar data only and (b) includes results from KamLAND. CL refers to Confidence Level, $\Delta m^2$ is the difference between the square of the masses of the relevant eigenstates of propagation of the neutrinos and $\tan^2\theta$ quantifies the strength of the mixing between the flavour and mass states.

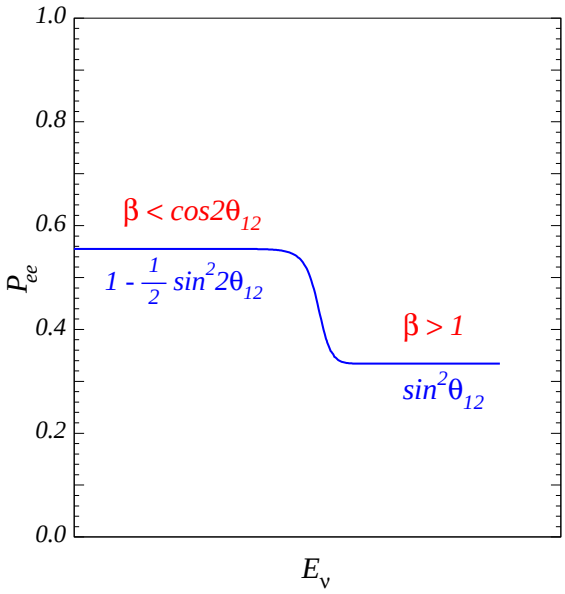


Figure 1.4: Schematic representation of electron neutrino survival probability as a function of energy up to 20 MeV for an LMA solution where $\beta = \frac{2\sqrt{2}G_F n_e E_\nu}{\Delta m^2}$ [25].

survival probability is identical to that for the vacuum oscillation case, i.e. $1 - \frac{1}{2}\sin^2 2\theta_{12}$. For energies between 2 and 10 MeV, the oscillation term is significant, but there is a transition between the two extreme states. A distortion of the energy spectrum in this region is expected but has not yet been experimentally observed. The neutrino survival probability as a function of energy for an LMA solution is shown in Figure 1.4.

## 1.10 Other Neutrino Experiments

In addition to solar neutrino measurements, a number of experiments have observed neutrino mixing. Some of these are now briefly described.

### 1.10.1 Atmospheric neutrino experiments

In addition to solar neutrino measurements, the Super-Kamiokande (Super-K) experiment provides a measurement of the flux of neutrinos produced in the atmosphere [26]. High energy protons from cosmic rays interact with oxygen and nitrogen nuclei in the upper atmosphere to produce pions ($\pi^+$). These subsequently decay producing neutrinos ($\nu_e$ and $\nu_\mu$) and muons ($\mu^+$) via the following processes

$$\pi^+ \rightarrow \mu^+ + \nu_\mu$$
$$\mu^+ \rightarrow \bar{\nu}_\mu + e^+ + \nu_e.$$

Super-K cannot distinguish between $\bar{\nu}_\mu$ and $\nu_\mu$, so the measured ratio of $\nu_\mu$ to $\nu_e$ is expected to be close to 2.

For neutrinos produced in the atmosphere, there will be a significant difference between the distance travelled through the Earth for those produced directly above and directly below the detector. The observed flux of muon neutrinos was found to be strongly dependent on zenith angle, with a large deficit of neutrinos recorded for events travelling through the Earth to the detector. No suppression or excess was observed for electron neutrinos, indicating that muon neutrinos were transforming into tau neutrinos [26]. Results were consistent with neutrino oscillation and the best fit parameters were found to be [26] $|\Delta m^2_{23}| = 2.5 \times 10^{-3}$ eV$^2$ and $\sin^2 2\theta_{23} > 0.96$ (90% CL), proving that neutrinos have mass, contrary to the Standard Model of Particle Physics.

### 1.10.2 Solar Neutrino detection with scintillator

The Borexino experiment is located in the Grand Sasso Laboratory, Italy. The detector consists of a spherical inner volume of organic scintillator doped with PPO (2,5-diphenyloxazole) which is a fluorescent dye. The inner volume is surrounded by a buffer zone containing pseudocumene and dimethylphthalate. The entire detector is surrounded by ultra pure water, to reduce backgrounds. Neutrinos elastically scatter in the inner volume, producing Čerenkov light which is detected by 2212 8 inch photomultiplier tubes.

The Borexino experiment was designed to explore the lower region of the MSW plot given in Figure 1.4 by detecting neutrinos from the monoenergetic $^7$Be process. The first results from the Borexino experiment [27] give a neutrino flux of $45 \pm 7$(stat) $\pm$ 12(syst) counts/(day.100 ton), compared to a Standard Solar Model prediction of $75 \pm 4$ counts/(day.100 ton). These results are consistent with the LMA solution.

### 1.10.3 Accelerator neutrino experiments

Accelerator neutrino experiments involve using an accelerator to produce a pure beam of neutrinos of one flavour and fire it through the Earth. To confirm an appearance or deficit of neutrino flavours, one detector is placed close to the source and another a few hundred kilometers away. The results from each detector are compared to see if the neutrinos have changed flavour. Several such experiments have taken place and the major ones are now briefly described.

#### K2K

The K2K experiment used the Super-K detector to measure a beam of $\nu_\mu$ that had been produced 250 km away at the KEK accelerator facility. Comparison of results from

the near and far detectors showed a deficit in $\nu_\mu$ at the far detector [28]. The best fit parameters were in good agreement with results from Super-K.

#### MINOS

The Main Injector Neutrino Oscillation Search (MINOS) is located at Fermilab and the Soudan mine in the USA. Protons from the Main Injector accelerator (at Fermilab) are used to produce an intense beam of muon neutrinos. This beam is fired a distance of 735 km through the Earth to a far detector located in the Soudan mine. The MINOS experiment was designed to test the atmospheric results and the first results from MINOS were $|\Delta m^2_{23}| = 2.74^{+0.44}_{-0.26} \times 10^{-3}$ eV$^2$ and $\sin^2 2\theta_{23} > 0.87$ (68% C.L.) [29] in good agreement with results from Super-K and K2K.

#### LSND and MiniBooNE

The LSND experiment used a beam of $\bar{\nu}_\mu$ to search for $\bar{\nu}_e$ appearance using a tank of liquid scintillator. If oscillations occurred, $\bar{\nu}_e$s would be detected via an inverse beta decay reaction. An excess of $\bar{\nu}_e$s was observed, but the results were inconsistent with a three flavour neutrino mixing model.

Designed to positively confirm or dismiss the LSND anomaly, MiniBooNE used an 800 tonne detector filled with mineral oil to detect neutrinos produced by the Fermilab booster accelerator approximately 500 m away. First results from the MiniBooNE experiment are consistent with both an absence of oscillations and a two-neutrino appearance only oscillation model [30].

#### T2K

The T2K experiment is currently under construction in Japan and should start taking data in 2009. A beam of $\nu_\mu$ will be produced by an accelerator at the JPARC facility and fired through the Earth to the Super-K detector, approximately 295 km away. The experiment is designed to measure a combination of $\theta_{13}$ and $\theta_{23}$. In the first phase, it is hoped to measure $\theta_{13}$ and if not, improve the current $\theta_{13}$ limit by a factor of 20. If $\theta_{13} \neq 0$ then it may be possible to measure the CP phase and a second experiment involving an upgrade to the Super-K detector would be developed to attempt to measure this. In addition to a measurement of $\theta_{13}$, T2K should make an improved measurement of $\theta_{23}$.

### 1.10.4 Reactor neutrino experiments

The Chooz experiment, located in Chooz, France detects $\bar{\nu}_e$ produced by a nuclear reactor located 1.05 km away from the detector. The experiment is only sensitive to $\theta_{13}$ and the

| Parameter | Value | Experiment |
|---|---|---|
| $\Delta m^2_{12}$ | $7.1^{+1.0}_{-0.3} \times 10^{-5}$ eV$^2$ | SNO/KamLAND |
| $\lvert\Delta m^2_{23}\rvert$ | $2 \times 10^{-3}$ eV$^2$ | MINOS/Super-K |
| $\theta_{12}$ | $32.5^{+1.7}_{-1.6}$ | SNO/KamLAND |
| $\sin^2 2\theta_{23}$ | $\sim 1$ | MINOS/Super-K |
| $\sin^2 2\theta_{13}$ | $< 0.10$ | Chooz |

Table 1.4: Summary of neutrino mixing parameters to date

associated mass difference $\Delta m^2_{13}$ and not matter effects. The results from the Chooz experiment place a limit (90 % CL) on the mixing angle $\theta_{13}$ of

$$\sin^2 2\theta_{13} < 0.10 \text{ for } \Delta m^2_{13} \geq 2 \times 10^{-3}\,\text{eV}^2$$

which limits mixing of $\nu_e \leftrightarrow \nu_\mu$ in atmospheric oscillations.

To improve upon this result, construction of a new experiment at the Chooz site is underway. The Double Chooz experiment will use two detectors located at distances of 1.05 and 0.3 km from the Chooz nuclear reactor. Double Chooz will explore the range of $0.2 > \sin^2 2\theta_{13} > 0.02$ in the first three years of data taking. An improved limit or measurement of $\sin^2 2\theta_{13}$ is expected as two detectors will reduce the systematic error significantly.

## 1.11 Summary of Neutrino Physics

From measurements of the $Z^0$ width at CERN, it is known that there are only three active flavours of neutrino [31]. Recent experiments have measured a number of the parameters associated with neutrino mixing and these are summarised in Table 1.4.

The sign of $\Delta m^2_{23}$ remains unknown along with the true values of $\sin^2 2\theta_{13}$ and $\Delta m^2_{13}$. It is not known whether the CP phase factor $\delta$ is non-zero and whether $m^2_2 < m^2_3$. It is hoped to measure these parameters in future neutrino experiments such as Double Chooz and T2K. Combining information from a Low Energy Threshold Analysis (LETA) of data from phases I and II of SNO, a competitive limit on $\theta_{13}$ should be obtained.

Though the exact mass is still unknown, the oscillation parameters demonstrate that the neutrino has mass which is not included in the Standard Model of Particle Physics. Several theoretical models have been proposed that would incorporate massive neutrinos into the Standard Model.

One theoretical model that would explain the small neutrino mass is that of the neutrino being a Majorana particle. The anti-particle and particle states of Majorana

particles are identical. If the neutrino was a Majorana particle, neutrinoless double beta decay would be allowed. In neutrinoless double decay, the anti-neutrino emitted by the beta decay of a neutron in a nucleus is captured as a neutrino by another neutron in the same nucleus. Energy released by the two beta particles would be equal to the difference in binding energy between the initial and final nuclei. Observation of such a decay would provide an insight into the nature of the neutrino and information about the effective neutrino mass, via the observed event rate.

Some models allow the possibility of a neutrino with mass if the neutrino is a Dirac particle, i.e. its particle and anti-particle states are distinct. A Dirac neutrino would exist in 4 states, left and right handed neutrinos and anti-neutrinos. Two new particles would be added to the Standard Model, namely the right handed neutrino and left handed anti-neutrino. These additional particles would be sterile as the weak interactions only occur with right handed anti-particles and left handed particles.

The third and final phase of the SNO experiment will provide an independent measurement of the total neutrino flux using purpose built Neutral Current Detectors (NCDs). Together with results from the first two phases, this will closely determine the neutrino mixing parameter $\theta_{12}$ and difference in squared masses $\Delta m^2_{12}$. It is expected that combining the data from the three phases of SNO, once analysis of phase III data is complete, will produce a more accurate measure of the Charged and Neutral Current fluxes.

## 1.12 Thesis Outline

This thesis is concerned with determining the neutrino fluxes in phase III of the SNO experiment, in particular the Neutral Current flux. To produce an accurate measurement of neutrino flux, a good understanding and measurement of radioactivity in the detector is required. Any radioactivity in the $D_2O$ can release gammas with energies greater than 2.225 MeV. These can break apart the deuterium nucleus producing a free neutron. This process is indistinguishable from a Neutral Current process and it is vital that this background is measured accurately. Several techniques used to measure this background are presented in this thesis.

A detailed description of the SNO detector is given in Chapter 2. The methods used to detect neutrinos in each of the three phases are outlined, with emphasis on the third phase. The chapter concludes with a discussion of the assay and purification systems used to measure the radioactive content of the detector water.

Sources of background in the detector are discussed in Chapter 3. It details how the majority of backgrounds can be easily excluded from the neutrino data using their charge, timing and PMT distributions. Sources of radioactivity and their effect on the

experimental results are discussed, in particular neutron production via photodisintegration. Two methods used to measure this photodisintegration background are presented in Chapters 4 and 5.

In Chapter 4, levels of uranium and thorium[¶] in the $D_2O$, NCD housings and PSUP[‖] $H_2O$ are determined using a statistical data analysis technique. The methods presented in this chapter are extensions of previous techniques. The number of neutrons produced is calculated using Monte Carlo simulations. These values are subtracted directly from the extracted number of Neutral Current neutrons. An independent measurement of thorium in the $D_2O$ and PSUP $H_2O$ is outlined in Chapter 5. This chemical assay technique extracts activity from the $^{232}$Th chain using Hydrous Titanium Oxide (HTiO) coated filters, connected directly to the water circulation systems underground. The extracted activity is removed from the filters, concentrated and counted using beta-alpha coincidence counting.

The beta-alpha counting system used in the assay technique was prone to failure due to its design and age. Chapter 6 discusses the development of a new, low level beta-alpha coincidence counting system, intended for counting samples from HTiO assays. These counters will be used in a number of forthcoming experiments.

A significant amount of radioactivity was discovered on the surface of one of the Neutral Current Detectors used in the experiment. It was noted that if the composition of this activity had remained unknown, it would have led to an unacceptably high systematic error on the neutrino flux measured during the final phase of the SNO experiment. The development of a chemical technique by the author to determine the composition of this surface contamination is described in Chapter 7. Finally, work presented in Chapter 8 investigates the feasibility of a PMT only measurement of the Neutral Current flux in the final phase of the SNO experiment.

[¶]Note that throughout this thesis, uranium and thorium are used as shorthands for $^{214}$Bi and $^{208}$Tl daughters. For the purposes of comparison it is assumed that they are in equilibrium with $^{232}$Th and $^{238}$U which in SNO is generally not true. The main consequence of this is a significant difference in the measured concentration of U chain activity in the $D_2O$ and $H_2O$ due to Rn ingress, resulting in a higher neutron background.

[‖]PMT Support Structure

# Chapter 2

# The SNO detector

As discussed in Chapter 1, the Sudbury Neutrino Observatory (SNO) experiment was developed to detect solar neutrinos and to investigate the solar neutrino problem. The experiment was divided into three phases, namely, pure $D_2O$, salt and NCD. In this chapter, the physics of neutrino detection in SNO will be outlined, with emphasis on the third phase of the experiment, which is most relevant to this thesis. Calibration of the detector and inspection of data quality is briefly discussed. The chapter concludes with a description of the assay and purification systems and their relevance to this thesis.

SNO was a heavy water ($D_2O$) Čerenkov detector capable of detecting all three flavours of neutrino, independently of electron neutrino flux. SNO's target was 1000 tonnes of $D_2O$ held within a 5 cm thick 12 m diameter acrylic vessel. Inside the acrylic vessel, during the third phase, 40 strings of Neutral Current Detectors (NCDs) were anchored. The vessel was surrounded by 1700 tonnes of ultra pure water ($H_2O$) and 9456 photomultiplier tubes (PMTs) mounted on a geodesic support sphere. The region between the support structure and the cavity wall was filled with approximately 5300 tonnes of ultra pure $H_2O$. The purpose of these two $H_2O$ regions was to reduce radioactivity from sources outside the $D_2O$. The SNO experiment was located underground in the CVRD-INCO Creighton Mine, Sudbury, Ontario, Canada, at a depth of 2039 m. At this depth, the norite rock overburden is equivalent to 5890 m of water. The rock shielded the detector from cosmic rays and muons, reducing the muon flux to approximately 70 events per day.

A 12 metre diameter acrylic sphere was used to contain the $D_2O$ and to ensure that it did not come into contact with the surrounding $H_2O$. A spherical design was chosen for the containment vessel to maximise the surface to volume ratio and to optimise stress distribution. This reduced the amount of acrylic needed and thus the radioactive content of the detector. The sphere was constructed from 122 individual acrylic panels, which were nominally 5.6 cm thick, with the exception of 10 rope grove panels in the equatorial plane that were 11.4 cm thick. The sphere had a centrally placed "neck", 6.8 m tall and

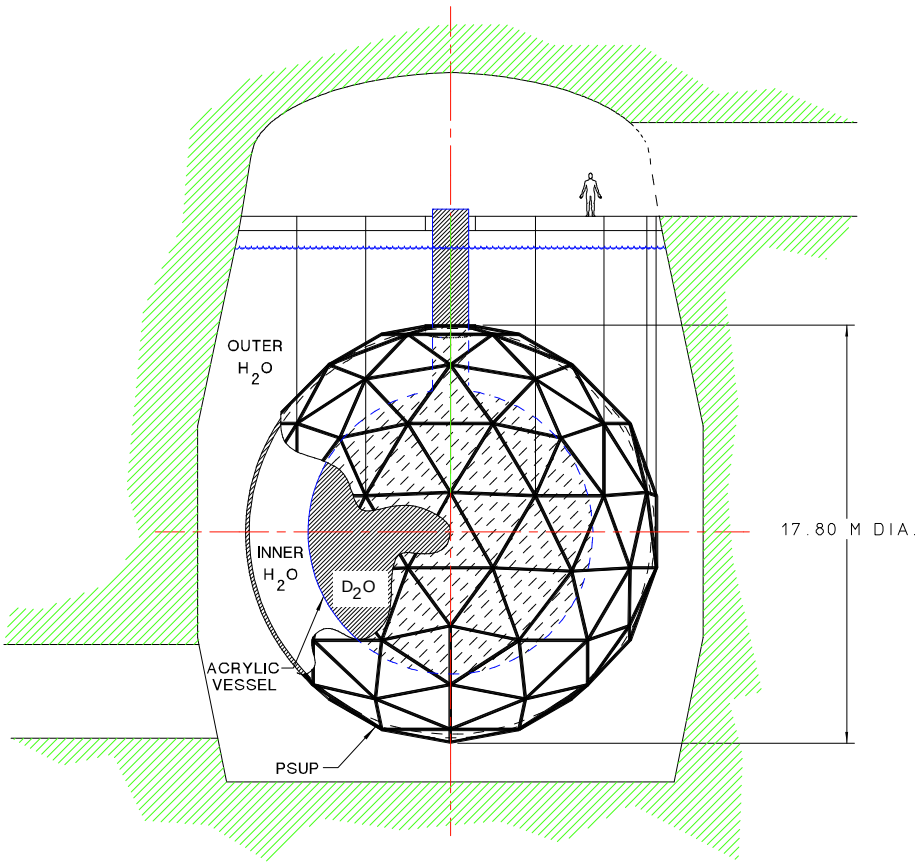


Figure 2.1: Schematic of the SNO detector.

1.5 m in diameter. This allowed calibration sources and the Neutral Current Detectors to be deployed into the $D_2O$ volume. In addition, piping for recirculation and assay purposes entered and exited the $D_2O$ volume through this neck. The SNO detector is shown in Figure 2.1 [32]. In this chapter, the neutrino detection methods and detector design are discussed. First, the phenomenon of Čerenkov radiation, the principle behind the detector design, will be discussed.

## 2.1 Čerenkov Radiation

When energetic charged particles pass through a dielectric medium with refractive index $n$ at a velocity greater than the speed of light in that medium $(c/n)$, each particle emits

a coherent wavefront of light. This is known as the Čerenkov effect, named after its discoverer. The wavefront forms the surface of a cone, with the particle trajectory as its axis, such that

$$\cos\theta = \frac{c}{vn}$$

where $c$ is the speed of light in vacuo, $v$ is the particle's velocity in the medium and $n$ is the refractive index of that medium. In $D_2O$, $n = 1.32$.

Electrons produced in the SNO detector with energies greater than the Čerenkov threshold emit photons with a Čerenkov angle of approximately 42°. The electrons will produce Čerenkov light until their energy drops below the Čerenkov threshold of about 262 keV. Neutrino interactions in the $D_2O$ produce Čerenkov light that is detected by an array of photomultiplier tubes. Each of these neutrino interactions is now discussed.

### 2.1.1 Charged Current

The Charged Current (CC) interaction is sensitive to electron type neutrinos only

$$\nu_e + \mathrm{D} \rightarrow \mathrm{p} + \mathrm{p} + \mathrm{e}^- \tag{2.1}$$

where D is the deuterium nucleus. The interaction proceeds via $W^+$ exchange and has a threshold of 1.44 MeV. The emitted protons are essentially produced at rest, implying that the energy of the recoil electron is effectively 1.44 MeV less than that of the incident neutrino. This relation allows the energy spectrum of the $^8$B solar neutrino flux to be determined.

The angular distribution of the recoil electron is weakly correlated to the direction of the incident neutrino with the form

$$f(\theta_\odot) \approx 1 - \frac{v_e}{3c}\cos\theta_\odot \tag{2.2}$$

where $\cos\theta_\odot$ is the cosine of the angle of the direction of the recoil electron relative to the Sun, $v_e$ is the initial speed of the recoil electron and $c$ is the speed of light in the medium [21]. The recoil electrons are emitted with sufficient energy to produce Čerenkov light and this is detected by the PMT array. If no neutrino oscillation takes place, the number of incoming neutrinos measured by this process should equal that predicted by the Standard Solar Model.

### 2.1.2 Elastic Scattering

The elastic scattering process is sensitive to all three flavours of neutrino. However, the cross-section for electron type neutrinos is approximately 6.5 times larger than that for a

muon or tau type as it may proceed by $Z^0$ or $W^+$ exchange,

$$\nu_x + e^- \rightarrow \nu_x + e^- \tag{2.3}$$

where $x$ is any flavour of neutrino. This produces an energetic electron that tends to travel in the same direction as the incident neutrino. The angular distribution of the electron is strongly correlated to that of the incident neutrino, confirming that these neutrinos do come from the Sun. As this is a scattering process, there is no threshold and its differential cross-section can be quoted directly from electroweak theory [33]:

$$\frac{d\sigma}{dT_e} = \frac{2G_F^2 m_e}{\pi}\left[g_L^2 + g_R^2\left(1 - \frac{T_e}{E_\nu}\right) - g_L g_R\left(\frac{m_e T_e}{E_\nu^2}\right)\right] \tag{2.4}$$

$$g_L = \left(\pm\frac{1}{2} + \sin^2\theta_W\right),\ g_R = \sin^2\theta_W,\ \sin^2\theta_W \sim 0.23$$

### 2.1.3 Neutral Current

The Neutral Current (NC) process:

$$\nu_x + \mathrm{D} \rightarrow \nu_x + \mathrm{p} + \mathrm{n} \tag{2.5}$$

is equally sensitive to all three active flavours of neutrino, where $x$ is any flavour of neutrino. The energy threshold of this process is set by the binding energy of the deuterium nucleus, 2.225 MeV. The reaction does not produce Čerenkov light directly, but it is detected by capturing the free neutron produced. Three methods have been used to detect this free neutron, each one corresponding to a phase of the SNO experiment.

In the pure $D_2O$ phase of the experiment, the free neutron was captured by the deuterium nucleus forming an excited state of tritium. This excited state decayed to its ground state by emission of a 6.25 MeV gamma. This gamma Compton scattered, producing electrons that generated Čerenkov light.

Following the pure $D_2O$ phase, 2 tonnes of ultra pure sodium chloride (NaCl) were added to the $D_2O$ to improve neutron detection efficiency and the amount of Čerenkov light produced. Neutron capture on $^{35}$Cl produced an excited state of $^{36}$Cl which relaxed to its ground state through a gamma cascade. The total energy of this cascade was 8.6 MeV. Again, these gammas Compton scatter, producing electrons capable of emitting Čerenkov light.

At the end of the salt phase, the $D_2O$ was de-salinated using a reverse osmosis unit and an array of 40 Neutral Current Detectors (NCDs) was deployed in the $D_2O$ region. The NCDs are $^3$He proportional counters which capture neutrons via the following reaction:

$$^3\mathrm{He} + \mathrm{n} \rightarrow \mathrm{p} + {}^3\mathrm{H} + 764\ \mathrm{keV}. \tag{2.6}$$

The ionisation produced by the proton and triton was detected by a central anode wire, producing a pulse. During the NCD phase, a small number of neutrons were captured by deuterium nuclei, identical to the pure $D_2O$ case described above. The potential of using this process to provide a measurement of the NC flux is discussed in Chapter 8.

The NC reaction gives neither spectral nor directional information about solar neutrinos. However, it is important in that it does give a flavour independent measurement of the total number of solar neutrinos. Comparison of the NC interaction rate with that of the CC interaction rate provides a model independent measurement of flavour changing solar neutrino oscillations. A non-unity ratio of NC to CC events indicates that non-electron type neutrinos are reaching the Earth from the Sun, supporting the theory of flavour changing neutrino oscillations.

## 2.2 Photomultiplier Tubes

The Hamamatsu R1409 photomultiplier tube (PMT) was selected for use in SNO. It consisted of an evacuated glass shell whose inner surface was covered with a thin layer of photocathode. Photons incident upon this layer liberated electrons via the photoelectric effect. The quantum efficiency of this photocathode was $\sim 10\%$ for wavelengths in the range of 250-500 nm [34]. The signal was amplified through a nine chain dynode stack with a total gain of $10^9$. Each PMT was supplied with a voltage in the range 1700-2100 V through a single 75 $\Omega$ cable which also connected the PMT to the front end electronics. The connection at the base of the PMT was made using a waterproof connection which was sealed with heat shrink tubing and thermal adhesive. The cavity inside the enclosure was filled with a dielectric silicone gel which acted as a second water seal.

Levels of $^{238}$U and $^{232}$Th in the PMTs were $< 120$ ng/g $^{238}$U (90% CL) and $< 90$ ng/g $^{232}$Th (90% CL), approximately a factor of 14 lower than the levels specified in the original design report [35]. These low levels were achieved using specially manufactured low radioactive glass (Schott 8246) in all of the PMTs.

There were 9438 PMTs facing inwards toward the acrylic vessel (AV) and these provided a photocathode coverage of 31%. To improve their efficiency, a 27 cm diameter light concentrator was mounted on each PMT, increasing effective photocathode coverage to around 54% [36]. Each concentrator was made from 18 pieces of thin dielectric coated aluminium sheets, each in a holder made of acrylonitrile-butadine-styrene (ABS) plastic. Every aluminium strip was coated with quarter wavelength thick layers of different refractive indices. These layers enhanced the reflectivity and also protected the aluminium layer from corrosion during its immersion in $H_2O$. The concentrators maximised the number of photons detected but limited the angular acceptance of the PMTs. The maximum

accepted angle corresponded to a radius of 7 m, which was in the inner light water region of the detector.

A further 91 PMTs faced outwards towards the rock walls of the detector cavity. These detected light from muons and other sources of activity outside the PMT support structure (PSUP). Another 23 tubes were attached to a sled and submerged in the cavity water to assess the impact of continuous submersion. This sled was removed during decommissioning and the tubes are being assessed. Finally, 4 smaller tubes were mounted in the neck of the acrylic vessel to veto any possible events originating from that region.

The PMTs were read by a set of custom built electronics. Each PMT cable was connected to one of 19 electronic crates located on the deck above the detector. The PMT cables were connected to one paddle card. Four paddle cards were mounted on a PMT Interface Card (PMTIC) which was connected to the backplane of the crate. In addition to reading out the signal from each PMT, the PMTIC controlled the high voltage supply to the tubes connected to it. Each PMTIC was connected to a Front End Card (FEC) containing 4 daughter boards (DBs). The DB digitised each signal and stored timing and charge information for the PMTs on capacitors. Each FEC processed 32 channels and had an associated PMTIC. Sixteen FECs and their associated PMTICs were held in a crate, each one of which was able to process signals from up to 512 PMTs.

The pulse from each PMT travelled along the PMT cable to the PMTIC. The signal was passed from the PMTIC to the FEC where a threshold was applied, via a discriminator. If the amplitude of a PMT pulse exceeded this threshold, the discriminator produced a 100 ns pulse. The 100 ns pulses from all 32 channels on the FEC were summed and the sum of the summed triggers for each FEC were summed in a Crate Trigger Card (CTC). Each of the 19 CTC values were sent to the Master Trigger Card Analogue (MTC/A) which was located in a Timing Rack. It was here that the signals were summed into an analogue pulse, whose amplitude was proportional to the total number of PMTs that fired within 100 ns of each other in the event. A 100 ns window was used to ensure all of the prompt and late light was collected for each event. As the PMT array was 17 m in diameter, photons from an interaction in the $D_2O$ may have a time spread of up to 66 ns.

The MTC/A had three discriminators: LOW, MED and HI. If the summed pulse exceeded any threshold, the MTC/A sent a pulse to the Master Trigger Card/Digital (MTC/D) which was also held in the Timing Rack. If the MTC/D received a signal from a trigger that it was configured to look for, a Global Trigger was sent to all crates in the system. The timing and charge information of each tube that had fired was digitised and stored on the FECs. Each FEC was read out by an XL2 interface card. Each XL2 card was read out by an XL1 located on the timing rack and the XL1 cards were read out by

Figure 2.2: Schematic diagram of the NCD array in SNO. The acrylic vessel and neck are shown along with part of the PMT array and part of the NCD array.

the embedded CPU (eCPU) computer. The eCPU computer read out the data to a Sun computer Data Acquisition System (DAQ) where the data was built into zdab files and written to tape.

## 2.3 Neutral Current Detectors

An array of 40 NCDs was deployed in the $D_2O$ region to provide an independent measurement of the NC flux as data taken by the NCDs and PMTs was completely independent. Figure 2.2 is a schematic representation of the SNO detector with part of the NCD array installed. The NCD counter data are not used directly in this thesis, however, their construction is important for the assessment of radioactivity which is discussed in Chapter

4. A schematic diagram of an NCD is given in Figure 2.3.

The neutron produced by a Neutral Current (NC) interaction in the $D_2O$ was detected once it had been captured. In the first phase of the SNO experiment, NC neutrons were captured by deuterium nuclei, producing an excited state of tritium that decayed to its ground state by emission of a 6.25 MeV gamma. This gamma subsequently Compton scattered, producing Čerenkov light. In the second phase of the experiment, 2 tonnes of sodium chloride was added to the $D_2O$. NC neutrons were captured by $^{35}Cl$, creating an excited state of $^{36}Cl$ which emitted 8.6 MeV of gamma rays that Compton scattered, producing Čerenkov light. At the end of the second phase, the salt was removed using a reverse osmosis unit and an array of 36 $^3He$ and 4 $^4He$ Neutral Current Detectors (NCDs) was installed in the $D_2O$ volume.

Each NCD housing was manufactured from purified nickel formed into 2 m long, 5.08 cm diameter tubes. Once received from the manufacturer, the tubes were cut to length, weighed, leak tested, straightened, flared at one end, electropolished, acid etched, rinsed in alcohol and baked under high vacuum overnight. The tubes were then used to make 2 or 3 metre long proportional counters. This was achieved by laser welding sections of nickel tube together, adding electrical feed throughs and end caps at either end. An anode wire was fed through the full length of the counter and then the counter was filled with purified $^3He$ gas. Three or four counters were coupled together electrically, forming an NCD string with a single read out wire. Finally, a cable assembly was added to the top and a delay line added to the bottom of the string.

Helium-3 was chosen for its large neutron capture cross-section, its use in neutron detection being well established. Neutrons entering the gaseous region of the $^3He$ counters induced the reaction given in Equation (2.6). This process produced a back to back proton triton pair of 764 keV, where the proton carried away 573 keV of the total energy. Both of these ions produced over 20,000 electron ion pairs in the gas. The electrons drifted towards a central anode wire where they underwent avalanche multiplication, producing a large number of secondary electron ion pairs, which produced a signal on the anode.

The resulting neutron spectrum was not a sharp peak at 764 keV. In some cases, a neutron was captured near the wall of the counter and the proton, triton or, in rare cases, (approximately 0.1% of the time) both could strike the wall before depositing all of the energy in the gas. In these instances, the energy deposited in the gas by the neutron would be less than 764 keV. A typical neutron energy spectrum is shown in Figure 2.4, taken from [37].

There were several mechanisms by which background events could appear in the range of the spectrum. Radioactive nuclei embedded in the counter body and anode wire could emit alphas that produced a broad spectrum of ionisation events. Electrons from

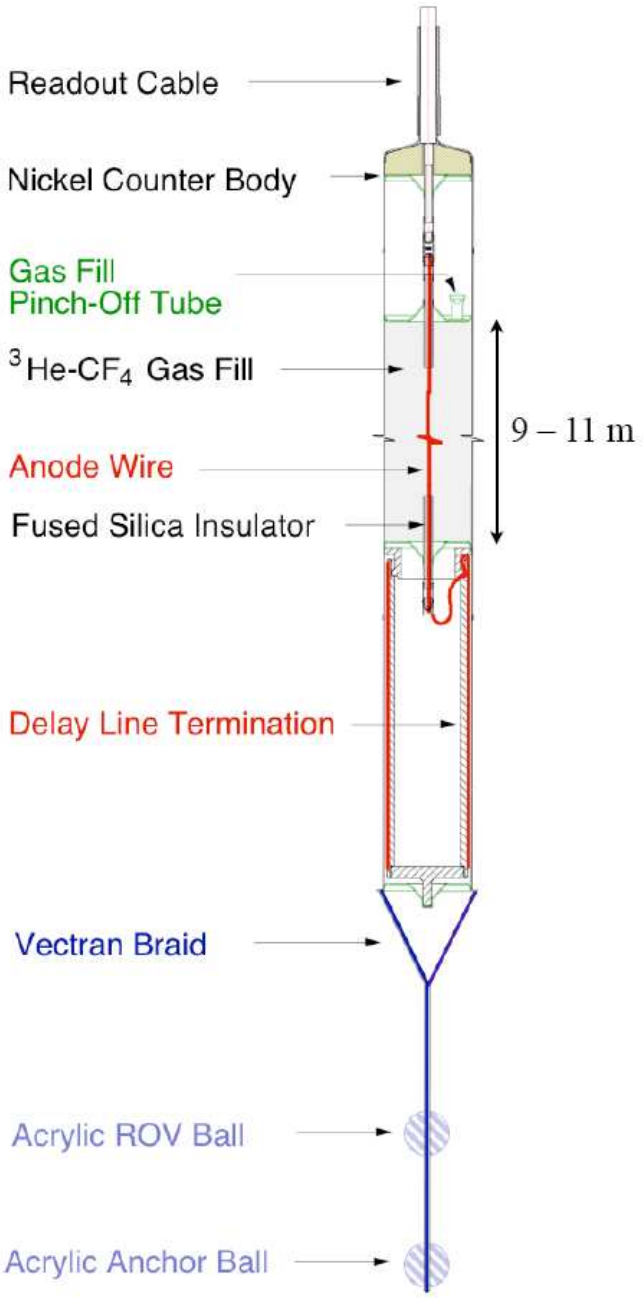


Figure 2.3: Schematic diagram of an NCD. Each NCD is constructed from 3 or 4 counters which are electrically coupled and welded together. Figure taken from [37]. Note that ROV is a shorthand for Remote Operated Vehicle, which was a submarine used to deploy and remove the NCDs from the detector.

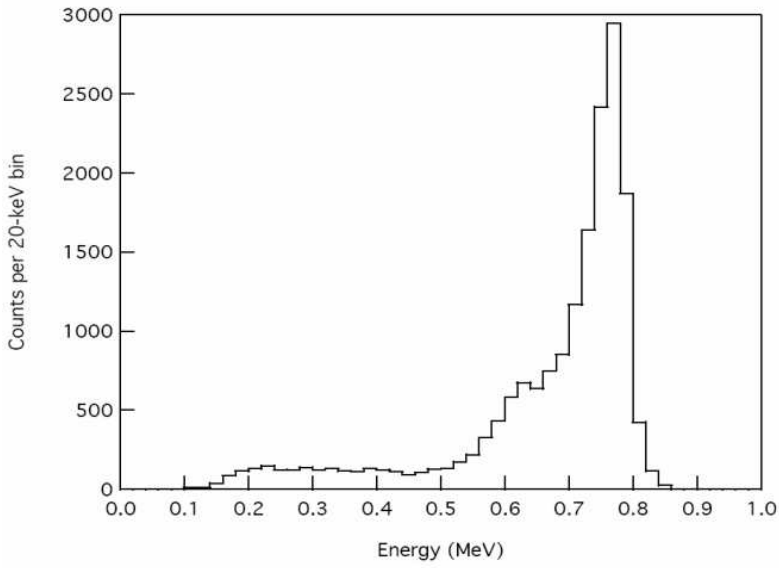


Figure 2.4: NCD array neutron capture spectrum from a uniformly distributed $^{24}$Na calibration. The peak at 764 keV corresponds to the deposition of the full triton and proton energies. The broad shoulder at 573 keV corresponds to the total absorption of the triton's energy in the wall.

beta decays, Compton scattering and photoelectrons required multiple scatters to deposit sufficient energy in the gas and as such these were not as serious a problem. The amount of tritium present in the gas was kept to extremely low levels to avoid pile up of betas from tritium decay. The amount of tritium in the NCDs was minimised by purification of the $^3$He gas. If the amount of tritium was low, the primary source of background would be from naturally occurring alpha emitters.

Each event detected by the NCDs was read out by a series of electronics designed to record the total charge of each event, record information at the kHz level in the case of a supernova and provide information that would allow pulse shape discrimination. This would allow neutrons to be distinguished from alphas and non-neutron non-alpha events. To ensure all of these were possible, two independently triggered read out systems were used; a fast data path using shaper ADCs and a multiplexing digitising path [38].

Each NCD was connected to a current pre-amplifier feeding into a multiplexer (MUX) box, which split the signal in two. One pulse entered shaping circuitry followed by an analogue to digital converter (ADC) where the current of the signal was integrated, producing a value that was directly proportional to the energy. Each channel had a shaper/ADC allowing high read rates, up to several kHz, in the event of a supernova.

The other pulse from the MUX box followed a different path, where the time profile

of the current reaching the anode wire was digitised. If the pulse passed the digitisation threshold, it was logarithmically amplified and sent through a 300 ns delay and summing junction to an oscilloscope, where it was digitised. In all, two oscilloscopes each with four channels were used. Each digitised event consisted of 15,000 points in 1 ns bins. The first 1,500 points, equivalent to 1.5 $\mu$s, occurred before the trigger and, thus, only contained baseline noise. After this, the MUX trigger occurred and the following 300 ns corresponded to the delay between the MUX and scope. The rest of the digitisation time was taken up with the pulse.

The two triggers, shaper and MUX were completely independent and many background events only triggered one of the two paths. The MUX trigger was based upon a fast integration of the current signal from the NCD and was, therefore, a current trigger. Small amplitude events would not trigger this path. The trigger for the shaper/ADC path was a charge trigger. The signal was shaped and integrated continuously over a 6 $\mu$s period. If the pulse exceeded a pre-determined threshold, the shaper/ADC was triggered and the shaped and integrated charge of the event recorded. Narrow events with a large amplitude triggered the MUX path, but not the shaper ADC path. In general, physics events triggered both the MUX and shaper/ADC channels.

The data from the NCD array were read out and recorded using the Object-orientated, Real-time Control and Acquisition (ORCA) software. This was designed and written by the University of Washington, purposely for the NCDs. Hardware settings could be controlled and monitored using ORCA.

## 2.4 Calibration

To determine accurately the energy, position, direction and timing of an event, the detector had to be calibrated. Regularly deployed calibration sources were used to assess the response of the detector as a function of time. Approximately 30% of the detector livetime was spent calibrating.

Calibrations could be split into three broad classes: electronic, optical and those involving sources to calibrate the response to physics events. Electronic calibrations assessed how the PMTs and NCDs responded once they received an input that passed the discriminator threshold. The optical calibrations measured the properties of the $D_2O$, $H_2O$, acrylic and PMTs.

Calibration sources were deployed through the neck of the acrylic vessel. Above the neck was the Deck Clean Room (DCR) which provided a clean environment for preparing calibration sources before they were deployed in the detector. A source manipulator system was connected to the neck and the source was deployed through this, minimising

the risk to the detector. The source could be moved around the detector using a series of ropes attached to the manipulator. The manipulator could not be used in the $H_2O$ region between the AV and PSUP but calibrations could take place using a series of guidetubes.

During the NCD phase several distributed sources were deployed into the $D_2O$ and inner $H_2O$ volumes. This involved injecting a liquid (activated sodium) or gas ($^{222}Rn$) directly into the water of the detector. This is described in greater detail in Section 2.4.5.

### 2.4.1 Electronics Calibration

There were two sets of electronics calibrations, one for PMT electronics and another for NCD electronics. There were two PMT calibrations: measurement of the PMT charge pedestals and TAC* slope readings for a channel. The PMT charge pedestal measured the zero offset of the ADC and the TAC slope measured the relationship used to convert from the measured TAC to time. Both of these measurements changed with time and were, therefore, performed twice weekly as well as after any electronics crate was turned on, for example following repair.

There were three weekly NCD calibrations; logamp, linearity and threshold. The logamp calibration measured the parameters associated with logarithmic amplification and waveform digitisation. Pulses were injected into each NCD preamplifier to trigger the DAQ system and approximately 30 pulses were collected on each of the 40 NCD channels. Parameters that described the amplification and digitisation were extracted from the data. The linearity calibration measured the gains and pedestal of each NCD and also tested the linear response of the system. Each shaper ADC channel was pulsed with a square wave at 50 Hz for 5 seconds. Over this time period, the amplitude of the pulse was increased to test the linearity of the shaper ADCs. Any non-linearity was quantified as the difference between the measured charge and best fit value. The intercept from the linear equation was then used along with the peak position in a neutron calibration spectrum to convert shaper ADC values to energies. The threshold calibration extracted the threshold for each MUX and shaper ADC in terms of the input pulse amplitude and total charge. Each NCD was injected with 1.0 $\mu$s sine waves with amplitudes between 6 and 31 mV at a rate of 10 Hz. This lasted for approximately 5 seconds on each NCD. The collected data were analysed to determine which of the pulses triggered the MUX and shaper ADC systems, making it possible to determine the threshold of each NCD.

*Time to Analogue Converter

### 2.4.2 PMT Calibration

The phototube calibration (PCA) measured the charge and timing response of a phototube. The discriminators used in the SNO electronics fired at fixed voltages. The charge pulse resulting from a single photon incident on a PMT could vary by as much as a factor of 2. Pulses with higher charges fired the discriminator earlier. This effect was referred to as "PMT walk". The difference in timing could be as much as 2 ns, which could impact upon the accuracy of the event fitters and energy estimators.

The PCA required a light source to fire the PMT. A specially designed "laserball" which emitted a short, 10 ns, pulse of light was deployed in a number of positions throughout the detector, at a number of different wavelengths, to assess this affect. The different wavelengths were produced using a 50 MHz laser producing 0.6 ns width bursts of 337.1 nm wavelength light and one of four dye cells.

The laserball was used to produce a profile of light behaviour in the detector. This profile was used to calculate optical constants and the relative efficiencies of the PMTs. In the NCD phase, the data were also used to assess the shadowing and reflectivity of the NCD array.

### 2.4.3 Energy Calibration

Nitrogen-16 ($^{16}$N) was the primary source used for energy calibration. $^{16}$N was produced via an (n,p) reaction on oxygen in $CO_2$. Once produced, $^{16}$N beta-gamma decayed with a 7.13 second half life. The dominant branch produced a single 6.13 MeV gamma which could be used to calibrate the energy estimator. The source was held in a stainless steel container (can) to absorb electrons released by the decay. The source can contained a PMT that triggered when a decay occurred, helping to reduce any non-source events in the calibration data set.

### 2.4.4 Neutron Calibration

Several sources were used to determine the neutron capture efficiency and profile. An Americium-Beryllium (AmBe) source was used to produce neutrons via a $^{9}$Be($\alpha$,n)$^{12}$C reaction, which has a $Q$-value of 5.701 MeV. This reaction almost always decays to the first excited state or ground state of the resultant carbon nucleus. If the decay is to the first excited state of $^{12}$C, a 4.44 MeV gamma is released. Careful study [39] found that the ratio of 4.44 MeV gammas to neutrons emitted by the source was 0.6 and was independent of the source preparation and geometry. The neutron could only be detected once it had been captured and it took a finite time to do this. The 4.44 MeV gamma was a prompt gamma and could, therefore, be used to tag the neutron.

| Region | Source | Date |
|---|---|---|
| $D_2O$ | $^{24}Na$ | October 2005 |
| $D_2O$ | $^{222}Rn$ | August 2006 |
| $D_2O$ | $^{24}Na$ | October 2006 |
| $H_2O$ | $^{222}Rn$ | November 2006 |

Table 2.1: Distributed sources deployed during the NCD phase.

The second neutron point source was a canned $^{252}Cf$ source. Approximately 3.1% of $^{252}Cf$ decays are spontaneous fission, releasing neutrons. The remaining decays are alpha emissions. The source was housed in a solid acrylic cylinder that absorbed betas released by fission fragments. Contamination from gammas remained but a radial cut around the source reduced this contamination, producing an almost pure neutron source.

### 2.4.5 Distributed sources

During the NCD phase a number of distributed sources were deployed. These sources were produced by injecting a small amount of liquid or gaseous radioactivity into one of the water regions of the detector. The activity was distributed and mixed using the water circulation systems. This type of calibration in SNO is commonly referred to as a spike. A full list of spikes in the NCD phase is given in Table 2.1. A small sample of salinated $D_2O$ was activated at a nuclear reactor in Kingston, Ontario. The neutrons produced by the reactor were captured by Na atoms in the solution, producing $^{24}Na$. Sodium-24 beta decayed, emitting a 1.38 and a 2.76 MeV gamma with a 14.95 hour half life. A small proportion of the source was measured using a germanium detector, located underground in the SNO laboratory, to determine the source strength. The sample was injected into the detector and the source was mixed using the water circulation systems. This produced a uniform source that could be used for neutron and also low energy background calibrations. Both sodium spikes were manufactured using identical methods.

A $^{222}Rn$ spike was produced by collecting radon from the lab air, using a degassing trap and a Lucas cell (see Section 2.7.3). Once collected in Lucas cells, the Rn was transferred into a Marinelli beaker and it was connected to the $D_2O$ water systems degasser which was operated in a regassing mode. The Rn was then circulated into and around the detector. The circulation direction was reversed after some time to speed up the mixing. The water systems are described in Section 2.7.

The $H_2O$ Rn spike was produced using a commercially available Ra source. This decays, producing Rn which was collected using a degassing trap and Lucas cell. To ensure that no Ra was present in the final sample, the gaseous Rn was passed through an

aqueous solution of HTiO. No significant amount of Ra was detected, using the techniques described in Chapter 5.

## 2.5 Data Quality

The NCD phase lasted 731 days, from November 27th 2004 to November 28th 2006. During this period, the detector was operated almost continuously with small shutdown periods for power outages and detector maintenance. During the time when the detector was operational (online), not all data taken was suitable for neutrino analysis. Calibration runs accounted for approximately 30% of the time and neutrino running 62.5%. The *run selection committee*[†] decided which runs were suitable for analysis. The total time of all of the selected "good" runs was referred to as the detector livetime.

Every shift operator on SNO had to fill in a report during their detector shift. The shift report was a summary of detector conditions, activities and procedures performed during the shift. Each shift report was read by two members of the run selection committee who would consider environmental factors, such as detector temperature and humidity, and check if the unusual conditions (UC) bit was set. The UC bit may have been set for a number of reasons, an assay might have been taking place, a source may have been "parked" in the neck overnight etc. In some circumstances the data was still usable. In addition to reading shift reports, the run selection committee monitored the output from two nearline SNOMAN[‡] processors and these are now described.

### 2.5.1 First pass selection

Each neutrino run was processed by the first pass selection (FPS) module in SNOMAN. The FPS module extracted the run mask from the data. The run mask, set by the detector shift operator, defined the type of run (neutrino, calibration etc.), whether an assay was taking place via the SL[§] or $D_2O$ was circulating and also whether anything unusual was happening in the detector (UC bit). FPS also extracted the number of electronics crates online (PMTs), number of NCDs online, the duration of the run, the fractional deadtime due to burst cuts and the voltage of each NCD. Selection criteria were then applied to this information and if all of the conditions were met the run was processed by the second pass selection module. The full set of selection criteria are outlined in [40].

[†]The author of this thesis was a member of this group from March 2005 until the end of data taking
[‡]SNOMAN = SNO Monte Carlo Analysis program. It is described in Section 2.6.
[§]SL assay is the name given to a sample line or Rn assay

### 2.5.2 Second pass selection

The second pass selection module (SPS) was used to apply a higher level of cuts to the data. In particular SPS looked at the PMT and NCD event rate during the run. The length of the run measured by the 10 and 50 MHz clocks was compared and checks on the PMT and NCD event rates were made.

Rarely, unsuitable runs passed the FPS and SPS checks. For example, if the cover gas of the $D_2O$ was disrupted Rn would have entered the detector and caused an elevated background rate. The affected runs would pass the FPS and SPS checks as the extra events would be genuine physics events. The run would, however, be rejected because of elevated background levels. Fortunately, no runs with elevated backgrounds were found in the NCD phase, but a number of runs were removed from the runlist for other similar concerns.

## 2.6 SNOMAN

The SNO Monte Carlo and ANanlysis code, SNOMAN, was the Monte Carlo analysis package used by the SNO collaboration [41]. It was used to process raw data from the detector for further analysis and to simulate the detector. The propagation of electrons, gammas and Čerenkov photons was modelled using EGS4 and neutron propagation was modelled using MCNP. The SNOMAN package contains a full description of the detector electronics, geometry, trigger system, data acquisition system and response functions.

## 2.7 Water Systems

Naturally occurring uranium-238 and thorium-232 cause an irreducible background to the Neutral Current process. To minimise the contribution from these isotopes, all materials used in the SNO experiment were specially selected for radioactive purity. Strict limits on the radioactive content of the three water regions were set and these will be discussed in the next chapter. Before use in the SNO detector, both the heavy and light water were purified to ensure that target radiopurity levels were met. Additionally, all plastic components of the water purification and circulation systems were built from low radioactivity polypropylene, referred to as SNO grade polypropylene.

There were two independent water systems; one for $D_2O$ and one for ultra pure $H_2O$. Both systems were used to purify and regularly assay the water in each detector region. These systems are now discussed.

### 2.7.1 Light Water

$H_2O$ was taken directly from the mine supply. After falling to a depth of 6800 feet, the water was saturated with air which had to be removed. The water passed through a deaerator to remove some of the dissolved $N_2$ and $O_2$. It then passed through a multi-media filter consisting of a bed of sand and charcoal to trap large particles. Immediately downstream of this filter was a 10 micron filter to trap any fine particles that remained. At this point the water entered the underground laboratory and passed through a charcoal filter to remove organic matter. It then entered a series of cation exchange resins to remove divalent ions. The addition of EDTA formed complexes with ionic species in the water. These were removed by the zeolite softeners. The water was passed through a reverse osmosis (RO) unit to remove insoluble inorganic matter. After the RO unit a UV lamp was used to break down any remaining organic matter into an ionic form which could be removed by the ion-exchange unit that followed.

A Process Degasser (PDG) was then used to thoroughly degass the water. Completely degassed water caused low pressures inside the PMT connectors which led to tube breakdown. To prevent this, the water was partially regassed with pure $N_2$. It was cooled to 10 °C before it entered the detector. The lower temperature was chosen as it helped reduce PMT noise and biological growth in the detector. An overview of the $H_2O$ systems is shown in Figure 2.5.

### 2.7.2 Heavy Water

To ensure high isotopic purity (99.92%), only $D_2O$ that had not been previously used in a nuclear reactor was loaned from Atomic Energy of Canada Ltd. Before being pumped into the acrylic vessel for the first time, the $D_2O$ was passed through a series of ion exchange columns and a reverse osmosis unit to further improve the quality of the water.

The primary function of the $D_2O$ water systems during the lifetime of the experiment was to purify and assay the existing $D_2O$. During an assay, $D_2O$ was circulated through MnOx or HTiO loaded columns on a regular basis to determine the amount of Th present. Once the water had passed through the assay columns, it flowed through an ultrafiltration unit to ensure that fines from the adsorbents did not pass into the detector. An overview of the $D_2O$ systems is given in Figure 2.6. The assay techniques will now be discussed.

### 2.7.3 Assays

The radiopurity of the water in each of the three water regions was measured by regular assay. The water systems were used to circulate water from the detector through the

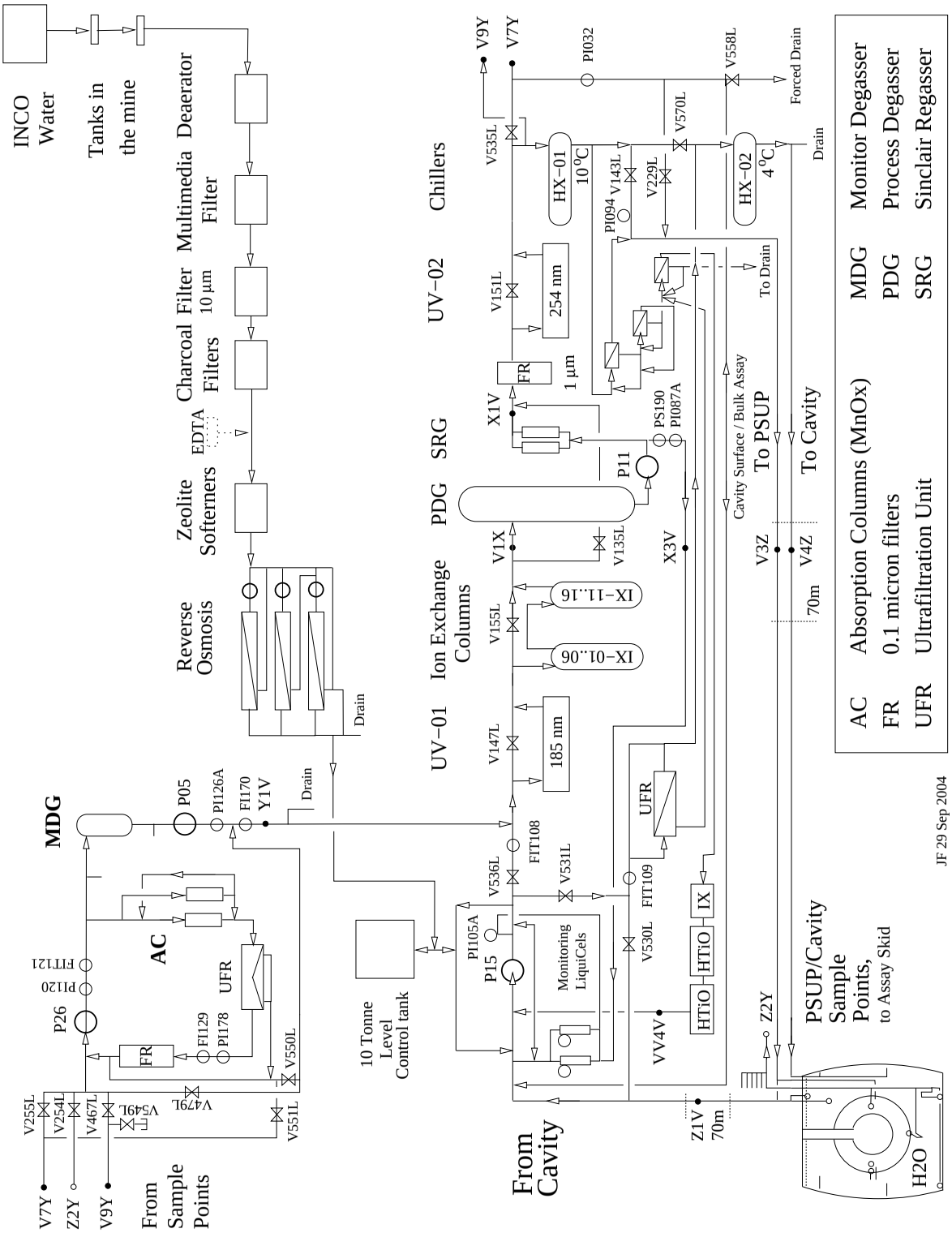


Figure 2.5: Overview of the $H_2O$ systems. Figure provided by J. Farine.

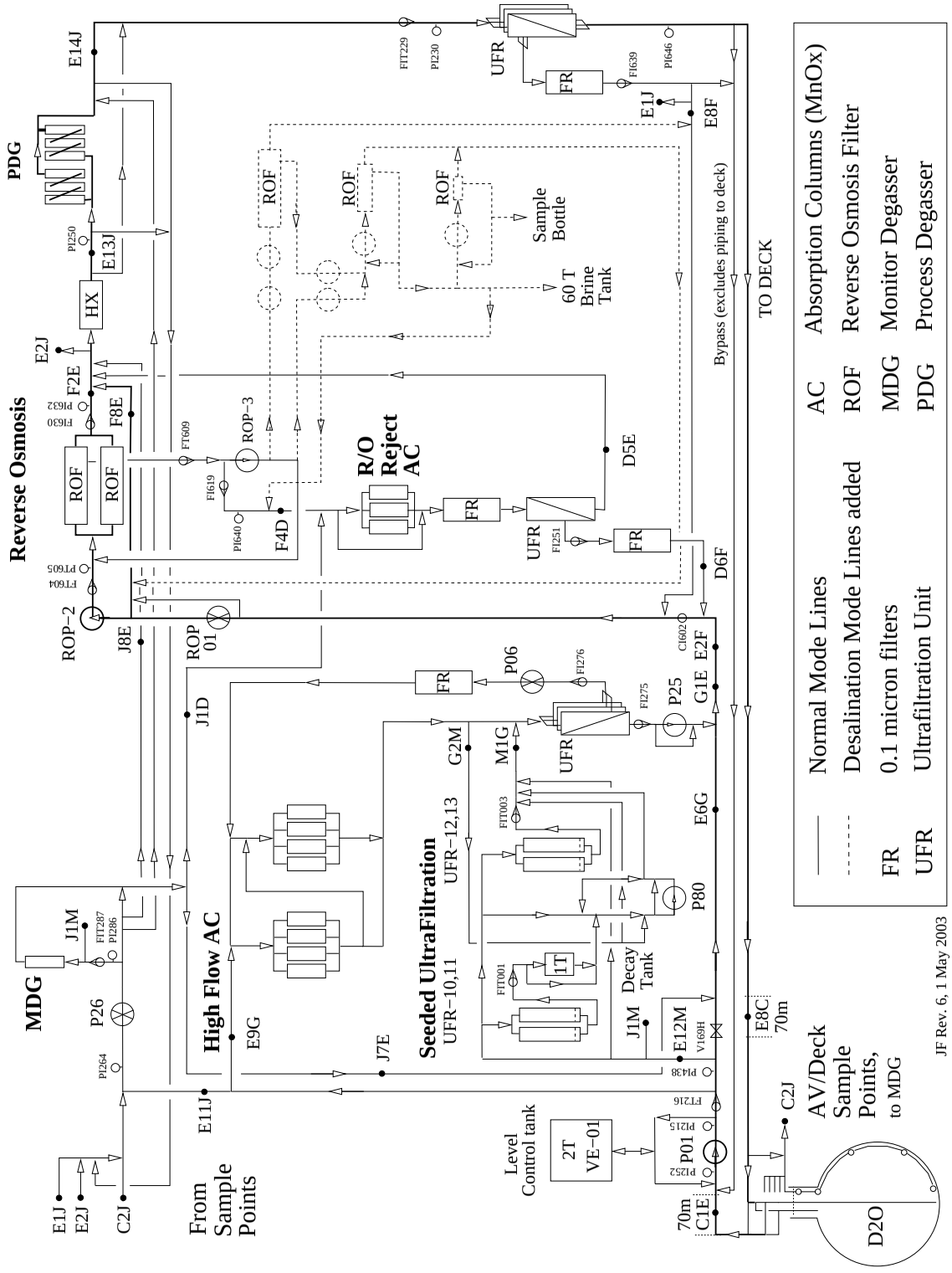


Figure 2.6: Overview of the $D_2O$ systems. Figure provided by J. Farine.

deck loop piping where it was assayed before it was returned to the detector. Three complimentary techniques were used and these are now described.

### Radon degassing

Water from the detector was passed through a degasser to remove dissolved gases. The degasser was connected to a vacuum system which removed Rn by taking advantage of its high boiling point compared with other gases. Rn was collected on a cold (liquid nitrogen temperature) trap until about 6 tonnes of $D_2O$ or 0.5 tonnes of $H_2O$ had been processed. After extraction, the accumulated Rn was transferred to a Lucas cell mounted on a PMT to count the alpha particles produced by the decay of $^{222}$Rn. The amount of Rn measured using this method was a direct measure of the amount of uranium chain activity in the detector. Technical details of this technique are given in [42].

### Manganese Oxide (MnOx) assay

Acrylic beads coated with Manganese Oxide (MnOx) were used to fill a polypropylene column. Water from one of the three detector regions was passed through two of these columns. Dissolved Ra was removed from solution and trapped on the beads. Once the assay was completed, the columns were removed, dried and connected to an Electrostatic Counter (ESC). Gaseous Rn, from the decay of $^{224}$Ra was forced into the ESC using nitrogen gas. Once inside the ESC, the Rn decayed producing charged polonium ions which were directed to a solid state alpha counter by means of an electric field. The amount of Ra and hence Th in the water was inferred from the amount of Po measured by the counters. Further details of this method can be found in [43].

### Hydrous Titanium Oxide (HTiO) assay

Water from one of the three regions of the detector was passed through two columns containing membranes coated with hydrous titanium oxide (HTiO). Radium, thorium and lead were absorbed by the HTiO. Once extraction was complete, the columns were removed from the water systems and taken to surface where the activity was removed by eluting the columns with 15 litres of 0.1 mol/$l$ HCl. This solution was concentrated to a final volume of 8 ml and added to liquid scintillator. The amount of Ra in the sample was determined using beta-alpha coincidence counting and the amount of Th and U present in the water was determined. This assay technique is discussed in detail in Chapter 5.

Levels of Ra and Th in the $D_2O$ were so low that any Ra or Th contamination in the piping between the output of the assay columns and the return to the detector was non-negligible. As these sources were after the columns, they did not affect the measured assay activity. However, they would result in finite amounts of activity being injected

into the detector. To minimise this background, a deck loop clean took place before each $D_2O$ assay. This involved circulating $D_2O$ around a closed loop which contained a single HTiO column for approximately 4 hours before a $D_2O$ assay began. This removed any significant Ra contamination. This procedure was not performed for $H_2O$ assays as the signal observed in the assay samples was approximately 20 times larger than this background. Results from the three *ex-situ* methods were time and volume weighted to provide a measurement of $^{232}$Th and $^{238}$U concentrations in each region of the detector.

# Chapter 3

# Backgrounds

This chapter examines, in greater detail, sources of background found in the SNO detector. Subsequent chapters deal with their measurement. Approximately 10-15 neutrino interactions were expected to occur each day in the SNO detector. The observed raw event rate could be anywhere between 40 and 60 Hz for the PMTs and around 0.4 Hz for the NCDs, indicating that additional non-neutrino events occurred in the detector. These background events were caused by a number of processes and could be divided into two broad classes; instrumental and physical. Instrumental backgrounds were associated with the PMT and NCD electronics and were said to be *non-physics* events. Physical backgrounds were events caused by real physics processes, such as spallation following the passage of a cosmic muon through the detector or radioactive decays. The majority of instrumental and physical backgrounds could be removed from the data set by applying selection criteria, or cuts, to the data. As the cuts were not 100% selective, a very small amount of these backgrounds remained in the data set and a very small amount of real data was lost. The cuts were tuned using Monte Carlo and calibration data and any contamination and sacrifice of the data accounted for. The two classes of background will now be discussed in detail.

## 3.1 Instrumental backgrounds

The main causes of instrumental backgrounds in SNO were associated with PMT or NCD electronics. Common modes for PMTs included electronic pick up, cross talk, breakdown, static discharge and failure of the PMT. For the NCDs, the effects included microdischarge, oscillatory noise, random noise fluctuations and "fork" events.

Electronic pickup affected both the NCD and PMT arrays. External influences on the read out electronics, such as a person walking on the deck above the detector or use of a piece of electronic equipment, caused high event rates. A high event rate on the

PMT array could cause pickup on the NCD electronics and vice versa. Pickup events were easily excluded from the PMT data set as they fired all channels on several crates and had a charge that integrated to zero. This was clearly unphysical. In the case of the NCDs, no clear peaks were observed and the pulse looked very flat, unlike a neutron or alpha event.

The most common PMT instrumental background was the flasher. Flashers occurred when one PMT gave off a large pulse of light, thought to be caused by static discharge somewhere inside the PMT, probably in the dynode stack. The pattern of hit PMTs for a flasher was usually a tight ellipse, observed on the opposite side of the detector to the PMT that produced it. This is very different to a neutrino event, where the pattern of hit PMTs was a smeared ring. This allowed good discrimination between neutrino and flasher events.

Breakdown, static discharge and PMT failure events were less common, but still needed to be removed from the data set. Their high charge and unusual crate distribution allowed them to be easily separated from neutrino events. A full description of these events and their removal from the data set is given in [44].

An NCD fork event was believed to be caused by discharge inside a string causing a pulse that was reflected. Such pulses had a decay time much shorter than that of a neutron, allowing it to be cut from the data [45]. The dominant source of NCD instrumental backgrounds was oscillatory noise caused by pickup in the DAQ system. These events could be removed by requiring events to trigger both the shaper-ADC and digitised data paths. Both paths had amplitude triggers which allowed some events to be rejected on the basis that they did not trigger one of the paths. Some non-physics events remained and these could be removed using a set of data cleaning cuts [45].

## 3.2 Physical backgrounds

Physical backgrounds describe any event caused by *real* physics. Examples include muon followers, ($\alpha$,n) reactions and radioactive decays. These events produce Čerenkov light distributions that can look similar to neutrino events and are thus harder to eliminate from the data. Types of physical backgrounds are now discussed.

### 3.2.1 Muons and muon followers

Even at the depth of SNO, cosmic muons could pass through the rock overburden and enter the detector, producing Čerenkov events. Due to their high energy, these muons activated (fired) a large number of PMTs; far more than any neutrino event. As such,

muons were easily removed from the data set by placing an upper bound on the energy of each event.

More difficult to remove were the events that followed the muons, called muon followers. As muons entering the SNO detector had high energies, they could cause spallation of deuterium and oxygen in the $D_2O$ region producing a burst of neutrons. The only effective way to eliminate these events from the data was to remove any event that occurred within 20 s of a muon. This resulted in a significant loss of detector livetime ($\sim 1.94\%$), but was necessary to remove muons from the data set.

### 3.2.2 Neutral Current induced reactions

During the salt phase, there was a small probability that a Neutral Current event could produce a background to itself. Neutrons were most likely to capture on $^{35}$Cl as its neutron capture cross-section was far larger than that of deuterium. Neutron capture on $^{35}$Cl created an 8.58 MeV excited state of $^{36}$Cl which decayed to its ground state by gamma emission via one or more of its 75 excited states. The neutrino interaction was then detected via Compton scattering of these gammas. However, if the gammas emitted from $^{36}$Cl decays had certain energy characteristics, there was a small probability that two events could be detected from one incident neutrino interaction. A double event could occur if the gamma cascade contained one gamma that had sufficient energy to photodisintegrate a deuteron i.e. an energy greater than 2.225 MeV and at least one other gamma capable of producing Čerenkov light above the detector energy threshold. The neutron produced by photodisintegration could then capture on $^{35}$Cl producing another gamma cascade. A detailed description of the analysis of these events is given in Appendix A.

Five double events were observed in the salt phase data [23] and it was hypothesised that this mechanism may have been responsible. Analysis of the salt Neutral Current Monte Carlo data set found 13 doubles in 267,617 Neutral Current events which agreed with a theoretical estimate of 10 double events in 267,617 Neutral Current events. The Monte Carlo was run at 200 times the rate of the neutrino data and the results were scaled to produce an estimate of the number of these events in the salt phase data set. The expected number of doubles was

$$\text{Number of doubles} = \frac{13}{200} = 0.065$$

Therefore, the 5 double events found in the salt neutrino data set were not due to this particular type of double event. They are thought to have been caused by neutron followers from muons, or incorrect modelling of atmospheric neutrinos [46]. As the salt

has now been removed from the detector these events are no longer of any concern in the NCD phase.

### 3.2.3 Radioactive backgrounds

The dominant physical background arose from natural radioactivity present in trace quantities in all components of the SNO detector. Radioisotopes such as $^{232}$Th and $^{238}$U (Figures 3.1 and 3.2 taken from [47]) decayed, releasing betas and gammas which had sufficient energy to produce detectable Čerenkov signals. Čerenkov light produced by these processes was indistinguishable from that produced by Charged Current interactions and could only be removed by imposing a lower energy limit on neutrino event selection. In addition, $^{232}$Th and $^{238}$U decayed to daughter products that emitted gammas with energies greater than 2.225 MeV, the binding energy of the deuteron. Such gammas could break the deuterium nucleus apart producing a free neutron and proton. This process is referred to as photodisintegration. The free neutron was captured, producing a signal identical to the Neutral Current interaction. Unlike the background to the Charge Current interaction it could not be removed from the data by means of an energy cut. The neutron background must be carefully monitored and measured with the aim of subtracting it from the final Neutral Current number. In order to obtain an accurate measurement of the Neutral Current flux, a good understanding of neutron production from radioactivity is crucial. The measurement and understanding of neutron production by radioactivity is the subject of this thesis and the methods used to measure it will be discussed in detail in later chapters. There were several mechanisms by which radioactivity could produce neutrons and these will now be discussed.

#### ($\alpha$,n) reactions

Naturally occurring $^{238}$U and $^{232}$Th decays produced alphas which could produce neutrons by interacting with nuclei such as $^{2}$H, $^{13}$C, $^{17}$O and $^{18}$O. These nuclei were present in the $D_2O$, $H_2O$ and acrylic ($C_5H_8O_2$) of the detector, making neutron production possible. Fortunately, the cross-sections for these reactions were very small, making the resulting number of neutrons small. The largest source of ($\alpha$,n) reactions was the acrylic. During construction, it was exposed to mine air containing a significant amount of $^{222}$Rn, whose daughters were electrostatically attracted to the acrylic. Although radon has a relatively short half life, 3.82 days, it eventually decays to $^{210}$Pb which has a half life of 22.26 years. $^{210}$Pb decays to $^{206}$Pb via $^{210}$Po and emission of a 5.30 MeV alpha. This 5.30 MeV alpha was thought to be the largest contributor to ($\alpha$,n) reactions in the detector. The presence of this 5.30 MeV alpha was confirmed by placing a silicon counter close to the surface of the acrylic in the neck and measuring the alpha activity.

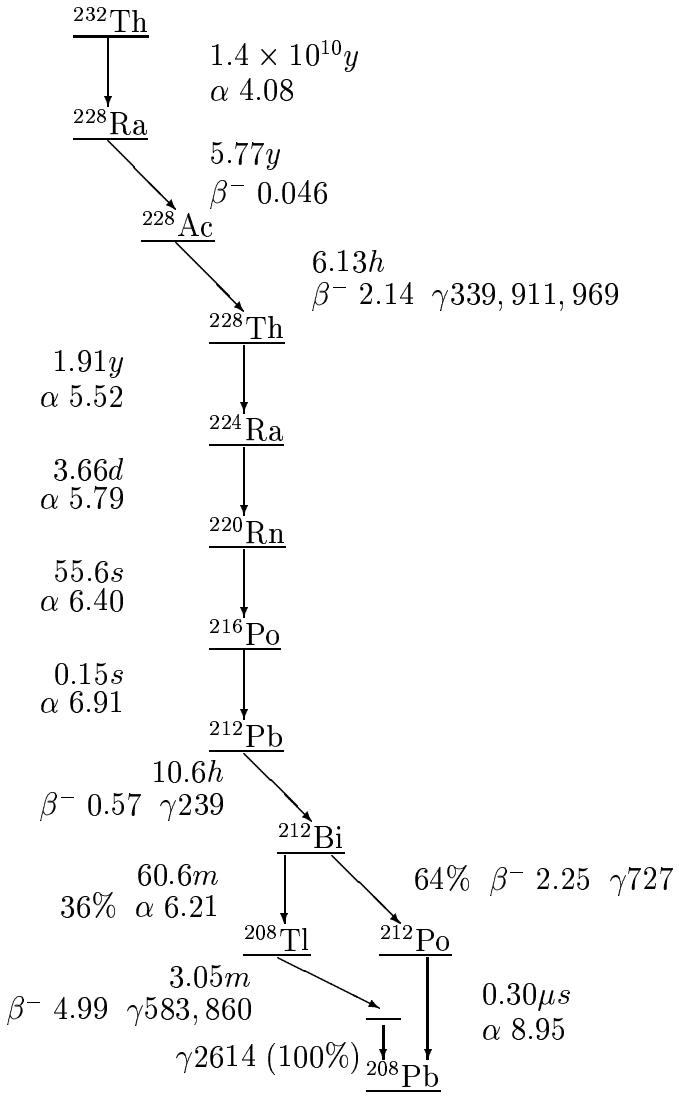


Figure 3.1: The decay chain of $^{232}$Th. All half-lives are shown, with the $Q$-values of beta and alpha decays in MeV, and gamma rays in keV.

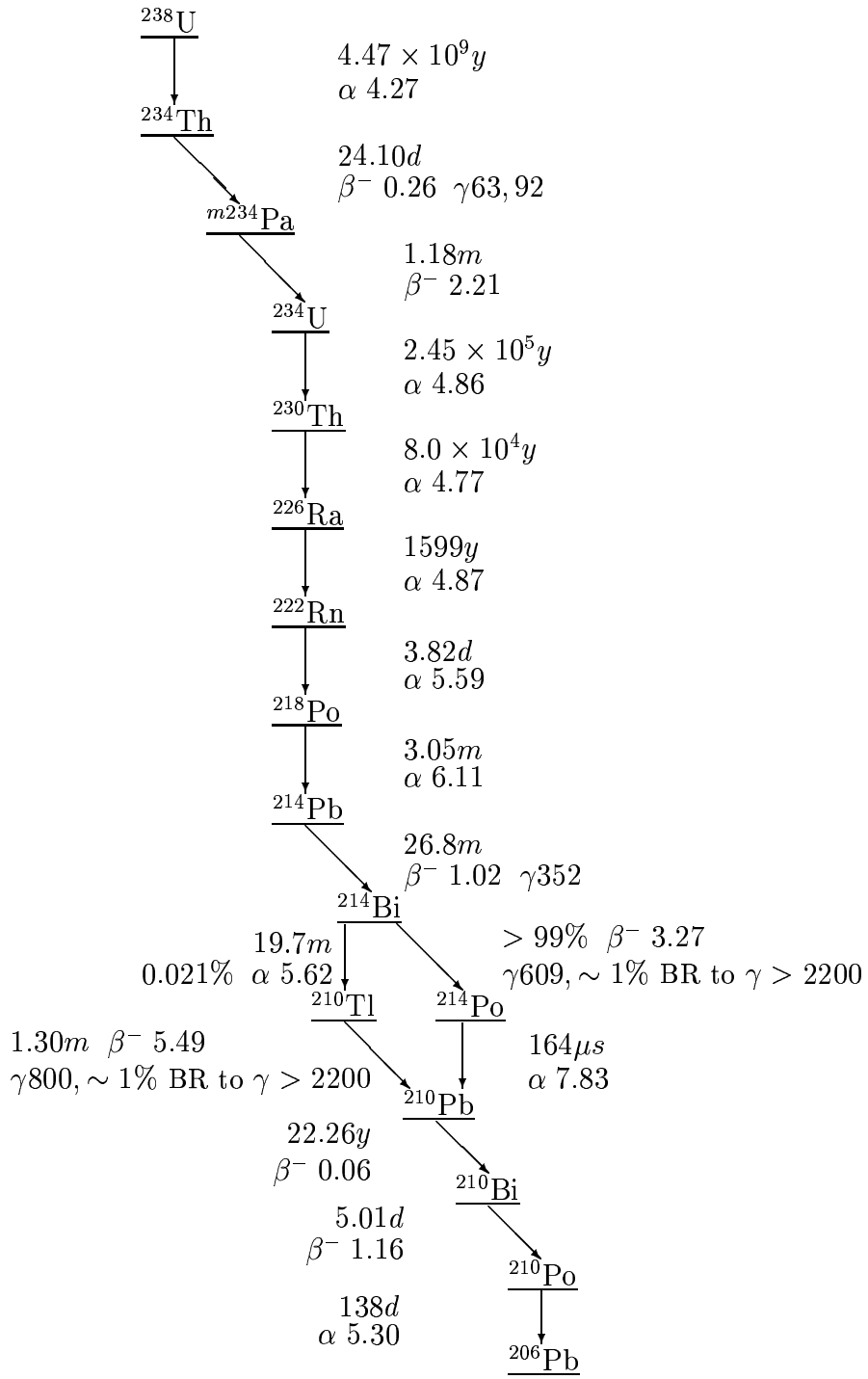


Figure 3.2: The decay chain of $^{238}$U. All half-lives are shown, with the $Q$-values of beta and alpha decays in MeV, and gamma rays in keV.

A small contribution to the total number of neutrons produced by ($\alpha$,n) reactions arose from $^{210}$Po present on the outer surface of the NCDs. The NCDs were electropolished before deployment in the detector, but a small amount of $^{210}$Po remained. After removal from the detector, a representative sample of the NCDs were counted using an external alpha counter [48] and the rate of neutron production determined to be $1.38 \pm 0.28 \times 10^{-2}$ neutrons per day.

#### Fission

Naturally occurring $^{238}$U can undergo spontaneous fission, with a half life measured to be $8.2(1) \times 10^{15}$ years, equivalent to a branching fraction of $5.45 \times 10^{-7}$ [49]. Fission events caused a burst of neutrons which could be removed from the data using the standard data cleaning cuts [45].

#### External beta-gamma events

Radioactivity in the $H_2O$, PMTs and construction materials of the PSUP produced betas and gammas. These could be misreconstructed into the neutrino signal window and an estimate of the contamination was made using an external thorium source. The source was used to construct radial probability density functions and these were used in a fit to the data. For energies above 6.5 MeV and radii less than 550 cm, $3.9^{+10.2}_{-2.4}$ events were found in the data [50] .

### 3.2.4 Photodisintegration

As mentioned in Section 3.2.3, any gamma with an energy greater than 2.225 MeV could break apart the deuterium nucleus releasing a free neutron, the signal from which was identical to that from the Neutral Current interaction. Naturally occurring radioactive isotopes emit such gammas during their decays. Due to their relatively high natural abundance, only $^{238}$U and $^{232}$Th were of concern in SNO. Both radioisotopes emit gammas with energy above 2.225 MeV towards the end of the decay chains.

The $^{232}$Th decay scheme, shown in Figure 3.1, has a 36% branching fraction to $^{208}$Tl. Thallium decays to $^{208}$Pb emitting among other particles, a 2.614 MeV gamma capable of photodisintegration. The decay scheme of $^{208}$Tl is shown in Figure 3.3. At 2.6 MeV, the Compton scattering cross section is much greater than that for photodisintegration, by a factor of approximately 500, reducing the probability of a $^{208}$Tl decay producing a neutron. The number of $^{208}$Tl decays required to produce one neutron was calculated, using SNOMAN [51], to be $482.8 \pm 6.9$ decays.

Approximately 10 Neutral Current neutrino interactions were expected to occur each day in the SNO detector. If the radioactive content of the detector was too high, neutron production via photodisintegration would be so great, that a measurement of the NC flux would be impossible. Therefore, upper limits on radiopurity levels corresponding to a neutron production rate of 1 per day were imposed in the $D_2O$ region.

Assuming that any $^{208}$Tl in the detector was in secular equilibrium with $^{232}$Th, the number of $^{208}$Tl decays required to produce one neutron could be used to calculate the limit in terms of the concentration of the activity. The radioactive decay law is

$$\text{Rate} = -\frac{dN}{dt} = \lambda N \tag{3.1}$$

where $\lambda$ is the radioactive decay constant for the radioisotope of interest and $N$ is the number of atoms of the radioisotope. If $^{232}$Th is in equilibrium with $^{208}$Tl then (3.1) may be written as

$$\text{Rate} = -\frac{dN}{dt} = 0.36\lambda_{Th}N_{Th} = \lambda_{Tl}N_{Tl}. \tag{3.2}$$

A production rate of one neutron per day is equivalent to 482.8 Tl decays per day. Substituting this and $\lambda_{Th}$ into (3.2) gave the number of $^{232}$Th atoms $\sim 9.8 \times 10^{15}$. This may be converted into a mass using Avogadro's number and the relative atomic mass of $^{232}$Th, giving rise to a limit of 3.7 $\mu$g of $^{232}$Th in the $D_2O$.

$^{238}$U decays to $^{206}$Pb via $^{214}$Bi as shown in Figure 3.2. Approximately 2.5 % of $^{214}$Bi decays emit a gamma with energy above 2.225 MeV. A simplified $^{214}$Bi decay scheme is shown in Figure 3.4. Approximately $32,051 \pm 962$ $^{214}$Bi decays were required to produce one neutron [51], calculated using SNOMAN. An analogous calculation to that for $^{208}$Tl, set a limit of 30 $\mu$g of $^{238}$U in the $D_2O$ if the background from $^{238}$U was to remain below one neutron produced per day.

## 3.3 Sources of radioactivity in SNO

During construction of the detector, all components were selected for radioactive purity. In spite of this, some traces of radioactivity remained and these were responsible for the radioactive background processes discussed in this chapter. In addition, the rock from which the cavity was excavated contained a non-negligible source of radioactivity. Sources of radioactivity in the detector are now discussed.

### Rock

The norite rock from which the SNO detector cavity was excavated contained $^{238}$U (1.2 ppm) and $^{232}$Th (3.3 ppm). The critical backgrounds were high energy gammas released

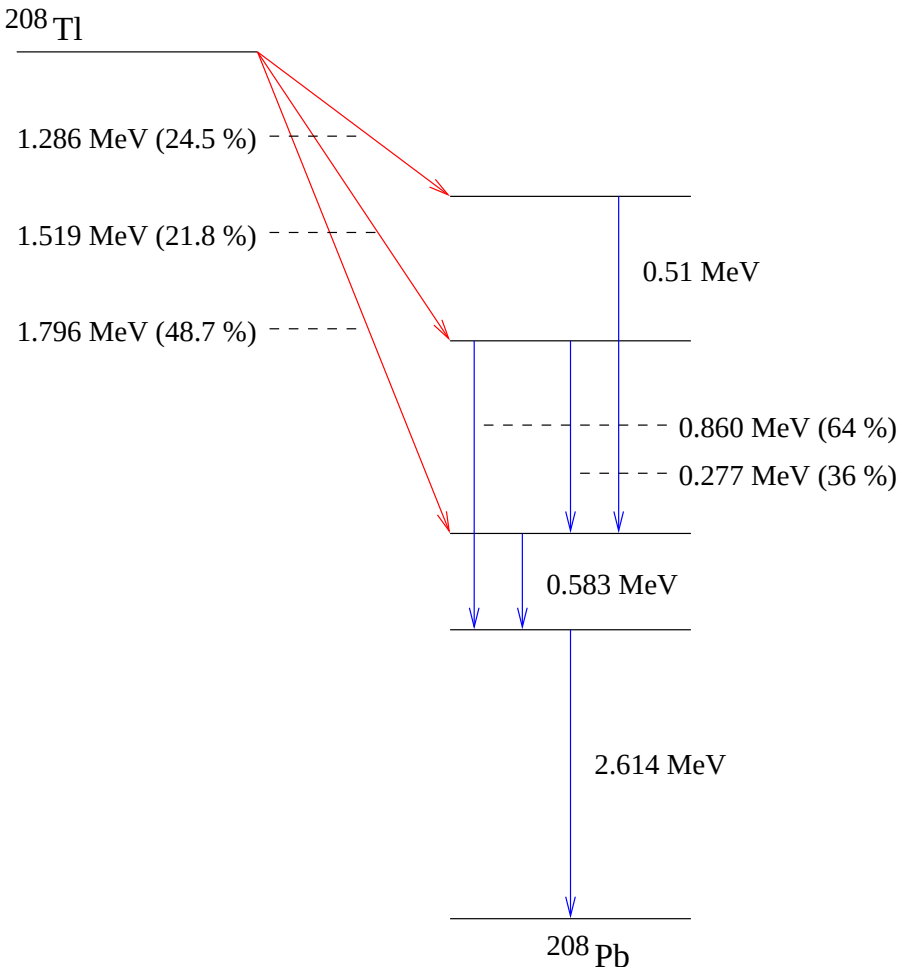


Figure 3.3: $^{208}$Tl decay scheme. Beta transitions are represented by red lines and gamma transitions by blue lines.

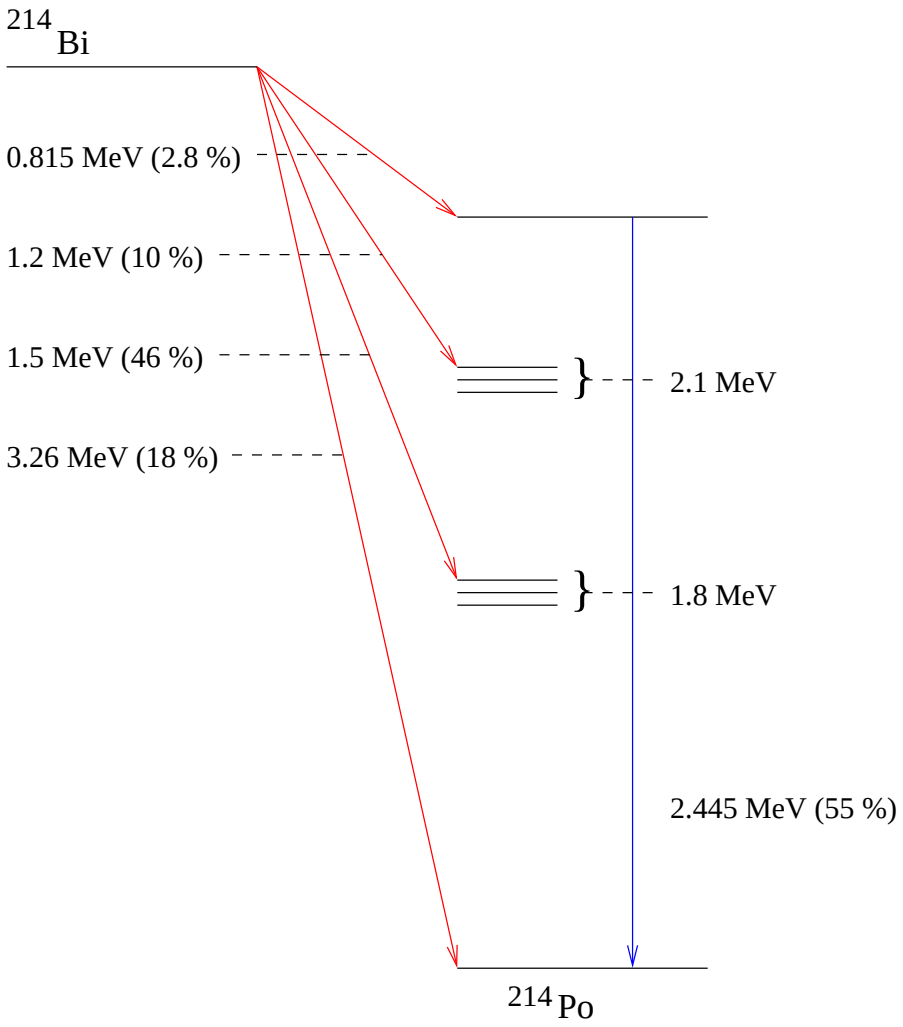


Figure 3.4: Simplified $^{214}$Bi decay scheme. Beta transitions are represented in red and gamma transitions are in blue. Some transitions that emit gammas above 2.225 MeV are not shown due to the complexity of the full decay scheme.

| | |
|---|---|
| $gU/gH_2O$ | $4.5 \times 10^{-13}$ |
| $gTh/gH_2O$ | $3.7 \times 10^{-14}$ |
| $gU/gD_2O$ | $3.0 \times 10^{-14}$ |
| $gTh/gD_2O$ | $3.8 \times 10^{-15}$ |

Table 3.1: Target radiopurity levels for the $D_2O$ and $H_2O$ (PSUP) regions.

by $^{238}U$ fission and neutron capture in the rock and liner materials. The effect of these neutrons was minimal as they were captured almost as soon as they entered the $H_2O$ shielding resulting in a harmless 2.223 MeV gamma ray. The cavern was coated in a layer of shotcrete* and urylon, but the gammas were principally attenuated by the $H_2O$ shielding before the PSUP and PMTs.

### Water

Thorium and uranium were both present in the heavy and light water regions of the detector but their presence was significantly reduced by regular assay and purification. Target levels of water purity are given in Table 3.1. The concentrations in the $D_2O$ correspond to the production of one neutron per day. Backgrounds from the $^{232}Th$ chain were relatively constant over the duration of the SNO experiment, but significant variations in $^{238}U$ chain activity were noted. These variations were caused by loss of the nitrogen cover gas over the neck of the detector, which allowed $^{222}Rn$ to enter the detector and cause periods of high backgrounds. Any periods where the backgrounds were found to be high were eliminated from the data set. No such periods were found in the NCD phase data.

### Acrylic vessel

Gammas and neutrons produced by the acrylic vessel posed a particular hazard as they were not shielded from the $D_2O$. The amount of radioactivity present in the acrylic was measured and found to be approximately $10^{-12}$g/g [52]. Signals arising from activity on the acrylic vessel could be eliminated from the data due to their distinctive radial profile.

### PMTs and PSUP

The photomultiplier tubes and support structure were shielded from the $D_2O$ by 1700 tonnes of ultra pure light water. Neutrons produced by ($\alpha$-n) reactions were captured by the shield and, provided the radioactive content of the materials was low (around 100 ppb†), they posed little risk within the $D_2O$. Beta-gamma decays were of more concern.

*A form of concrete applied using high pressure jets, commonly used in the mining industry

†parts per billion

The Čerenkov light produced by such decays could leak by mis-reconstruction into the $D_2O$ region and limit the lowest energy neutrinos that could be seen in the data.

### NCD bulk

The NCD bodies were made from ultra pure Chemical-Vapour-Deposited (CVD) nickel. In the CVD process, carbon monoxide was reacted with nickel at a temperature of 50°C, forming nickel carbonyl, $Ni(CO)_4(g)$. The gas was heated until it reached a temperature of 175°C, at which point it decomposed into Ni and CO. The Ni was deposited onto a surface to form the final product. For the NCDs, Ni was deposited onto an aluminium mandrel to form cylindrical counter bodies. This process reduced the impurity content of nickel, including contributions from $^{238}$U and $^{232}$Th. Uranium and thorium formed gaseous carbonyls which did not decompose at these temperatures and were therefore not significantly redeposited on the Ni surface.

Prior to their deployment, NCDs were stored underground in a tunnel near Index, Washington, USA to minimise cosmogenic activation. During this storage period, the Ni bodies were exposed to radon rich air allowing $^{210}$Pb and $^{210}$Po to plate onto their surfaces. This contamination was removed by electropolishing and acid etching of the inner and outer NCD surfaces [37].

The amount of uranium and thorium remaining in the Ni bodies of the NCDs was measured to be of the order of $10^{-12}$ g/gNi prior to deployment [53]. A measurement of the $^{232}$Th and $^{238}$U content of the Ni bulk will be presented in Chapter 4.

### NCD surface

The electropolishing and acid etch of the NCD surface removed the majority of surface activity. However, analysis of the data found one string, K5 (string 18), that appeared to be much more active than all other strings in the array. Further analysis, presented in Chapter 4, indicated that the activity appeared to be some form of $^{232}$Th dominated surface contamination. This theory was confirmed using the methods described in Chapter 7.

## 3.4 Measurement of radioactivity

Measurement and understanding of the radioactive backgrounds in the detector is crucial when determining the neutrino fluxes. Methods used to determine the contribution of radioactivity are discussed in later chapters. Chapter 4 outlines how the amount of radioactivity can be inferred directly from the neutrino data set. Chapter 5 describes the Oxford led Hydrous Titanium Oxide (HTiO) assay technique used to measure $^{232}$Th in

the $D_2O$ and $H_2O$ regions and the associated beta-alpha counting system is discussed in Chapter 6. An adapted version of this assay technique for assaying NCD surface activity is presented in Chapter 7.

# Chapter 4

# *In-situ* analysis of radioactive backgrounds

This chapter will concentrate on the *in-situ* analysis performed during the NCD phase to calculate the number of neutrons produced by photodisintegration. The methods used and calculation of results for the $D_2O$, NCD bulk, hotspots and PSUP $H_2O$ will be presented, beginning with the $D_2O$ region.

Based upon an original idea by Moorhead, the *in-situ* technique was pioneered by Chen [54] and developed by McGregor [51] and Sims [47] for the $D_2O$ and salt phases respectively. The *in-situ* method measured radioactivity present in the detector using the neutrino data. Cuts were applied to the data to select the background dominated region. These cuts defined the *in-situ* analysis window, between 4.5 and 5.0 MeV total energy, in which the selected events were dominated by $^{214}$Bi and $^{208}$Tl, from the $^{238}$U and $^{232}$Th chains respectively. The amount of each was determined by exploiting differences in the pattern of hit PMTs produced when Čerenkov light, from decays, was detected. In the $D_2O$ region differences in the radial profile of events were used as an additional separation parameter. Compared with *ex-situ* radioassay measurements, the *in-situ* method had the following advantages:

1. Continuous monitoring of backgrounds in the neutrino data set. This allowed any variation in background levels to be seen and investigated.

2. It provided direct measurements of radioisotopes that cause photodisintegration. Čerenkov events in the energy window used by the *in-situ* analysis were dominated by the decays of $^{214}$Bi and $^{208}$Tl, both of which could cause photodisintegration. The *in-situ* method measured these contributions without making any assumptions about equilibrium in the decay chain. All *ex-situ* methods measured longer lived isotopes higher up the $^{238}$U and $^{232}$Th chains and assumed equilibrium between the radioisotope they measured and those that cause photodisintegration. Comparison

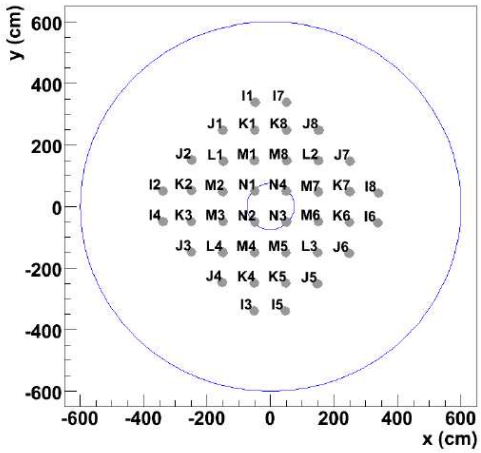


Figure 4.1: Schematic diagram of the NCD array. The small blue circle centred at (0,0) represents the position of the neck and the large blue circle represents the position of the acrylic vessel. All dimensions are in cm. NCDs are referred to by their "name" (i.e. K5, I6 etc) and in some cases by their string number. The name and string number of each NCD is given in Appendix B.

of Ra and Rn assays showed that the majority of activity in the $^{238}$U chain was due to ingress of $^{222}$Rn into the detector. However, for the $^{232}$Th chain, Rn ingress was not a problem due to the short half life of $^{220}$Rn (55.6 seconds). The origin of $^{224}$Ra and daughters in the water was due to the presence of $^{228}$Th.

For comparison with *ex-situ* results, the number of $^{214}$Bi and $^{208}$Tl events were converted into equivalent amounts of $^{238}$U and $^{232}$Th by assuming secular equilibrium and using Monte Carlo simulations*.

The deployment of NCDs increased the amount of radioactivity in the detector. Thorium and uranium in the NCD nickel (bulk) could not be measured using *ex-situ* assays† and the amount of each radioisotope could only be measured by *in-situ* methods. In addition to NCD bulk activity, two areas of increased activity, referred to as *hotspots*, were discovered on the NCD array, on strings 31 (K2) and 18 (K5) [55]. The NCD array is shown in Figure 4.1. Several new *ex-situ* methods were developed to measure the radioactivity of these hotspots [56].

*Note that in the rest of this thesis, Monte Carlo will be used as a shorthand for Monte Carlo simulation
†Methods described in Chapter 2

## 4.1 Backgrounds in the $D_2O$ region

The $D_2O$ region was the region of heavy water held within the acrylic vessel. There were approximately 1000 tonnes of heavy water in this region. There were four main radioactive signals in the $D_2O$ region; $^{238}U$ and $^{232}Th$ in the $D_2O$ and $^{238}U$ and $^{232}Th$ in the NCD bulk. As the probability of detecting a background neutron was strongly dependent on where it was produced and whether the contamination was $^{238}U$ or $^{232}Th$, the total number of backgrounds had to be separated into four signal types. The total number of background events was obtained by selecting the background dominated region of the data and the number of each component was obtained using a maximum likelihood method.

### 4.1.1 Analysis cuts

The final NCD phase dataset of 1995 runs and its corresponding Monte Carlo were used in this work. The following cuts were applied to select background events

- DAMN: CCF56FE1 (PMT) and 00000140 (NCD)
- $4.5 < E_{RSP} < 5.0$
- ITR $> 0.55$
- $-0.12 < \beta_{14} < 0.95$
- $R_{xyz} < 450$
- $x < -40$, $x > 150$, $y < -350$, $y > -150$, $z < -220$ and $z > 80$
- $x < -300$, $x > -210$, $y < -10$, $y > 140$, $z < -360$ and $z > -240$

where $R_{xyz}$, $x$, $y$ and $z$ were measured in cm and $E_{RSP}$ (energy) in MeV. The $x$, $y$ and $z$ coordinates are defined such that the centre of the vessel is at $(x, y, z) = (0, 0, 0)$ and the neck is located symmetrically about the positive $z$ axis and $R_{xyz} = \sqrt{(x^2 + y^2 + z^2)}$. Each cut will now be described in detail.

The Data Analysis Mask Number (DAMN) cuts ensured that the instrumental backgrounds discussed in Chapter 3 were removed from the data set. The masks CCF56FE1 (PMT) and 00000140 (NCD) were used. A full description of the DAMN cuts can be found in [44].

To ensure consistency with other PMT analyses, RSP energy was used [57]. The resolution and scale uncertainties were computed for the RSP[‡] energy estimator by the

[‡]RSP is the name of the energy calibration processor in the SNO experiment. RSP is used to distinguish between the calibrated and "raw" energy of events.

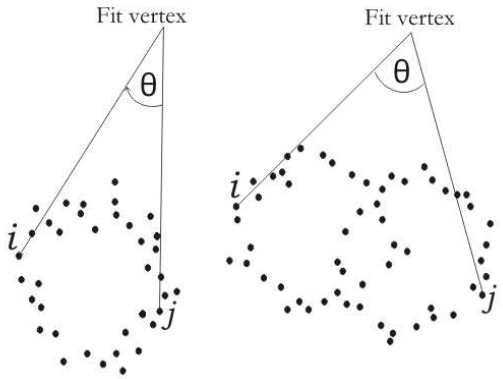


Figure 4.2: Definition of $\theta_{ij}$ . The angle between each pair of hit PMTs is calculated.

Energy and Optics group [58]. The use of RSP energy for analysis made the assessment of systematic uncertainties in this work easier. The lower cut on energy reduced contamination from the decay of other daughter nuclei in the $^{238}$U and $^{232}$Th chains and also from detector inefficiencies. The upper cut on energy ensured that this analysis took place in the background dominated region, thus reducing any neutrino contamination.

The In Time Ratio (ITR) cut provided a measure of fitter performance. The time recorded by the fitter bank was compared with the time it took for the light from the event to reach each PMT. If this time difference fell between -2.5 and 5 ns then the event was correctly fitted. For any PMT event, the ITR was the ratio of the total number of correctly fitted hits to the total number of hits. A Čerenkov event was fairly instantaneous and therefore had a high ITR, about 0.75. Mis-reconstructed and non-Čerenkov events, such as electronic noise, produced light spread over a longer period of time and thus had smaller values of ITR.

$\beta_{14}$ is a measure of event isotropy and therefore, a measure of the distribution of fired PMTs in an event. It was calculated using the angular distribution of hits in an event, $\theta_{ij}$, as shown in Figure 4.2. The angle relative to the fitted vertex between each hit pair of PMTs in the event, $\theta_{ij}$, was used in a linear combination of Legendre Polynomials, referred to as $\beta_{14}$. $\beta_{14}$ was defined as $\beta_1 + 4\beta_4$ where

$$\beta_l = \frac{2}{\mathrm{N(N-1)}} \sum_{i=1}^{\mathrm{N-1}} \sum_{j=i+1}^{\mathrm{N}} P_l(cos\theta_{ij}),$$

N is the total number of PMTs that fired in the event and $l$ is the order of the Legendre Polynomial [25].

In the *in-situ* energy interval, the Čerenkov light produced was dominated by the direct beta decay of $^{214}$Bi to the ground state of $^{214}$Po with an end point of 3.27 MeV. $^{208}$Tl

decays almost always emitted a 2.614 MeV gamma, accompanied by one or more lower energy gammas and a beta with an end point of up to 1.8 MeV. $^{208}$Tl events produced a more isotropic Čerenkov light distribution when compared with $^{214}$Bi events and it was this difference in isotropy that was used to separate background components. Compared with single ring events, multiple ring events were more isotropic, leading to a larger value of $\theta_{ij}$ and thus a smaller value of $\beta_{14}$. The ring of Čerenkov light detected by the PMTs was significantly broadened by multiple scattering of electrons. As a result, discrimination between single and multiple cone Čerenkov events using ring fitting algorithms was difficult. However, the isotropy parameter gave good discrimination between single and multiple events.

Good Čerenkov events lay between the values of the isotropy parameter used in this cut. The upper cut excluded mis-reconstructed events, as those events had very contained angular distributions and thus high values of $\beta_{14}$. The lower value cut excluded very isotropic events that appeared to originate from the acrylic vessel. These events were thought to be caused by either stress relief of bonds or bubble formation on the surface of the acrylic. The exact mechanism is not understood. All good events had $\beta_{14}$ values in the range specified by this cut.

A radial cut of $R_{xyz} < 450$ cm was applied to remove external beta-gamma events from the PSUP $H_2O$ that mis-reconstructed inside the $D_2O$. This volume was 42% of the total $D_2O$ volume but was sufficient to provide an estimate of the activity in the full $D_2O$ volume as the water was regularly recirculated for assays, typically twice every three weeks. Therefore, any activity in the $D_2O$ could be assumed to be uniformly distributed.

Two areas of increased activity were found on NCD strings 18 and 31 (K5 and K2). These were measured using a separate analysis, outlined in Section 4.2. The cuts used to exclude the two hotspots were $-40 < x$, $x > 150$, $y < -350$, $y > -150$, $z < -220$ and $z > 80$ for K5 and $-300 < x$, $x > -210$, $y < -10$, $y > 140$, $z < -360$ and $z > -240$ for K2. Monte Carlo simulations of the hotspots were used to optimise the cuts and only a small number ($< 2\%$) of events remained once these were applied[§]. This translated to less than 1 event from each hotspot remaining in the data once cuts were applied. These cuts are shown in Figure 4.3.

An event that passed all of the above cuts was a candidate background event. As the rate of neutron production was dependent upon whether an event was $^{214}$Bi or $^{208}$Tl [59], candidate background events had to be separated into the four signals present in the $D_2O$ region. This could not be done on an event by event basis, so maximum likelihood separation methods were used on the full set of background candidates. Probability

[§]These simulations were performed using SNOMAN and $^{208}$Tl and $^{214}$Bi were simulated on the surface of K5.

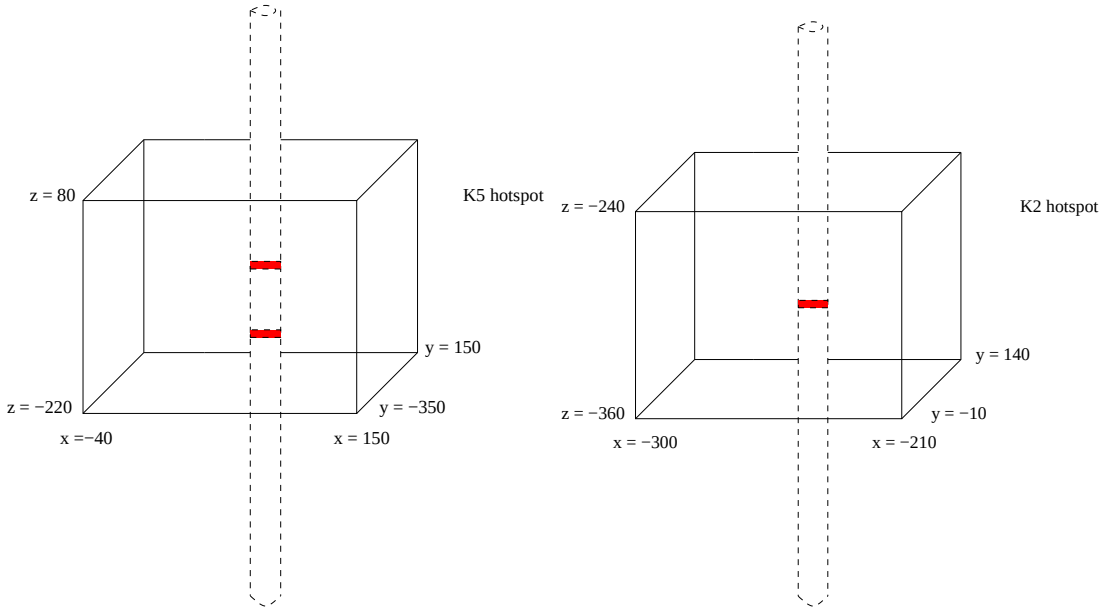


Figure 4.3: Exclusion cuts for the K5 and K2 hotspots. The diagrams are not to scale and the red bands represent the hotspots.

Density Functions (pdfs) were constructed from Monte Carlo and used in a maximum likelihood fit to the data.

Before attempting any likelihood separation of the data, several variables were chosen that were capable of statistically separating the candidate events into different subsets. In total, two variables, event radius and event isotropy, were used in a 2D fit to the data to separate events into Bi $D_2O$, Tl $D_2O$ and NCD events. Note that no variable was found to distinguish between Bi and Tl in the NCD bulk and these were treated as one background.

### 4.1.2 Energy Separation

The energy spectra of $^{208}$Tl and $^{214}$Bi are given in Figure 4.4. At low energies, the energy spectra of $^{208}$Tl and $^{214}$Bi are identical in shape. Thus, using energy spectra alone, it is impossible to distinguish $^{208}$Tl and $^{214}$Bi. As the ratio of neutrons produced to Čerenkov light in the window is different, it is important that the contributions are separated. This is performed using isotropy.

### 4.1.3 Isotropy Separation

At low energies, Čerenkov light produced by $^{214}$Bi decays is dominated by the direct beta decay to the ground state of $^{210}$Po with an end point of 3.27 MeV. Thallium-208 decays

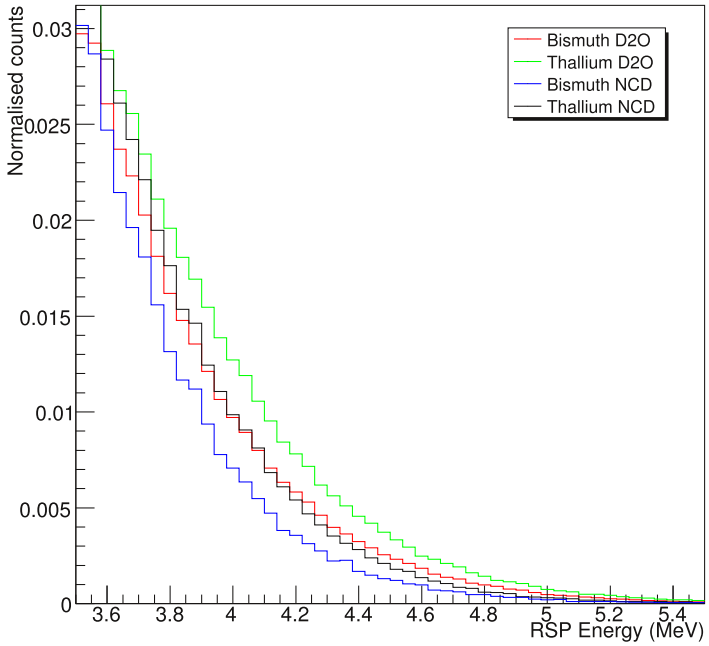


Figure 4.4: Energy distributions for $D_2O$ and NCD MC events in the *in-situ* monitoring window.

by beta emission to one of three excited states of $^{208}$Pb, all of which decay by a series of gamma emissions to the 2.614 MeV state. This subsequently decays to the ground state of $^{208}$Pb by emission of a 2.614 MeV gamma. Čerenkov light produced by $^{208}$Tl decays in $D_2O$ was dominated by that from several betas and gammas. However, Čerenkov light produced by $^{208}$Tl decays in the NCD bulk was dominated by that from gammas, mainly the 2.614 MeV gamma. There was very little contribution from betas as nearly all of them were stopped in the nickel of the NCD counter housing. Thus, NCD bulk $^{208}$Tl events were less isotropic and had a higher average value of $\beta_{14}$, when compared with Tl $D_2O$ events. The mean value of $\beta_{14}$ for these events was very similar to that of Bi in $D_2O$. Bismuth decays in the NCD bulk were rarely seen and were very similar in isotropy to Bi $D_2O$ events.

Figure 4.5 shows isotropy distributions for the four background signals present in the $D_2O$ region of the detector. Bi $D_2O$, Bi NCD and Tl NCD isotropy distributions were very similar, but they were significantly different from that of Tl $D_2O$. Therefore, the inclusion of isotropy in a fit to the data would yield information about the $^{208}$Tl and, hence, $^{232}$Th content of the $D_2O$. It would not be possible to fit all of the components using isotropy alone, as the small differences between NCD bulk and Bi $D_2O$ distributions were

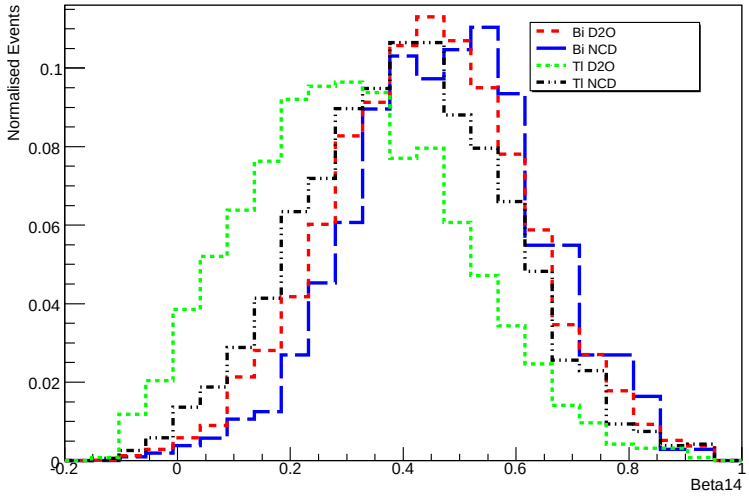


Figure 4.5: Isotropy distributions for $D_2O$ and NCD MC events in the *in-situ* monitoring window.

not great enough to provide an accurate fit. Combining radial and isotropy information, the Tl $D_2O$, Bi $D_2O$ and NCD components may be separated.

### 4.1.4 Isotropy distribution verification

The ability of the Monte Carlo to recreate the isotropy distribution correctly was tested by comparing calibration source data and Monte Carlo. Any difference in the mean or width of $\beta_{14}$ distributions would have had important consequences in the *in-situ* analysis of the low energy backgrounds. If the data were more isotropic than the MC, it would be likely that the amount of $^{232}$Th in the $D_2O$ had been overestimated. Conversely, if the data had been less isotropic, the amount of $^{232}$Th would have been underestimated. Comparison of calibration data and its associated Monte Carlo indicated a non-negligible difference in the centrally fitted Gaussian means of the isotropy distributions.

In addition to the distributed Na and Rn spikes, $^{16}$N point sources were used to assess the offset between data and Monte Carlo. Data cleaning (DAMN), energy, isotropy and ITR cuts were applied to all sources and an additional trigger cut applied to the $^{16}$N data. A central Gaussian fit was made to events that passed the cuts and the results are given in Table 4.1.

Plots of the $\beta_{14}$ distributions for the 2005 $^{24}$Na and $^{222}$Rn spikes are shown in Figures 4.6 and 4.7. For all three sources, the centrally fitted Gaussian mean was lower in data than in MC implying that the data was more isotropic. There was no significant difference

| Source | Data Mean | MC Mean | Data - MC |
|---|---|---|---|
| $^{16}$N | $0.4026 \pm 0.0008$ | $0.4140 \pm 0.0011$ | $-0.0114 \pm 0.0014$ |
| $^{24}$Na 2005 | $0.2504 \pm 0.0007$ | $0.2600 \pm 0.0012$ | $-0.0096 \pm 0.0014$ |
| $^{222}$Rn | $0.4423 \pm 0.0041$ | $0.4546 \pm 0.0030$ | $-0.0123 \pm 0.0051$ |

Table 4.1: Results from the analysis of source data and MC for specified calibration sources. In the case of $^{16}$N, a volume and error weighted mean of source runs was taken.

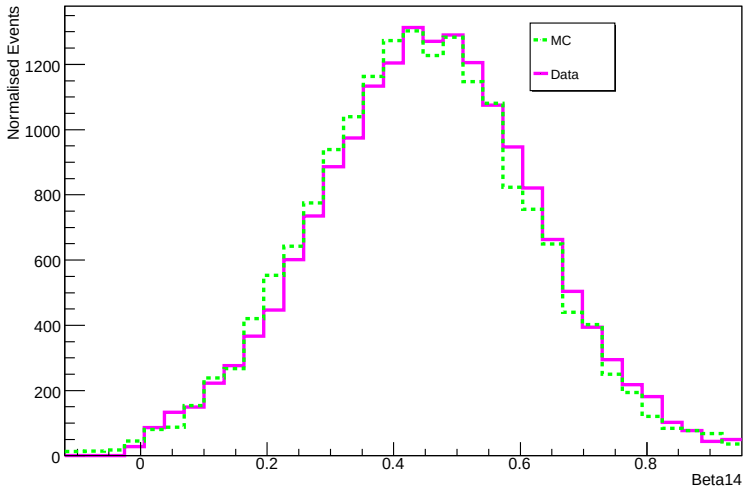


Figure 4.6: Data (Magenta) and MC (Green) isotropy distributions for the $^{222}$Rn spike. The MC has been normalised to the data.

in the width of the data and MC distributions. It is known that $\beta_{14}$ is very sensitive to backscattered light [25] and it was suspected that the difference could be due to the modelling of NCD reflectivity in SNOMAN.

The difference between NCD reflectivity in the data and MC was expected to be small. To test whether the NCD reflectivity could cause such an effect, the NCD reflectivity values used in SNOMAN were increased by a multiplicative constant of 5.5. The value of this multiplicative constant was chosen as it ensured that the reflectivity remained physical i.e. less than 100%. Initially, 5 MeV kinetic energy electrons were simulated[¶] with both the normal and increased reflectivity. $^{208}$Tl decays were also simulated with the increased and normal reflectivities. The results are given in Table 4.2 and show that increasing the reflectivity of the NCDs made events more isotropic. They indicate that the difference in means was independent of the simulated particle. Intermediate val-

[¶]SNOMAN version 5_0285 was used in this work

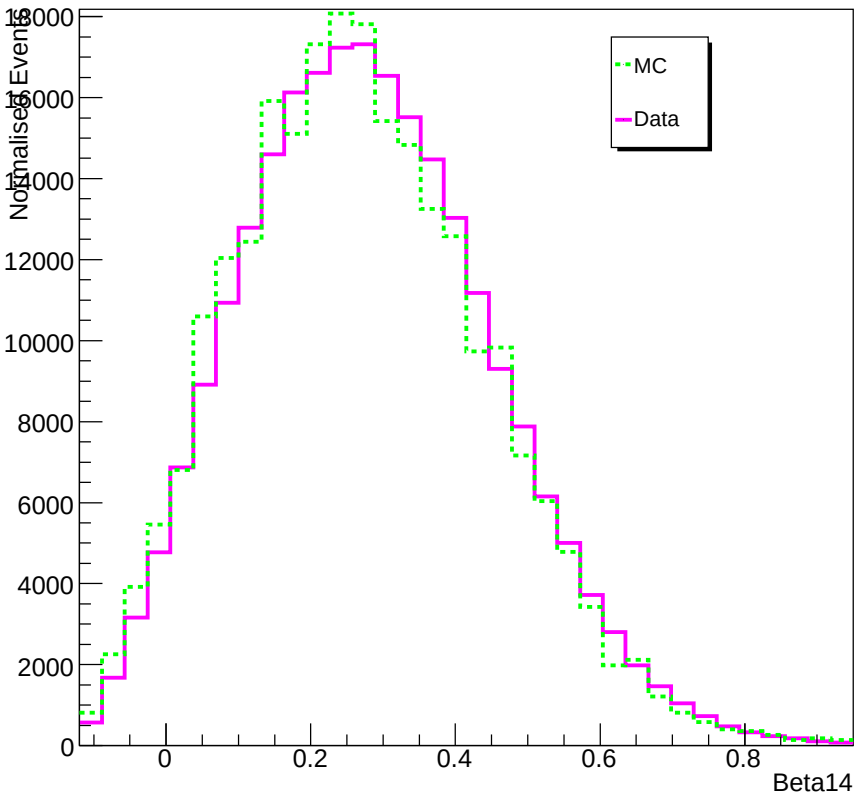


Figure 4.7: Data (Magenta) and MC (Green) isotropy distributions for the 2005 $^{24}$Na spike. The MC has been normalised to the data.

ues of reflectivity were simulated to confirm that the shift in the mean $\beta_{14}$ was directly proportional to the increase in NCD reflectivity.

As the NCD reflectivity was directly proportional to the difference in means implied that a 1% increase in reflectivity gave rise to a difference of $-9.849 \times 10^{-5}$‖. The comparison of data and MC for sources gave a shift of $-9.494 \times 10^{-3}$, which is equivalent to the NCDs being 96% more reflective in the data. This suggested that the reflectivity in SNOMAN was underestimated by a factor of approximately 1.96. A rough check showed that this would have affected the RSP energy by less than 1%.

It has been demonstrated that NCD reflectivity affects the isotropy distribution. It is thought that the observed difference between data and MC in the NCD phase was caused by modelling of NCD reflectivity in SNOMAN and that reflectivity had been

‖The linearity was confirmed using intermediate values of reflectivity

| Particle | Increased | Normal | Difference |
|---|---|---|---|
| Electron | $0.4069 \pm 0.0011$ | $0.4610 \pm 0.0009$ | $-0.0542 \pm 0.0014$ |
| Thallium | $0.2702 \pm 0.0120$ | $0.3173 \pm 0.0150$ | $-0.0471 \pm 0.0192$ |

Table 4.2: Results for $\beta_{14}$ from simulations of 5 MeV (kinetic) energy electrons and $^{208}$Tl decays with normal and increased NCD reflectivity.

underestimated by a factor close to 2. Given that reflectivity in SNOMAN varied from approximately 8.5% to 18%, over wavelengths of 250-800 nm, a factor of 2 increase would not be unphysical.

It was decided that the value of $\beta_{14}$ for each Monte Carlo event should be shifted by -0.00949 and the uncertainty on this shift used to obtain a systematic error associated with $\beta_{14}$. No difference between data and MC was found for the width of the distributions. Therefore, a shift was applied to the MC as the application of a scaling factor would have broadened the MC distribution. The shift was applied on an event by event basis. Once applied, there was no significant difference between the data and MC distributions.

### 4.1.5 $\beta_{14}$ Radial profile

To assess the behaviour of the isotropy parameter, $\beta_{14}$, as a function of radius, the mean value of $\beta_{14}$ for all good $^{16}$N runs in the $D_2O$ was calculated for both data and MC. Figure 4.8 shows $\beta_{14}$ versus radius for data (red) and Monte Carlo (blue). The spread of points at larger radii was similar for data and MC and was also similar in magnitude to that seen in the salt phase [25]. The small spread of $\beta_{14}$ values at larger radii would be accounted for with a systematic error associated with $\beta_{14}$.

### 4.1.6 Radial separation

The radial profiles of $D_2O$ and NCD events are shown in Figure 4.9. Clearly, events originating from the NCD bulk had a different radial profile when compared with events originating in the $D_2O$. This is because NCD events only originated from well defined regions in the fiducial volume, whereas $D_2O$ events were uniformly distributed throughout the fiducial volume. Hence the $D_2O$ distribution was flatter compared with the NCD distribution. This significant difference between the two radial distributions could be used to separate events originating in the $D_2O$ from NCD events.

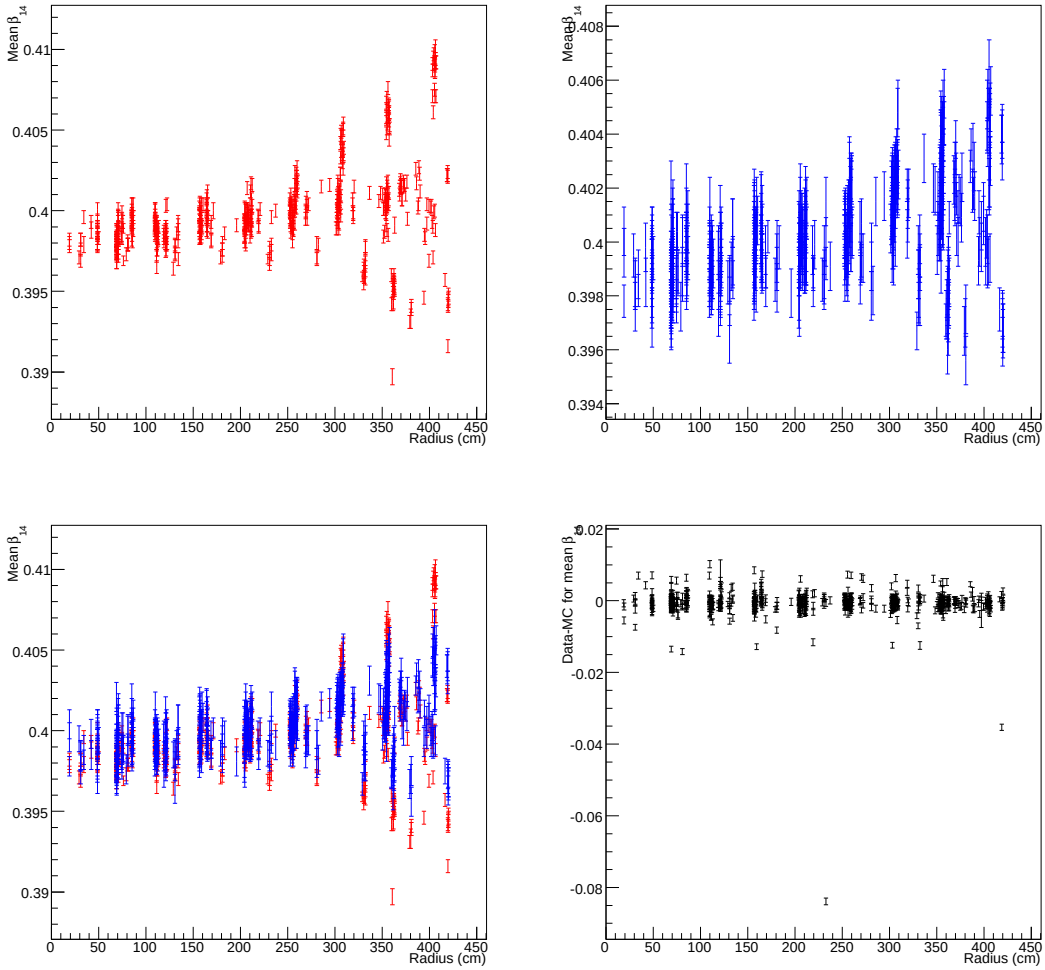


Figure 4.8: Gaussian mean $\beta_{14}$ value versus radius for $D_2O$ $^{16}N$ runs. Red is data and blue is MC. Note that the appropriate shift has been applied to the MC values. The black points show the difference in the Gaussian mean of $\beta_{14}$ of calibration data and MC data. The observed radial trend is modelled in both the Monte Carlo and calibration data and the small radial dependence is accounted for with a systematic error.

### 4.1.7 Verification of radial distributions

The ability of the MC to reproduce the radial distributions correctly was assessed by comparison of calibration source and MC data. The $D_2O$ radial distribution was verified by comparing data and MC for the 2005 $^{24}Na$, 2006 $^{24}Na$ and 2006 $^{222}Rn$ spikes. These spikes were injected into the detector and circulated to produce a near uniform distribution of activity in the $D_2O$. Figure 4.10 shows the radial distribution of the 2005 $^{24}Na$ spike data compared with Bi and Tl $D_2O$ MC. Agreement between spike data and MC was

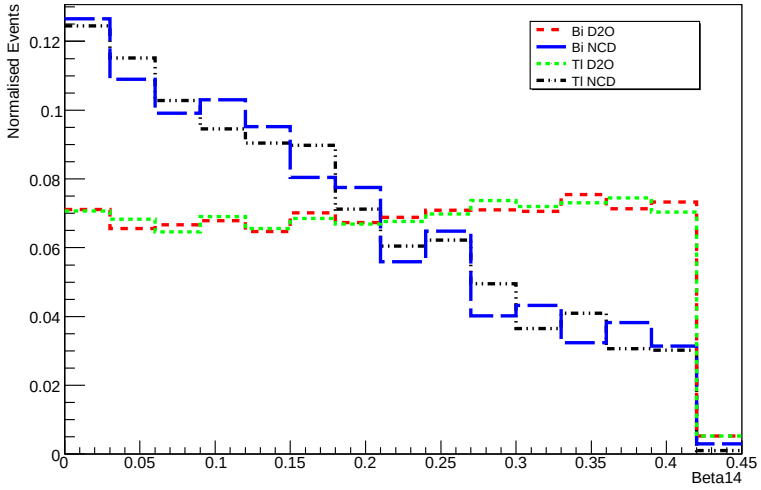


Figure 4.9: Radial distributions for NCD and $D_2O$ backgrounds in the *in-situ* monitoring window. The highest radius bin is significantly lower due to the upper analysis cut on radius.

good, implying that the Monte Carlo accurately reproduced the distribution.

No calibration sources were deployed sufficiently near to the NCDs for an accurate comparison of the radial distribution. Fortunately, the NCD hotspots could be used to investigate reconstruction close to NCDs and also the radial profile of events originating from the NCDs. Figure 4.11 shows the K5 hotspot and NCD MC radial profiles. There was good agreement between the two, again indicating that the MC accurately reproduced the distribution. Further work [60] has shown that the reconstruction near an NCD was not badly affected by shadowing from the NCDs, indicating that the MC reproduced the data well.

### 4.1.8 Maximum likelihood fit to the data

Data passing the selection criteria were predominantly made up of $^{214}$Bi and $^{208}$Tl from the $D_2O$ and NCDs. Assuming that these were the dominant contributions to the data set, a 2D maximum likelihood method could be used to determine how much of each background was present in the observed signal. The event isotropy (measured by $\beta_{14}$) and radial distributions were used as the separation parameters in a 2D radial+isotropy fit to the data.

The normalised Probability Density Function (pdf) associated with each background was determined from Monte Carlo studies of $^{214}$Bi and $^{208}$Tl from the $D_2O$ and NCDs.

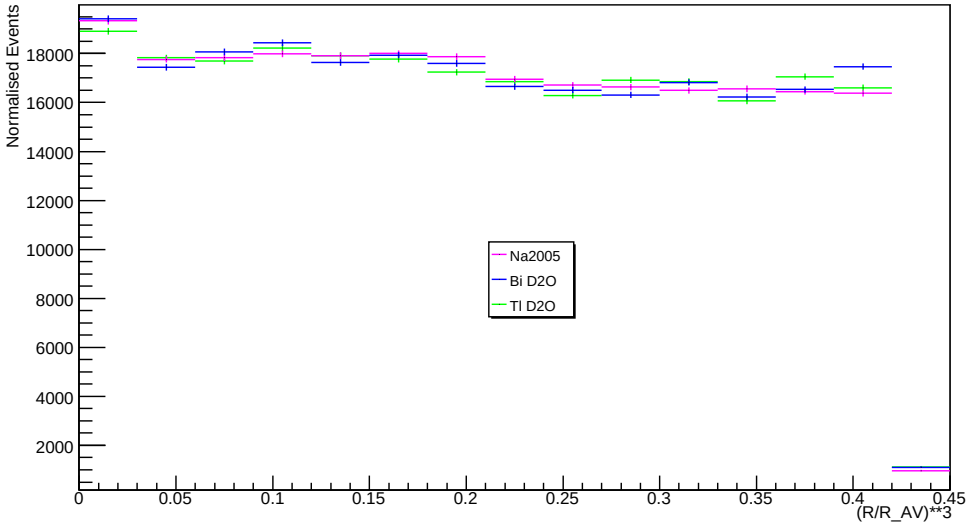


Figure 4.10: Radial distributions for Bi $D_2O$ (Blue), Tl $D_2O$ (Green) and Na 2005 (Magenta) data. The highest radius bin is significantly lower due to the upper analysis cut on radius.

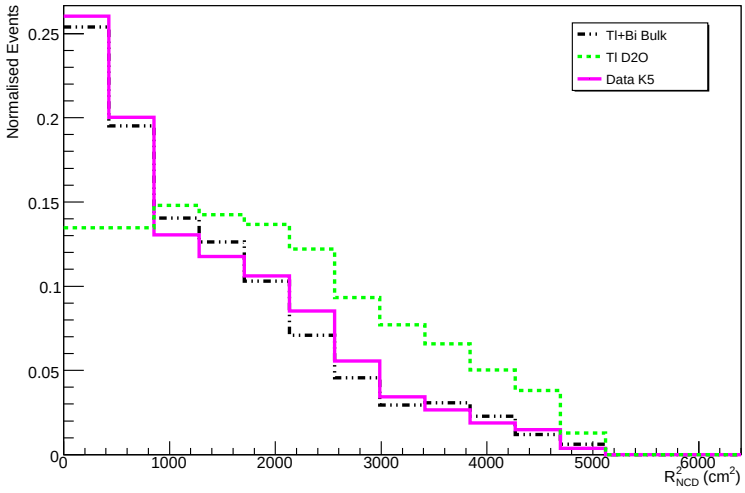


Figure 4.11: Radial distributions for Bi+Tl surface, Tl $D_2O$ and K5 hotspot data. In this plot, $R^2_{NCD} = (x_{EVENT} - x_{NCD})^2 + (y_{EVENT} - y_{NCD})^2$, where $x_{NCD} = x$ coordinate of the NCD, $x_{EVENT} = x$ coordinate of the event vertex and similarly for $y$.

NCD bulk and $D_2O$ $^{214}$Bi and $^{208}$Tl decays were generated by separate SNOMAN simulations and events were selected using identical cuts to the data. For the data and each

background, a 2D pdf of $\beta_{14}$ and $\frac{R^3_{xyz}}{R^3_{AV}}$ was constructed**.

The 2D pdfs were used to calculate the likelihood function. As the number of events in the data set was drawn from a Poissonian distribution about the true mean number of events, the probability of measuring $N$ events in the data should be included in the likelihood estimate

$$\mathcal{L} = \ln(L) = \sum_{i=1}^{N} \ln\left(\sum_j a_j P_{ji}\right) - \sum_j a_j \tag{4.1}$$

where, $N$ is the total number of events in the data set, $P_{ji}$ is the normalised probability that event $i$ is a type $j$ signal and $a_j$ is trial number of events of type $j$. The values of $a_j$ were varied until the maximum value of the likelihood was obtained. The most probable combination of Tl $D_2O$, Bi $D_2O$ and Bi+Tl NCD occurred when $\mathcal{L}$ was maximised.

In this work, the likelihood was calculated using two independent computer programs, one written by the author and another using the ROOT class TFractionFitter [61]. Preliminary fake data tests showed that both programs performed equally well, see Table 4.3, but the ROOT code could perform the fits much more quickly; less than one minute compared with approximately 30 minutes for the prototype code. The decision was made to use the ROOT class and further fake data tests were performed to optimise the number of isotropy and radial bins used in the fit to the data.

Once the Bi $D_2O$, Tl $D_2O$ and NCD contributions had been calculated from the maximum likelihood fit to the data, the concentrations of each isotope could be determined. This is discussed in the following section.

### 4.1.9 Calculation of the concentrations

The concentration of $^{232}$Th and $^{238}$U in the $D_2O$ and NCDs was calculated using information from the likelihood fit and the MC. The generation rate of MC events for each background class was known and the corresponding concentration (in g/g) could be obtained assuming secular equilibrium. The radioactive decay law may be written as follows,

$$\text{Rate} = \lambda_{Bi} N_{Bi} = \lambda_U N_U = 4 \text{ Hz}$$

where N is the number of atoms of each isotope

$$4 = \lambda_U N_U.$$

Noting that

$$\lambda_U = \left(\frac{ln2}{T_{\frac{1}{2}}}\right)$$

**Note that $R_{AV}$ is the radius of the acrylic vessel and was taken to be 600 cm.

| Fake Bi $D_2O$ | Fake Tl $D_2O$ | Fake NCD | Prototype Bi $D_2O$ | Prototype Tl $D_2O$ | Prototype NCD |
|---|---|---|---|---|---|
| 500 | 0 | 0 | $500 \pm 0.1$ | $0 \pm 0.1$ | 0 |
| 0 | 500 | 0 | 0 | $499 \pm 5$ | $1 \pm 5$ |
| 0 | 0 | 500 | $5 \pm 21$ | 0 | $495 \pm 21$ |
| 250 | 250 | 0 | $210 \pm 30$ | $270 \pm 30$ | $20 \pm 30$ |
| 250 | 0 | 250 | $233 \pm 53$ | $1 \pm 53$ | $266 \pm 53$ |
| 0 | 250 | 250 | 0 | $248 \pm 23$ | $256 \pm 23$ |
| 300 | 200 | 100 | $278 \pm 30$ | $153 \pm 30$ | $185 \pm 30$ |
| 470 | 80 | 50 | $477 \pm 28$ | $62 \pm 28$ | $62 \pm 28$ |

| Fake Bi $D_2O$ | Fake Tl $D_2O$ | Fake NCD | ROOT Bi $D_2O$ | ROOT Tl $D_2O$ | ROOT NCD |
|---|---|---|---|---|---|
| 500 | 0 | 0 | $499 \pm 5$ | 0 | $0 \pm 5$ |
| 0 | 500 | 0 | $1 \pm 5$ | $497 \pm 5$ | $2 \pm 5$ |
| 0 | 0 | 500 | $4 \pm 10$ | 0 | $496 \pm 10$ |
| 250 | 250 | 0 | $220 \pm 32$ | $260 \pm 32$ | $10 \pm 32$ |
| 250 | 0 | 250 | $210 \pm 45$ | $4 \pm 45$ | $285 \pm 45$ |
| 0 | 250 | 250 | 0 | $273 \pm 45$ | $227 \pm 45$ |
| 300 | 200 | 100 | $260 \pm 45$ | $202 \pm 45$ | $138 \pm 23$ |
| 470 | 80 | 50 | $494 \pm 26$ | $71 \pm 26$ | $35 \pm 26$ |

Table 4.3: Results from preliminary fake data tests of the two 2D likelihood fitting routines. Prototype is the code written by the author and ROOT is the TFractionFitter code.

substitute in

$$4 = \left(\frac{ln2}{T_{\frac{1}{2}}}\right) N_U$$

$$N_U = \frac{4\, T_{\frac{1}{2}}}{ln2}.$$

The mass in grammes of uranium can be calculated using,

$$\text{Mass in g} = \frac{238 \times N_U}{N_A}$$

where $N_A$ is Avogadro's number. For the 4 Hz Bi $D_2O$ MC this mass was found to be

$$\text{Mass in g of } ^{238}\text{U} = 3.210 \times 10^{-4}.$$

| Background | Generated rate | Generated concentration |
|---|---|---|
| Bi $D_2O$ | 4.00 Hz | $3.21 \times 10^{-13}$ gU/g$D_2O$ |
| Tl $D_2O$ | 0.17 Hz | $1.16 \times 10^{-13}$ gTh/g$D_2O$ |
| Bi NCD | 2.00 Hz | $8.52 \times 10^{-10}$ gU/gNi |
| Tl NCD | 0.17 Hz | $6.13 \times 10^{-10}$ gTh/gNi |

Table 4.4: Generated rates and concentrations for each background MC in the $D_2O$ region of the detector. A mass of 1000 tonnes of $D_2O$ and 189 kg of Ni were used.

The concentration of $^{238}$U was therefore,

$$\text{gU/gD}_2\text{O} = \frac{\text{Mass of uranium}}{\text{Mass of D}_2\text{O}}$$
$$\text{gU/gD}_2\text{O} = \frac{3.210 \times 10^{-4}}{1.0 \times 10^{9}}$$
$$\text{gU/gD}_2\text{O} = 3.21 \times 10^{-13}.$$

The Bi NCD bulk calculation proceeds in exactly the same manner, with the generation rate replaced by 2 Hz and the mass of $D_2O$ replaced by the mass of Ni in the NCD array. The calculation of $^{232}$Th concentrations was slightly complicated by the 36% branching fraction to $^{208}$Tl from $^{232}$Th. This branching fraction implied that a maximum of only 36% of the true number of $^{232}$Th events could be observed in the analysis window. The initial stage of the thorium calculation was therefore,

$$\text{Rate} = \lambda_{Tl} N_{Tl} = 0.36 \lambda_{Th} N_{Th} = 0.17 \text{ Hz}.$$

The calculation was then analogous to the Bi case with the appropriate generation rate, half life and mass substitutions made. A summary of generation rates and concentrations is given in Table 4.4 and these may be used to calculate the concentration of each background in the data, using the following relationship:

$$\text{g/g} = \frac{\text{Number of data events}}{\text{Number of MC events}} \times \text{Generated concentration}. \tag{4.2}$$

The number of each event type found in the data using the maximum likelihood fits are given along with the corresponding concentration in Table 4.5.

### 4.1.10 Systematic Errors

The systematic errors for each background are summarised in Tables 4.6 and 4.7. Each systematic error was calculated using the same general method. For a given variable, the MC was shifted by a specified amount and the concentrations re-calculated. The

| | Bi $D_2O$ | Tl $D_2O$ | Bi NCD | Tl NCD |
|---|---|---|---|---|
| Data | 450 | 95 | 4.41 | 34.59 |
| MC | 18303 | 10545 | 1746 | 5193 |
| g/g | $7.89 \times 10^{-15}$ | $1.04 \times 10^{-15}$ | $2.15 \times 10^{-12}$ | $4.08 \times 10^{-12}$ |

Table 4.5: Number of events obtained from the maximum likelihood fit to the data. Note that the number of Tl NCD and Bi NCD events were obtained using the ratio given in [53]. The number of events passing each cut in the corresponding MC are given, along with the resulting concentrations. The normalisation has not been applied to these values.

| | Th $D_2O$ | U $D_2O$ |
|---|---|---|
| Energy Resolution | +0.00%, -16.07% | +0.00%, -5.36% |
| Normalisation | +14.50%, -14.50% | +14.50%, -14.50% |
| $\beta_{14}$ | +5.26%, -3.16% | +1.78%, -3.56% |
| $\beta_{14}$ temporal | +15.79%, -12.63% | +1.11%, -1.33% |
| $\beta_{14}$ radial | +12.83%, -10.33% | +1.23%, -0.76% |
| NCD $\beta_{14}$ pdf | +14.34%, -4.59% | +1.46%, -2.67% |
| Radius | +3.04%, -2.97% | +3.16%, -2.49% |
| Hotspot volume | +5.00%, -5.00% | +7.00%, -7.00% |
| Statistical | +10.26%, -10.26% | +4.71%, -4.71% |
| Total | +31.18%, -30.08% | +15.83%, -18.40% |

Table 4.6: Summary of systematic errors for the *in-situ* analysis of Th and U $D_2O$ backgrounds.

difference between the concentrations derived using the shifted variables and the central values was taken to be a measure of the systematic error for the shifted variable. The origin of the shifts applied to each variable are now presented in turn.

### Energy resolution

The uncertainty in energy resolution was taken from [58]. One hundred random numbers were generated using a Gaussian function with a mean of one and width that corresponded to the energy resolution uncertainty. These 100 numbers were used to smear the energy scale in the MC and the average of the 100 trials was used to calculate the uncertainty due to the energy resolution.

### Normalisation

The *in-situ* method may be used to determine the strength of distributed sources in the detector. If the strength of the distributed source is well known, the *in-situ* result can be compared and the normalisation factor computed. The normalisation factor is, therefore,

| | Th NCD | U NCD |
|---|---|---|
| Energy Resolution | +0.00%, -43.46% | +0.00%, -42.95% |
| Normalisation | +14.50%, -14.50% | +14.50%, -14.50% |
| $\beta_{14}$ shift | +28.21%, -12.82% | +28.21%, -12.82% |
| $\beta_{14}$ temporal | +17.95%, -23.08% | +17.95%, -23.08% |
| $\beta_{14}$ radial | +11.01%, -22.51% | +11.01%, -22.51% |
| NCD $\beta_{14}$ pdf | +4.16%, -5.71% | +4.16%, -5.71% |
| Radius | +1.13%, -1.16% | +1.57%, -1.24% |
| Hotspot volume | +6.00%, -6.00% | +6.00%, -6.00% |
| NCD Bulk Composition | +12.74%, -12.74% | +15.04% -15.04% |
| Statistical | +16.01%, -16.01% | +16.01%, -16.01% |
| Total | +43.44%, -61.57% | +44.18%, -61.74% |

Table 4.7: Summary of systematic errors for the *in-situ* analysis of Th and U bulk NCD backgrounds.

| Spike | Strength | Estimated strength | Normalisation |
|---|---|---|---|
| Na 2005 | 504 Bq | 595 Bq | 0.82 |
| Rn 2005 | 202 Bq | 225 Bq | 0.89 |
| Na 2006 | 4300 Bq | 5120 Bq | 0.84 |
| | | Weighted Mean | 0.84 |

Table 4.8: Summary of results from the *in-situ* analysis of the three distributed sources deployed in the $D_2O$ region during the NCD phase.

a measurement of the energy scale uncertainty. To determine the normalisation factor, the strengths of the three $D_2O$ spikes ($^{24}$Na 2005, $^{24}$Na 2006 and $^{222}$Rn 2005) were calculated and compared with the known strengths of each source [62]. The results are summarised in Table 4.8. Both the $D_2O$ and NCD bulk central values given in Table 4.5 should be multiplied by the average normalisation factor to provide the true central values for each class of background.

It was not possible to perform the *in-situ* analysis using a lower energy window because of contamination from the hotspots. At kinetic energies below 3.8 MeV Čerenkov tails from the hotspots dominated, making it extremely difficult to perform an *in-situ* analysis.

### $\beta_{14}$ shift

As discussed in Section 4.1.4, an offset between data and MC was observed for $\beta_{14}$. This was found to be as a result of the NCD reflectivity being underestimated in SNOMAN. To account for this difference, the MC data was shifted appropriately as described in Section

4.1.4. The uncertainty in this correction factor was used to determine the systematic uncertainty in $\beta_{14}$. No significant difference in the widths of the $\beta_{14}$ distributions between data and MC was observed and it was, therefore, reasoned that the uncertainty in the correction factor applied to the MC would dominate the systematic error associated with the $\beta_{14}$ shift. The correction factor was determined to be $-0.00949 \pm 0.00139$ and to assess the systematic error associated with $\beta_{14}$, shifts of -0.01088 and -0.00810 were applied to the data. The difference in the extracted concentrations in each case, compared with the -0.00949 shift, was taken to be the systematic error.

### $\beta_{14}$ temporal

Each source position in Figure 4.8 had points from a number of source runs performed during the NCD phase. Over the NCD phase, variation in the value of the Gaussian mean distribution at each source position was found to be $3.5 \times 10^{-3}$. Each event in the MC was shifted by this value and the concentrations re-calculated. The difference between this concentration and the central values was taken to be the uncertainty due to temporal variation in $\beta_{14}$.

### $\beta_{14}$ radial

Figure 4.8 shows that at higher radii, the Gaussian mean $\beta_{14}$ differed from that at the centre of the detector by $\pm 0.005$. This was propagated by shifting the MC and the concentrations were re-derived. The systematic error was taken to be the difference between this and the central concentrations for each background.

### NCD $\beta_{14}$ pdf

The NCD $\beta_{14}$ pdf used in the 2D fit to the data was a combination of $\beta_{14}$ for $^{208}$Tl and $^{214}$Bi in the NCD bulk. As small differences existed between the Tl and Bi bulk $\beta_{14}$ distributions, a systematic error was assigned to cover this. To assign such an error, two fits were made; one using only the Tl NCD bulk pdf and the other using only the Bi NCD bulk pdf. The concentrations were re-extracted for each case. The uncertainty associated with the pdf was taken to be the difference between this and the central concentrations for each background.

### Radius

The uncertainty in the reconstructed $x$, $y$ and $z$ positions of each event (taken from [63]) were used to calculate the uncertainty on $R_{xyz}$ for each event. The uncertainty on the

radial position, $R_{xyz}$, of each event was calculated using the following expression:

$$\sigma_r^2 = \frac{x^2\sigma_x^2 + y^2\sigma_y^2 + z^2\sigma_z^2}{r^2}.$$

The radial shift was applied on an event by event basis to determine the uncertainty due to the position uncertainty.

There was a small anomaly in the fitter reconstruction at 450 cm, but studies have shown that the effect on the *in-situ* analysis would be minimal [63] and would be smaller than the radial uncertainty. As the radial uncertainty dominated, the effect due to this anomaly should be covered by the radial uncertainty.

#### Hotspot volume

As the hotspots were removed from the analysis by excluding a volume around each one, a systematic error associated with the uncertainty in this volume had to be calculated. To assess this uncertainty, the excluded volume around each hotspot was varied and the $D_2O$ and NCD bulk concentrations re-calculated. Figure 4.12 shows that after a certain exclusion volume, the fitted concentrations stabilised, demonstrating that the hotspot was excluded from the data. Using the uncertainty in the reconstructed $x$, $y$ and $z$ positions of each event (taken from [63]), the uncertainty on the exclusion volumes was determined.

#### Composition

The percentage of $^{238}$U and $^{232}$Th in the NCD bulk was calculated using the ratio given in [53] and was found to be 89% Th and 11% U. The uncertainty in this ratio would result in an uncertainty in NCD bulk composition and this is given in Table 4.7.

### 4.1.11 Uniformity of NCD bulk backgrounds

Any significant non-uniformity in the NCD backgrounds could have affected the $D_2O$ concentrations derived using the likelihood method described in Section 4.1.8. Čerenkov events arising from localised NCD activity would have extended further into the fiducial volume and would have biased the radial fit leading to an overestimate of NCD activity.

To assess the uniformity of the NCD bulk activity, cuts were applied to exclude a cylindrical fiducial volume around each NCD. The Th and U $D_2O$ concentrations were calculated and compared with the case with no radial exclusions. This was repeated for several different sized holes and the results are shown in Figure 4.13. The fit was found to be stable, as a function of excluded radius, suggesting that the assumption of uniform NCD bulk radioactivity was valid.

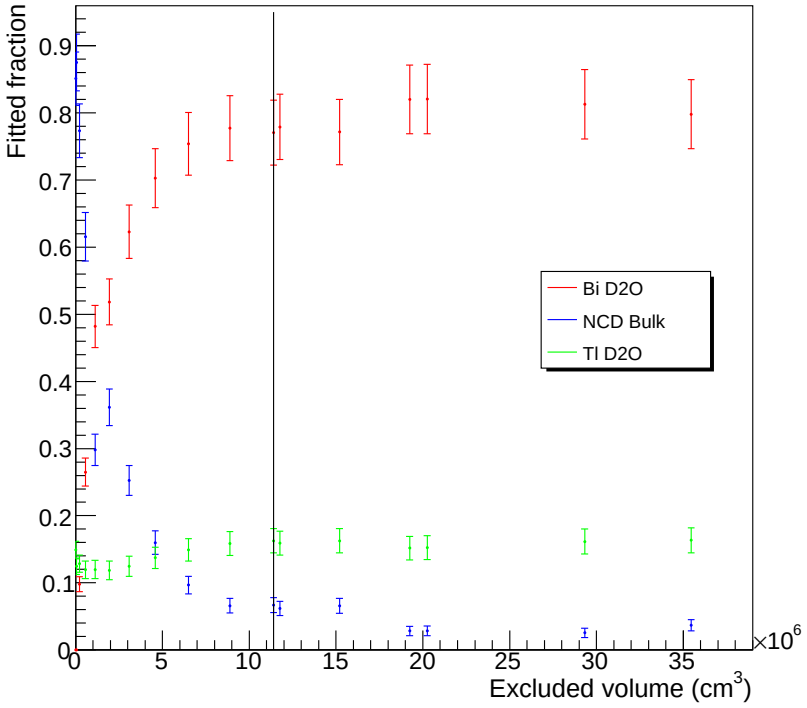


Figure 4.12: Fitted fraction of events for different exclusion volumes around K5. Once the effect of the hotspot was removed from the data, the fitted fractions and hence concentrations stabilised. The black line indicates the cut used in this work.

### 4.1.12 Recommended $D_2O$ and NCD concentrations

The recommended concentrations for the $D_2O$ and NCD bulk are given below

$$\begin{aligned} \mathrm{gTh/gD_2O} &= 0.88^{+0.27}_{-0.27} \times 10^{-15} \\ \mathrm{gU/gD_2O} &= 6.63^{+1.05}_{-1.22} \times 10^{-15} \\ \mathrm{gTh/gNCD} &= 3.43^{+1.49}_{-2.11} \times 10^{-12} \\ \mathrm{gU/gNCD} &= 1.81^{+0.80}_{-1.12} \times 10^{-12}. \end{aligned}$$

The $D_2O$ concentrations agreed with the values obtained from the *ex-situ* assays performed during the NCD phase [64]. The NCD bulk results agree with values obtained in [53]. The correlation matrix for the 2D fit is given in Table 4.9 and shows that the amount of $ThD_2O$, U $D_2O$ and NCD activity are not statistically independent.

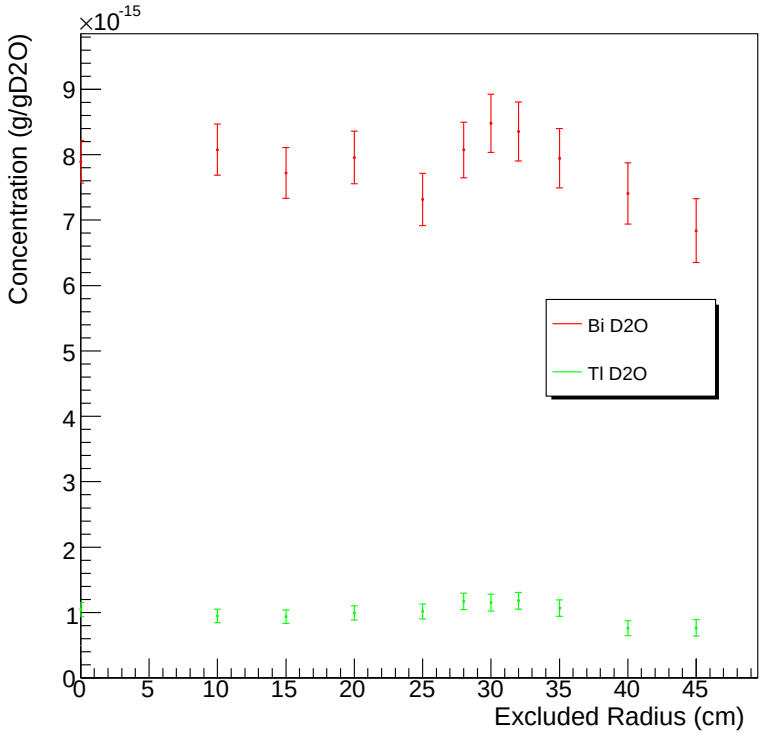


Figure 4.13: Excluded radius versus concentration for Tl and Bi $D_2O$ backgrounds. Statistical errors only are shown. Red = Bi $D_2O$ and Green = Tl $D_2O$

## 4.2 NCD Hotspots

As mentioned at the beginning of this chapter, two areas of increased activity were found on the NCD array in positions consistent with K2 (string 31) and K5 (string 18) [55]. The $z$ distributions of activity for these strings and two uncontaminated strings are shown in Figure 4.14.

Any uncertainty in hotspot composition would lead to an unacceptably large systematic error on the derived NCD phase Neutral Current (NC) flux. The *in-situ* analysis saw an excess of events for both these strings, but it could not prove conclusively that these events were caused by radioactivity. In particular, the isotropy distribution of K5 events was more isotropic than that of the NCD bulk. This implied either surface radioactivity or a scintillator on the surface of the NCD that enhanced the bulk radioactivity. If the hotspot was radioactive, there should have been an excess of neutrons captured by the hotspot string [65]. No significant excess neutron signal was found on K5. This was later shown to have been due to a leaking counter [66]. No excess alphas were seen on either hotspot string [53]. The lack of alphas for K2 could have been explained by

| | Bi $D_2O$ | NCD | Tl $D_2O$ |
|---|---|---|---|
| Bi $D_2O$ | 1.000 | -0.915 | -0.004 |
| NCD | -0.915 | 1.000 | -0.316 |
| Tl $D_2O$ | -0.004 | -0.316 | 1.000 |

Table 4.9: Correlation matrix for the 2D fit.

the fact that the *in-situ* analysis indicated that the K2 contamination was close to the weld between the anchor and anchor-middle counters. This region is shown in Figure 4.15. If in the dead region, the alphas would not have been seen in the NCD data stream. The hotspot(s) on K5 were found to be further away from the weld. This suggested that they had not been detected because the contamination was on the external surface of the counter. The *in-situ* analysis of the hotspots will now be discussed.

### 4.2.1 K5

Figure 4.14 shows that the distribution of activity on K5 has two clear peaks, one around $z = -50$ cm and the other at $z = -125$ cm. The isotropy distribution of these events is shown in Figure 4.16. The isotropy distribution of K5 events agrees very well with those of surface thallium which is slightly more isotropic than thallium bulk and slightly less isotropic than thallium $D_2O$. $^{208}$Tl decays by beta emission to one of three excited states of $^{208}$Pb, all of which decay by a series of gamma emissions to the 2.614 MeV state. This subsequently decays to the ground state of $^{208}$Pb by emission of a 2.614 MeV gamma. Čerenkov light produced by $^{208}$Tl decays in the $D_2O$, is dominated by that from several betas and gammas. However, the Čerenkov light produced by $^{208}$Tl decays in the NCD bulk is dominated by that from gammas. There is very little contribution from betas, as they lose energy during their passage through the nickel of the NCD counter housing. Thus, NCD bulk $^{208}$Tl events are less isotropic, i.e. have a higher average value of $\beta_{14}$, when compared with $^{208}$Tl $D_2O$ events. Surface $^{208}$Tl is slightly more complicated: some of the betas do not pass through nickel and produce events that are very similar to those from $^{208}$Tl in the $D_2O$. Conversely, some events do pass through the nickel and produce events that are very similar to those from the bulk. Thus, it is not surprising that the surface distribution is more isotropic than the bulk but less isotropic than the $D_2O$.

The isotropy distribution suggests that the activity was dominated by surface thallium-like contamination. Given that no excess alphas were seen in this string, this indicated that the contamination was likely to be located on the external surface of the NCD.

One further piece of evidence supporting the surface activity theory was the redeployment of K5. Soon after K5 was deployed in January 2004, it was noticed that the gain

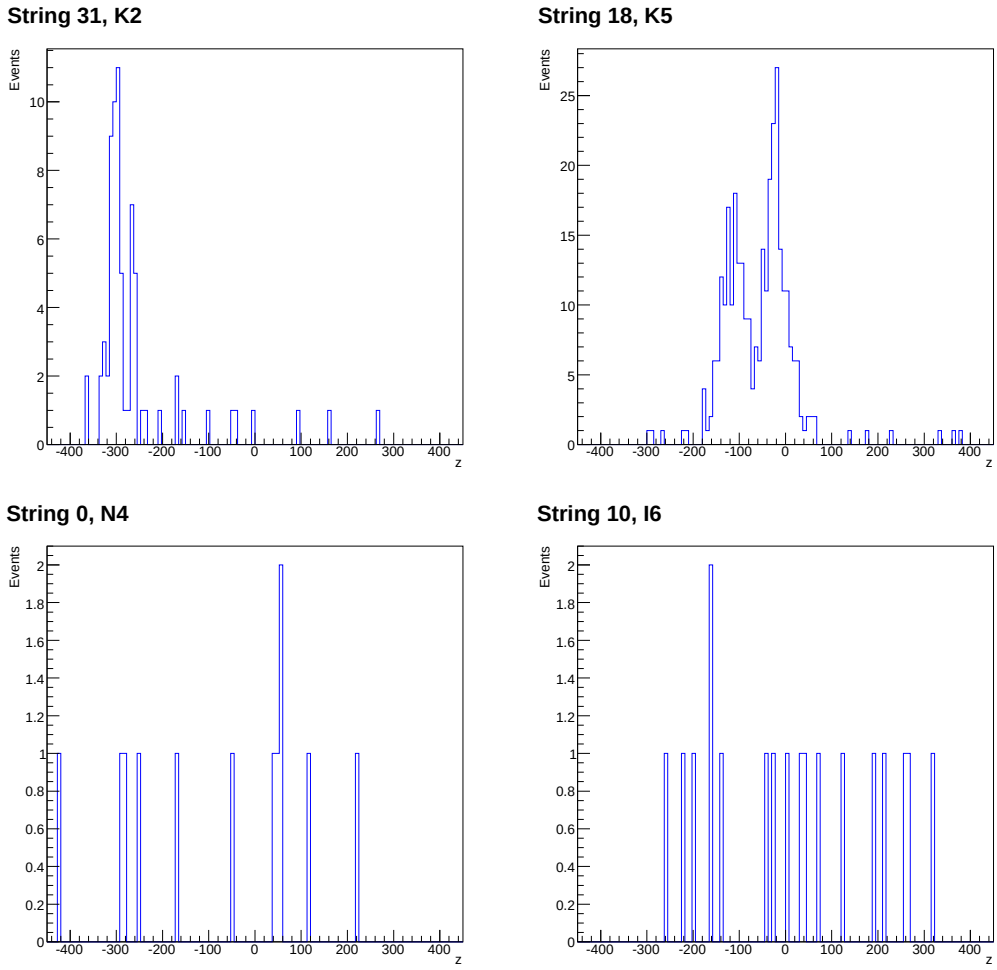


Figure 4.14: $z$ distribution of events on K2 (string 31) and K5 (string 18). For comparison, the $z$ distribution of events on two clean strings (I6 and N4). All data shown are for the 385.17 day dataset.

was drifting in one of the counters. This was due to a leak. To check that the string was not leaking $^3$He into the $D_2O$, a leak test was performed on April 18th 2004. The string was removed from the detector and a plastic bag was taped over the suspect counter. A $^3$He leak detector was placed in the bag. The counter was left clamped and hanging out of the detector overnight. The following day, the bag was removed and the string redeployed. To determine whether the re-deployment could have caused the hotspot, a study of approximately 142 hours of good neutrino data taken between January 2004 and April 2004 was compared with 142 hours of open month data. This is shown in Figure 4.17. Although Rn levels were much higher during the commissioning data[††], the hotspot

[††]due to lack of cover gas in the neck

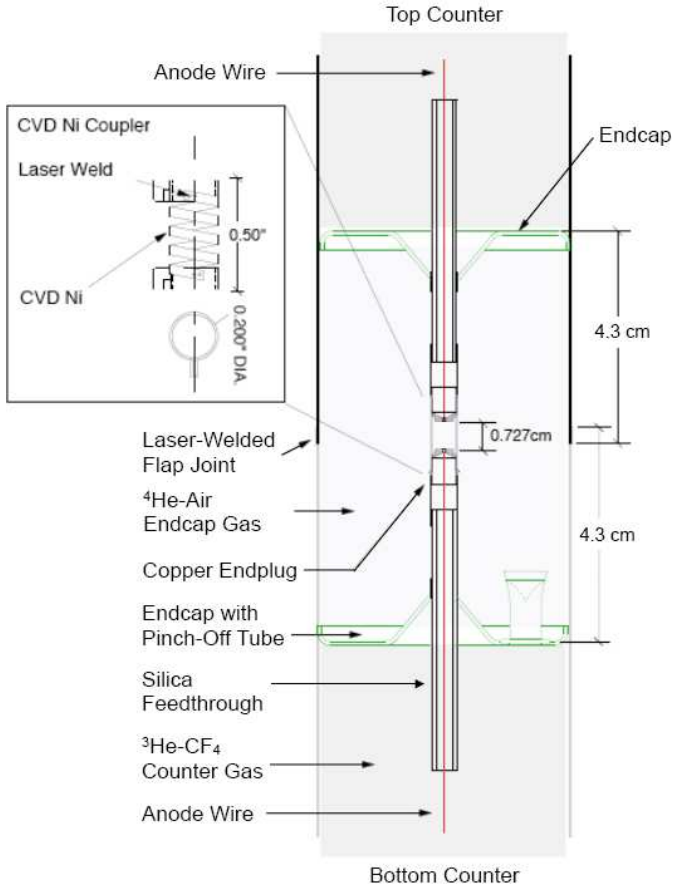


Figure 4.15: The endcap region of two joined NCDs. A resistive coupler was used to provide an electrical contact between the two counters. The $^4$He-Air region is the dead region of the counter. Figure taken from [37]

should still have been visible. The lack of a hotspot signal in the commissioning data set analysed suggested that the contamination occurred during the re-deployment of K5 and, therefore, would be on the external surface of K5.

As surface contamination was highly unlikely due to all of the precautions taken during deployment, the *in-situ* analysis could not completely rule out the possibility that some form of scintillating material had become attached to the counter surface during the re-deployment of April 2004. It was decided to measure the activity of K5 using *ex-situ* methods, once it had been removed from the detector. Two independent *ex-situ* methods were developed; external alpha counting using a specially constructed wire counter and acid elution using methods based upon the HTiO assay technique (described

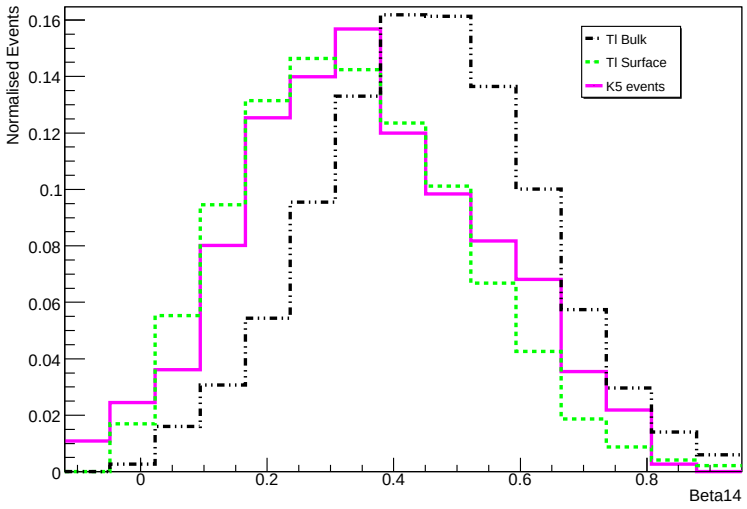


Figure 4.16: $\beta_{14}$ distribution of events originating from K5 (string 18).

in Chapter 5). Both methods showed that there was a significant amount of $^{232}$Th on the surface of the counter and the alpha counting results showed that it was localised in two locations. These were consistent with those identified by the *in-situ* analysis [56]. The *ex-situ* methods will be discussed in Chapter 7.

Knowing that the hotspot had definitely been caused by radioactivity, an estimate of its strength and composition could be made using the *in-situ* method. This is discussed in the following sections.

### 4.2.2 Composition and strength of the K5 hotspot

With the exception of the $x$, $y$ and $z$ cuts, all of the cuts used in the K5 analysis were those used for the $D_2O$ region *in-situ* analysis. The $x$, $y$ and $z$ cut was changed to $x > -40$, $x < 150$, $y > -350$, $y < -150$, $z > -220$ and $z < 80$.

After the $D_2O$ background was accounted for, a total of 349 events were seen from the K5 hotspot. As the surface thallium distribution was different from surface bismuth, a signal separation could be performed. An extended maximum likelihood fit to the K5 data was performed using $\beta_{14}$ as the separation parameter.

As described in previous sections, the mass of $^{232}$Th and $^{238}$U comprising the hotspot could be calculated using an MC generated at a known rate and thus a known mass. For the hotspot, $^{208}$Tl was simulated at 2 Hz and $^{214}$Bi was simulated at 2 Hz. The masses corresponding to these rates could be calculated using the methods described in Section 4.1.9. The masses and rates are given in Table 4.10. and the mass of Th and U in the

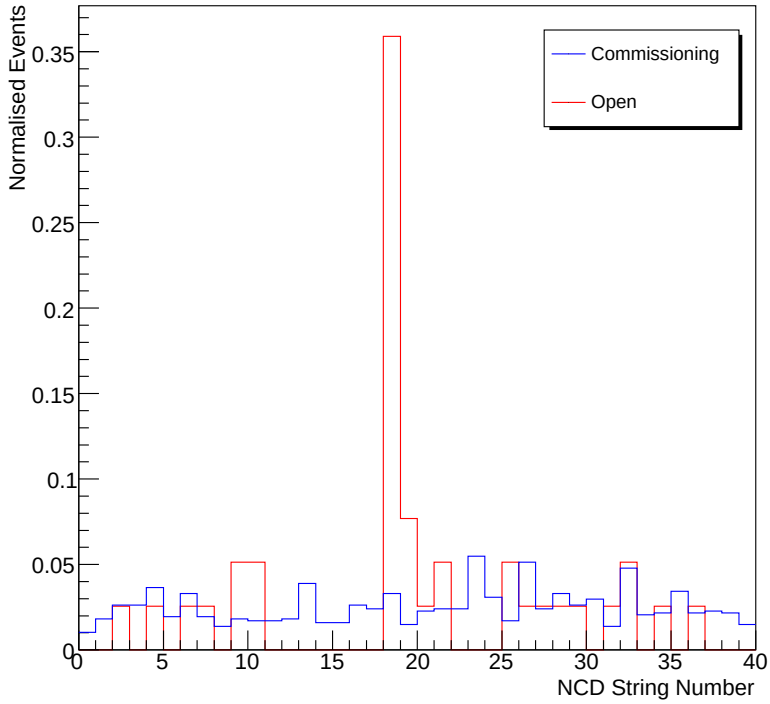


Figure 4.17: 142 hours of commissioning data compared to 142 hours of open month data. Note that the K2 hotspot was outside the fiducial volume used in this study.

hotspot can be calculated from the MC using the following expression:

$$\text{Mass in g} = \frac{\text{Number of events in data}}{\text{Number of events in MC}} \times \text{Mass of MC}$$

The number of each event type found in the data using the maximum likelihood fit is given along with the corresponding masses in Table 4.11.

### 4.2.3 Error Analysis

The systematic errors associated with the K5 measurement are summarised in Table 4.12. The systematic errors were calculated using the methods used for $D_2O$ and NCD bulk which are outlined in Section 4.1.10. The estimated contributions of K5 are

$$\text{Mass of } ^{232}\text{Th} = 1.48^{+0.24}_{-0.27}\,\mu\text{g}$$
$$\text{Mass of } ^{238}\text{U} \ = 0.77^{+0.19}_{-0.23}\,\mu\text{g}.$$

| | Tl NCD | Bi NCD |
|---|---|---|
| Rate (Hz) | 2.0 | 2.0 |
| Mass (g) | $1.36 \times 10^{-3}$ | $1.60 \times 10^{-4}$ |

Table 4.10: Rates and masses (of parent nuclei) for the K5 Monte Carlo.

| | Tl surface | Bi surface |
|---|---|---|
| Data | 304.38 | 44.62 |
| MC | 280441 | 11244 |
| Mass | 1.48 $\mu$g $^{232}$Th | 0.77 $\mu$g $^{238}$U |

Table 4.11: Number of events obtained from the maximum likelihood fit to the data. The numbers of events passing the analysis cuts in the corresponding MC are given, along with the resulting masses. The normalisation has been applied to these numbers.

### 4.2.4 K2

Figure 4.14 shows that the activity associated with K2 was localised around a $z$ position of approximately -300 cm. The isotropy distribution of K2 events is shown in Figure 4.18 and was found to be very bulk like.

The absence of any alpha excess in K2 indicated that the hotspot was either surface activity or activity in the dead region. *In-situ* analysis indicated that activity was either surface activity dominated by uranium or bulk activity. To determine whether or not the activity was on the external surface, the string was counted following its removal from the detector, using the External Alpha Counter (EAC). No evidence of activity was found on the surface of the string, implying that the activity was in the NCD bulk.

*In-situ* analysis was unable to differentiate between $^{232}$Th and $^{238}$U in the NCD bulk and was thus unable to do anything more than to provide a worst case scenario estimate of neutron production[‡‡].

K2 was cut into small sections (about 7-8 cm long) and counted using the underground germanium detector on site. The signal was found in the second section, which included the endcap of the NCD. It is thought that the activity was most likely to be near the endcap in the dead region of the counter [68].

### 4.2.5 An upper limit of the K2 hotspot mass

In the worst case scenario, the hotspot would be all $^{232}$Th chain activity as this would produce more background neutrons when compared with $^{238}$U. As the amount of $^{232}$Th

[‡‡]Note that for bulk activity, the ratio of Čerenkov light to neutron production is not as different when compared to the surface case. The difference in neutron production rates is approximately 30% [67].

| | Th Surface | U Surface |
|---|---|---|
| $\beta_{14}$ | +0.96%, -1.04% | +7.06%, -6.57% |
| Position | +4.48%, -4.73% | +10.25%, -9.70% |
| Energy Resolution | +0.00%, -8.74% | +0.00%, -17.30% |
| Normalisation | +14.50%, -14.50% | +14.50%, -14.50% |
| Statistical | +5.73%, -5.73% | +14.97%, -14.97% |
| Total | +16.25%, -18.52% | +24.27%, -29.51% |

Table 4.12: Summary of systematic errors for the *in-situ* analysis of the K5 hotspot.

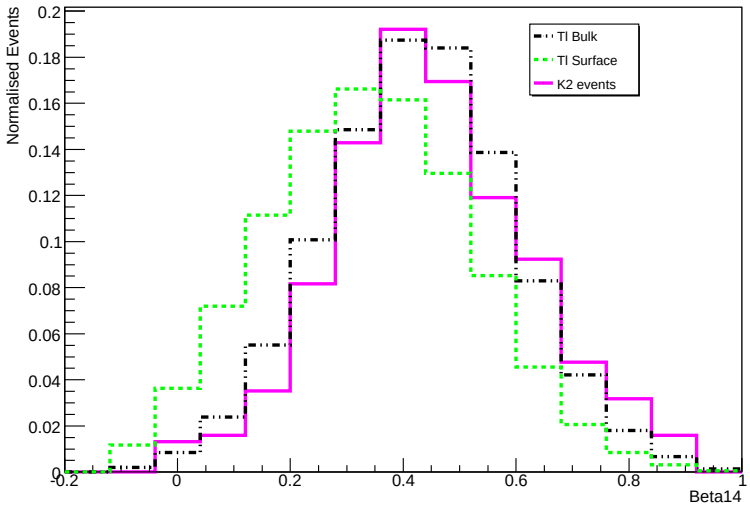


Figure 4.18: $\beta_{14}$ distribution of events originating from K2 (string 31).

required to produce one neutron per day is significantly lower when compared with $^{238}$U, assuming that the hotspot was all $^{232}$Th would give an upper limit on neutron production from the K2 hotspot. Adding the upper systematic error to this central value would give a limit on the hotspot mass and the number of neutrons produced per day.

After accounting for the $D_2O$ and NCD bulk backgrounds, a total of 61 K2 events passed all of the *in-situ* cuts. The K2 $^{208}$Tl bulk MC was run at a rate of 2 Hz and a total of 110,672 MC events passed the analysis cuts. Following the calculations outlined previously and the inclusion of normalisation, a mass of 0.55 $\mu$g of $^{232}$Th was obtained for the hotspot.

| | Th Bulk |
|---|---|
| Normalisation | 14.50%, -14.50% |
| Radius | +1.16%, -0.69% |
| Energy Scale and Resolution | +66.22%, -36.69% |
| Composition | +0.00%, -27.00% |
| Statistical | +12.60%, -12.60% |
| Total | +67.80%, -47.81% |

Table 4.13: Summary of systematic errors for the *in-situ* analysis of the K2 hotspot.

**Error analysis**

Systematic errors were calculated using the methods outlined in Section 4.1.10. An additional uncertainty, due to composition uncertainty, was included. Composition uncertainty is a measure of the uncertainty in the neutron production rate. This arose from the nature of the hotspot, i.e. all $^{238}$U or $^{232}$Th. A summary of the errors is given in Table 4.13. There was no uncertainty due to $\beta_{14}$ as no maximum likelihood analysis was performed. If assumed to be all $^{232}$Th, the K2 hotspot would be equivalent to a mass of $0.55^{+0.37}_{-0.26}$ $\mu$g of $^{232}$Th. The activity obtained by the *in-situ* method was not included in the final evaluation of the neutron background as it could only provide a limit. The neutron background arising from the K2 hotspot was calculated from masses obtained from Ge counting of contaminated sections, described in [56]. The *in-situ* limit provided a useful cross check of the Ge result, and this is discussed further in Chapter 7.

### 4.2.6 *Ex-situ* hotspot measurements

Once NCD phase data taking was complete, several *ex-situ* tests of hotspot composition were undertaken. In total, two independent measures were made of the K5 hotspot; external alpha counting and acid elution. One measurement of the K2 hotspot was made using a germanium detector. A full discussion of these methods, their results and how they compare with the *in-situ* results are given in Chapter 7.

## 4.3 PSUP $H_2O$

The PSUP $H_2O$ was the region of light water between the acrylic vessel and the Photomultiplier Support Structure (PSUP). There were approximately 1700 tonnes of $H_2O$ in this region. The dominant backgrounds in this region were $^{238}$U and $^{232}$Th in the $H_2O$, PMTs and on the acrylic. The amount of $^{238}$U and $^{232}$Th on the AV and in the PMTs was not thought to have changed much during the lifetime of the SNO experiment. The

aim of the *in-situ* analysis in the PSUP $H_2O$ was to determine the amount of $^{232}$Th and $^{238}$U in the $H_2O$.

Background candidates were those that satisfied all of the following cuts

- DAMN: CCF56FE1 (PMT) and 00000140 (NCD)
- ITR $> 0.55$
- $-0.12 < \beta_{14} < 0.95$
- $650 < \mathrm{R}_{xyz} < 680$
- $28.82 < \mathrm{N}_{corr} < 34.82$
- $\mathbf{u}.\mathbf{r} > 0.8$

The RSP energy estimator was not used in this region as it was not calibrated. Optical calibrations in the $H_2O$ were difficult as the positions at which the calibration sources could be deployed were limited by the positions of the guidetubes. As no neutrino analysis took place in the PSUP $H_2O$, calibrations in this region were not a priority. The prompt light based energy estimator, $N_{corr}$ is defined as

$$N_{corr} = \frac{9456\,(N_{win} - N_{dark})}{N_{work}}$$

where $N_{win}$ is the number of PMTs that fired in the prompt time window of the event, $N_{dark}$ is the number of noise PMTs for the event, 9456 is the total number of inward looking tubes and $N_{work}$ is the number of working PMTs for the run. This prompt light estimator was used with $^{16}$N $H_2O$ source runs to define the energy window. The energy window was then moved upward slightly to avoid a small discontinuity in the prompt light estimator "energy" spectrum. This anomaly was caused by a discontinuity in the relationship between the number of Čerenkov photons and the number of hit phototubes in an event. The $\mathbf{u}.\mathbf{r}$ cut was used to select outward travelling light only. The event direction is defined as

$$\frac{\mathbf{u}.\mathbf{r}}{|\mathbf{r}|} = \cos\theta$$

where $\mathbf{u}$ is the unit vector of the event direction, $\mathbf{r}$ is the radial position of the fitted event vertex and $\theta$ is the angle between the two vectors. Forward travelling events are those with positive values of $\mathbf{u}.\mathbf{r}$ and backward travelling events have negative values of $\mathbf{u}.\mathbf{r}$. Figure 4.19 shows a diagram of $\mathbf{u}.\mathbf{r}$ for an outward travelling event. The $\mathbf{u}.\mathbf{r}$ cut used in the PSUP $H_2O$ analysis helped to reduce contributions from PMT beta-gamma events.

Events passing these cuts were separated into $^{208}$Tl and $^{214}$Bi using a 1D extended maximum likelihood fit using isotropy. $\beta_{14}$ pdfs were used as the separation parameter.

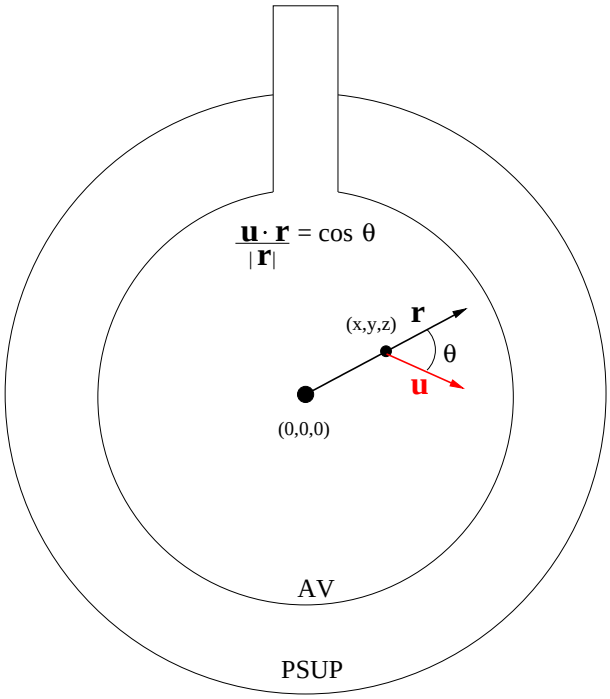


Figure 4.19: Diagram of **u**.**r** for an outward going event [25].

| | Bi | Tl |
|---|---|---|
| Data | 3169.60 | 457.40 |
| MC | 8521 | 12092 |
| g/g$H_2O$ | $35.01 \times 10^{-14}$ | $30.35 \times 10^{-15}$ |

Table 4.14: Number of events obtained from the maximum likelihood fit to the data. The number of events passing each cut in the corresponding MC are given, along with the resulting concentrations.

The number of each event class is given in Table 4.14 along with the number of each event. Concentrations of $^{238}$U and $^{232}$Th equivalent to the fitted values of $^{214}$Bi and $^{208}$Tl were calculated using the methods described previously. The appropriate substitutions for generation rates were made.

### 4.3.1 Error analysis

The systematic errors associated with each cut are given in Table 4.15 and the methods used to obtain them are now described.

| | Th $H_2O$ | U $H_2O$ |
|---|---|---|
| $\beta_{14}$ Mean and width | +8.2%, -8.6% | +1.1%, -1.2% |
| Reconstruction uncertainty | +12.8%, -10.8% | +8.7%, -6.7% |
| Energy scale | +26.2%, -14.6% | +26.9%, -7.4% |
| PMT $\beta - \gamma$ contamination | +0.00%, -57.4% | +0.00%, -5.4% |
| AV $\beta - \gamma$ contamination | +0.00%, -19.7% | +0.00%, -10.5% |
| Statistical | +1.7%, -1.7% | +0.2%, -0.2% |
| Total | +30.3%, -63.9% | +28.3%, -15.5% |

Table 4.15: Summary of errors for the *in-situ* analysis in the $H_2O$ PSUP region.

### $\beta_{14}$ Mean and width

Two sets of $^{16}$N calibrations were performed in the NCD phase, one in January 2006 and the other in November 2006. The Gaussian Mean of the data and MC distributions for each run within the defined fiducial volume were calculated and compared. As with the $D_2O$, a shift between data and MC was observed and this was found to be similar to that in the $D_2O$. A full explanation of this is given in Section 4.1.4. It is unlikely that the shift observed in the $H_2O$ region was caused by underestimating the NCD reflectivity. It was thought that it was likely due to mis-modelling of the AV reflectivity, AV transmission and inclusion of small amounts of PMT beta-gamma events in the data. The uncertainty associated with the mean and width of $\beta_{14}$ was calculated by adjusting the shift by the error on the shift. This gave the errors stated in Table 4.15. The difference between data and MC for $^{16}$N calibrations performed in the NCD phase are shown in Figure 4.20. The difference in $\beta_{14}$ between data and MC for the $H_2O$ Rn spike was $0.0124 \pm 0.020$ and this correction was applied to the Monte Carlo on an event by event basis.

### Reconstruction uncertainty

Using $^{16}$N runs, the difference in the reconstructed positions of $x$, $y$ and $z$ were calculated and found to be approximately 4 cm, 1 cm and 5 cm respectively for runs within the fiducial volume defined by $650 < R < 680$ cm. To calculate the associated systematic error, these corrections were applied on an event by event basis to the MC data. The concentrations were re-calculated and the difference between the central value obtained when the shift were and were not applied was taken to be the systematic error.

### Energy scale

The Gaussian Mean of the $N_{corr}$ distribution was compared for $^{16}$N runs within the fiducial volume (defined by $650 < R < 680$). The energy cut described at the start of this section

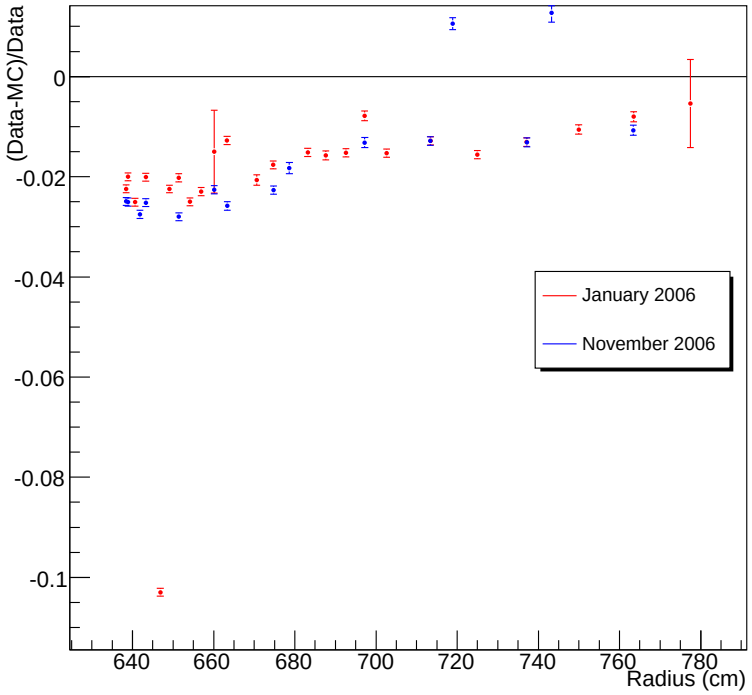


Figure 4.20: (Data-MC)/Data for $\beta_{14}$ versus radius for $H_2O$ $^{16}N$ scans in the NCD phase.

was derived using $^{16}N$ runs at the centre of this fiducial volume. The Gaussian mean of $N_{corr}$ was found to differ by $\pm 1$ $N_{corr}$ at the edges of the fiducial volume (i.e. $R = 650$ cm and $R = 680$ cm. See Figure 4.21. This variation in $N_{corr}$ was used to estimate the systematic error due to the uncertainty in the energy scale and the MC data was shifted by $\pm 1$ $N_{corr}$ to determine its effect on the extracted concentrations.

### PMT beta-gamma contamination

PMT beta-gamma events were predominantly inward travelling events and thus had negative values of **u**.**r**. By relaxing the **u**.**r** cut, the uncertainty associated with beta-gamma events may be determined. The **u**.**r** distributions for data, $^{214}Bi$ and $^{208}Tl$ MC are shown in Figure 4.22. To ensure the uncertainty due to PMT beta-gamma contamination was not overestimated, a cut close to the standard **u**.**r** cut was chosen and the size of this window was the same magnitude. If the **u**.**r** cut was too wide or too low, the PMT beta-gamma contamination would be overestimated. A **u**.**r** cut of $0.6 < \mathbf{u}.\mathbf{r} < 0.8$ was therefore chosen to assess this systematic error.

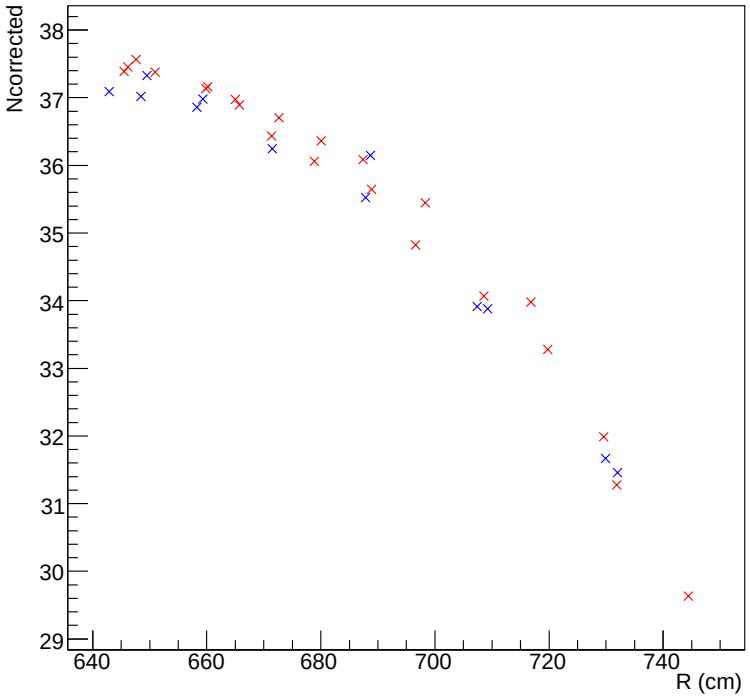


Figure 4.21: $N_{corr}$ versus radius for $H_2O$ N16 scans in the NCD phase. The red points are the January 2006 scan and blue points are the November 2006 scan.

#### AV beta-gamma contamination

The fiducial volume was changed to $640 < R < 670$ cm. The error due to AV beta-gamma contamination was taken to be the difference between the concentrations extracted using this new volume and those extracted using the usual fiducial volume. The range of AV beta-gamma events was approximately 10 cm, which motivated the choice of 10 cm for this shift.

### 4.3.2 Analysis of the $H_2O$ Rn spike

An *in-situ* analysis of the $H_2O$ Rn spike (November 2006) was performed to test the analysis methods. The cuts described earlier in this section were applied to the Rn spike data and MC was generated for the appropriate runs. An estimate of the $^{222}$Rn half life was made using the spike data using only runs 66797 to 66881 inclusive. Run 66797 was the first good run after power was restored to the detector following the annual Creighton Mine power outage. Figure 4.23 shows the event rate for each run. The gradient of the

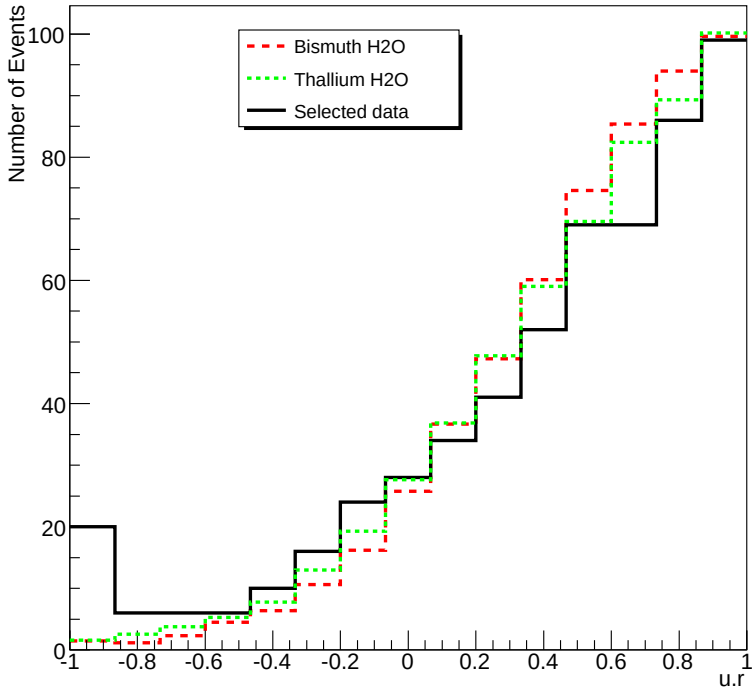


Figure 4.22: **u.r** distributions for selected data, Bi MC and Tl MC in the $H_2O$ region. Both MC distributions have been scaled to the data. The rise in the data at **u.r** values close to -1 is due to PMT beta-gamma events.

fitted line is the decay constant, $\lambda$, from which the half life was found to be $1.61 \pm 0.03$ days.

The inferred half life does not agree very well with the known $^{222}$Rn half life of 3.82 days. The main reason for this is diffusion of the spike into the cavity region of the detector leading to a shorter than anticipated half life. In addition, the source was not uniformly mixed until relatively late on in the spike data set. This was expected to make a small contribution to the observed shorter half life. However the half life estimate using this method is in agreement with values obtained by independent analysts [69].

The initial strength of the $^{222}$Rn could be calculated using *in-situ* methods. The ratio of data events passing cuts to Bi $H_2O$ events passing the cuts was calculated and the concentration of uranium in the data ($gU/gH_2O$) was found by scaling the MC concentration by this ratio. The average rate of radon activity over the runs analysed can be derived from the concentration of uranium. The activity at the time of injection may be

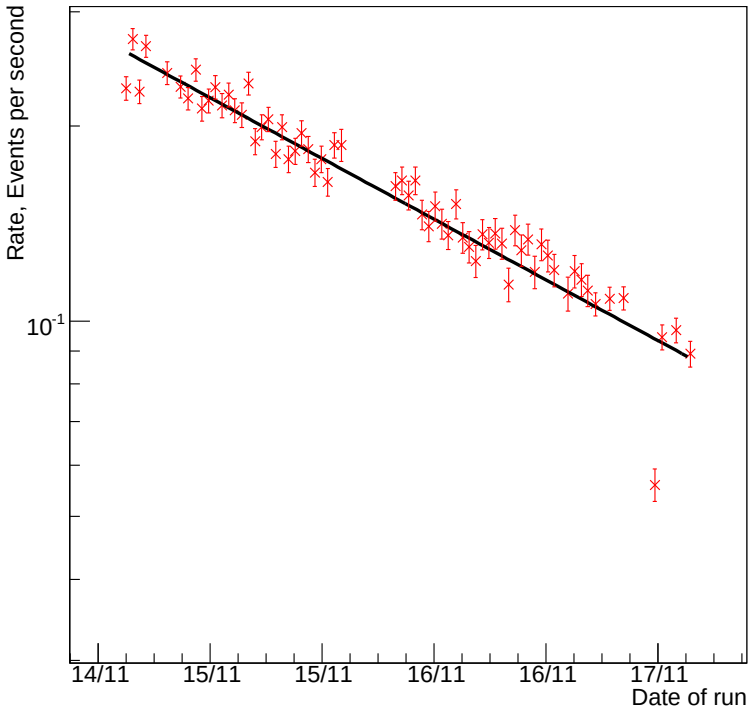


Figure 4.23: Number of events passing the *in-situ* analysis cuts as a function of time. The gradient of the linear fit is the decay constant, $\lambda$ which gives a half life of $1.61 \pm 0.03$ days for $^{222}$Rn.

found using (4.3):

$$R = R_0 \frac{\left(e^{-\lambda t_{start}} - e^{-\lambda t_{end}}\right)}{\lambda\left(t_{start} - t_{end}\right)} \tag{4.3}$$

where $R$ is average activity across the analysis period, $R_0$ is activity at the time of injection, $\lambda$ is the radioactive decay constant of $^{222}$Rn, $t_{start}$ is the time interval between the injection and the start of the first run used in this analysis and $t_{end}$ is the time interval between injection and the end of the final run analysed. The time of injection was taken to be 20:21 (Sudbury time) on November 8th 2006 and the effective half life of 1.61 days (calculated from the data) was used to obtain a value of $\lambda$.

The *in-situ* analysis found an initial spike strength of 64 kBq, which was in good agreement with results obtained using the Germanium detector [62, 70]. No normalisation factor was therefore required for the $H_2O$ *in-situ* results.

| | Bi $H_2O$ | Tl $H_2O$ |
|---|---|---|
| Bi $H_2O$ | 1.000 | -0.771 |
| Tl $H_2O$ | -0.771 | 1.000 |

Table 4.16: Correlation matrix for the $H_2O$ fit.

| | Neutrons produced per day |
|---|---|
| Th $H_2O$ | $0.23^{+0.07}_{-0.15}$ |
| U $H_2O$ | $0.35^{+0.10}_{-0.05}$ |
| Th $D_2O$ | $0.24^{+0.04}_{-0.06}$ |
| U $D_2O$ | $0.23^{+0.04}_{-0.04}$ |
| Th NCD Bulk | $0.18^{+0.07}_{-0.09}$ |
| U NCD Bulk | $0.01^{+0.01}_{-0.01}$ |
| Th K5 | $0.48^{+0.08}_{-0.09}$ |
| U K5 | $0.03^{+0.01}_{-0.01}$ |
| K2 | $0.17^{+0.11}_{-0.08}$ |

Table 4.17: Summary of neutron production via photodisintegration in the NCD phase.

### 4.3.3 Recommended $H_2O$ concentrations

The recommended concentrations for the $H_2O$ PSUP region are

$$\mathrm{gTh/gH_2O} = 30^{+9.2}_{-19.4} \times 10^{-15}$$
$$\mathrm{gU/gH_2O} = 35^{+9.9}_{-5.4} \times 10^{-14}.$$

The correlation matrix is given in Table 4.16. The amount of Bi and Tl are strongly statistically correlated.

## 4.4 Summary of photodisintegration backgrounds

The measured levels of $^{232}$Th and $^{238}$U in the $D_2O$ and $H_2O$ measured by the *in-situ* and *ex-situ* techniques are in good agreement. The *in-situ* measurement of bulk NCD activity agrees with pre-deployment radioassays and also with NCD internal alpha counting.

The number of neutrons produced per day was dependent upon the region and whether the background was $^{232}$Th or $^{238}$U. Monte Carlo studies [47, 53, 59] show that in the $D_2O$ region, 3.79 $\mu$g of $^{232}$Th produced one neutron per day and 29.85 $\mu$g of $^{238}$U produced one neutron per day. For $^{238}$U and $^{232}$Th in the $H_2O$ PSUP region, 221 $\mu$g of $^{232}$Th produced one neutron per day and 1700 $\mu$g of $^{238}$U produced one neutron per day [71]. The number of neutrons produced per day are given in Table 4.17. The total number of neutrons produced by each background was obtained by multiplying the numbers in

Table 4.17 by the livetime of 385.17 days. These totals were multiplied by the relevant neutron detection probabilities to give the total number of detected neutrons. The number of detected background neutrons is constrained in the extraction of the neutrino fluxes.

# Chapter 5

# The Hydrous Titanium Oxide assay

The Hydrous Titanium Oxide (HTiO) assay technique [72, 73] was developed over a number of years by the Oxford water group to measure the amount of $^{224/226}$Ra in the three water regions of the detector, namely the $D_2O$, PSUP $H_2O$ and cavity $H_2O$. HTiO is an inorganic ion exchanger capable of removing heavy ions such as lead, thorium and radium from water. Preliminary experiments [74, 75, 76] indicated that HTiO was suitable for use in SNO and led to the development of the full scale assay technique [76] used successfully throughout the SNO experiment.

Before use in the SNO experiment, both the $H_2O$ and $D_2O$ were purified using the methods outlined in Chapter 2, which removed a significant amount of radioactivity. The amount of Ra in the detector water was, therefore, expected to be small. HTiO assays were used to measure the activity of the $^{232}$Th and $^{238}$U chains by extracting $^{228}$Th, $^{224}$Ra, $^{226}$Ra and $^{212}$Pb from the water. Very little $^{226}$Ra was measured, indicating that the majority of $^{238}$U like activity observed in the detector came from a daughter nuclei lower down the decay chain. The most likely cause was thought to be $^{222}$Rn ingress from the air in the lab and this was measured using a Rn degassing assay method. $^{224}$Ra was clearly seen by both HTiO and MnOx assays. It was thought that this activity was supported by $^{228}$Th which was plated onto the walls of the detector and water systems piping.

To measure the concentration of $^{224}$Ra and $^{226}$Ra in the water, HTiO was deposited onto a pair of 1 m (or 30 cm for $H_2O$ assays) filters. These filters were housed in polypropylene columns, which were sealed and transported underground. Once underground, the pair of columns were connected directly to the detector water systems and water from the detector was passed through them for a pre-determined period of time, during which Ra isotopes were removed from the water by the HTiO-loaded filter. Following extraction, the columns were taken back to the surface lab and the Ra isotopes were removed by flowing 15 $l$ of 0.1 mol/$l$ hydrochloric acid through the columns. The acidic solution that

contained the activity was then concentrated to a volume of a few millilitres and this was added to ∼42 g of liquid scintillator. The scintillator sample was counted using beta-alpha delayed coincidence counters. In this chapter, the HTiO assay technique is presented and the analysis and results of NCD phase assays discussed.

## 5.1 Properties of HTiO

As mentioned above, Hydrous Titanium Oxide (HTiO) is an inorganic ion exchanger. Its hydroxide structure enables amphoteric behaviour allowing anionic exchange at low pH and cationic exchange at higher pH. In SNO, the pH of the $D_2O$ and $H_2O$ is 6.8 thus the hydrous oxide behaves as a cation exchanger and proceeds via the following reaction

$$\text{M-OH} + \text{OH}^- + \text{N}^+ \leftrightharpoons \text{M-O}^-\text{N}^+ + \text{H}_2\text{O}$$

where M-OH is the hydrous oxide and $N^+$ is the heavy ion. Hydrous oxides are well suited to extracting heavy ions from water as they are particularly selective, having a greater affinity for $2^+$ ions. Hydrous titanium oxide has been used in a wide variety of applications in the nuclear industry, including removal of uranium from seawater [77]. This was the main motivation for its use in SNO. The preparation of HTiO will now be discussed.

## 5.2 Preparation of HTiO

The HTiO used in the assay process was prepared on site by SNO staff. It was manufactured by precipitation from titanium (IV) sulphate ($Ti(SO_4)_2$) solution. One molar sodium hydroxide (NaOH) was added to a known volume of 15% $Ti(SO_4)_2$ solution and the resultant solution stirred. Sodium hydroxide was added until the pH stabilised. The reaction is complex and many different ionic species in the $Ti(SO_4)_2$ solution may be involved, but it can be summarised as [74]:

$$\text{Ti}(\text{SO}_4)_2 + \text{NaOH} \rightarrow \text{Ti}(\text{OH})_2(\text{ONa})_y.\text{xH}_2\text{O}_{(\text{s})} + 2\text{Na}_2(\text{SO}_4)_{(\text{aq})} \tag{5.1}$$

where $Ti(OH)_2(ONa)_y.xH_2O_s$ is HTiO. To remove the solid HTiO precipitate, the solution was centrifuged and the supernatant decanted. The solid precipitate was rinsed using ultra pure water (UPW) to form an HTiO suspension. Size of the HTiO particles ranged from 1 $\mu$m to 100 $\mu$m with the mode occurring at 10 $\mu$m [75]. For use in an assay, the HTiO suspension was deposited onto membranes with pore size 0.1 $\mu$m.

## 5.3 The HTiO assay

The HTiO assay was a five stage process; deposition, extraction, elution, secondary concentration and counting. To minimise any radioactive backgrounds and to ensure that the chemical efficiency was as high as possible, analytical grade reagents and ultra pure water were used in all stages of the technique. The five stages are now described.

### 5.3.1 Deposition

HTiO was deposited onto ultra-filtration membranes held inside polypropylene columns. The columns were attached to a specially constructed elution and deposition rig, a schematic diagram of which is given in Appendix C. This elution rig allowed liquids to flow through the columns around a closed path at various flow rates. Aqueous HTiO was placed in the stock reservoir of the rig and diluted to a volume of 15 litres using ultra pure $H_2O$ (UPW). The solution was circulated through the columns at a flow rate of 20 $l$/min for approximately 30 minutes and the amount of HTiO was set such that the coverage of HTiO on the membranes was 2.5 g per metre squared of membrane (referred to as g/m$^2$). Two 40 inch columns were used for typical $D_2O$ assays and two 10 inch columns for $H_2O$ assays. Choice of column length was motivated by the expected signal in each region.

At this stage, a background check was performed to assess the contribution of the equipment and reagents used in the chemical processing of the columns, once the assay had taken place. The columns were eluted with hydrochloric acid (HCl). The acid solution was then concentrated and counted. The background sample was counted for approximately one week prior to the assay taking place. Once the background sample has been processed, the filters were cleaned by rinsing them with 0.5 mol/$l$ HCl at a rate of 80 $l$/min for approximately 40 minutes, after which they were left to soak in 0.5 mol/$l$ HCl for up to 15 hours. Following this, the filters were rinsed with UPW to a near neutral pH and reloaded with HTiO. The columns were then sealed using polypropylene end caps, packaged and taken underground for assay.

### 5.3.2 Extraction

Following deposition, the columns were sealed and transported underground for the extraction stage. A schematic of an HTiO column and the flow path of water is shown in Figure 5.1. If a $D_2O$ assay was taking place, the filters had to be deuterated prior to extraction. Deuteration displaced any UPW that remained trapped deep within the pores of the filter, by filling the columns slowly over a two hour period with approximately 10 kg of $D_2O$. Any remaining UPW was displaced out of the top of the columns. The filters

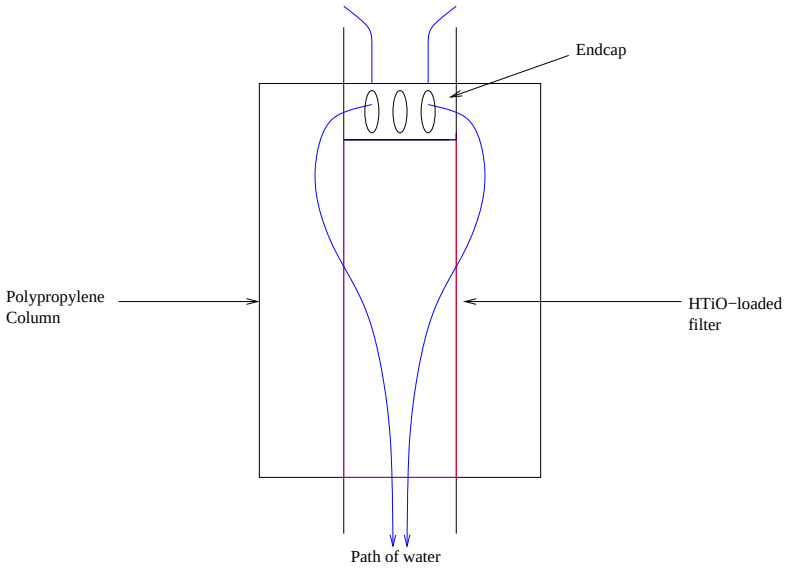


Figure 5.1: Schematic diagram of an HTiO loaded filter in a polypropylene column. The blue lines indicate the path of water through the column during extraction.

were then left to soak in $D_2O$ for up to 15 hours and following this, 20 kg of $D_2O$ was passed through the columns. Deuteration ensured that the high isotopic purity of the $D_2O$ in the detector was maintained. It did not take place if the columns were used for an $H_2O$ assay.

Once underground, the columns were connected to the detector water systems. During assay, water was extracted from one of the detector regions, passed through the columns and returned to the detector. $D_2O$ assays typically processed around 300 tonnes of water over 4 days. $H_2O$ assays processed around 30 tonnes of water during a two day period. The difference in running time and amount of water processed was because the $D_2O$ was approximately 10 times less radioactive when compared with the $H_2O$. As the water flowed through the columns, Ra and Th isotopes were absorbed by the HTiO on the filters. Once the assay had been shut down, the columns were removed from the water systems and transported to the surface lab, where the activity had to be removed from the columns.

### 5.3.3 Elution

Once on surface, the columns were connected to the elution and deposition rig. The reservoir was filled with 15 $l$ of 0.1 mol/$l$ HCl and this was circulated through the columns at a flow rate of 80 $l$/min for 20 minutes to remove the activity. The resulting 15 $l$ of eluate was concentrated to allow counting to take place.

### 5.3.4 Secondary concentration

The HTiO eluate was concentrated in preparation for counting. During the salt phase, a significant decrease in secondary concentration efficiency was observed [78]. This was attributed to increased levels of Mn in the HTiO eluate caused by elevated levels of Mn in the $D_2O$ leaching from the beads used in MnOx assays. In the original HTiO assay method, Ra was removed from the filters using 15 $l$ of dilute $HNO_3$. This eluate was concentrated by co-precipitation with HTiO and then by passing it through a series of three MediaKap-10 filters. Each filter was subsequently eluted three times to ensure removal of all activity, resulting in three final samples per assay. The extracted Mn was removed during elution of the filters with 15 $l$ of dilute $HNO_3$. It was found to form hydrous manganese oxide during the co-precipitation step of secondary concentration. The hydrous manganese oxide absorbed some Ra present in the sample which could not be removed by subsequent HCl elution of the MediaKap filters. This resulted in a decreased secondary concentration efficiency.

The levels of Mn affected the efficiency of the HTiO assays to such an extent that the method became unusable and the HTiO $D_2O$ assay programme was abandoned in the salt phase. A new secondary concentration method was then developed for use in the salt phase [73]. Due to the time taken to develop this new method, it was not actually used in the salt phase. It was used in the NCD phase and had several advantages:

1. It was less sensitive to trace impurities in the eluate.
2. Fewer channels of the beta-alpha counting system were required; only two compared with six previously.
3. The time required to process the filters once the assay had been completed was reduced from 12 hours to around 5-6 hours.

Once the salt was removed from the $D_2O$, the reverse osmosis unit could be run on a regular basis. As a result, levels of Mn were stabilised and were much lower than in the salt phase. However, as there were other advantages to the new secondary concentration method, it was decided to use this for all NCD phase assays.

The resulting 15 $l$ of acid+activity from the elution stage was passed through a cation exchange resin* at a rate of 250 ml/min. Radium and thorium in the 15 $l$ HTiO eluate were extracted onto the resin. Once the 15 $l$ eluate had been processed, the resin was rinsed with UPW in preparation for selective removal of Ra. As the majority of Ra and Th were extracted by the first few cm of resin at the top of the column, the column was inverted for Ra removal. Approximately 100 ml of 0.25 M EDTA† (pH 12) was

*Dowex 50WX8

†ethylenediaminetetraacetic acid

passed through the ion exchange resin at a rate of 5 ml/min. During this EDTA elution, approximately 15% of any thorium on the resin was also removed. The column was sealed with parafilm once all of the EDTA had passed through the resin. Upon addition of 8 m$l$ of concentrated nitric acid ($HNO_3$) to the eluate, a white precipitate of EDTA was formed. To decompose the EDTA, the solution was boiled for 15 minutes at which point a second aliquot of concentrated $HNO_3$ was added and boiling continued for a further 15 minutes.

Once boiling was complete, the next step involved co-precipitation with HTiO. Approximately 250 ml of UPW was added to the residual solution and mixed. After a short time, 2 ml of 15% titanium sulphate[‡] was added and mixed. The solution was titrated to pH 9 using 10 M NaOH until a white precipitate was formed. The white solid was a co-precipitate of Ra and HTiO. At this point, approximately 7% of thorium extracted during the assay by the HTiO filters was present. To remove the HTiO co-precipitate, the solution was centrifuged at a rate of 3400 revolutions per minute (rpm) and the supernatant solution was decanted. The HTiO precipitate was dissolved in 1.5 ml of concentrated HCl and diluted to a volume of 8 ml using UPW. This final sample was added to approximately 42 g of Optiphase HiSafe 3 liquid scintillator cocktail and counted using a beta-alpha coincidence counting system for 10-14 days.

It was possible to make an estimate of the amount of $^{228}$Th extracted during an assay. $^{228}$Th would be present in the HTiO eluate as HCl elution of the HTiO-loaded filters removed Th with an efficiency of 65%. The ion exchange resin would extract this Th from the 15 $l$ eluate and only $\sim$ 15% of Th present on the resin was removed during the EDTA elution. If the column was sealed once the EDTA elution was complete, it could be left for 9-10 days, allowing the equilibrium between $^{228}$Th and $^{224}$Ra to be re-established. Once equilibrium was re-established, the resin could be re-eluted with EDTA and the secondary concentration proceeded as before. Overall efficiency at 27% was, however, lower than that for the first Ra concentration. Although never used for assay samples in the NCD phase, this method proved successful during measurements of hotspot activity, described in Chapter 7.

### 5.3.5 Counting

Towards the end of the $^{232}$Th decay chain, $^{212}$Bi decays by beta emission to a short lived state of $^{212}$Po which decays by alpha emission with a half life of 0.30 $\mu$s. There exists a similar delayed coincidence in the $^{238}$U chain where $^{214}$Bi decays by beta emission to $^{214}$Po, which subsequently decays by alpha emission with a half life of 164 $\mu$s. The half lives for these two processes are sufficiently different to allow discrimination between the

[‡]60 mg in Ti

two chains. The rate of these coincidences was directly proportional to the amount of Bi present in the sample and by fitting time spectra to the rate of Bi events, activity of extracted Ra could be derived assuming secular equilibrium holds. The activity of any extracted Th could also be determined from the time fit to the spectrum. A beta-alpha coincidence counting system was developed by Oxford to detect and differentiate between the two chains [72, 75].

The sealed sample to be counted was optically coupled to a 5 cm diameter photomultiplier tube[§] (PMT). The PMT was read out by a NIM[¶] electronics system in which a series of threshold and logic conditions determined whether a genuine coincidence had occurred. All coincidences that occurred in a 0.03-500 $\mu$s window were read out by a CAMAC[‖] unit to a data acquisition computer. The measured efficiency of this system was determined to be $45 \pm 5\%$ for $^{224}$Ra and $60 \pm 10\%$ for $^{226}$Ra. A detailed technical description of beta-alpha counting is given in Chapter 6. The analysis and interpretation of this data is now discussed.

## 5.4 Analysis of NCD phase HTiO assays

During the NCD phase, defined as November 2004 to November 2006, 16 $D_2O$, 25 PSUP and 12 cavity assays were performed. In this work, $D_2O$ assays will be referred to as RDAX, where RDA stands for Radium $D_2O$ Assay and X is an integer used to label the assay. PSUP and cavity assays will be referred to as LWAX where LWA stands for Light Water Assay and X is an integer used to label the assay.

Results were obtained for 50 of the 53 assays performed during the NCD phase. Three assays were "lost" for different reasons. A $D_2O$ assay (RDA34) was lost due to failure of the beta-alpha counting system. The beta discriminator unit failed during the crucial first 48 hours of counting. As the amount of bismuth in the counting sample builds up and reaches a maximum after 32 hours of counting, the time spectrum fitter cannot fit the data effectively if the first 48 hours of counting are interrupted. A similar incident resulted in the loss of a PSUP assay (LWA59). An unexpected power outage underground caused the loss of a cavity assay (LWA55), as the amount of water processed was insufficient to produce a measurable signal. It was not possible to gain any information about the amount of activity extracted from these assays and hence they are referred to as being "lost". One further assay, LWA54, was excluded from the final analysis because it returned a very low, unphysical, concentration. The result was thought to be due to an error during deposition of HTiO on the columns before use underground. The analysis of

[§]Electron Tubes Ltd. 9266KB
[¶]Nuclear Instrument Module
[‖]Computer Automated Measurement and Control

the raw counter data is now discussed.

### 5.4.1 Data Analysis

Analysis of HTiO assay data can be divided into three separate stages. First, data from the beta-alpha coincidence counters is analysed to determine the amount of $^{224}$Ra and $^{226}$Ra in the final sample. Next, the rate at which water flowed though the columns during the assay was analysed to determine the decay factor and the total mass of water processed by the columns **. Finally, time corrections were applied to account for the time between the end of extraction and the start of counting. The final flow and time corrected rates were converted into masses of $^{224}$Ra and $^{226}$Ra. The concentration of activity in the assayed region was obtained by dividing the Ra masses by the mass of water processed during the assay. The amount of $^{226}$Ra had always been below the detection limit in all three water regions. The remainder of this chapter explains how results were obtained for $^{224}$Ra and $^{232}$Th concentrations in each region.

#### Analysis of counter data

Activity from elution was determined by fitting time spectra to the beta-alpha coincidence rate. Before a fit could be made to the data, cuts had to be applied that selected only genuine beta-alpha coincidences referred to as signal events. Background events could be caused by beta-beta coincidences, where the second beta pulse was smeared by noise in the system. To discriminate between signal and background events, a plot of alpha ADC charge versus the pulse shape discrimination variable (psd) of the second event in the coincidence was made for each PMT in the counter data. For a pulse, the psd value is defined as

$$\text{psd} = \frac{\text{full charge} - \text{tail charge}}{\text{full charge}}.$$

The second (alpha) pulse of a genuine beta-alpha coincidence had a psd of approximately 0.35 whereas background events had a psd (of the second pulse) of around 0.20. The method of pulse shape discrimination is described in more detail in Chapter 6 and [75].

Typical assay data is shown in Figure 5.2. Two distinct bands can be seen; one signal (upper band) and one background (lower band). The position of each band is known from (separate) calibration runs performed with $^{228}$Th sources. Taplin [75] attributed this lower band to beta-beta coincidences, where the second beta pulse was broadened by noise in the system, increasing the psd value of the second beta pulse to around 0.2. This is still

**the decay factor accounts for the amount of activity captured by the columns that decayed before the assay ended

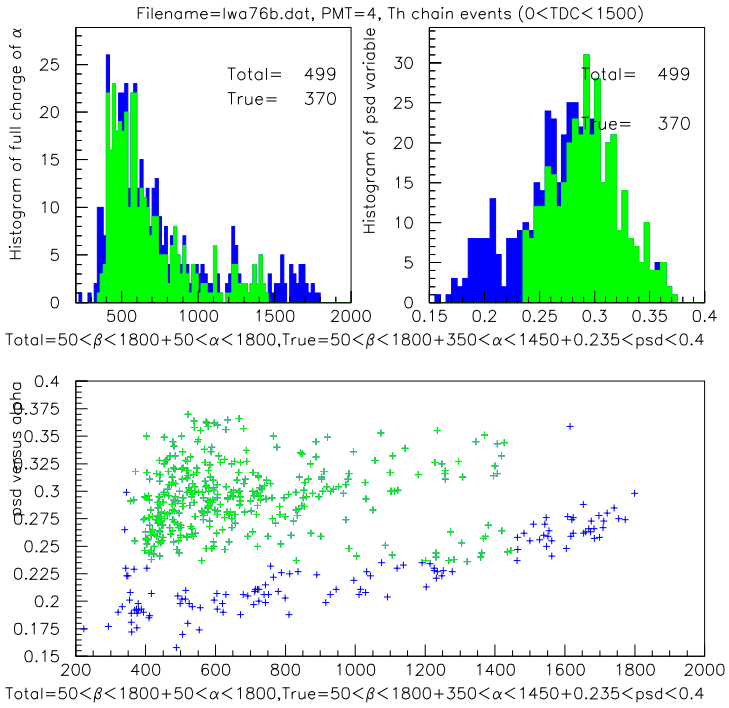


Figure 5.2: An example of data taken by the beta-alpha coincidence counters. The green points are genuine events selected by the analysis cuts. The blue points are the system background. In the upper left graph, the x axis is the alpha ADC value and in the upper right plot, it is the value of the psd variable. The x axis in the lower plot is alpha ADC value.

sufficiently different from a genuine beta-alpha coincidence and these events can easily be removed by applying analysis cuts to the counter dataset.

The original counter data analysis program (written by Taplin, McGregor and Dai) only allowed the analyst to select a rectangular box around the signal. This box was defined by specifying lower and upper limits for alpha ADC and psd variables. For all PMTs, there was clear separation between signal and background. However, for some tubes the gradient of the background region was very steep, making it very difficult to select only the signal region. Occasionally, some of the signal was sacrificed to minimise the amount of background included in the fit. This became a more serious problem in the NCD phase, where radioactivity levels in all three water regions were very small. A new method, using diagonal cuts, was developed to improve the acceptance of genuine beta-alpha coincidences and rejection of background events.

Plots of psd versus alpha for $^{228}$Th and $^{226}$Ra sources were made and looked similar

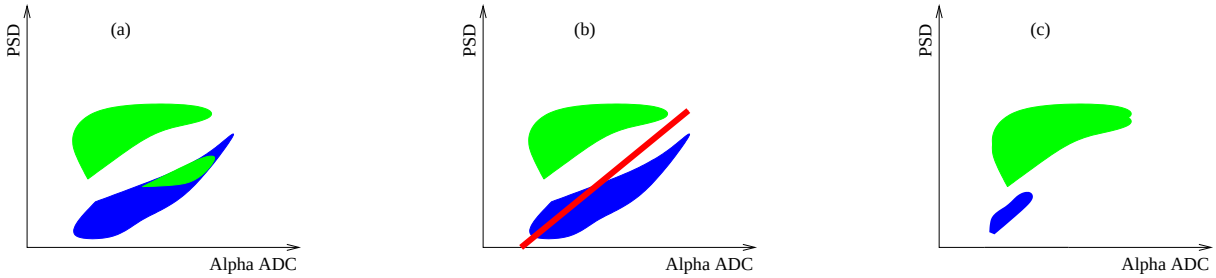


Figure 5.3: A schematic representation of the the diagonal cutting method. (a) shows the normal counter data. (b) shows the proposed diagonal cut.(c) shows the data once the diagonal cut had been applied.

to the representation given in Figure 5.3 (a). The upper band consists of genuine beta-alpha coincidences and the lower band background coincidences. The green regions in Figure 5.3 (a) show data that was selected by the analysis cuts and it can be clearly seen that these cuts selected a proportion of background events. To exclude as much background as possible a diagonal cut was applied. Figure 5.3 (b) shows the proposed cut in this case. The diagonal cut for each PMT was calculated using calibration data from sources ranging in strength from 0.5 mBq to 1 Bq. The diagonal cut was then applied to the data, resulting in a psd versus alpha plot similar to that shown in Figure 5.3 (c). It was then possible to select the signal region using a rectangular box without including any backgrounds.

The gradient of the diagonal cut used in the analysis differed for each of the 8 PMTs used on the system, as they operated at different high voltages. Only the PMT voltage affected the gradient of the alpha ADC versus psd plot and, provided that the PMT HV remained stable, the cut would also remain stable as a function of time. The High Voltage (HV) of each PMT was checked and recorded before each counter run took place. Only one change in HV was noted during the NCD phase and it was traced to the failure of a resistor in the base of a PMT. This base was replaced and, subsequently, no change in HV was noted.

The gradient of the diagonal cut was set for each PMT and applied to all counter data files. After cutting each file, the data were analysed using the programs written by Taplin, McGregor and Dai. Results from both the new diagonal method and the previous method were compared and found to agree at the one sigma level. The diagonal method had several advantages over the old method: it produced results with smaller fit uncertainties and it ensured no backgrounds were included in the signal analysis. For these reasons, it was decided to use this diagonal method for all NCD phase assays.

Once genuine beta-alpha coincidences had been selected in the data, the fit to the

data using time spectra was made. The total beta-alpha coincidence rate was determined by the contribution of all radionuclides in the decay chain. The initial coincidence rate was dominated by the 10.6 hour half life of $^{212}$Pb, which built up to a maximum approximately 32 hours after counting began. The coincidence rate then decayed at a rate determined by the 3.66 day half life of $^{224}$Ra. It is important to note that Th, Ra and Pb were all efficiently extracted from the underground water systems and the presence of Th in the counting sample could have influenced the amount of Ra inferred from the data. Fortunately, very little Th was eluted from the filter and only 7% of Th extracted by the HTiO filters was present in the final sample and this was accounted for in the time fitting. Figure 5.4 shows a typical fit to assay data. The fit results for $^{212}$Pb and $^{212}$Bi in Figure 5.4 were significantly greater when compared with the fitted rate of $^{224}$Ra. This suggested that there was a possible disequilibrium in the chain and the same behaviour was noted in the background samples. This was explained by ingress of radon daughters from the air into the sample during the elution and secondary concentration stages. This resulted in an additional source of $^{212}$Pb and thus $^{212}$Bi. An increase in the amount of $^{212}$Pb and $^{212}$Bi present in assay samples was found following the move of the chemistry lab to the new surface building on site. The new surface building was constructed from concrete, which is known to emanate $^{220}$Rn and thus $^{212}$Pb. As both isotopes occur below $^{224}$Ra and were fitted for, the elevated levels were not of concern and did not affect the fitted value of $^{224}$Ra. Assay and background samples were counted for 7-10 days to determine any contribution from $^{228}$Th, as it would give a constant non-zero background. Following the initial counting period of 7-10 days, the samples were left for up to two weeks and were then re-counted for another week to determine the $^{228}$Th background accurately.

A maximum likelihood fit of time spectra for these radioisotopes was made to determine the amount of Ra present in the sample. The majority of information in the fit was taken from the first 48 hours of counter data and, if the system failed or counting was interrupted during this period, the assay could have been lost. The rate of $^{224}$Ra obtained from the fit was used in the analysis.

### Analysis of flow data

The rate of water flowing through the columns during the assay was recorded each second. To calculate the mass of water processed, the average flow rate was multiplied by the duration of the assay. The flow analysis calculated the amount of $^{224}$Ra that decayed whilst the assay took place. This decay factor was non-negligible as the half life of $^{224}$Ra was 3.66 days.

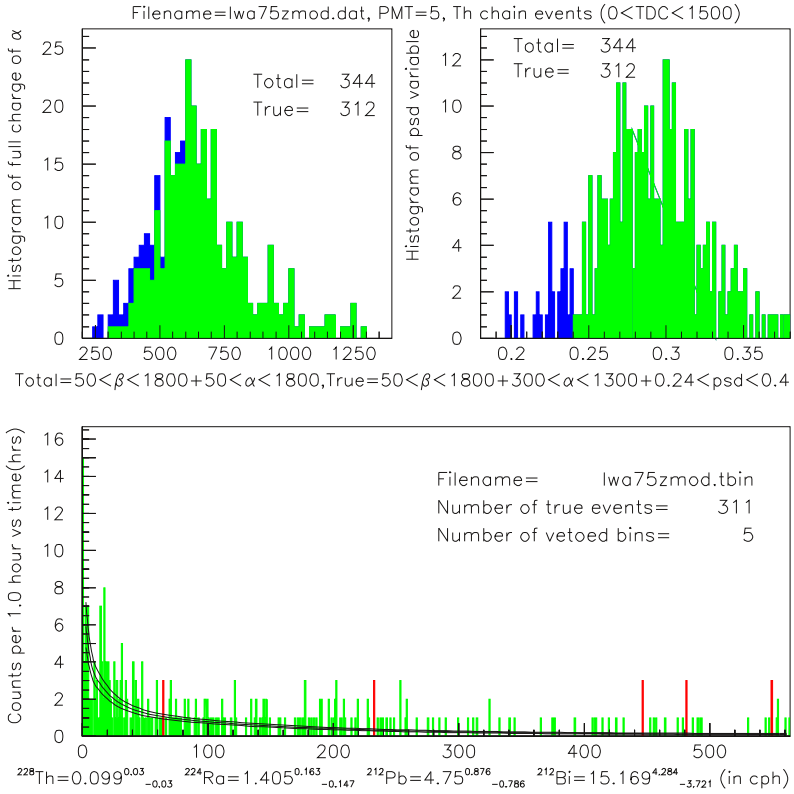


Figure 5.4: The fitting of true beta-alpha coincidences binned per hour for LWA75 for Th chain activity. Red bins indicate when new runs were started and these bins have been excluded from the fit. The x axis shows time since start of counting. The central exponential (black line) is the results from the fit and the other exponentials are 1 sigma statistical errors.

### Time corrections

Once the decay factor had been calculated, time corrections had to be applied to the data to account for $^{224}$Ra decay between the end of extraction and beginning of counting. This was split into two time intervals; time between end of extraction and start of elution and the time between start of elution and start of counting. Two time periods were used since a small amount of Ra entered the sample from the equipment and reagents used in the elution and secondary concentration stages. This background is discussed in Subsection 5.4.2.

Once all of the counting, flow and time information was known, the concentration of $^{224}$Ra measured by the assay could be calculated.

### 5.4.2 Equipment and Reagent background

The equipment and reagents used in HTiO assays may have contributed Ra to the sample. To measure this contribution a background measurement was made for every assay. Once HTiO had been deposited onto the filters, it was removed by elution. The eluate was concentrated and the resultant solution counted, in a manner identical to an assay. The filters were cleaned and HTiO was re-loaded onto them. The background sample was counted for 7-10 days before the assay took place. The contribution was non-negligible, but small compared with the observed assay signal.

Identical methods were used to process $D_2O$ (RDA) and $H_2O$ (LWA) assays, but two different elution rigs were used. Two rigs were used to avoid cross contamination between heavy and light water assays. The PSUP $H_2O$ was approximately 10 times less pure compared with the $D_2O$. In addition, two elution rigs allowed more assays to be performed during each phase of the experiment.

Both rigs were constructed from ultra pure polypropylene and were based upon the same design. However, the $D_2O$ elution rig used a diaphragm pump and the $H_2O$ elution rig used a mechanical pump. The diaphragm pump in the $D_2O$ rig ensured that acid used in elution and other associated processes on the rig did not come into contact with any mechanical parts, which would have been a possible source of contamination. The mechanical pump used on the $H_2O$ rig had plastic coated metal parts which came into contact with the acid. As these were plastic covered, the acid should not have come into contact with any significant source of activity.

Measured background levels were found to be very stable for NCD phase $D_2O$ assays; typically 0.330 counts per hour of $^{224}$Ra. This was not found to be the case for $H_2O$ assays. During the NCD phase, backgrounds measured for assays using the $H_2O$ rig fluctuated and in a few extreme cases, produced background samples that were greater than or equal to the activity recorded by the assays. The results of these assays are shown in Figure 5.5, where it can be seen that the majority of assay results were consistent. As the concentration and counting stages were identical for LWA and RDA, the cause of the problem was therefore the elution rig.

A number of procedures were implemented in an attempt to control the rig background. These included replacing several pump parts, a pre-deposition acid rinse and a pre-deposition HTiO rinse. None of these solved the problem and, in September 2006, it was decided to perform all LWA depositions and elutions using the $D_2O$ rig. All assays after but not including LWA72 were performed using the $D_2O$ rig and the measured background for these assays was found to be very stable and in agreement with those measured for $D_2O$ assays.

The majority of PSUP assays in the NCD phase were performed using the $H_2O$ rig.

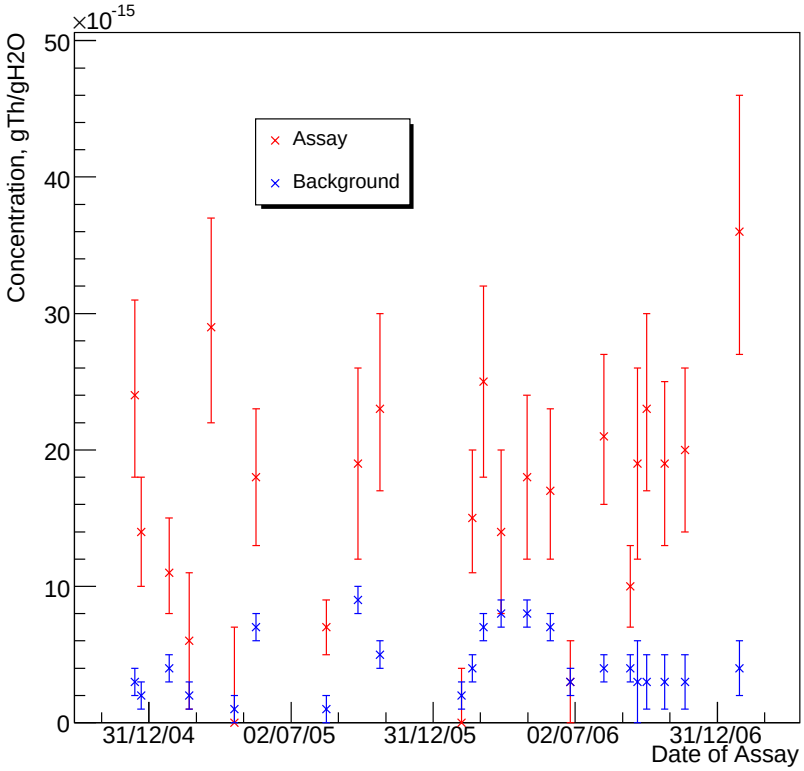


Figure 5.5: NCD phase HTiO assay results for the PSUP region. The rig background fluctuations have not been included in the error bars. There is no additional error for the last 5 points as those assays were performed using the $D_2O$ rig.

Even though the results were in agreement with each other, see Figure 5.5, the uncertainty associated with a variable background had to be accounted for in the final results.

### 5.4.3 Accounting for fluctuating rig backgrounds

The measured backgrounds for $H_2O$ assays were found to vary significantly, with observed rates of $0.110 \pm 0.070$ cph and $1.611 \pm 0.151$ cph for the maximum and minimum count rates respectively. In some cases the high background resulted in a negative (unphysical) assay result. It was thought that in these cases, the $H_2O$ elution rig background was overestimated, which would have resulted in the assay concentrations being underestimated. The effect of varying rig backgrounds had to be accounted for in the LWA results up to and including LWA72. It was decided that the fluctuations in rig background should be treated as an uncertainty as there was no obvious time structure to the data.

The following method was used to assign an upper and lower uncertainty due to rig

background fluctuations

1. Calculate the central value for each assay using the measured background and assay values.

2. Assign the upper systematic uncertainty due to background fluctuations by calculating a new central value for each assay using the lowest observed background count rate for a PSUP assay. The systematic error is the difference between this central value and that obtained from step 1.

3. Assign the lower systematic uncertainty by calculating a new central value for each assay using the highest observed, physically possible background count rate for a PSUP assay. "Physically possible" means the highest recorded background that returned a non-negative assay result. The systematic error is the difference between this central value and that obtained from step 1.

4. Combine this systematic error in quadrature with the other systematic and statistical errors and use the central value obtained from 1 as the concentration and associated uncertainty for each assay.

Table 5.1 shows the systematic errors due to uncertainty in the rig background. The central value of the concentration for the assay using the measured background is also given. As can be seen from Table 5.1, the background fluctuations appear to have had an effect on PSUP assays. The observed differences are included as an additional systematic on the final HTiO numbers and are added in quadrature to the other systematic errors. This leads to increased systematic errors for all HTiO assays up to and including LWA72. Figure 5.6 shows a comparison between results with and without the additional systematic. This leads to increased systematic errors for all HTiO assays up to and including LWA72.

The final Ra number for the PSUP is obtained by combining the HTiO and MnOx results using the model described in [79]. In this model, greater weight will be given to the later PSUP assays, post LWA72, where there were no problems with the rig backgrounds. Even without the background corrections, the affected HTiO assays agreed with MnOx results at the 1.5 to 2 sigma level and with the *in-situ* results at the 1 sigma level. The additional background uncertainty was included to explain a number of assays that returned a very low value, such as LWA51, LWA61 and LWA68. However, the background problem failed to explain why LWA54 returned a low value which was thought to be caused by poor HTiO deposition. The results from this assay were excluded from the final number.

| Sample name | Region | Measured concentration | Background uncertainty systematic error |
|---|---|---|---|
| LWA42 | Cavity | 68 | +2, -32 |
| LWA43 | PSUP | 24 | +6, -19 |
| LWA44 | PSUP | 14 | +5, -5 |
| LWA45 | Cavity | 79 | +8, -55 |
| LWA46 | PSUP | 11 | +6, -3 |
| LWA47 | PSUP | 6 | +33, -6 |
| LWA48 | Cavity | 67 | +4, -11 |
| LWA49 | PSUP | 29 | +6, -5 |
| LWA50 | Cavity | 52 | +11, -5 |
| LWA51 | PSUP | 0 | +14, -0 |
| LWA52 | PSUP | 18 | +11, -2 |
| LWA53 | Cavity | 38 | +5, -12 |
| LWA54 | PSUP | 7 | +0, -7 |
| LWA56 | PSUP | 19 | +15, -4 |
| LWA57 | Cavity | 49 | +13, -13 |
| LWA58 | PSUP | 23 | +5, -10 |
| LWA60 | Cavity | 64 | +20, -32 |
| LWA61 | PSUP | 0 | +14, -0 |
| LWA62 | PSUP | 15 | +4, -9 |
| LWA63 | PSUP | 25 | +8, -4 |
| LWA64 | PSUP | 14 | +19, -6 |
| LWA65 | PSUP | 18 | +13, -0 |
| LWA66 | Cavity | 43 | +9, -43 |
| LWA67 | PSUP | 17 | +9, -2 |
| LWA68 | PSUP | 3 | +20, -3 |
| LWA70 | PSUP | 21 | +4, -6 |
| LWA72 | PSUP | 10 | +6, -1 |

Table 5.1: Central values of Th concentration and absolute systematic error due to uncertainty in the rig background measurements for PSUP and cavity HTiO assays in the NCD phase. Values given are $gTh/gH_2O \times 10^{-15}$.

The inclusion of a systematic error due to uncertainty in the rig background improved agreement with the MnOx results and also explained a number of anomalously low assay results, which were known to have unphysically high backgrounds.

### 5.4.4 Extraction efficiency

The ability of HTiO to remove Ra from water can be measured directly by an assay. In each $H_2O$ assay, two columns were connected in series, the first of which was referred to

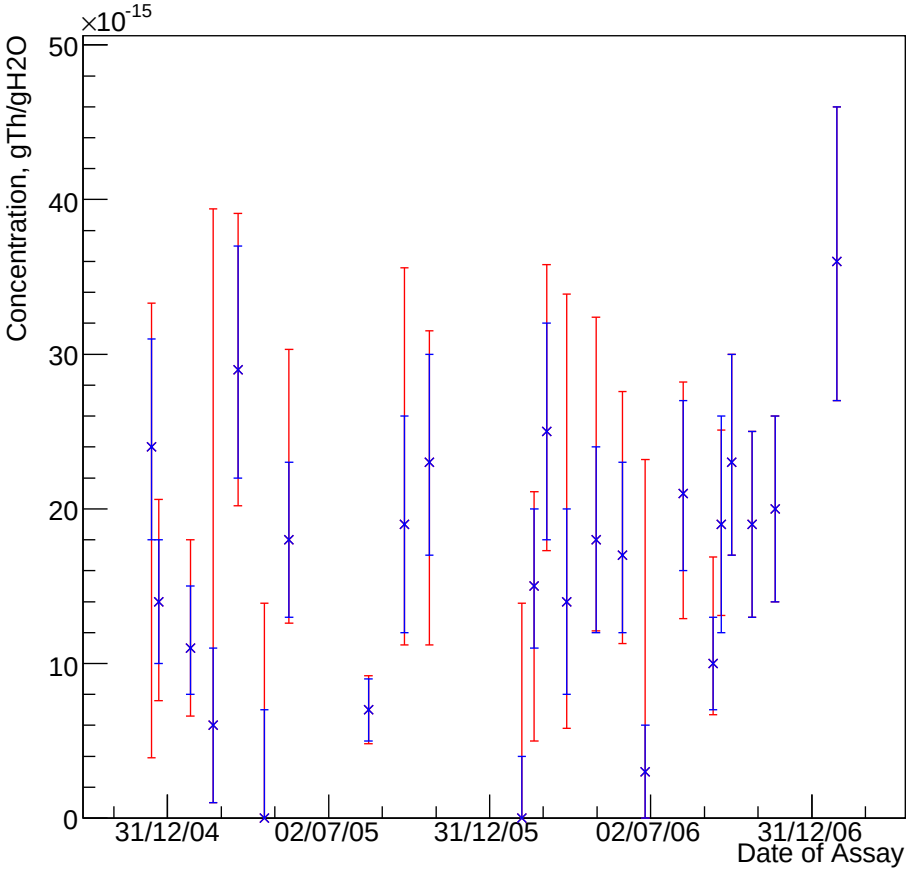


Figure 5.6: Comparison between results with and without the additional background error. There is no additional error for the last 5 points as those assays were performed using the $D_2O$ rig.

as the upstream column and the second as the downstream column. For a $D_2O$ extraction efficiency assay, two sets of two columns in series were used in parallel. The first column in each set was referred to as the upstream column and the second as the downstream column. The amount of Ra extracted by each column was measured by eluting and concentrating each separately. The extraction efficiency was calculated using the following expression

$$\epsilon_{ext} = 1 - \frac{\text{Activity on downstream column}}{\text{Activity on upstream column}}. \tag{5.2}$$

A number of efficiency checks were carried out in the $D_2O$ and both $H_2O$ regions. Two $D_2O$ extraction efficiency checks were performed and results are given in Table 5.2. Due to the extremely small amount of Ra in the $D_2O$, the downstream column returns

| Sample name | Efficiency% |
|---|---|
| RDA31 | $100^{+0}_{-31}$ |
| RDA36 | $67^{+33}_{-33}$ |

Table 5.2: Results from the $D_2O$ efficiency check assays.

| Sample name | Efficiency % |
|---|---|
| LWA 42 | $72^{+19}_{-19}$ |
| LWA 45 | $88^{+10}_{-10}$ |
| LWA 66 | $99^{+1}_{-9}$ |
| LWA 77 | $98^{+2}_{-2}$ |
| Weighted mean | $98^{+1}_{-1}$ |

Table 5.3: Results from the cavity efficiency check assays.

little activity, resulting in a very large statistical error. The extraction efficiency was measured in the PSUP and cavity regions where the signal was higher than that in the $D_2O$ region. As the chemistry of $H_2O$ and $D_2O$ was identical and if a large amount of activity was extracted efficiently, any activity in the $D_2O$ should also be extracted efficiently.

Several checks of the PSUP extraction efficiency were made during the NCD phase but all reported spurious results due to fluctuating elution rig backgrounds. An estimate of extraction efficiency in the PSUP region for these assays could be inferred using non-background corrected count rates to give a minimum value of the extraction efficiency. This gave a more realistic lower bound on the extraction efficiency of greater than 88% for the PSUP region, compared with that of 96% [72] in previous phases.

Two PSUP extraction efficiency checks were performed after the official end of running. Unfortunately, the first of these was lost due to a problem with the beta-alpha counter system. The second of these, and the last ever HTiO assay, was successful and gave an extraction efficiency measurement of $97 \pm 3\%$, at a flow rate of 19.4 litres/min/m$^2$, in agreement with all previous measurements of extraction efficiency in the PSUP region.

Four extraction efficiency checks were carried out in the cavity, the results of which are given in Table 5.3. The first two cavity assays suffered from the fluctuating backgrounds problem that hindered PSUP measurements. The weighted average of the extraction efficiencies was found to be $98 \pm 1\%$ for a two column assay. Results of the cavity extraction efficiency assays are given in Table 5.3.

In addition to checks using underground water systems, a number of experiments had been carried out previously at the Carleton University test facility, using spiked batches of water at a flow rate similar to that used in assays. This work is described

in [72]. To test the extraction efficiency, one tonne of water was spiked with a known amount of activity and this was circulated through two HTiO-loaded filters for a known period of time. Following circulation, the columns were processed and resulting samples counted. The extraction efficiency was calculated using (5.2). The measured extraction efficiency from these experiments agreed with that measured by underground assays. The extraction efficiency derived from these tests of $95 \pm 5\%$, was used for every assay and the extraction efficiency checks performed in each region were used to crosscheck and verify this measurement. The dependence of extraction efficiency on flow rate is discussed in the following section.

## 5.5 Flow rates for PSUP assays

The rate at which water flowed through the columns used in an assay was dependent on the stroke rate of the pump. This was determined by the pressure of compressed air provided by the operating company of the mine. Variations in this air pressure, caused differences in the average flow rate from assay to assay. During the NCD phase, a large variation in the flow rate for PSUP assays was observed with values of 18.1 litres/min/m$^2$ and 30.2 litres/min/m$^2$ recorded for the minimum and maximum flow rates. The highest observed flow rate coincided with an unusually low assay result, suggesting a possible decrease in extraction efficiency at high flow rates. Figure 5.7 shows flow rate versus measured concentration. If the extraction efficiency decreased at higher flow rates, the measured concentration would decrease as flow rate increased. Figure 5.7 shows no obvious correlation and it can be concluded that the extraction efficiency is independent of flow rate at the observed values.

The average thorium concentration was calculated for assays where flow rate was less than 24 litres/min/m$^2$ and was found to be $15.6 \pm 1.4 \times 10^{-15}$ gTh/g$H_2O$ (statistical errors only are quoted). The average thorium concentration for assays where the flow rate was greater than 24 litres/min/m$^2$ was found to be $14.8 \pm 1.6 \times 10^{-15}$ gTh/g$H_2O$ (statistical errors only are quoted). As these values agree at the one sigma level, it was concluded that the extraction efficiency does not appear to decrease at higher flow rates, up to 31 litres/min/m$^2$. Therefore, an extraction efficiency of $95 \pm 5\%$ may be assumed for all assays with flow rates up to and including 31 litres/min/m$^2$.

## 5.6 HTiO assay efficiency

Ra efficiencies for each stage of the HTiO assay were determined by spike experiments. In a spike experiment, a known amount of radioactivity was processed, in this case $^{226}$Ra.

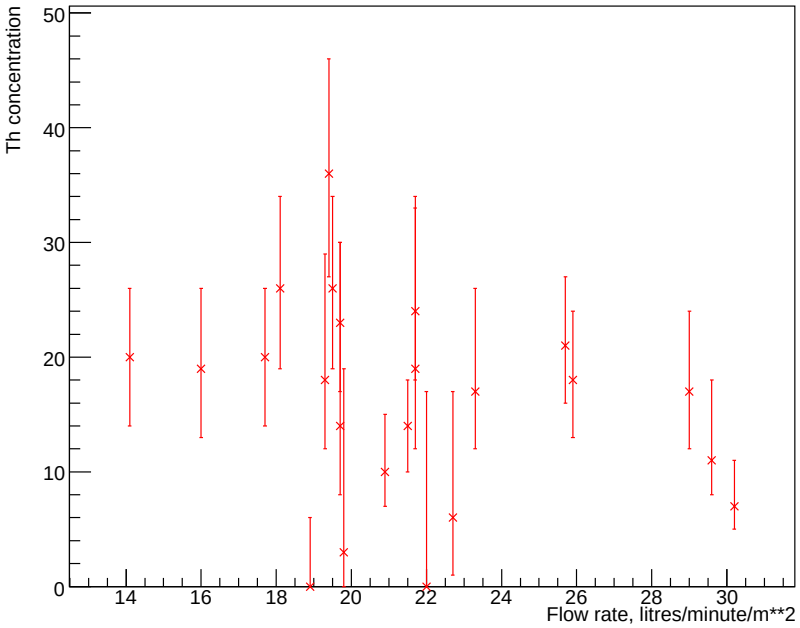


Figure 5.7: The variation of thorium concentration for different flow rates in PSUP assays. There was no obvious dependence of concentration on flow rate.

| Efficiency | $^{224}$Ra | $^{226}$Ra |
|---|---|---|
| Extraction | $95 \pm 5\%$ | $95 \pm 5\%$ |
| Elution | $90 \pm 10\%$ | $90 \pm 10\%$ |
| Secondary Concentration | $58 \pm 6\%$ | $58 \pm 6\%$ |
| Counting | $45 \pm 5\%$ | $60 \pm 10\%$ |
| Total | $22 \pm 4\%$ | $30 \pm 7\%$ |

Table 5.4: Summary of efficiencies for the new HTiO procedure.

The total chemical recovery for Ra was determined to be $50 \pm 8\%$. Combining this with the counting efficiencies (see Table 5.4), the total procedural efficiencies were $30 \pm 7\%$ for $^{226}$Ra and $22 \pm 4\%$ for $^{224}$Ra. A summary of the efficiency of each stage is given in Table 5.4 and the errors are discussed in the following section.

## 5.7 Systematic errors

In addition to the systematic errors associated with the efficiency of each stage, a number of other errors must be accounted for in assays. A summary of these errors for NCD phase

| Error Source | $^{224}$Ra, $D_2O$ | $^{224}$Ra, $H_2O$ | $^{226}$Ra, $D_2O$ | $^{226}$Ra, $H_2O$ |
|---|---|---|---|---|
| Water sampling | | | | |
| Processes mass | 5 | 2 | 5 | 2 |
| Re-sampling correction | $< +10$ | 0 | $< +10$ | 0 |
| Feedback correction | 0 | +3,-6 | 0 | +3,-6 |
| Chemical procedures | | | | |
| Extraction | +11,-5 | 4 | +11,-5 | 4 |
| Elution | 12 | 12 | 12 | 12 |
| Secondary concentration | 10 | 10 | 10 | 10 |
| Counting | | | | |
| Counting efficiency | 11 | 11 | 17 | 17 |
| Alpha peak drift | 1 | 1 | 1 | 1 |
| Sample cloudiness | $< +3$ | 0 | $< +3$ | 0 |
| Data analysis | | | | |
| Software cuts | 5 | 5 | 5 | 5 |
| Fitting | 5 | 5 | 10 | 10 |
| Background subtraction | 7 | N/A | 7 | N/A |

Table 5.5: Systematic errors for $D_2O$ and $H_2O$ assays. All errors are percentages.

HTiO assays is given in Table 5.5. The calculation of each of these errors is discussed in turn.

### 5.7.1 Processed mass

The mass of water processed by the filters during an assay was calculated using the flow rates recorded during the assay. Flow meters underground recorded the rate of water passing through the columns, in litres per minute, for each second during the assay. The average flow rate was calculated from these values and the mass obtained by multiplying the average flow rate by the length of the extraction period. The $D_2O$ flow meters were calibrated by flowing water into a tank of known volume and measuring the rate at which this volume increased. The flow meters in the $H_2O$ systems were calibrated by flowing water into a vessel on a balance and measuring the rate of change of the mass of the vessel. The uncertainty in the time used in these measurements was used as the basis for the average uncertainty on the volume of water processed in an assay which was found to be $\pm 5\%$ for $D_2O$ assays and $\pm 2\%$ for $H_2O$ assays.

### 5.7.2 Re-sampling correction

A typical $D_2O$ HTiO assay would run for 3-4 days and processed around 300 tonnes of water at a flow rate of 80 litres per minute. Water was taken from the detector, passed

through the columns and returned to the detector, where it was mixed with water that had not been assayed. There was a small probability that assayed water was removed from the detector and re-assayed. As Ra had been removed from this water, the amount of Ra in the detector would be slightly underestimated. By assuming that the assayed water was fully mixed on its return to the detector and the decay of Ra was negligible, an upper limit for the re-sampling error can be calculated. Under such circumstances, the Ra concentration obeys the following expression

$$C_t = C_0 \exp\left(\frac{-F \times t \times \epsilon_{ext}}{V}\right)$$

where $C_t$ is the Ra concentration at time t, $C_0$ is the concentration at t = 0, $F$ is the flow rate, $t$ is the time period of the assay, $\epsilon_{ext}$ is the extraction efficiency and $V$ is the volume of the vessel. To minimise the re-sampling contribution, the return point was as far away from the sampling point as possible, ensuring that the mixing was far from total. The re-sampling correction for $^{224}$Ra would be smaller than the 10% predicted using the above expression as it was constantly replenished by $^{228}$Th decay during the course of the assay. However, 10% was used as a conservative estimate. The volumes processed in the $H_2O$ were much smaller, around 30 tonnes and re-sampling was thought to be negligible.

### 5.7.3 Feedback correction

In both water systems, an ultrafiltration filter immediately followed the HTiO columns to prevent any fine particles returning to the detector. In all $H_2O$ assays, the concentrate from the ultrafiltration filter was fed back to the input of the HTiO column, to improve performance of the unit. The feedback loop is shown in Figure 5.8. The flow rate of this return loop was measured using a flow meter. As the feedback leg connected to the input of the columns before the flow meter was used to determine the flow through the columns, the flow from the feedback loop must be subtracted from the total flow. This resulted in a concentration uncertainty of $\pm$3%. During the assay, fine particulates of HTiO could have been removed from the column and trapped in the ultrafiltration unit. As the fines may have absorbed Th/Ra before they were lost from the column, there was a possibility that trapped fines could contain Ra. It was also possible that fine particulates from previous assays could be trapped on the ultrafiltration filter and fed back to the input of the column where they could be re-absorbed. In this case, the amount of extracted Ra on the columns could be overestimated. To address this, a lower systematic error should be assigned to account for this uncertainty, but it would be small. The filtration unit was drained occasionally and it is estimated that this error was less than -5% [80]. Adding this in quadrature to the flow correction gave the values in Table 5.5.

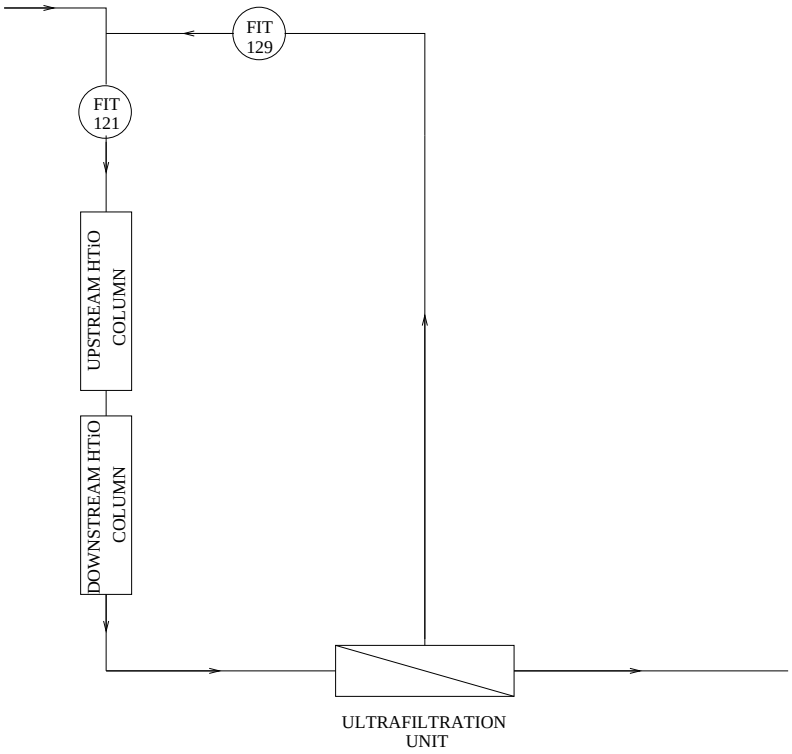


Figure 5.8: A diagram of the feedback loop used in PSUP and cavity assays. The arrows indicate the direction of flow.

The feedback was not used in $D_2O$. Therefore, there was no additional systematic error.

### 5.7.4 Extraction and elution

The extraction efficiency for Ra was discussed above and found to be $95 \pm 5\%$. The elution systematic error was measured using small scale spike tests. These small scale tests used HTiO-loaded MediaKap filters, that had identical pore size to the columns used in assays. The elution efficiency of Ra was found to be $\sim 90\%$ for HCl concentrations ranging from 0.1-0.5 mol/$l$. The elution efficiency at an HCl concentration of 0.1 mol/$l$ was measured to be $90 \pm 10\%$.

### 5.7.5 Secondary concentration

The secondary concentration method comprised three main stages; extraction onto an ion exchange resin, selective elution of Ra from the resin and HTiO co-precipitation. To test the efficiency of each stage, $^{226}$Ra spikes were used. A complete description of this work can be found in [73]. The total systematic for the secondary concentration stage

was measured to be ±10%.

### 5.7.6 Counting efficiency

The systematic uncertainty associated with the beta-alpha counting system was determined by regular calibration source runs. The measured count rate from a calibration source was compared with the expected strength of the source. Several calibration runs were performed using a range of source strengths (0.5 mBq to 2 Bq) and the observed variation in counter efficiency was taken to be the systematic error associated with counting. The counting efficiency was measured to be 45±5% for $^{224}$Ra and 60±10% for $^{226}$Ra. The difference in efficiency is due to the branching fractions and time windows used for each chain.

### 5.7.7 Alpha peak drift

Each assay sample was initially counted for between 7 and 10 days and then counted again after a rest period of approximately 1-2 weeks to establish the contribution of $^{228}$Th and any background. During this period, the alpha ADC peak may have drifted. In a severe case, this would have made the signal and background distributions indistinguishable. The main cause of peak shift was the failure of a resistor in the base of a PMT which caused the operating voltage to shift by around 50 V. This occurred in approximately 4 counting runs during the NCD phase. The effect of base failure was examined by placing a calibration source on the PMT before and after the base was replaced. The difference in the fitted activities was taken to be a measurement of the systematic error and it was estimated to be less than 1%.

### 5.7.8 Sample cloudiness

High amounts of Ni or Mn could have reduced the counting efficiency as both have absorption bands between 350 and 500 nm, which correspond to the region of wavelengths to which the PMT is most sensitive. The final assay sample always looked off-white in colour, due to the large amount of Ti present following HTiO co-precipitation. Sources were doped with different concentrations of Ti and the peak position did not move appreciably. This indicated that the light was scattered and not absorbed by the Ti and, as such, the counting efficiency was not significantly affected. The efficiency of the counting system for these samples was tested by adding HTiO to calibration spikes and no obvious decrease in counting efficiency was observed. To account for any possible effect, an upper systematic uncertainty of 3% was assigned, based upon the standard deviation of the

average count rate observed in these runs. This error would be reduced by performing further source tests.

### 5.7.9 Software cuts

During the analysis of counter data, background events could be easily separated from the signal through the use of diagonal cuts. The analysis cuts applied to each assay may have varied slightly as the signal region was selected by the analyst. At lower alpha ADC values, it was difficult to separate the signal from the background, even using diagonal cuts. This slight overlap gave rise to a systematic error of $\pm 5\%$.

### 5.7.10 Fitting

To calculate the amount of Ra in an assay sample, a maximum likelihood fit to the decay spectrum of counter events that passed the analysis cuts was performed. Monte Carlo data was generated to test the fitting program [75] and the uncertainty due to fitting was found to be not more than $\pm 5\%$ for $^{224}$Ra and $\pm 10\%$ for $^{226}$Ra.

### 5.7.11 Background subtraction

As discussed previously, a measurement of the equipment and reagent background was performed approximately one week before an assay. Background arose from three main parts; the elution rig, the HTiO-loaded filter and the chemicals used in the work up of the sample. It was found that the contribution of the HTiO-loaded filter was negligible. The contribution from the chemicals was measured to be 0.1-0.2 counts per hour. For $D_2O$ backgrounds, the average background for $^{224}$Ra was approximately 0.3 counts per hour, indicating that the elution rig contribution to the background sample was 0.1-0.2 counts per hour. The same quantities of chemicals were used for each assay and background so the uncertainty was negligible. The elution rig background was likely to have been caused by $^{228}$Th somewhere on the rig. Regular cleaning with 0.5 mol/$l$ HCl helped to minimise this background, but its contribution must be accounted for in the analysis. The background was dominated by the contribution from chemicals, but a small amount may have arisen from Ra build up from a Th source in the elution rig. As the time interval between successive elution rig operations was not constant, a small uncertainty in the background may have arisen and this was not higher than $\pm 7\%$ for $D_2O$ assays.

The case for $H_2O$ backgrounds was treated separately in an earlier section.

| Region | Concentration |
|---|---|
| $D_2O$ | $0.64^{+0.18}_{-0.17} \times 10^{-15}$gTh/g$D_2O$ |
| PSUP | $21^{+6.2}_{-5.6} \times 10^{-15}$gTh/g$H_2O$ |
| Cavity | $57^{+17}_{-15} \times 10^{-15}$gTh/g$H_2O$ |

Table 5.6: Error weighted mean $^{232}$Th concentrations for each region from the HTiO assays.

| Region | HTiO | MnOx | *Ex-situ* merged | *In-situ* |
|---|---|---|---|---|
| $D_2O$ $\times 10^{-15}$ gTh/g$D_2O$ | $0.64^{+0.18}_{-0.17}$ | $0.54^{+0.19}_{-0.17}$ | $0.58^{+0.35}_{-0.35}$ | $0.88^{+0.27}_{-0.27}$ |
| PSUP $\times 10^{-15}$ gTh/g$H_2O$ | $21^{+6}_{-6}$ | $37^{+11}_{-11}$ | $27^{+12}_{-12}$ | $30^{+9}_{-19}$ |
| Cavity $\times 10^{-15}$ gTh/g$H_2O$ | $57^{+17}_{-15}$ | $77^{+24}_{-23}$ | $70^{+21}_{-19}$ | $N/A$ |

Table 5.7: Comparison of *ex-situ* and *in-situ* Th chain results.

## 5.8 Assay results

Using the methods discussed in this chapter, the activity in each detector region was calculated. By assuming secular equilibrium between $^{224}$Ra and $^{232}$Th, an equivalent $^{232}$Th concentration was calculated and compared with the results obtained from the *in-situ* method. The results are given in Table 5.6 for each assayed region.

Small corrections were applied to the HTiO and MnOx results to account for small amounts of activity in the pipework between the outlet of the assay columns and the return to the detector. Sources of contamination in this deck loop were identified and measured using peristaltic assays [79]. These assays were performed by allowing water surrounding a component in the circulation systems to become stagnant. During the stagnation period, $^{224}$Ra activity in the water reached radioactive equilibrium with any $^{228}$Th source that was plated on the internal surface of the component. Once the stagnation period was complete, the water was passed in a closed loop through MnOx columns to remove Ra. A portable pump was used to circulate the water through the temporary closed loop. The activity extracted by the MnOx columns was calculated and taken to be a measure of the $^{224}$Ra and hence $^{228}$Th content of the water systems component that was assayed.

A model was developed to take into account these sources and any dependence on the flow path taken during an assay. In addition to the results from the peristaltic and clean up assays, the measured activity for each MnOx and HTiO assay were used as an input to the model. The model found no significant time dependence in the data, which was in agreement with rate analysis of the PMT data. The results of the model are given in Table 5.7.

The results given in Table 5.7 show good agreement between the results of the two

independent assay methods and the *in-situ* method. As agreement was good, the error weighted mean of the *in-situ* and *ex-situ* concentrations in the $D_2O$ and PSUP region were calculated to produce a single concentration for each detector region. The error weighted mean results were calculated to be

$$\begin{aligned} \mathrm{gTh/gD_2O} &= 0.77^{+0.21}_{-0.21} \\ \mathrm{gTh/gH_2O} &= 28^{+10}_{-10} \end{aligned}$$

for the $D_2O$ and PSUP $H_2O$ regions respectively. The agreement between the *ex-situ* and *in-situ* results demonstrates that radioactivity in the water is well understood and has been accurately measured during the NCD phase of the SNO experiment.

# Chapter 6

# The Oxford Beta-Alpha coincidence counters

As discussed in Chapter 5, the NIM/CAMAC* beta-alpha coincidence counting system [75] was prone to failure due to its age and design. A new system using printed circuit boards was designed and built by the University of Oxford.

This chapter begins with a description of the theory behind beta-alpha coincidence counting, followed by an overview of the new counting system. The response of the system to input pulses is described using an example coincidence. Finally, results from calibration and assay measurements using the system are described.

## 6.1 Beta-alpha coincidence counting

By the end of the experiment, two counter systems existed at the SNO site. The *old* system had been constructed in the late 1990s using NIM and CAMAC units. Towards the end of the experiment, individual units in the system became increasingly prone to failure and replacement units were difficult to find. In 2004, therefore, a replacement system was designed and built at Oxford and shipped to the SNO site. This *new* system was manufactured using printed circuit boards and as a result was far more compact and reliable.

Both counter systems were designed to measure the number of beta-alpha coincidences arising from the decay of daughter nuclei in the $^{232}$Th and $^{238}$U chains. Towards the end of the $^{232}$Th decay chain, $^{212}$Bi decays with a 64% branch by beta emission to a short lived state of $^{212}$Po. This in turn decays by alpha emission to $^{208}$Pb with a 0.3 $\mu$s half life. The signature for this decay is a beta decay with a $Q$-value of 2.25 MeV followed around 0.3 $\mu$s later by a 8.95 MeV alpha. There exists a similar coincidence toward the

*NIM = Nuclear Instrument Module, CAMAC = Computer Automated Measurement and Control

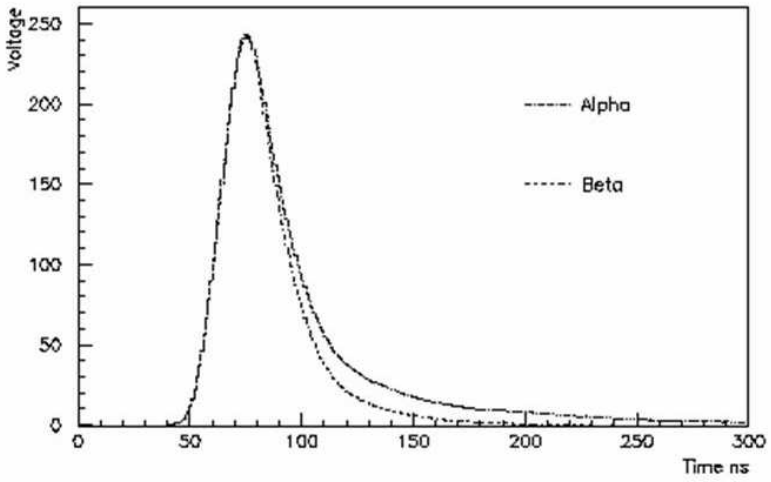


Figure 6.1: Plot of average pulse shape for betas and alphas. Taken from [75]

end of the $^{238}$U chain where $^{214}$Bi decays by beta emission to $^{214}$Po which subsequently decays by alpha emission to $^{210}$Pb with a half life of 164 $\mu$s. The signature for this is a beta decay with a $Q$-value of 3.27 MeV followed around 164 $\mu$s later by a 7.83 MeV alpha. Both Po and Pb nuclei give rise to a beta followed by an alpha and the difference in the Po-Pb half lives can be used to separate U from Th. To observe these coincidences, alphas and betas must be detected and separated.

To detect the alphas and betas, liquid scintillator can be spiked with small amounts of radioactivity ($<$ 10 Bq) and the light produced detected using a PMT. The majority of scintillation light is produced by prompt fluorescence of the material. However, in many scintillators a longer lived component is also observed, corresponding to delayed fluorescence. The composite decay curve is well represented by the sum of two exponentials: one that represents the fast component and the other the slow component. The fast component dominates the light yield of the scintillator, with the slow component giving rise to a long tail. The fraction of light in the tail is strongly dependent upon the nature of the ionising particle, as shown in Figure 6.1. A particle with a high energy loss per unit length will produce a high density of excited molecules in the scintillator. Two such molecules can interact and produce a molecule in the lowest (singlet) excited state and another in the ground state. The excited state molecule then de-excites leading to (delayed) fluorescence. The dependence of the fraction of light in the tail on the energy loss of the ionising particle may be used to differentiate between particles. This method is generally referred to as pulse shape discrimination [81, 82].

The pulse shape discrimination method can be used to separate beta and alpha particles. Compared with betas, alphas have a higher energy loss per unit path length in a scintillator, resulting in a larger fraction of delayed fluorescence. Therefore, scintillation pulses produced by alpha particles have a much longer tail than those produced by beta particles and a greater fraction of the total charge deposited by the pulse will be present in the tail. Discrimination between betas and alphas is possible by taking the ratio of the charge observed in the tail of the pulse with that observed in the full pulse.

The difference between the tail of beta and alpha pulses may be used to discriminate between them and reduce any background from beta-beta, beta-gamma and beta-noise coincidences. In a genuine beta-alpha coincidence, the fraction of charge in the tail of the pulse of the second particle, the alpha, will be greater than that of the second pulse of a beta-beta or beta-gamma. The backgrounds can be greatly reduced by applying selection criteria to the second pulse. The combination of coincidence counting and pulse shape discrimination was used in the HTiO method as the basis for the beta-alpha counting system that is now described.

## 6.2 System Overview

The beta-alpha system can be broken down into three subsystems; the PMTs, the beta-alpha electronic unit and the data acquisition (DAQ) PC. Radioactive decays in the sample produced scintillation light that was detected by a photomultiplier tube (PMT). The output pulse from each PMT was fed into one of the boards via an attenuator box and filter. This box ensured that the voltage of the PMT was in the middle of the operating range specified by the manufacturer and that pulses produced by the PMT rose and fell smoothly, which is necessary for an accurate determination of the fraction of charge in the tail of the alpha pulses. Each incoming pulse was subjected to a series of logic operations to determine whether or not a beta-alpha coincidence had occurred. If a coincidence occurred, information about the coincidence was read out to and stored by the DAQ PC.

In this system, a maximum of 8 PMTs could be used in a high voltage interlock cage. The interlock cage provided a ground connection for each PMT shield and also prevented PMTs from being opened whilst the high voltage was on. The system was designed to count multiple samples due to the timing of assays. At any one time, a number of samples were counted on the system and thus a number of PMTs was required. The original beta-alpha system was an 8 channel NIM system and could therefore use up to 8 PMTs. As this number of PMTs were found to be sufficient and also because the PMTs were transferred from the old system to the new, the new system was designed to use 8 PMTs. The sample was held in a 50 ml polymethylpentene jar and optically coupled to

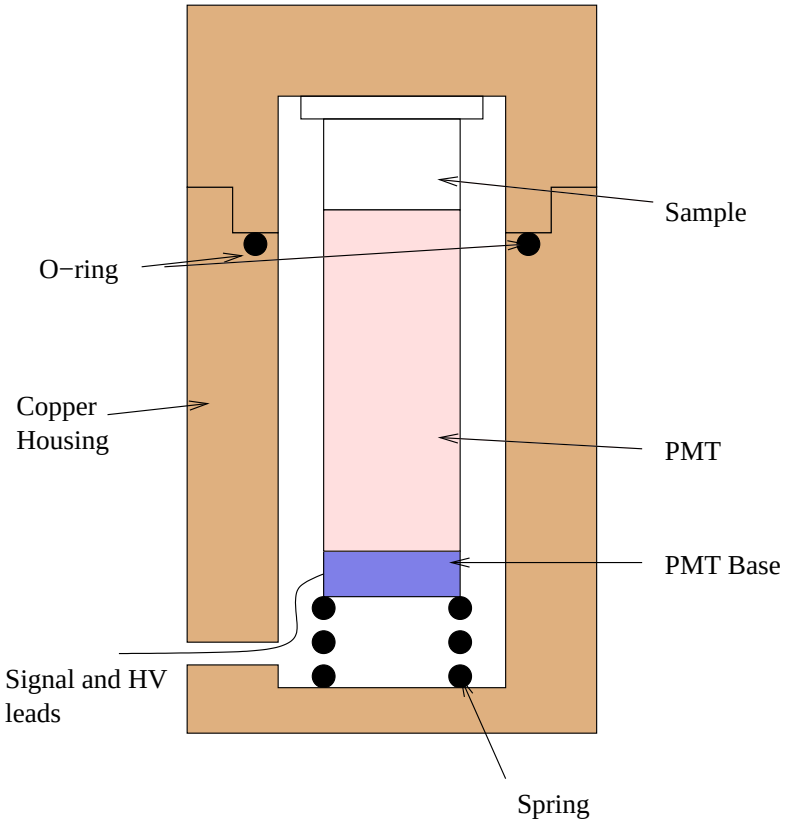


Figure 6.2: Schematic diagram of the source, PMT and copper housing.

the surface of a PMT using vacuum grease. The sample and PMT were housed in a 2 inch thick shield made from Oxygen Free High Conductivity (OFHC) copper, which helped to minimise accidental coincidences arising from soft room gammas. This is shown in Figure 6.2. The PMT was an Electron Tubes Ltd 9266 KB with a C647A series B14A voltage divider base. Each PMT was supplied with its own high voltage (HV) from an 8 channel unit.

The output of each PMT passed through a filter box and into one of the eight single beta-alpha units. The filter box contained a $\pi$ network attenuator in conjunction with a 330 pF capacitor, shown in Figure 6.3. This circuit smoothed the pulse and attenuated its amplitude by approximately a factor of two. The resulting pulses had a rise time of about 10 ns and a fall time of about 25-35 ns. When the amplitude of the alpha pulses at the input to the beta-alpha boards was in the region of 60 mV, the alphas peaked around channel 900. Up to 8 boards were held in a crate. Each board received power from, and was read out by, the backplane of the crate.

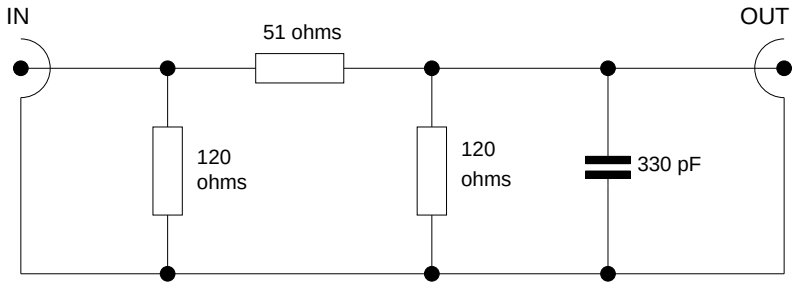


Figure 6.3: Circuit diagram of the smoother unit. There was a separate attenuator unit for each channel and each one was housed in a metal box to eliminate pick up.

## 6.3 Pulse handling

This section describes the response of the beta-alpha boards to the incoming signal from the PMT (via the attenuating box). Any signal received by the board was subjected to a number of pre-determined threshold, timing and logic constraints to determine whether or not it was part of a beta-alpha coincidence. Logic operations were controlled by a Field Programmable Gate Array (FPGA) chip. The FPGA governed the communication between the boards and the DAQ PC. It contained a 40 MHz clock, which was the reference point for all timings associated with the board. There were three thresholds: RUN, ALPHA and MU. Each of these is now discussed.

### 6.3.1 RUN threshold

The amplitude of each smoothed PMT pulse received by the board was compared with this threshold. Only those pulses with amplitudes above the threshold were accepted and stored by the electronics. This threshold helped reduce the number of noise pulses accepted by the system, however, a small fraction of genuine beta pulses was lost, resulting in a slightly lower system efficiency. The exact setting of the run threshold was a compromise between noise rejection and beta acceptance.

### 6.3.2 ALPHA threshold

This threshold was only applied to the second pulse in a coincidence. Due to quenching in the scintillator, the amplitude of an 8 MeV alpha in a genuine coincidence was slightly reduced. However, since it was still greater than that of a beta, the amplitude threshold on the second pulse could be set at a higher level. As the energy spectrum of the alpha particle did not extend to zero (due to the two body nature of alpha decay) a non-zero threshold setting would not affect the acceptance of genuine alpha pulses. The threshold

was set such that the whole alpha energy spectrum was accepted and low energy noise was rejected. If the second pulse in the coincidence failed this threshold, the event was discarded and the electronics reset.

### 6.3.3 MU threshold

This was an upper limit on pulse amplitude designed to remove large pulses from the data. Such signals were usually produced by cosmic muons interacting in the scintillator, hence the name of the threshold. Any coincidence where either pulse crossed this threshold was discarded and the electronics reset.

If the RUN threshold was crossed by the incoming signal from the PMT, a voltage ramp and integrator were started. The amplitude of the voltage ramp decreased linearly as a function of time. This was used to define time intervals. The amplitude of the voltage ramp was compared with three well defined thresholds, corresponding to three integration times; FIRST, SHORT and LONG, relative to the start of the ramp[†]. These are now discussed.

### 6.3.4 FIRST time interval

The FIRST threshold defined the time interval over which the beta pulse was integrated. It extended over the pulse peak to the point at which the pulse had fallen to about 50% of its maximum amplitude. It was set to ensure that the system deadtime between the beta and alpha was as small as possible and the beta spectrum was not significantly affected. When the voltage ramp crossed the FIRST threshold, the charge stored on the integrator (capacitor) was stored by the FPGA and the circuit was reset. The system waited for a second pulse to trigger the RUN threshold. The time between pulses was measured by the number of clock cycles that elapsed between the first and second pulse triggering the RUN thresholds. The clock cycle time was 25 ns and the average minimum time between a beta and an alpha pulse in a beta-alpha coincidence that could be detected was roughly 55 ns.

### 6.3.5 SHORT time interval

The SHORT threshold was set such that all but the tail of the alpha pulse (the second pulse in the coincidence) was integrated. This corresponded to integrating the first 80% of the charge of the pulse.

[†]Note that the electronics had been designed such that the voltage ramp was temperature independent

| | Default integration time (ns) |
|---|---|
| FIRST | 31.0 |
| SHORT | 49.0 |
| LONG | 100.0 |

| | Threshold voltage (mV) |
|---|---|
| RUN | $\sim 10$ |
| ALPHA | $\sim 30$ |
| MU | $\sim 200$ |

Table 6.1: Default values for all thresholds and timings as set on the Sudbury and Oxford boards, August 2007.

### 6.3.6 LONG time interval

The LONG threshold defined the time interval over which the full alpha pulse was integrated. It was set to extend just beyond the full tail of the alpha pulse.

The default settings for all timings and thresholds are given in Table 6.1. The thresholds were set using the probe points described in Section 6.6. The threshold voltages refer to the amplitude of the input pulse to the beta-alpha boards coming from the filter box. All of the thresholds and timings will now be discussed in the context of an example coincidence.

## 6.4 An example coincidence

An example coincidence and associated timing graphs are given in Figure 6.4. In this example, it is assumed that: both pulses are above the RUN threshold, the second pulse is greater than the ALPHA threshold and both pulses are below the MU threshold. Therefore, both pulses will be detected by the board.

The crossing of the RUN threshold by the first (beta) pulse starts a voltage ramp and integrator. This can be seen in Figure 6.4 as the start of the beta pulse coincides with the switching of RUN to a positive value and the beginning of the voltage ramp. The voltage ramp decreases until it crosses the FIRST threshold, approximately 31 ns after the start of the beta pulse, causing FIRST to go positive. At the end of the beta pulse, RUN falls back to zero, the value of the integrator is stored on a capacitor and then it is reset along with the voltage ramp. FIRST is not reset and remains positive. The system waits for another pulse.

If another pulse arrives within 1.6 ms, a coincidence has been detected[‡]. RUN goes

[‡]A 16 bit counter in the FPGA is used to determine this time

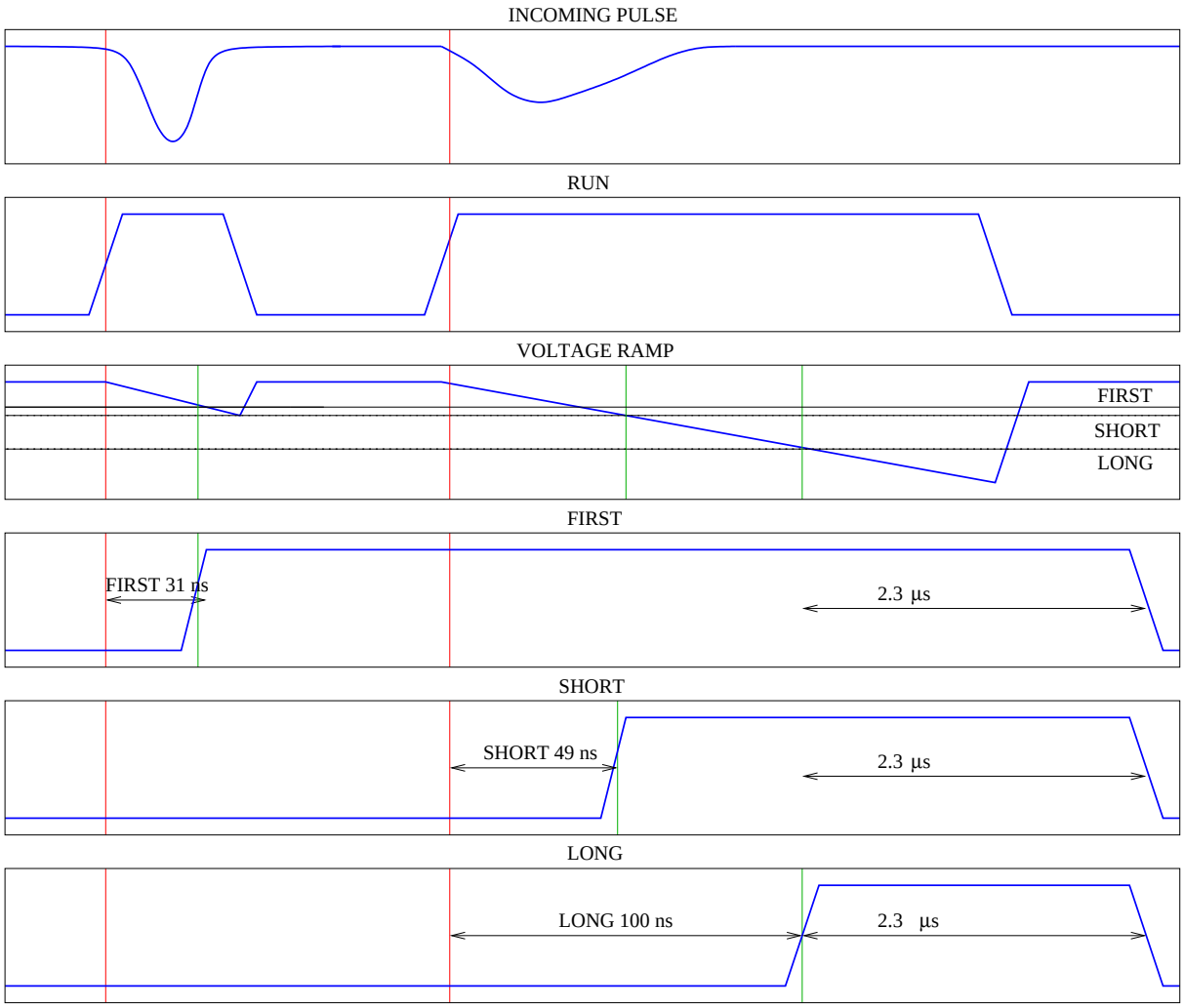


Figure 6.4: An example coincidence, with pulses separated by 100 ns. From left to right the graphs are: The coincidence signal, the RUN threshold, the voltage ramp used for timing (with FIRST, SHORT and LONG thresholds marked), FIRST threshold, SHORT threshold and LONG threshold. For the FIRST, SHORT and LONG thresholds, the change in gradient is the point at which the voltage ramp crosses the threshold. The vertical red lines indicate when the integrator starts integrating. The time taken for the system to reset is 2.3 $\mu$s as indicated at the end of the graphs.

positive and the ramp and integrator are started again. In Figure 6.4 a second pulse is detected. Approximately 49 ns after the start of the second (alpha) pulse, the SHORT threshold is crossed. The value of the integrator is stored on another capacitor, but the ramp and integrator are not reset. About 51 ns later (~100 ns after the start of the $\alpha$ pulse) the LONG threshold is crossed, making SHORT positive. The value of the integrator is read out onto a third capacitor. All of the signals are reset following a dead time of approximately 2.3 $\mu$s.

The three values from the integrator are converted individually by a 12-bit Analogue to Digital Converter (ADC). These three values along with the number of clock cycles between the coincident pulses (determined by RUN logic signals) and two other counters form an event. One of the two "other" counters records the number of times the RUN threshold was crossed and the second of the two counters records the number of times a coincidence was observed. These two counters give information on the number of background events. Finally, the event is stored in a four-level FIFO[§], before being read out by the system.

## 6.5 Read out of the system

The boards were read out through the backplane of the crate. The backplane supplied each board with 5 V DC and connected the cards to the Data Acquisition (DAQ) PC via a PCI card. Each board had a unique address associated with the data acquisition software, which also acted as an identifier in the data. The board address was an integer between 1 and 8 and each board in the crate had a unique address.

Information from the boards was written by the DAQ system to a data file that contained the address of the board that detected the coincidence, time since the start of the run, time interval between the beta and alpha, beta integral (ADC counts), alpha integral (ADC counts), tail fraction, flag, time and date [83]. In addition to the data file, there was a log file containing information about sources and samples on the system, PMT high voltage and any additional information about samples.

## 6.6 Setting up and testing the system

In this section, practical set up of the boards is described. The methods presented in this section were used to set up counter systems in Sudbury and Oxford. The initial settings were optimised using a number of different strength calibration sources. A general description of these runs is given in this section.

[§]FIFO = First in, first out

| Probe point | Corresponding threshold/timing |
|---|---|
| LK1 | Incoming pulse after amplification |
| LK7 | RUN threshold |
| LK8 | ALPHA threshold |
| LK9 | MU threshold |
| LK12 | RUN logic pulse |
| LK16 | FIRST logic pulse |
| LK17 | SHORT logic pulse |
| LK18 | LONG logic pulse |

Table 6.2: Probe points and thresholds

Before the system was used for the first time, a pedestal check was performed, to measure the zero offset of each discriminator. Once the pedestal check was complete, the offsets for each board were stored in a data file. Each time the DAQ system was used, the values from this file were loaded by the system. A pedestal check was performed every few months and no significant variation in zero offsets was observed.

### 6.6.1 Setting the thresholds

To set the thresholds and timings of each board, a double pulser was used to produce fake coincidences. The amplitude of the first pulse was set to $\sim$ 10 mV. The width of each pulse was approximately 60 ns and the time interval between the pulses was $\sim$ 100 ns. All thresholds and timings were adjusted using the appropriate potentiometer on the circuit board. The thresholds and timings corresponding to each probe points are given in Table 6.2. The adjustment of each threshold is described below.

#### RUN

If the RUN threshold was raised sufficiently, the IN LED would stop flashing. The pulser was set so that the amplitude of the pulse, measured at the output of the smoothing unit, was approximately 10 mV. The output of the smoothing unit was connected to the board. The RUN threshold was adjusted until the IN LED did not flash for the pulse, i.e. the event rejected. The amplitude of the pulse was then increased slightly to check that the board accepted pulses with amplitudes greater than 10 mV. The value of RUN was measured using a DC multimeter (mV DC setting) connected to LK7 and ground. The recorded value was used to set the RUN threshold on the other boards, by probing LK7 whilst adjusting the relevant potentiometer.

#### ALPHA

Setting ALPHA required analysis. The total decay spectrum was obtained from the data, to determine the cut off which was approximately equal to an ADC value that was one full width at half maximum below the alpha peak. The alpha threshold was raised until the spectrum was cut off at the desired value. This required between 10 and 15 trial runs using a 1 Bq $^{226}$Ra source. Once one board had been set, the ALPHA threshold was measured using LK8 and the measured value used to set the other boards, as with the RUN threshold.

#### MU

If the MU threshold was lowered, the OUT LED would stop flashing and events would be rejected. The pulser was set to its maximum value and connected to the input of the board. The signal entering the board was viewed using an oscilloscope connected to LK1 and ground. The pulses had a flattened peak. The amplitude of the pulser was adjusted until the pulse was no longer deformed (i.e. the peak was no longer flat) and the MU threshold was set to reject this pulse. The MU threshold was recorded using the LK9 probe point and the value used to set the other boards.

### 6.6.2 Setting the timings

Measurement of the three time intervals required a double pulser and a dual channel oscilloscope. The output of the double pulser was connected via the smoother box to the input of the board. The amplitude of the pulser was adjusted until both the IN and OUT LEDs on the front of the board flashed. The run threshold, LK12, was connected to Channel 1 of the oscilloscope. The oscilloscope was set to trigger on the rise of this pulse. Another oscilloscope probe was connected to Channel 2 of the oscilloscope and it was used to measure the appropriate timing interval, described below.

#### FIRST

Channel 2 of the scope was connected to LK16 to observe the FIRST signal. The rise of the FIRST signal occurred after the start of the RUN pulse. To adjust the time interval, the potentiometer labelled FIRST was adjusted to a value equivalent to a time separation of 31 ns.

#### SHORT

Channel 2 was connected to LK18 to observe the SHORT signal. The time separation between the start of the second rise of the RUN pulse and the rise of the SHORT pulse

was 49 ns for a knob setting of 3.70. Note that the SHORT timing could be adjusted using the knob on the front of each board. This may be necessary if a different scintillator is used.

#### LONG

Channel 2 was connected to LK17 to observe the LONG signal. The time interval between the rise of the second RUN pulse and the rise of the LONG pulse was set to 100 ns.

Once the timing and thresholds of the boards had been set, the voltage of each PMT was adjusted to ensure that the position of each peak (alpha ADC, tail fraction and beta ADC) occurred at the same point. To compensate for PMT to PMT variations, the high voltage (HV) applied to each tube was different and is described in the following subsection.

### 6.6.3 Setting the PMT HV

A custom made high voltage unit, using Matsusada high voltage units, supplied each PMT with an individual voltage. To ensure that the response of the system to each PMT was similar, the HV of each PMT was set such that the $^{228}$Th alpha peak occurred in an ADC bin between 950 and 1000[¶]. A 2 Bq $^{228}$Th source was placed on each PMT and the peak position observed. If the peak occurred below the desired region, the HV was increased and the run restarted. Conversely, if the peak occurred above 1000 ADC counts, the HV was decreased. The HV was adjusted and runs repeated until the peak was around 950 ADC counts. Once the PMT HV had been set, the system was ready for calibration using lower rate sources.

## 6.7 System calibration

Once all thresholds, timings and PMT voltages had been set, the system had to be calibrated. The first stage of calibration was to define the signal and background regions of the data. To do this, a number of calibration source runs were performed. The system was designed for use with a 50 mm diameter PMT onto which a 50 ml sample[‖] was coupled. The sources used to test the system ranged from 0.5 mBq to 2 Bq and contained $^{228}$Th, $^{226}$Ra or a mixture of both. A typical assay was around 0.8-1.0 mBq. Also a set of

[¶]Extensive testing at Oxford found that the system performance was best in this alpha ADC region with the thresholds and timings as set above

[‖]42 g of which is Optiphase HiSafe-3 liquid scintillator and the rest a mixture of hydrochloric acid and activity

blanks was used, containing 10 ml of 0.5 mol/$l$ HCl and 42 g of Optiphase HiSafe-3 liquid scintillator, to define the background region.

First, a relatively strong $^{228}$Th source was used to check that on each board, the alpha peak occurred between 900 and 1000 ADC counts and the tail fraction (psd) peak was around 0.20. The $^{228}$Th source was replaced with a high rate (1.0 Bq) $^{226}$Ra source, which emits a lower energy alpha, to ensure that the full alpha spectrum was still present.

Once the peak positions had been verified, a blank sample was placed on each PMT to measure the background count rate of the system. Each blank sample was counted for at least a week to acquire enough statistics to provide a good measure of the background region. The background region spanned the same ADC region as the signal, but was flat and its tail fraction peaked at around 0.10, much lower than the signal.

Once the signal and background regions were known from running the high rate and blank samples, a low rate source was placed on the system. A low rate source was defined as activity in the range of 0.5 to 5.0 mBq. These sources were usually an equal strength mixture of $^{226}$Ra and $^{228}$Th. They were strong enough to show a clear signal, but weak enough to show the background. They provided the best measure of separation of signal from background and could be used to measure the counting efficiency.

To determine the counting efficiency, a known strength source was counted using the system and the measured value was compared with the actual source strength. The counting efficiency was defined as

$$\text{Efficiency} = \frac{\text{Measured source strength}}{\text{Actual source strength}}.$$

The activity of the sample was determined by fitting time spectra to the beta-alpha coincidence rate measured by the system. The total beta-alpha coincidence rate was determined by the contribution of all of the radionuclides in the decay chain. A maximum likelihood fit of time spectra for these radioisotopes was made to determine the amount of each present in the sample [59].

Initial measurements of low rate sources without using a smoother box showed poor separation between signal and background. Such poor separation tightened the analysis cuts applied to the data, which led to an unacceptably low counting efficiency of less than 10%. It was clear that some improvement to the system was needed to make it usable for assay measurements. After investigation, it was found that the pulse from the PMT was not completely smooth: the boards were triggering on spiky pulses, which affected measurement of the ratio of tail to full charge. The separation was improved by increasing the RUN and ALPHA thresholds, but this significantly reduced the already poor counting efficiency. To allow the thresholds to be set at a low enough level to give a good counting efficiency, a smoothing unit was built for each channel.

Besides smoothing the input pulse, the smoothing box also acted as an approximate 75 Ω terminator. Moreover, the attenuation of the pulse allowed each PMT to run at a voltage that was within the guideline operating range of the PMT, unlike the old system. A single 8 channel attenuator unit was tested but proved to be too sensitive to pickup. As a result, individual units were manufactured. The circuit diagram is shown in Figure 6.3.

Use of the smoother box greatly improved the signal background separation and the counting efficiency. The average counting efficiency was found to be

$$50 \pm 5\% \text{ for } ^{224}\text{Ra}$$
$$62 \pm 7\% \text{ for } ^{226}\text{Ra}.$$

Figure 6.5 shows the results from the thorium chain for a source containing 5 mBq of $^{226}$Ra and 5 mBq of $^{228}$Th. Good separation between the signal and background regions can be seen.

## 6.8 Assay results using the new counter system

It was hoped that the new counting system would be used for all NCD phase assays. This did not occur as is was difficult to identify reasons for the poor separation between signal and background. Once solved, the system was used to count two cavity assays at the end of the NCD phase and these are now discussed.

### 6.8.1 Light water assay 71

Light Water Assay 71 (LWA71) was used to compare the performance of the new counting system with the old system. LWA71 was an assay of the region of water between the rock wall and reverse side of the PMTs, known as the cavity. The observed activity in the cavity region was approximately 3 times higher than that in the PSUP region and the assay was expected to produce a strong $^{224}$Ra signal. It was felt that activity was high enough to allow the sample obtained from the secondary concentration to be split in two and one part counted using each system. Approximately 9.4 g was counted using the new system and 10.3 g using the old system. The small difference in mass was accounted for in the calculation and the equivalent concentrations of $^{232}$Th were

$$21.0^{+7.5}_{-7.0} \text{ gTh/g}H_2O \text{ from the new system}$$
$$17.0^{+6.9}_{-6.6} \text{ gTh/g}H_2O \text{ from the old system.}$$

As the sample was split between the two systems, the statistical error in each case was larger than usual. Good agreement between the two systems was found and the total

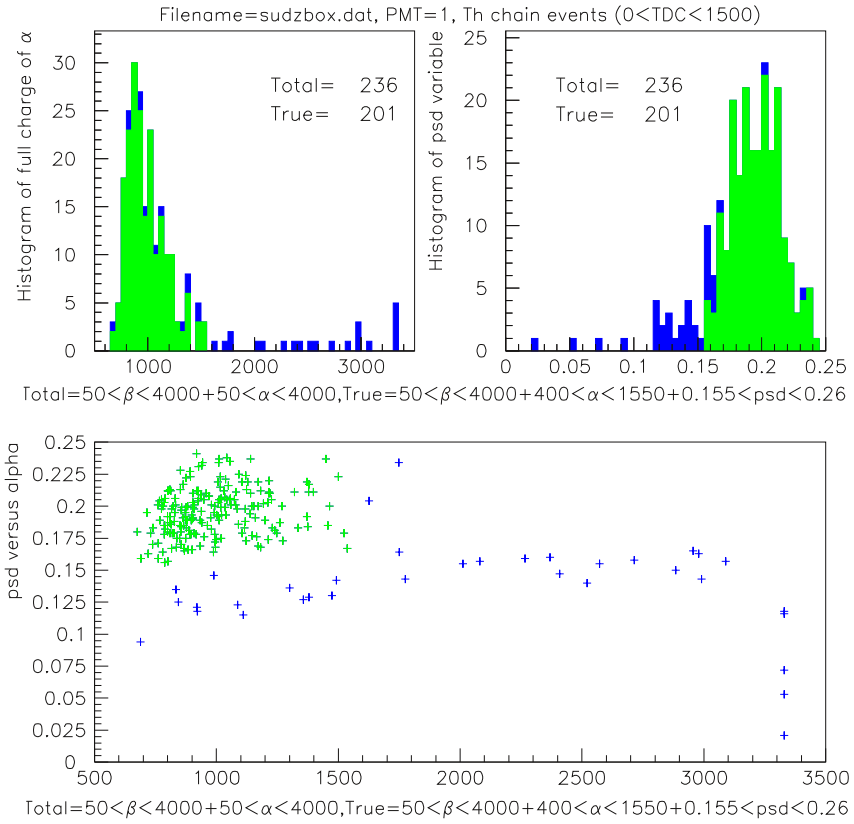


Figure 6.5: Thorium chain results from a typical run using a 5 mBq $^{228}$Th source. Green points are events which passed the analysis cuts (signal events) and blue events are those which did not pass the analysis cuts (background events).

activity agreed with previous measurements of cavity activity. In both cases, the error is the sum of the systematic and statistical errors and this is dominated by the systematic error of approximately 20%.

### 6.8.2 Light water assay 80

Light Water Assay 80 (LWA80) was a cavity assay, performed just after the official end of NCD data taking. The assay was processed using the standard HTiO assay method described in Chapter 5 and the sample counted using the new system. The equivalent thorium concentration was found to be

$$96^{+31}_{-28}\ \mathrm{gTh/gH_2O}$$

in agreement with other NCD phase cavity assays. Again the error is dominated by the systematic error of around 20%. The results from all NCD phase HTiO and MnOx assays are shown in Figure 6.6.

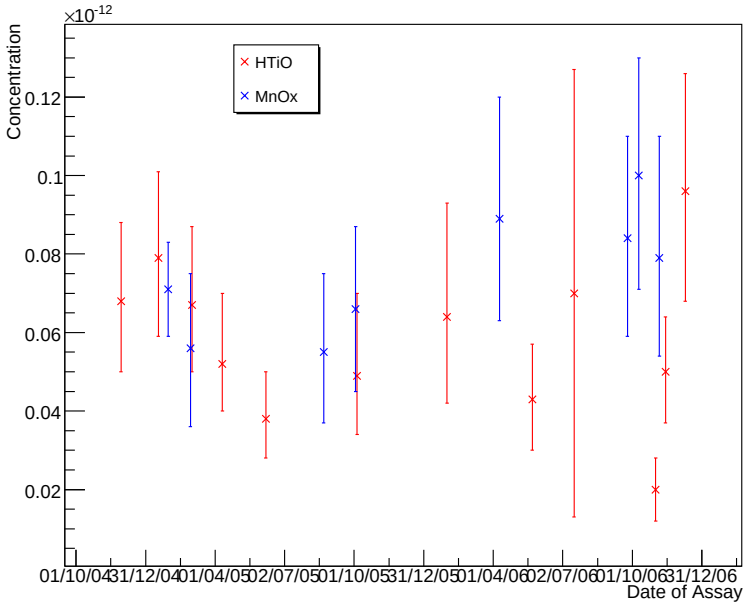


Figure 6.6: Results from NCD phase cavity assays. The last red point (i.e. furthest right) corresponds to the assay counted using the new system.

The result from LWA80 agrees with the other cavity assay measures, but the central value appears slightly higher. It is suspected that removal of the Berkeley sled of test PMTs, which were located close to the sampling point, may have disturbed some radioactivity which could have been extracted by the assay, leading to a higher central value. It was not possible to verify this hypothesis.

## 6.9 Conclusions

Following testing and calibration, the new beta-alpha coincidence counting system successfully measured the activity in two assays in the NCD phase of SNO. Direct comparison of the new and old systems demonstrated that the performance of the new system was comparable with that of the old system. Improved filtering of the input signal and optimisation of the thresholds led to a final counting efficiency marginally better than the old system. The success of the assay and calibration source measurements have led to the use of this beta-alpha counting system in a number of other physics experiments, including SNO+, Daya Bay and Picasso.

# Chapter 7

# Measurements of NCD hotspots

This chapter begins with a summary of predictions of hotspot composition and location made by the *in-situ* analysis. As discussed in Chapter 4, several *ex-situ* methods were devised to measure the composition and strength of the hotspots. In this chapter, a complete description of the acid elution measurement is given along with an outline of the external alpha counting and germanium results. Finally, all of the results are combined to produce a recommended number of neutrons produced per day by each hotspot.

Early in the NCD phase, several areas of increased radioactivity associated with the NCD array were identified using the *in-situ* method [55]. The locations of these areas of increased activity were found to be consistent with K2 (string 31) and K5 (string 18). They became known as *hotspots* and it was shown [84] that if the composition of this activity remained unknown, the associated systematic error could severely affect the accuracy of the Neutral Current (NC) flux measurement made during the NCD phase [84]. The *in-situ* method could not exclude the possibility that the excess count rate was due to something other than radioactivity. For example, the increased activity could have been due to a deposit on the surface of the NCD capable of scintillating. This would have enhanced any small amount of radioactivity that was present. As radioactivity would produce neutrons, an attempt was made to search for excess neutrons in both of the affected strings [66]. The majority of neutrons should capture back on the affected string [65]. Unfortunately, both strings suffered from problems, not related to the hotspot, and this analysis proved inconclusive. As only knowledge of the composition and strength could reduce the uncertainty associated with the NC flux, a number of post-undeployment tests of the affected NCDs were planned. Two independent methods were developed to measure the surface activity on K5: an External Alpha Counter (EAC) was built by the University of Washington and an acid elution technique was developed by the author. The EAC was used to confirm the bulk nature of the K2 hotspot and sections were counted using a germanium detector.

| | |
|---|---|
| $^{232}$Th | $1.48(+0.24, -0.27)$ $\mu$g |
| $^{238}$U | $0.77(+0.19, -0.23)$ $\mu$g |

Table 7.1: Results from the *in-situ* analysis of the K5 hotspot. Total errors (systematic + statistical) are given.

## 7.1 *In-situ* analysis

As described in Chapter 4, a measurement of the hotspot activity could be made using the *in-situ* method. However, the *in-situ* method could not confirm if the increased count rate associated with the two contaminated strings was caused by radioactivity.

However, if it was assumed that the excess signal was caused by radioactive deposits dominated by $^{238}$U and $^{232}$Th, the *in-situ* method could be used to predict the composition of each hotspot. The method could be used without any assumption to determine the location of the activity. Plots of the (x,y), (x,z), (y,z) and (x,y,z) distributions of reconstructed events are given in Figure 7.1. A summary of measurements for each hotspot using the *in-situ* method now follows.

### 7.1.1 K5 hotspot

The *in-situ* analysis indicated that the K5 hotspot could be localised in two places, consistent with $z = -50$ cm and $z = -125$ cm. The two peaks could not be clearly resolved, as the vertex resolution of the fitter used was approximately 30 cm. More counts were present in the peak at $z = -50$ cm, indicating that two hotspots of different strength were present on the string. The $z$ distribution of K5 events is shown in Figure 4.14 in Chapter 4.

The mean isotropy of K5 events was found to be consistent with that of surface $^{208}$Tl. If radioactive, this would suggest that the contamination was dominated by activity from the $^{232}$Th chain on the surface of the NCD. Surface contamination was possible as a result of the leak testing of K5, during which the counter was taped in a bag and left suspended above the detector for 24 hours. Analysis of data taken before this event shows no evidence of a hotspot.

The *in-situ* method was used to estimate the composition and strength of the hotspot. A 1D maximum likelihood fit using surface isotropy distributions was made to the K5 data. The expected number of $D_2O$ and NCD bulk backgrounds were subtracted from the total number of K5 events. The estimated activity is given in Table 7.1.

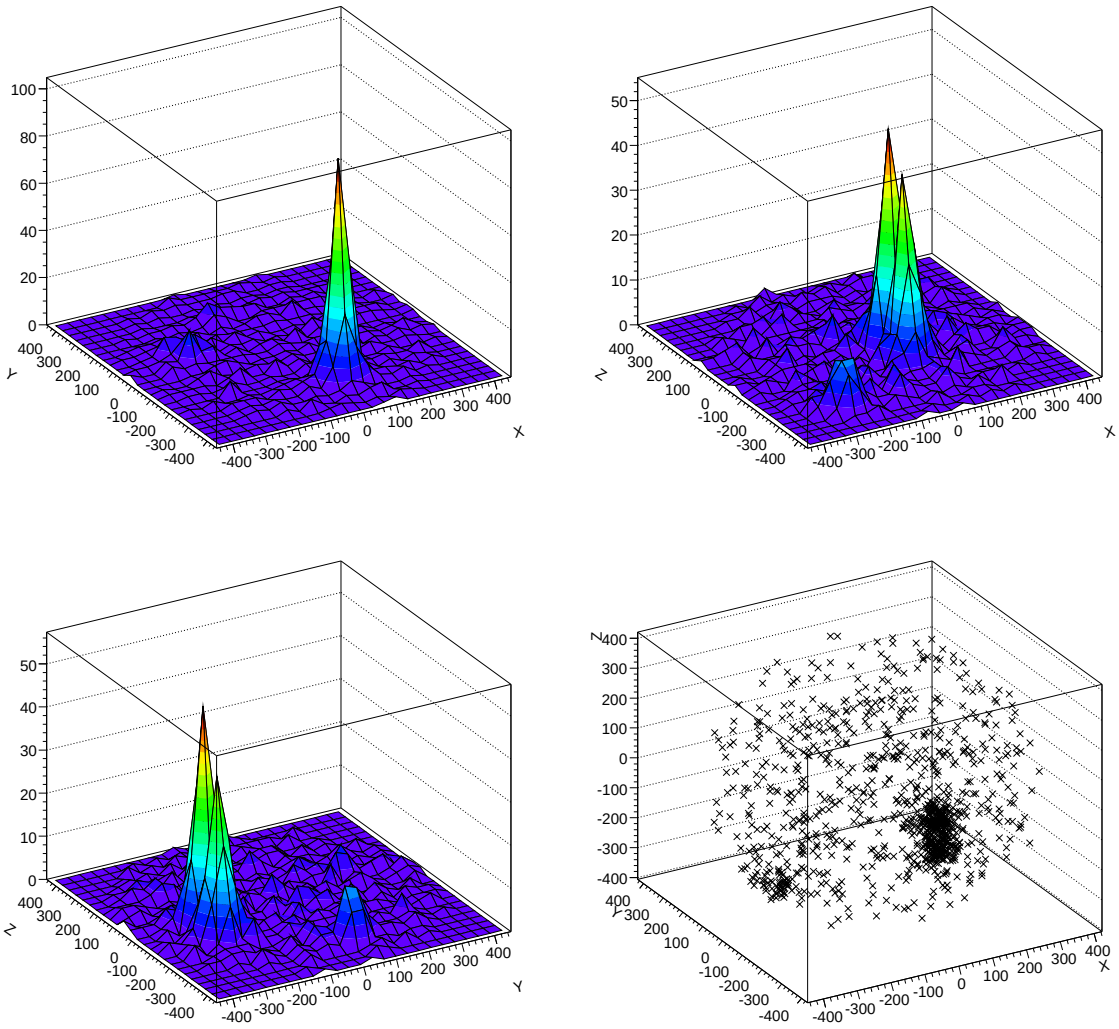


Figure 7.1: Plots of the (x,y), (x,z), (y,z) and (x,y,z) distributions of reconstructed events. The peak at (50,-250,-50) corresponds to the upper K5 hotspot, (50,-250,-125) corresponds to the lower K5 hotspot and the peak at(-250,50,-300) corresponds to the K2 hotspot.

### 7.1.2 K2 hotspot

The $z$ distribution of K2 events is shown in Figure 4.14 in Chapter 4. The $z$ distribution of K2 peaked at $z = -300$ cm, which was consistent with the position of the weld between the anchor and anchor-middle counters in the NCD string. This, and the fact that the distribution was more localised when compared with K5, suggested that the hotspot was bulk contamination.

The isotropy distribution of K2 events was in good agreement with that of bulk thallium and bismuth. In Chapter 4, it was explained that it was not possible to separate bulk thallium and bismuth events. As the accurate measurement of the Neutral Current flux was dependent on knowledge of the number of background neutrons, an estimate of the maximum number of neutrons produced by K2 contamination was made. The maximum number of neutrons would be produced if the contamination was all thallium in the bulk of the NCD. Making this assumption, a limit of $< 0.925$ $\mu$g $^{232}$Th (68% CL) was calculated, equivalent to 0.24 neutrons produced per day.

## 7.2 Hotspot searches

Concerns over the discovery of two hotspots on the NCD array led to efforts to determine whether low level hotspots existed on the array and to assess any impact on the accurate measurement of the NC flux. A comprehensive search of the $D_2O$ region found no evidence of any further hotspots.

Sensitivity to hotspots was tested using Monte Carlo simulations. $^{208}$Tl and $^{214}$Bi decays from the surface of one of the innermost strings, N4, at a $z$ position of $-50$ cm were simulated. The simulation data were combined with the expected number of *in-situ* $D_2O$ and NCD bulk events. In each case the number of hotspot events was varied to test sensitivity. It was found that a hotspot could be detected at the level of 0.035 $\mu$g of $^{232}$Th or 0.055 $\mu$g of $^{238}$U. This was equivalent to 0.009 and 0.014 neutrons produced per day respectively. Therefore, it was unlikely that any further significant hotspots existed on the NCD array and the only impact on the accuracy of an NC flux measurement would be the lack of a detailed knowledge of the K5 and K2 hotspots. This is now discussed further.

## 7.3 The need for *ex-situ* measurements

Results from the *in-situ* analysis provided estimates or limits of the equivalent amounts of $^{232}$Th and $^{238}$U in the hotspots. This analysis was unable to determine whether the hotspots were definitely $^{238}$U or $^{232}$Th. In particular, the isotropic nature of the Čerenkov

light produced by the K5 hotspot suggested that something capable of scintillation could have been deposited on the surface of K5. This would have enhanced any existing activity on the surface or in the bulk and would have produced no excess neutrons. This meant that the number of neutrons produced by the hotspots could in fact be zero and with no additional knowledge, the uncertainty would be effectively +1.72 $\mu$g (68% CL) or 0.45 neutrons produced per day. Taking the neutron capture efficiency of the NCD array to be approximately 28% for such neutrons, this gave an uncertainty of $\pm 0.13$ neutrons detected per day by the NCD array. Approximately 3.1 neutrons from the Neutral Current process would be captured by the array each day, so an uncertainty of $\pm 0.12$ neutrons detected per day would give rise to an uncertainty of $\sim 4\%$ on the Neutral Current flux, from K5 alone. This would increase once the uncertainty from the K2 hotspot was included. This was unacceptably high and it could only be improved by *ex-situ* investigation. Two *ex-situ* methods were proposed; acid elution of the NCD surface and measurements of alpha rates using an External Alpha Counter. Both methods will be discussed in this chapter, but emphasis will be given to the elution method as this was devised by the author.

## 7.4 Acid elution of an NCD

Analysis of the data strongly suggested that the contamination of K5 was on the surface of the anchor-middle counter. If this contamination was radioactivity, any Ra on the Ni surface could be easily removed by rinsing with weak (0.1 mol/$l$) hydrochloric acid (HCl). The radioactive content of the acid eluate could be determined by concentrating the solution to a volume of a few millilitres and counting this sample using beta-alpha coincidence counting. As discussed in Chapter 6, beta-alpha coincidences existed in both the $^{232}$Th and $^{238}$U chains, but the time interval between the beta and alpha is sufficiently different to make discrimination between the two chains possible. The method of eluting the contaminated NCD was based upon the techniques used in HTiO assays (see Chapter 5) and is now described.

Elution of the NCD consisted of 3 stages: elution, secondary concentration and counting. The elution and secondary concentration stages are described in detail in Chapter 5. The counting system is described in Chapters 5 and 6. The counting system efficiency was verified by a series of calibration runs, approximately one week before hotspot elution took place.

The NCD elution presented a risk of high concentrations of Ni being present in the 15 $l$ HCl eluate. High levels of Ni could affect the secondary concentration efficiency, as Ni could have been taken up in preference to Ra or Th by the ion exchange resin, limiting the sensitivity and effectiveness of the method. A number of experiments, performed to

determine the amount of Ni present in a 15 $l$ eluate, following a 20 minute elution, and the overall efficiency of the method are now described.

### 7.4.1 ICP-MS analysis of Ni concentration in the HCl eluate

The secondary concentration method used in HTiO assays was developed to be insensitive to trace amounts of Ni, Mn and Ti. During development of this improved secondary concentration method, Ni concentrations up to 9333 ppb were tested and found not to affect the efficiency. There was a possibility that the elution of an NCD section could result in a concentration of Ni that exceeded this limit. If the amount of Ni present in a 15 $l$ HCl eluate was greater than 9333 ppb, the efficiency of the secondary concentration stage might have been significantly reduced.

To determine the concentration of Ni in the eluate, a 14 cm length of NCD (from N2) was eluted for 20 min, using 15 $l$ of 0.1 mol/$l$ HCl. A 30 ml sample of HCl was taken from the elution rig reservoir, both before and after elution. Both samples were sent to Geolabs in Sudbury for analysis using Inductively Coupled Plasma Mass Spectrometry (ICP-MS). ICP-MS is a highly sensitive form of mass spectrometry, capable of measuring concentrations less than 1 ppb. The aqueous sample is vaporised and then ionised using an argon plasma. The resulting gaseous ions are focused into a beam and separated into mass fractions using a magnetic field [85]. The amount of each element present in the sample is then calculated. ICP-MS results found that the pre-elution HCl sample contained 4.81 ppb of Ni, while the post-elution sample contained 671 ppb of Ni.

The elution of K5 would involve two 90 cm sections of NCD. Assuming that the amount of Ni leached from an NCD section was directly proportional to the length of NCD eluted, it was estimated that 4314 ppb of Ni would be present in the 15 $l$ eluate for a 90 cm length of NCD, well below the safe limit of 9333 ppb. In an HTiO assay, it was common practice to elute one column using 15 $l$ of HCl, then elute the other column using the same 15 $l$ of acid. If this method was used for the K5 elution, the Ni concentration would have been likely to exceed 8600 ppb, which is sufficiently near the limit to cause concern. Therefore, it was decided to elute each hotspot separately and this would give information on the composition of each region.

## 7.5 Spike experiments

The elution and secondary concentration efficiencies are very well understood for HTiO-loaded filters. These were discussed in Chapter 5. As the work described in this chapter uses a section of Ni instead of a filter, known efficiencies for a filter cannot be assumed. A series of spike experiments was performed between January and April 2007 to measure

these efficiencies.

Sections of N2* and the leaking section of K5† were used to conduct spike tests. For each spike experiment, a section of NCD was capped at each end, placed in a weak $^{228}$Th solution and left for a period of time, details of which are given in Table 7.2. During this time, thorium plated onto the outer surface of the NCD, where it remained once the NCD was removed from solution. The amount of activity plated onto the NCD, $A_{NCD}$, was given by

$$A_{NCD} = S_{Start} - S_{End} - W - E \tag{7.1}$$

where $S_{Start}$ is the activity of the solution at the start of the soak test, $S_{End}$ is the amount of activity that remained in solution once the NCD had been removed from the solution. $W$ and $E$ refer to the amount of activity that plated on the walls of the container and end caps respectively.

The activity remaining in solution, $S_{End}$ was determined by HTiO co-precipitation and counting. Contributions to $W$ and $E$ were determined by experiments described later. The combined elution and secondary concentration efficiencies are given by

$$\epsilon_{elution}\epsilon_{sec\,conc} = \frac{A_{elution}}{A_{NCD}} \tag{7.2}$$

where $A_{elution}$ is the activity measured by elution of the NCD section and $A_{NCD}$ is the expected activity on the NCD section, calculated using (7.1).

To make the test realistic, a soak solution strength of 7 mBq was chosen as it was similar to the expected strength of the K5 hotspot. The soak solution was prepared by a two step dilution of a strong stock solution. For this purpose, a 10 Bq/ml $^{228}$Th stock solution, prepared on 31st January 2003, was used. The first diluted stock solution was prepared on 26th January 2007, by diluting a sample of the strong stock solution using ultra pure water (UPW) to form a 14 mBq/ml stock solution. The final 7 mBq soak solution was prepared by sampling 0.5 ml of the 14 mBq/ml stock solution.

Each NCD soak used a 14 cm length of NCD that had not been soaked previously. To ensure Th plated only to the outer surface of the NCD, the ends were capped using polypropylene end caps and the NCD-end cap interface was sealed using PTFE tape. To test the integrity of the seal, the sealed NCD was soaked for 10 minutes in a clean 1 litre bottle containing UPW. The solution and container were weighed before and after the UPW soak test. The mass of water remained unchanged, demonstrating that the seal was robust and indicating that minimal activity should plate on the inside of the NCD during the soak.

*A severe earthquake occurred the day after the official shutdown of the experiment and destroyed N2.

†2 m away from the hotspot region

| Spike # | NCD | Soak start | Soak end | Soak time |
|---|---|---|---|---|
| 1 | N2 | Jan 26 | Jan 27 | 32 hours |
| 2 | N2 | Feb 23 | Feb 28 | 5 days |
| 3 | K5 | Feb 28 | Mar 07 | 7 days |
| 4 | K5 | Mar 14 | Mar 15 | 24 hours |
| 5 | N2 | Mar 23 | Mar 29 | 6 days |
| 6 | K5 | Apr 05 | Apr 10 | 5 days |
| 7 | K5 | Apr 26 | Apr 27 | 24 hours |

Table 7.2: Start and end dates for the NCD spike samples. All tests took place in 2007.

Following the seal test, the NCD section was removed, 0.5 ml of the 14 mBq/ml stock solution was added to the UPW and the solution stirred for approximately 5 minutes. Once mixed, the sealed NCD section was placed back into solution, the top of the container was sealed using parafilm and the sample was left to soak. In all, 7 spiked NCDs were prepared and their soak times are given in Table 7.2.

After soaking was complete, the NCD was removed from the solution and left to drip dry. The end caps were removed and replaced with baskets in preparation for elution. The NCD section was placed inside a 10 inch polypropylene column and sealed. The remaining soak solution was concentrated to determine how much activity had plated onto the NCD, using the method now discussed.

### 7.5.1 Soak solution concentration

One ml of concentrated $HNO_3$ and 2 ml of 15% titanium sulphate, $Ti(SO_4)_2$, were added to the remaining soak solution, and stirred. This solution was titrated to pH 9 using NaOH causing a white precipitate of HTiO to form, which co-precipitated with Ra and Th. The sample was centrifuged for 3 minutes at 3400 rpm and the supernatant solution decanted. The remaining solid precipitate was dissolved using 2 ml of concentrated HCl and added to 8 ml of UPW. Approximately 42 g of Optiphase HiSafe 3 liquid scintillator cocktail was added to this final solution and the sample counted for 7-10 days using the beta-alpha coincidence counting system described in Chapters 5 and 6.

Counting results must be corrected to take into account the counting and HTiO co-precipitation efficiencies. The counting efficiency was measured using $^{228}$Th and $^{226}$Ra sources and is known to be 45±5 % for the $^{232}$Th chain and 60±10% for the $^{238}$U chain [75]. These efficiencies have been recently verified for all PMTs using both strong and weak sources.

### 7.5.2 HTiO co-precipitation efficiency

The ability of HTiO to co-precipitate along with any heavy radioisotope in solution was investigated. A 7 mBq $^{228}$Th solution, identical to that used to soak NCD sections, was left in a sealed one litre bottle for 18 hours. After this time, the solution was concentrated and counted. The raw results obtained from the beta-alpha counting system were corrected for the counting efficiency and compared to the expected activity of the solution, i.e. 7 mBq. The HTiO co-precipitation efficiency for the soak solution was found to be $54 \pm 9\%$. This was slightly lower than that quoted for the HTiO assay secondary concentration stage[‡]. It is known that in this experiment some of the activity plated onto the sides of the polypropylene container. Although the pH was lowered to below 2, not all the Th returned to solution[§] as the solution was not left for a sufficient length of time. Therefore, the HTiO co-precipitation efficiency would have been slightly lower than that measured for assays. The HTiO co-precipitation efficiency measured by this experiment, $54 \pm 9\%$, was thought to be more representative and was therefore used in the analysis of the spike experiments. Activity may have also plated onto the end caps used to seal the NCD section and this is now discussed.

### 7.5.3 $^{228}$Th plating onto polypropylene

In addition to plating onto the NCD, activity in the soak solution may have plated onto the polypropylene end caps or sides of the bottle used for the soak. Activity that plated onto the bottle would have been accounted for in the HTiO co-precipitation measurement discussed in Section 7.5.2. The end caps were removed from the solution along with the NCD prior to the co-precipitation step and therefore had to be treated separately.

The two polypropylene end caps were fixed together using parafilm, to ensure that the same surface area was exposed for this test as for the NCD tests. The end caps were soaked in 7 mBq $^{228}$Th solution for 4 days and then removed. To determine the fraction of activity that plated onto the end caps, the solution was concentrated using the HTiO co-precipitation method and the remaining solution counted. The results were corrected for the co-precipitation and counting efficiencies. Less than 5% of the solution was found to plate onto the polypropylene end caps.

[‡]HTiO co-precipitation is one of the stages in the secondary concentration procedure of the HTiO assay. The co-precipitation is carried out almost immediately with the solution being very acidic making plate out unlikely.

[§]It is known that for near neutral pH solutions, Th plates onto surfaces, but for low values of pH it stays in or returns to solution. A detailed description of Th chemistry is given in [86].

## 7.6 Results from the spike experiments

In all, 7 spike experiments were performed using the methods described in Section 7.5. Several problems were experienced with some of the spike tests and these are outlined in this section. Results from each experiment are given, followed by general conclusions.

### 7.6.1 Background

As for HTiO assays described in Chapter 5, a measurement of the contribution from the equipment and reagents used in the elution measurement was made before the spike experiments began. A 14 cm section of N2, which had not been soaked in $^{228}$Th, was eluted and concentrated using the methods described in Section 7.4. The measured background was $0.220 \pm 0.120$ counts per hour (cph) for $^{224}$Ra and $0.626 \pm 0.130$ cph for $^{226}$Ra and agreed with those measured for HTiO assays in the NCD phase.

### 7.6.2 Spike 1

Elution of the spiked NCD went according to procedure and a sample of the remaining soak solution was taken and counted. It was originally thought that a 10 ml sample of the final soak solution would be sufficient to determine its activity, but the sample was too weak and counting would have been too lengthy. It was decided to concentrate the remaining soak solution using the HTiO co-precipitation method to form a more active sample. This would be easier to count and thus provide a more accurate result.

The activity of the concentrated soak solution sample was found to be

$$18.94 \pm 1.57 \text{ dph} = 5.26 \pm 0.44 \text{ mBq}$$

this took into account activity that plated onto the container and end caps used during the NCD soak. Subtracting the activity given above from the original soak solution strength, indicated that $1.74 \pm 0.14$ mBq of Th had plated onto the NCD. To determine the secondary concentration and elution efficiencies, this number was compared to the activity measured by elution of the NCD section.

The spike elution sample was counted using the beta-alpha coincidence counters on site. The raw data from the counters had to be corrected to provide the final result. First, the background was subtracted from the elution measurement. As the half life of $^{224}$Ra is 3.66 days, a time correction was also applied to account for the difference in the time taken to concentrate the background sample and that taken to concentrate the elution sample. The time correction was:

$$\text{Corrected cph} = N_{elution} - N_{bkg} e^{-\lambda_{Ra224} \Delta t}$$

where $N_{elution}$ is the count rate obtained from the spiked NCD elution, $N_{bkg}$ is the count rate obtained from the background sample and $\lambda_{Ra224}$ is the radioactive decay constant of $^{224}$Ra. $\Delta t$ is the difference in time taken to concentrate the background and elution samples. The elution to counting time difference for the blank sample was 3 hours 20 minutes for the background sample and 3 hours 35 minutes for the elution sample, resulting in a $\Delta t$ of 0.25 hours. The corrected count rate was found to be $1.24 \pm 0.22$ cph for the elution sample.

The amount of $^{224}$Ra at the start of elution must now be calculated. If the secondary concentration stage was 100% efficient and the counter efficiency was $45 \pm 5\%$ for $^{224}$Ra, the amount of $^{224}$Ra at the start of elution, in terms of decays per hour (dph), is calculated as follows:

$$\begin{aligned} \text{eluted } ^{224}\text{Ra} &= \frac{\text{corrected cph}}{0.45 \times \exp\left(-\lambda_{Ra\,224} t\right)} = \frac{1.241}{0.45 \times \exp\left(-0.007891 \times 3.58\right)} \\ &= 2.86 \text{ dph.} \end{aligned}$$

The statistical error was found to be $\pm 0.49$ dph. Assuming that at the start of elution, $^{224}$Ra was in equilibrium with $^{228}$Th, the rate of $^{228}$Th decays would be

$$2.86 \pm 0.50 \text{ dph} = 0.79 \pm 0.14 \text{ mBq.}$$

The activity of $0.79 \pm 0.14$ mBq does not account for the chemical efficiency of the secondary concentration stage. To find the combined elution and secondary concentration efficiency, the activity that plated onto the NCD was compared with what was found on the NCD. This gave a combined efficiency of $46 \pm 11\%$ in agreement with that measured for HTiO assays.

### 7.6.3 Spike 2

The activity that remained in the soak solution sample was very similar to that measured in the Spike 1 experiment, indicating that activity did plate onto the NCD. Surprisingly, the activity measured from the spiked NCD elution was consistent with the rig background measurement, in contrast to the solution measurement. It appeared that no Ra had been picked up by the elution. To determine whether or not the problem was due to elution of the NCD or secondary concentration, the ion exchange resin was tested for Th. Th should have been removed from the surface of the NCD during elution and should have been trapped on the ion exchange resin during the processing of the 15 $l$ eluate. EDTA was used to remove Ra selectively, and any Th trapped on the resin should have remained there. The resin was rinsed with 20 ml of UPW to ensure no traces of EDTA remained. Once neutral, the resin was eluted with 50 ml of 4 mol/$l$ $H_2SO_4$ at a rate of 5 ml/min.

Approximately 250 ml of UPW was added to the residual solution along with 2 ml of 15% $Ti(SO_4)_2$ (60 mg in Ti). The solution was titrated to pH 9 using NaOH, at which point a white precipitate of HTiO was formed. This co-precipitated with any Th present in solution. The solution was centrifuged at a rate of 3400 rpm for 3 minutes and the HTiO solid was rinsed with UPW until the supernatant became cloudy.

The HTiO precipitate was dissolved using 10 ml of concentrated $HNO_3$ and the solution passed through an anion exchange resin[¶] at 2 ml/min. The resin was then rinsed with 20 ml of 6 mol/$l$ $HNO_3$. The column was then rotated through 180°. The resin was eluted with 80 ml of 0.5 mol/$l$ HCl at a rate of 2 ml/min and the resulting solution was evaporated to near dryness. The small final volume was added to 10 ml UPW and 42 g of Optiphase HiSafe 3 liquid scintillator.

Counting indicated that no Th had been eluted from the NCD. The pH measurement of a small amount of liquid found in the elution rig indicated that the acid had been added[‖], however, when the housing was opened, the NCD was found to have "imploded". It is thought that this occurred during the priming of the elution rig.

During priming, acid was pumped from the bottom of the column toward a vent at the top, allowing air within the column to escape and the housing to fill with acid. Once the column was full, the vent was closed and the pump speed increased. This was performed at the same time as the outlet to the column was opened, allowing circulation of the acid. If the outlet was not opened, the pressure inside the column could increase. High pressure could cause damage to the contents of the column, in this case an NCD. The pressure inside the column built up and the NCD section was crushed. It was thought that this caused the NCD to implode. As a result acid did not flow over the NCD surface properly and a significant amount of acid, and thus activity was trapped inside the deformed NCD. This was not processed during the concentration stage, which explains why very little Ra was found in the elution sample.

### 7.6.4 Spike 3

The activity of the soak solution from this spike agreed with the values from the first and second spikes. Once again the final sample was consistent with the background count rate. It was decided to perform a Th work up on the ion exchange resin. Unfortunately, an error was made during this work up resulting in the loss of the sample, so the presence of Th on the ion exchange resin was never proved.

[¶] 4.0 g of Dowex 1X8 resin, 100 mesh

[‖] 0.1 M HCl was mixed in the reservoir of the rig by adding 125 ml of concentrated HCl to 15 litres of UPW. The solution was mixed by circulating the reservoir stock around a closed loop on the rig before being used to elute the column(s).

It is believed that during the soaking of the spike, Ra produced by the decay of Th on the surface of the NCD leached back into the stock solution. This would have broken the Th-Ra equilibrium on the surface of the NCD. As the NCD was eluted either on the day it was removed from the soak solution or the day after, there was not sufficient time for that equilibrium to be restored. Thus, the amount of Ra on the surface on the NCD would have been lower than the true activity (i.e. Th) present on the surface. A Th elution would have confirmed this. This behaviour was also noticed with the 6th spike.

### 7.6.5 Spike 4

The 4th spike work up went to plan, but unfortunately the counter system failed approximately 22 minutes after the sample was placed onto the system. System failures could usually be predicted as the system would stop counting for short periods of time and the fault could be fixed before the whole system failed. It was not possible to predict the fault on this occasion. On investigation, it was found that an ADC unit had failed. The unit was replaced and the system efficiency verified by running calibration sources on all PMTs for 27 hours. The ion exchange column had been saved for a Th work up, but it was decided to leave the column for 10 days to allow the Th-Ra equilibrium to be re-established and a Ra elution performed again.

Analysis of the second radium elution sample was very similar to that outlined in the first spike experiment. However, as the Ra had been built up from Th, several additional efficiency factors had to be applied to the raw counter data. First, the elution efficiency for removing Th from the NCD using 0.1 mol/$l$ HCl is $65 \pm 5\%$ (compared to $90 \pm 10\%$ for Ra) and the first Ra elution removed 15% of the Th trapped on the column. This implied that only 55% of the Th originally present on the NCD survived to build up Ra. Accounting for all of these factors, the secondary concentration efficiency was found to be $45 \pm 24\%$.

### 7.6.6 Spike 5

The 5th spike returned a very low value of activity for both the soak solution and elution samples. The resin was left to re-establish the Th-Ra equilibrium and the elution was repeated 10 days later. The amount of radium was found to be significantly lower than results obtained in other experiments. If the results were scaled such that the solution was the same strength as the other solution samples, the derived efficiency would be in agreement. It is suspected that an error was made during preparation of the soak solution.

### 7.6.7 Spike 6

The 6th spike also returned a low value for the first elution. However, the measured solution sample was very similar to that from the first spike test. No problems were encountered during the work up. The ion exchange column was left for 10 days and subsequently eluted for Ra. This time, a much larger Ra signal was seen, indicating that some form of disequilibrium between Ra and Th occurred on the NCD. It is thought that Ra produced by Th that had plated onto the NCD leached off the NCD surface into solution during the soak period. It is suspected that this was responsible for the 3rd Spike but conclusive proof could not be obtained as the resin had been lost. The analysis was identical to that for the 4th spike and the efficiency was found to be $43 \pm 18\%$.

### 7.6.8 Spike 7

The 7th spike was left for several weeks to build up Ra from Th as a test of disequilibrium. The NCD was eluted on June 13th, 48 days after it was removed from solution. The equilibrium between Th and Ra should have been well established by the time of elution, though the amount of $^{228}$Th would have decreased by approximately 5%. After this decay was taken into account, the efficiency was found to be $45 \pm 18\%$. The result was in agreement with the other one day soak tests, showing that disequilibrium, i.e. Ra leaching back into the soak solution, did not occur appreciably during a 24 hour soak period.

### 7.6.9 Overall conclusions from the spike tests

Spike experiments have shown that radioactivity can be removed from the surface of an NCD using acid elution, concentration and counting. Results indicated that Th plated onto Ni very rapidly within the first 24 hours of soaking and Ra produced by Th decay seems to leach from the NCD surface into solution. This may have occurred with the hotspot in the detector but, since its removal from the $D_2O$, the Th-Ra equilibrium would have been restored.

The efficiency of the secondary concentration technique obtained from these experiments is in agreement with that used for HTiO assays. As a large proportion of the error quoted for the efficiencies obtained from these experiments was due to spike soaking, it is reasonable to use the secondary concentration efficiency of the HTiO assay technique of $58 \pm 6\%$ for the NCD elution. Combining this with the counter efficiency gives overall efficiencies of

$$^{238}\mathrm{U} = 31 \pm 7\%$$
$$^{232}\mathrm{Th} = 23 \pm 4\%.$$

Therefore, the elution method should be capable of measuring the activity and composition of the K5 hotspot.

## 7.7 Sensitivity

The ability of the elution method to detect radioactivity was limited by the radioactive backgrounds associated with the reagents and equipment used in the process. To determine the contribution from the equipment and reagents, a blank NCD sample was processed and counted. For a 90 cm section of NCD, the background levels were found to be

$$^{224}\text{Ra} = 0.222 \pm 0.127 \text{ cph}$$
$$^{226}\text{Ra} = 0.626 \pm 0.191 \text{ cph}$$

where the quoted error is statistical plus systematic. A lower limit of detection could be derived using these background numbers and it was defined as three times the uncertainty [72], resulting in the following count rates

$$^{224}\text{Ra} = 0.381 \text{ cph}$$
$$^{226}\text{Ra} = 0.573 \text{ cph}.$$

Taking into account the efficiencies of the elution, secondary concentration and counting stages** the decay rate of Ra was found to be

$$^{224}\text{Ra} = 4.505 \times 10^{-4} \text{ Bq}$$
$$^{226}\text{Ra} = 5.082 \times 10^{-4} \text{ Bq}.$$

Assuming that radioactive equilibrium held before elution, the decay rates are equivalent to the following masses of $^{232}$Th and $^{238}$U

$$^{232}\text{Th} = 0.111 \ \mu\text{g}$$
$$^{238}\text{U} = 0.041 \ \mu\text{g}.$$

These are the lower limits of detection for the acid elution method.

## 7.8 Elution of K5

Prior to the elution of the K5 hotspot a background measurement was performed to determine the contribution to the signal from the equipment and reagents used in the

**90% and 58% for both Ra isotopes for elution and secondary concentration. 60% and 45% counting efficiencies for $^{226}$Ra and $^{224}$Ra respectively.

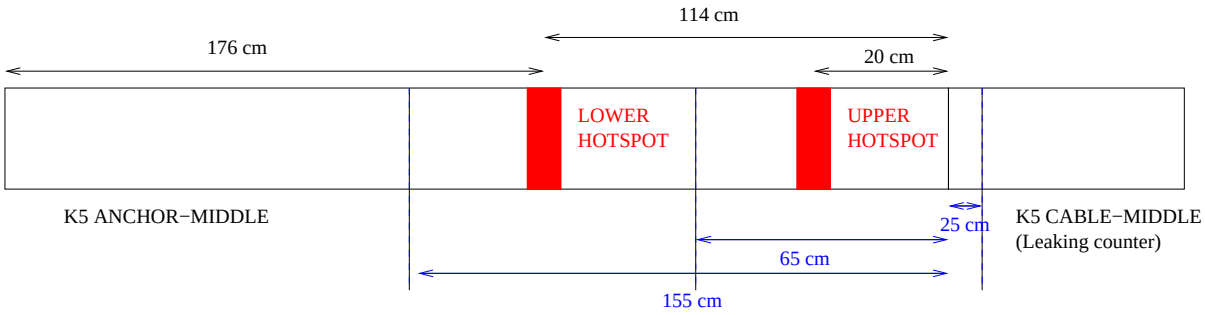


Figure 7.2: Location of cuts and approximate locations of the two K5 hotspots. The red bands are where the EAC localised the hotspot.

technique. A 90 cm length of the K5 cable-middle section was placed inside a 40 inch column and eluted. The eluate was processed using the method described in section 7.4. Following this, the elution rig was cleaned by circulating 0.5 mol/$l$ HCl for approximately 40 minutes and then rinsed with UPW until a near neutral pH was reached. The background measurement was performed approximately 5 days before the hotspot elution. Analysis of the background sample found levels of

$$^{224}\mathrm{Ra} = 0.222 \pm 0.127 \text{ cph}$$
$$^{226}\mathrm{Ra} = 0.626 \pm 0.191 \text{ cph},$$

which were consistent with all previous measurements made using the elution rig.

Once the results of the background measurement were known, preparation for the hotspot elution could begin. It was known that due to restrictions on the size of columns that could be used with the elution rig, the contaminated NCD would need to be cut into two sections. The decision as to where to cut was simplified by the external alpha counter results. These had successfully located two active regions with a resolution of approximately 10 cm. The position of the cuts and approximate hotspot locations are given in Figure 7.2.

The cuts were made using a pipe cutter taken from the chemistry clean laboratory in the surface building. As a precautionary measure, the pipe cutter was ultrasonically cleaned with dilute radiac solution, rinsed, sealed and taken underground. The contribution of radioactivity from the cutter should have been negligible as it was used to cut various test sections of NCD and no excess activity was seen. Once cut, each NCD was placed in a 40 inch polypropylene housing[††] and transported to the surface lab.

Once in the surface lab, the column containing the lower hotspot section was connected to the elution rig and eluted first, as it had been found to be less active when

[††]These were used in the past for HTiO $D_2O$ assays and were cleaned using 0.5 mol/$l$ HCl before use with the hotspot NCDs

compared to the upper hotspot. When elution was complete, the acid in the rig was drained back to the rig reservoir and it was noted that only 13 $l$ of acid were present. As normal, any remaining acid in the pipework was forced to drain using a nitrogen purge of the system, resulting in a total of 13.5 $l$ of HCl, significantly lower than the anticipated 15 $l$.

As stated in Chapter 5, HCl used in the elution was prepared in the rig reservoir by adding 125 ml of concentrated HCl to 12.5 $l$ of UPW and then making this solution up to a volume of 15 $l$ using UPW. It was suspected that either a mistake was made during preparation of the acid or a portion of acid remained trapped inside the rig. It was decided to remove the column containing the NCD to investigate the possibility of trapped acid in this part of the rig. The column contained a significant amount of acid, the majority of which was poured from the housing into the vessel containing the 13.5 $l$ of eluate. Approximately 1 litre of eluate was lost. Upon opening the column, it was found that the upper basket had become detached during elution, which had allowed the NCD to fill with acid. Although this would have contributed an insignificant amount of radioactivity to the sample, it could have caused the concentration of Ni to be twice as high, making it close to the known safe upper limit of the technique. An experimental test of this situation is described later in this section.

Following this incident, the elution rig was cleaned using 0.5 mol/$l$ HCl and rinsed with UPW until a near neutral pH was reached. To ensure the baskets on the upper section of the hotspots would not become loose during elution, PTFE tape was wrapped around the o-ring that provided the seal between the NCD and basket. No problems were encountered with the upper section elution.

Both samples were concentrated separately using the method outlined in Section 7.4. During the EDTA elution of the ion exchange resin of the lower hotspot sample, the eluate was bright blue, indicating a high Ni content. Most elutions from NCD phase $D_2O$ assays and the NCD spike tests had been pale blue or green[‡‡]. No other problems were encountered.

The two samples were placed on two PMTs of the beta-alpha counting system. Unfortunately, the counting system stopped counting approximately 54 hours into the run after developing an intermittent fault. Counting between 54 hours and 81 hours was sporadic and complete system failure occurred after approximately 81 hours of running. Fortunately, only the first 48 hours of counting are crucial as the bismuth activity takes approximately 32 hours to build up and reach equilibrium with Ra in the sample. Thus, as long as the build up and part of the decay is counted without interruption, the results are reliable. Further counting took place once the system had been repaired, to reduce

[‡‡]Trace amounts of Ni were present in the $D_2O$ due to the presence of the NCDs

the statistical error by improving the quality of the fit to the tail of decay. It was not possible to fix the system immediately (as the relevant persons were in Oxford) and it was decided to transfer the samples to the new beta alpha counting system. As the efficiencies of the two systems were very similar, it was felt that the data from both systems could be combined.

Data from both beta-alpha systems was analysed using the same program. A plot of alpha ADC versus the pulse shape discrimination variable was made and genuine coincidences are selected by applying ADC and psd cuts to the data. A maximum likelihood fit of decay spectra (of $^{228}$Th, $^{224}$Th, $^{212}$Pb, $^{212}$Bi) was performed to the decay spectrum of the (selected) genuine beta-alpha coincidences. Combining data from both systems was slightly complicated by the fact that the psd and ADC peaks occur in slightly different places. A multiplicative factor was applied to the new system data, to shift it into the same ADC/psd region as the old system data. As there was clear separation between the signal and the background in each case, the selected region easily contained all data and also, because the amount of Ra was determined solely on the basis of timing, which was identical for both systems, there was no increase in systematic error.

### 7.8.1 Testing for Ni interference

In hindsight, it was realised that a sample of the lower NCD hotspot eluate should have been sent for ICP-MS to test the Ni concentration. As this had not been done, the lower hotspot incident was recreated using the 90 cm blank section of K5 (anchor-middle) and eluted without the upper basket in place. A 30 ml sample of both the pre and post elution acid was sent to Geolabs for ICP-MS Ni analysis. A concentration of 5374 ppm of Ni was found in the post elution sample.

The remaining 15 $l$ was transported to Laurentian University, where a spike test took place. A 1.0 Bq $^{228}$Th solution was added to the eluate and it was processed in an identical manner to the hotspot samples. The sample was counted and yielded an activity of $0.64 \pm 0.07$ Bq, indicating that the secondary concentration efficiency was $64 \pm 7\%$ which agreed with that measured during the development of the HTiO technique [73].

## 7.9 Elution results

The samples were counted using the Oxford beta-alpha system. The raw results from the counter data are given in Table 7.3. To determine the amount of activity present on the NCD just before elution began, the efficiencies of each stage must be taken into account. The efficiencies are given in Table 7.4. Correcting the observed count rate for the reagent and equipment background and the efficiencies above gives the decays per hour, which

| | $^{224}$Ra (cph) | $^{226}$Ra (cph) |
|---|---|---|
| K5 Blank | $0.22 \pm 0.12$ | $0.63 \pm 0.13$ |
| Upper H/S | $2.28 \pm 0.53$ | $0.57 \pm 0.05$ |
| Lower H/S | $1.23 \pm 0.38$ | $0.83 \pm 0.01$ |

Table 7.3: Results from the elution of the K5 hotspots. Errors are statistical only. The K5 blank refers to the measurement of the equipment and reagent background performed before the elution of the hotspot(s) took place. All numbers are in counts per hour (cph).

| Stage | $^{224}$Ra (cph) | $^{226}$Ra (cph) |
|---|---|---|
| Elution | $90 \pm 10\%$ | $90 \pm 10\%$ |
| Secondary Concentration | $58 \pm 6\%$ | $58 \pm 6\%$ |
| Counting | $45 \pm 5\%$ | $60 \pm 10\%$ |
| Overall efficiency | $23 \pm 4\%$ | $31 \pm 7\%$ |

Table 7.4: Efficiencies for each stage of the acid elution technique.

can be converted into Bq. Assuming that just prior to starting elution, $^{224}$Ra was in equilibrium with $^{232}$Th and $^{226}$Ra was in equilibrium with $^{238}$U the amount of each may be calculated and the results are given in Table 7.5. In the case of the upper hotspot, a limit of activity is given.

## 7.10 External Alpha Counting of K5

An External Alpha Counter (EAC) was constructed at the University of Washington to count alpha particles released from the external surface of an NCD. The EAC is a multiwire proportional counter designed to contain the full circumference of a 1 metre length of NCD. Alpha particles deposit energy in the gas and this is proportional to the charge collected by the anode wires. Resistive wires are used to allow spatial localisation of events. The data acquisition system stores a time stamp for each event which allows data to be used in alpha-alpha coincidence measurement. The design, construction and calibration of the EAC is discussed in [56].

### 7.10.1 Location of the K5 hotspot(s)

The *in-situ* analysis indicated that the K5 hotspot was possibly two independent localisations of activity, but it could not confirm this due to the position resolution of the event fitter. Results from the EAC showed that two independent hotspots did exist at locations consistent with those predicted by the *in-situ* analysis. A comparison is shown in Figure

| | $^{232}$Th $\mu$g | $^{238}$U $\mu$g |
|---|---|---|
| Upper H/S | $0.61 \pm 0.17$ | $< 0.04$ |
| Lower H/S | $0.30 \pm 0.12$ | $0.11 \pm 0.03$ |
| Total activity | $0.91 \pm 0.21$ | $0.11 \pm 0.03$ |
| Neutrons produced per day | $0.24 \pm 0.06$ | $0.004 \pm 0.003$ |

Table 7.5: Masses of $^{238}$U and $^{232}$Th measured by acid elution. The corresponding number of neutrons produced per day is given.

7.3.

### 7.10.2 Measurement of composition

EAC data was analysed using two independent methods. The first fitted Monte Carlo data to the observed peaks in the alpha ADC spectrum and the second used an alpha-alpha coincidence method. These will be described in turn.

The observation of alphas by the EAC confirmed that the hotspot was a radioactive deposit on the surface of K5. The data was analysed separately for the two hotspots on K5 and it was assumed that it consisted of $^{238}$U and $^{232}$Th only. As Ra was particularly soluble in water, the possibility of disequilibrium occurring at the long lived Ra isotopes in the $^{232}$Th and $^{238}$U chains was accounted for by fitting for the lower and upper parts of each chain separately.

The energy spectrum of the background subtracted data set in Figure 7.4 [56] shows a clear peak from alpha decay of $^{232}$Th for both the upper and lower hotspots. The upper part of the $^{232}$Th chain consists of a single alpha decay, namely

$$^{232}\mathrm{Th} \rightarrow ^{228}\mathrm{Ra} + \alpha.$$

The emitted alpha has an energy of around 4 MeV and the number of $^{232}$Th alphas was determined by fitting a Gaussian distribution over an energy range of 3.2 to 4.4 MeV. As this peak could be easily and well determined, it was used to assess the stability of the EAC energy scale during the period of data acquisition.

Monte Carlo simulations of the upper and lower $^{232}$Th and $^{238}$U energy spectra were generated and fitted to the data. The relative amounts of each part of each chain were varied to minimise the $\chi^2$ between the data and Monte Carlo distributions. Once the number of each part of each chain had been obtained and the efficiency of the EAC accounted for, the equivalent mass of each contaminant was calculated for both hotspots. The results that best described the EAC data are given in Table 7.6. As both the photodisintegration and Čerenkov backgrounds are produced by the lower parts of both the $^{232}$Th and $^{238}$U

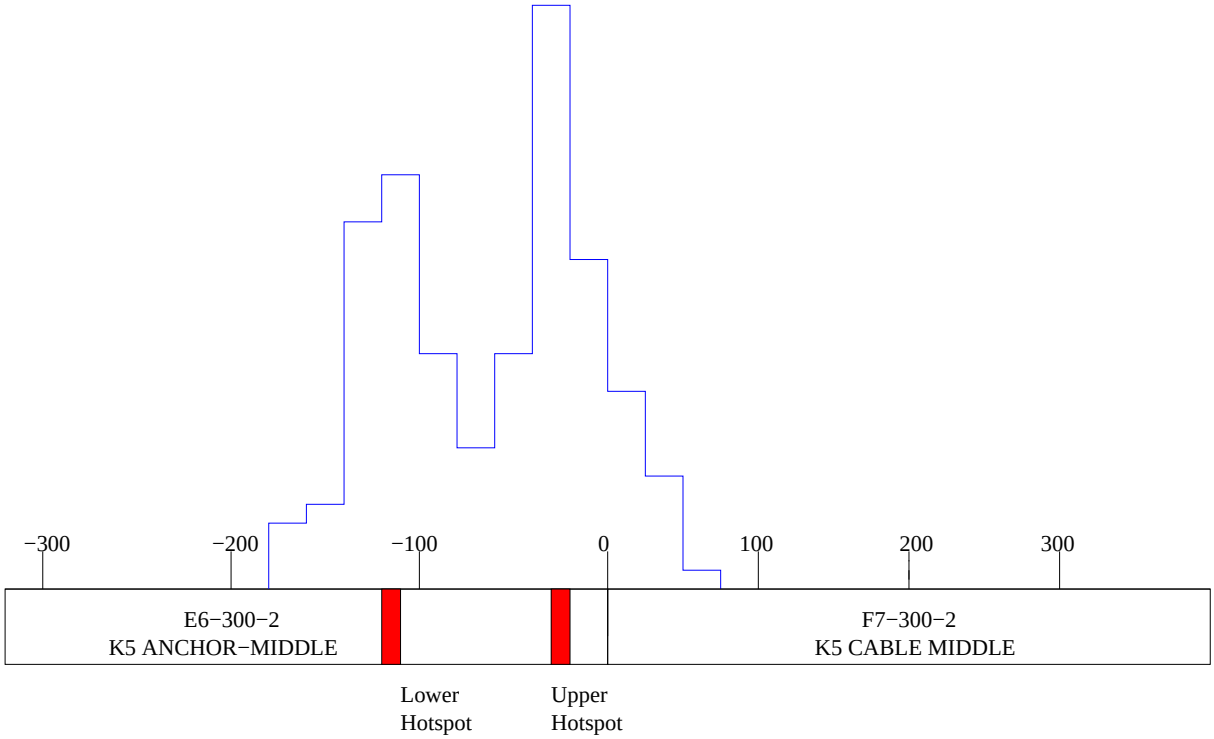


Figure 7.3: Comparison of EAC and *in-situ* results for the K5 distribution. The join between F7-300-2 and E6-300-2 is approximately $z = 0$ cm in detector coordinates. The red bands indicate where the EAC found the activity to be localised. The upper hotspot is close to where the plastic bag was fixed during leak testing of the string in April 2004. The bag covered the central weld ( between F7-300-2 and E6-300-2) and it was thought that some of the tape may have accidentally come into contact with the NCD surface. The lower hotspot is close to where the NCD was held in place overnight using a clamp in the neck of the detector.

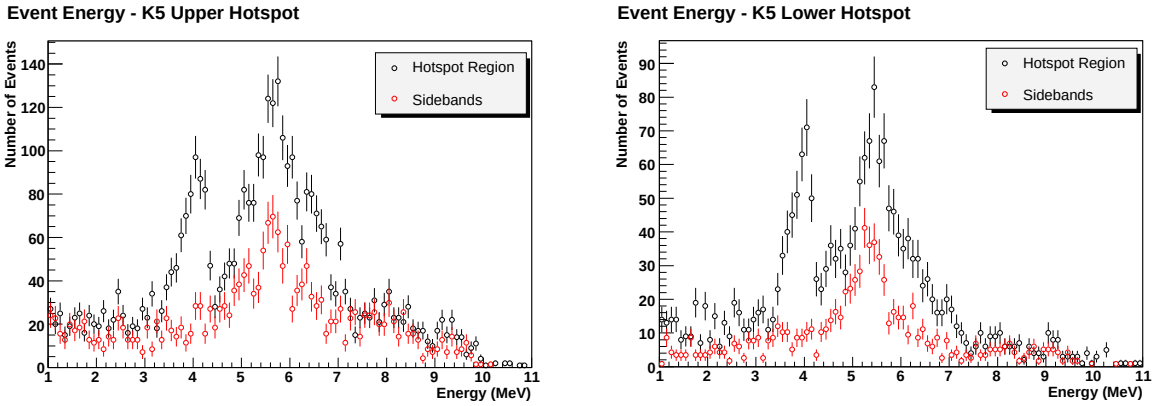


Figure 7.4: The $\alpha$-energy spectra of the K5 hotspots. Shown are the total spectra of events (black) and the spectra of background events (red) in the hotspot region.

| Hotspot | $m_{\mathrm{Th}}^{\mathrm{up}}$ ($\mu$g) | $m_{\mathrm{Th}}^{\mathrm{lo}}$ ($\mu$g) | $m_{\mathrm{U}}^{\mathrm{up}}$ ($\mu$g) | $m_{\mathrm{U}}^{\mathrm{lo}}$ ($\mu$g) |
|---|---|---|---|---|
| K5 Upper | 2.41±0.15 | 1.03±0.09 | 0.00±0.01 | 0.04±0.03 |
| K5 Lower | 1.60±0.14 | 0.34±0.06 | 0.10±0.02 | 0.04±0.02 |

Table 7.6: The hotspot strengths which best describe the EAC data. The numbers for the lower $^{238}$U and $^{232}$Th chains are the amounts of the parents which would produce the observed spectrum if the chains were in equilibrium.

chains, it is only these results that are applicable to the NCD phase analysis. A decay of the lower part of the chain is equivalent to a complete chain in terms of photodisintegration. If the equilibrium had not been broken in the chain, approximately 1.4 times more background neutrons would have been produced by the K5 hotspots, which would have caused problems when extracting the Neutral Current flux. Fortunately, equilibrium was broken.

### 7.10.3 Coincidence analysis

The coincidence analysis provided a measure of the activity in the lower part (i.e. below $^{228}$Ra) of the $^{232}$Th chain. The short lived isotope, $^{222}$Rn decays by emission of a 6.40 MeV alpha to $^{216}$Po with a half life of 55.6 s. $^{216}$Po subsequently decays to $^{212}$Pb by emission of a 6.91 MeV alpha with a half life of 0.15 seconds. Analysis cuts were applied to the raw EAC to select events that occurred within 0.3 seconds and 10 cm of each other and also in which the energy of the first event was between 5.3 and 7.3 MeV and that of the second was between 5.8 and 7.8 MeV.

| Hotspot | Mass of $^{232}$Th ($\mu$g) |
|---|---|
| K5 Upper | $0.67 \pm 0.09$ |
| K5 Lower | $0.41 \pm 0.08$ |

Table 7.7: Results from the coincidence analysis of the EAC data.

The coincidence analysis results measured the activity of the lower part of the $^{232}$Th chain and are given as an equivalent mass of $^{232}$Th as if the lower part was in equilibrium with the upper proportion of the chain. The coincidence analysis results are given in Table 7.7.

## 7.11 Measurements of K2

EAC results showed no significant activity on the surface of K2, confirming that the activity was located in the bulk of the counter. *In-situ* analysis predicted a position consistent with the weld between the anchor and anchor-middle counters of K2. No excessive bulk alphas were seen from this string [68], suggesting that the hotspot was in the dead region of the counter, i.e. on the end cap of the counter, in the region that did not contain $^{3}$He. The low background high purity germanium counter was used to measure the radioactivity of several sections in the affected K2 region. The activity was found to be approximately 10 cm from the weld that joined the anchor and anchor-middle counters and was thought to be on the end cap of the anchor-middle counter, in the dead region of the counter [56]. During un-deployment it was noted that the flare used to join these two sections together was unlike any other in the array. It was subsequently confirmed that the flare had been produced by an external contractor and because of this, the weld was not as pure as the other welds in the array.

No uranium like activity was found in the K2 hotspot, but a significant signal for $^{232}$Th was observed. All of the gammas expected from the decay chain were present, indicating that equilibrium was present. The equivalent mass of $^{232}$Th was measured to be $1.43 \pm 0.17$ $\mu$g.

## 7.12 Results and conclusions

The results from all of the hotspot measurements are given in Table 7.8. The error weighted mean of the *ex-situ* and *in-situ* results was calculated and used to derive the neutron production rates given in Table 7.9. Only the elution and EAC singles results were used in the calculation of the *ex-situ* mean due to the large uncertainty on the model

used in the coincidence data. The elution and singles uncertainties were multiplied by a factor of 1.5 to achieve a $\chi^2$ of approximately 1. This "enlarged" error is quoted on the weighted means. The *ex-situ* and *in-situ* results are not combined as the *in-situ* analysis could not resolve the two hotspots sufficiently well enough to provide two results. The *in-situ* does provide a useful verification of the *ex-situ* methods.

| | | $^{232}$Th $\mu$g | $^{238}$U $\mu$g |
|---|---|---|---|
| EAC Singles | K5 Upper | $1.03 \pm 0.09$ | $0.04 \pm 0.03$ |
| | K5 Lower | $0.34 \pm 0.06$ | $0.04 \pm 0.02$ |
| | K2 | N/A | N/A |
| Coincidence | K5 Upper | $2.20 \pm 0.90$ | N/A |
| | K5 Lower | $1.55 \pm 0.65$ | N/A |
| | K2 | N/A | N/A |
| Elution | K5 Upper | $0.61 \pm 0.18$ | $< 0.04$ |
| | K5 Lower | $0.30 \pm 0.12$ | $0.11 \pm 0.03$ |
| | K2 | N/A | N/A |
| Germanium detector | K5 Upper | N/A | N/A |
| | K5 Lower | N/A | N/A |
| | K2 | $1.43 \pm 0.17$ | $< 0.40$ |
| Error weighted mean | K5 Upper | $0.95 \pm 0.12$ | $0.04 \pm 0.04$ |
| | K5 Lower | $0.33 \pm 0.08$ | $0.06 \pm 0.03$ |
| | K2 | $1.43 \pm 0.17$ | $< 0.40$ |
| Total *ex-situ* | K5 | $1.28 \pm 0.14$ | $0.10 + 0.05, -0.05$ |
| Total *in-situ* | K5 | $1.48 + 0.24, -0.27$ | $0.77 + 0.19, -0.23$ |
| Total *ex-situ* | K2 | $1.43 \pm 0.17$ | $< 0.400$ |
| Total *in-situ* | K2 | $< 0.93$ | N/A |

Table 7.8: Masses of uranium and thorium measured by each technique for the K5 and K2 hotspots. In the calculation of the error weighted mean *ex-situ* numbers, only the elution and singles results were used.

| | $^{232}$Th | $^{238}$U |
|---|---|---|
| K5 total | $0.31 \pm 0.03$ | $0.004 \pm 0.001$ |
| K2 | $0.38 \pm 0.06$ | $< 0.01$ |

Table 7.9: Neutrons produced per day by each hotspot.

The exact cause of each hotspot is unlikely ever to be determined for certain. The surface contamination on K5 was most likely to have been caused during the leak testing of the counter in April 2004. The difference in composition between the two K5 hotspots suggested that they were caused by different mechanisms. The location of the upper

hotspot was close to where the bag was taped during the leak tests and the location of the lower hotspot was close to where the string was clamped in position overnight. However, the same clamp was used to hold a number of strings in position during deployment. Therefore, if it had been severely contaminated, the array would probably have been much hotter. However, Th chemistry is complicated and it was found that during the elution development, Th plating onto Ni took about 12-24 hours. It is therefore possible that the activity was not transferred onto strings that were held for short periods of time (i.e. less than 4 hours).

The case of K2 is similarly complicated. The *in-situ* analysis indicated that the activity was located in the region of the lowest weld on the string (between the anchor and anchor-middle counters). Initial inspection of the NCD post-deployment suggested that the weld was different from all other welds in the array. The flare had been produced by an external company. The Ge detector found a strong signal in a 7 cm section that included the end cap of the detector. The absence of any excess of alphas on K2 [68] indicated that the contamination was most likely on the end cap in the dead region of the detector.

Despite remaining uncertain as to the cause of the hotspots, the work described in this chapter has shown that their composition and strength is understood. This knowledge will significantly reduce the uncertainty on the final Neutral Current number derived in the NCD phase of SNO.

# Chapter 8

# Signal Extraction

The Neutral Current Detectors were designed to provide an independent verification of the Neutral Current fluxes measured by the $D_2O$ and salt phases. The majority of neutrons produced in the $D_2O$ region were captured by the NCDs, but a small number were captured by deuterium nuclei, emitting Čerenkov light that was detected by the PMTs. The number of Neutral Current (NC), Charged Current (CC) and Elastic Scattering (ES) events could be determined by using an extended maximum likelihood fit to the PMT data. As analysis of the NCD phase data was still ongoing, the work presented in this chapter, describes fits to Monte Carlo data to determine the potential for a "PMT only" measurement of the NC flux in the NCD phase.

## 8.1 Event selection

Neutrino events were selected from the cleaned data using the following analysis cuts

- $6.5 < E_{RSP} < 20.0$ MeV
- $-1.0 < \cos\theta_{\odot} < 1.0$
- $R_{xyz} < 550$ cm
- $-0.12 < \beta_{14} < 0.95$.

$E_{RSP}$ is the total energy of an event measured by the RSP energy estimator*, $R_{xyz} = \sqrt{(x^2+y^2+z^2)}$ and is the fitted radius of an event. $\beta_{14}$ is a measure of event isotropy and therefore, a measure of the distribution of fired PMTs in an event. $\cos\theta_{\odot}$ is the fitted angle of an event with respect to the position of the Sun. These cuts were also applied to Monte Carlo data to form probability density functions that were used in a maximum likelihood fit to the data.

*See Section 4.1.1

## 8.2 Extended maximum likelihood

Assuming that the events selected by the analysis cuts were dominated by NC, CC and ES events and that there were variables that could be used to distinguish them, the number of each event type could be determined using a maximum likelihood technique. The most probable combination of NC, CC and ES events for a given data set was found by maximising the likelihood function, where the likelihood function was the probability of obtaining the data, given the probability distributions of the event types expected in the data.

The variables used to distinguish between the three signals were energy ($E$), radial position ($R$) and solar angle ($\cos\theta_\odot$), the angle of the fitted event with respect to the Sun. These distributions are shown in Figure 8.1. For each signal type, a 3 dimensional probability density function (pdf) containing these variables was constructed using Monte Carlo data. These pdfs were used to calculate the likelihood function

$$L = \prod_{i=1}^{N} \sum_{j} a_j P_{ji}$$

where $N$ is the total number of events in the data set, $P_{ji}$ is the normalised probability that event $i$ is a type $j$ signal and $a_j$ is the trial number of events of type $j$. The values of $a_j$ were varied until the maximum value of the likelihood was obtained.

Since the number of events in the data set has a Poisson distribution with the true (mean) number of events, the probability of measuring $N$ events in the data should be included in the likelihood estimate. The likelihood function can then be expressed as

$$\mathcal{L} = \ln(L) = \sum_{i=1}^{N} \ln\left(\sum_{j} a_j P_{ji}\right) - \sum_{j} a_j$$

where the most probable combination of NC, CC and ES events occurred when the likelihood, $\mathcal{L}$ was maximised. The parameters used to distinguish between the three neutrino fluxes are now described.

## 8.3 Extracting the signals

To extract the number of NC, CC and ES events in the data, simultaneous fits of $R$, $E$ and $\cos\theta_\odot$ were made. The maximum likelihood extraction was carried out using a program written by McGregor, Wilson and Loach [59, 87, 88]. This program, known as MXF, used MINUIT to maximise the extended likelihood and find the most probable combination of events. The code was tested extensively during its development.

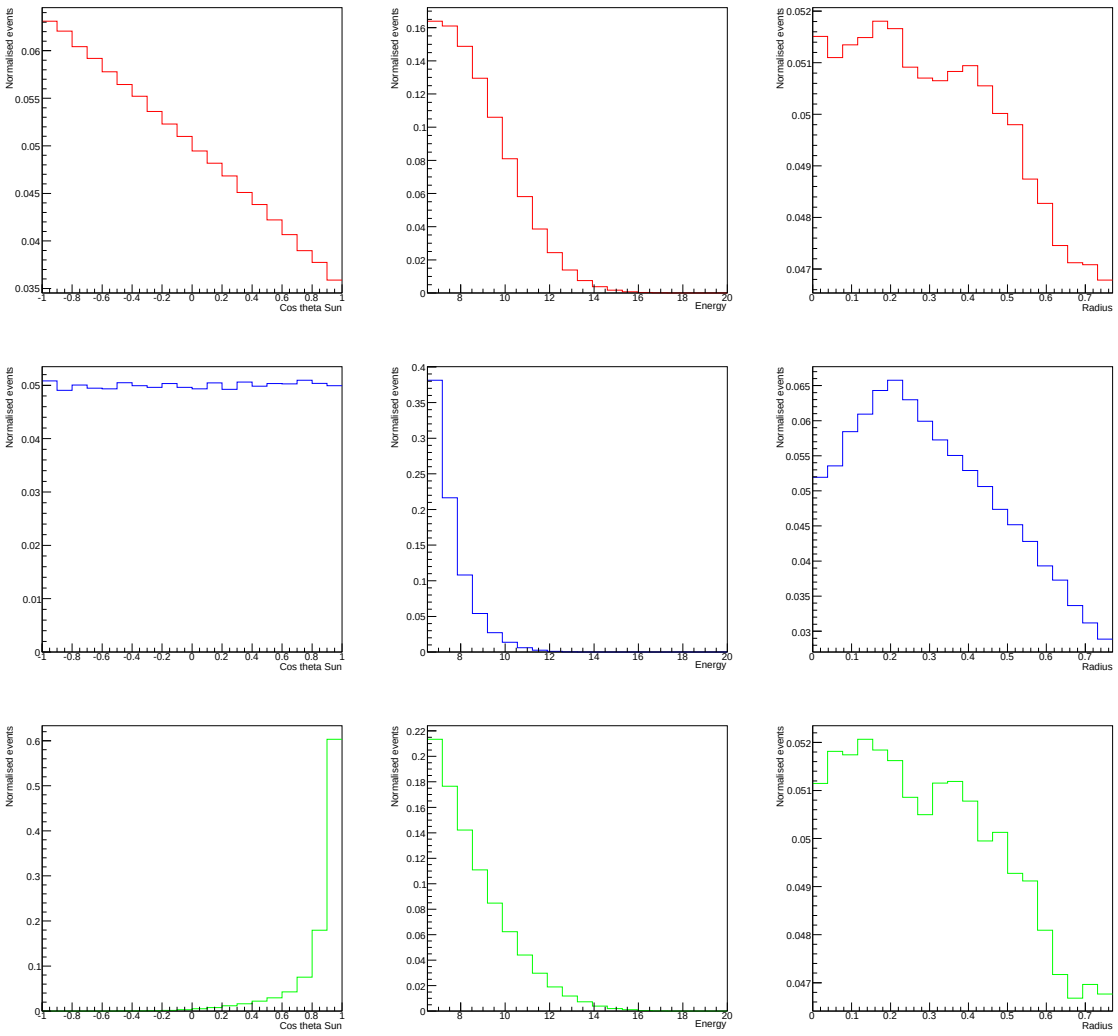


Figure 8.1: Histograms of $E$, $R$ and $\cos\theta_\odot$ for CC (red), NC (blue) and ES (green) events.

| Event | Fake | Fitted |
|---|---|---|
| CC | 1865 | $1846^{+66.9}_{-65.9}$ |
| ES | 222 | $219^{+23.0}_{-22.2}$ |
| NC | 238 | $250^{+53.5}_{-52.8}$ |

Table 8.1: Average results from Fake data fits. Statistical errors only are given.

Since the aim was to investigate the potential of a measurement of each flux, an energy constrained fit was performed. The CC and ES measurements would be sensitive to MSW distortions in their energy spectra, but none was expected in the high energy window used in this phase. Constraining the energy spectrum of the NC flux was always allowed, as it does not depend on the neutrino energy spectrum. The observed energy spectrum of NC events is that of neutron events used to detect them.

To test the potential of a PMT only signal extraction in the NCD phase, fake data sets of known content were created. The Monte Carlo generated for CC, ES and NC events was divided in half. One half was used to create 25 fake data sets and the other used to create pdfs. The fake data sets contained the expected number of NC, CC and ES events for the NCD phase, based upon predictions of neutrino fluxes using the Standard Solar Model. The signal extractions discussed in this chapter used the following binning

- 1 MeV bins for energy up to 13 MeV and one bin for 13-20 MeV
- 25 bins of $\cos\theta_{\odot}$ from -1 to 1
- 10 bins for $\frac{R^3}{R^3_{AV}}$ up to 0.77

## 8.4 Fits to fake data

Tests of the MXF fitter were performed using fake data sets that contained only NC, CC and ES events. The datasets were constructed using the Monte Carlo data that was produced using the full SNOMAN simulation of the detector. The average of the 25 fake data sets is given in Table 8.1. In all cases, the average fitted values were within 1 sigma of the known content of the data.

In the limit of high statistics, the likelihood function became Gaussian about the minimum value. The one sigma uncertainty was given by the standard deviation and in the case of the likelihood function, this point was where the likelihood was within $\pm 0.5$ of the minimum value.

Following the initial tests, background events were added to the fake data to investigate what effect they would have on the fit. The contribution of Čerenkov light

| Source | CC error % | ES error % | NC error % |
|---|---|---|---|
| $x$ | +0.01,-0.01 | +0.02,-0.02 | +0.10,-0.10 |
| $y$ | +0.02,-0.02 | +0.01,-0.01 | +0.14,-0.14 |
| $z$ | +0.40,-0.39 | +0.10,-0.10 | +2.51,-2.57 |
| Energy scale | +2.74,-2.74 | +0.45,-0.62 | +19.9,-18.4 |
| Backgrounds | +0.00,-0.00 | +0.00,-0.00 | +2.52,-2.63 |
| Statistical | +3.60,-3.60 | +10.50,-10.10 | +21.40,-21.21 |
| Total | +4.54,-4.54 | +10.51,-10.12 | +29.44,-28.32 |

Table 8.2: Summary of systematic errors for the fake data trials.

from background events was minimal [89] at energies above 6.5 MeV and only neutrons produced by photodisintegration, (alpha,n) etc would have remained. These background neutrons would have been identical to those produced by Neutral Current processes and it was expected that all of the background events would have been fitted as NC events, if only NC, CC and ES pdfs were used. To test this hypothesis, the approximate number of each background was added to each fake data set. The amount of each background was based upon the results from the *in-situ* analysis presented in this thesis and other analyses [90]. Investigations showed that when background events were included in the fake datasets and fits were performed using only NC, CC and ES pdfs, all of the backgrounds were fitted as NC events. This implied that the fitted number of NC events could be corrected by subtracting the expected number of neutron backgrounds to produce the number of NC events and thus the NC flux.

## 8.5 Systematic Errors

Systematic uncertainties on the parameters used in the fit may have changed the number of events in the data set and altered the number of extracted events. To assess the uncertainty, the pdfs was shifted or scaled appropriately and the fit to the data was performed again. The difference between the central values obtained using the shifted pdfs and the original central values were taken to be the systematic uncertainty. In previous phases, the largest systematic errors were energy scale, vertex position and background subtraction. As the analysis of all systematic parameters had not been completed at the time of writing, only the dominant systematic errors have been assessed. A summary of these dominant systematic errors derived from the fake data tests is given in Table 8.2. These systematic errors are only valid for PMT data and the systematic + statistical uncertainty on the NC flux measured by the NCDs is expected to be approximately 9%.

The energy scale uncertainty was calculated by comparing $^{16}$N calibration data

with SNOMAN simulated data. This work was performed by the energy and optics group [58]. The energy scale uncertainty was determined to be $\pm 1.19\%$. This uncertainty was applied on an event by event basis and increased (decreased) the event energy in the pdf. The uncertainty in the reconstructed $x$, $y$ and $z$ position of an event were calculated by comparing $^{16}$N calibration data with SNOMAN simulated data. The uncertainty was found to be $\pm 4\%$ for $x, y$ and $z$ [63]. Again these uncertainties were applied on an event by event basis to the pdf. The background uncertainties were taken directly from the uncertainties given on the concentrations presented in this thesis.

## 8.6 Conclusions

The errors quoted in Table 8.2 are dominated by statistical errors. The expected statistical errors for the CC and ES measurements are similar to those quoted from the previous phases [22]. However, the expected statistical error associated with the NC flux (for a PMT only measurement) is approximately 5 times greater than previously. This is a direct consequence of the NCDs and the high energy threshold. The neutron detection efficiency of the NCDs was much greater when compared with that of $D_2O$. As a result, the majority of neutrons were captured by the NCDs. Only a small proportion of NC events would be captured by deuterium and detected by the PMT array.

Compared with previous phases, the systematic error associated with energy scale uncertainty is much larger for the NC flux in the NCD phase. This is due to a combination of poor statistics and a higher energy threshold. The NC energy spectrum, shown in Figure 8.1, rises steeply around the energy threshold. Therefore, any small uncertainty in energy scale will cause a large difference in the number of NC events and give rise to a large systematic error.

Therefore, a NC flux measurement using only PMT data will not be competitive with those from previous phases. The best measurement of the NC flux during the third phase of SNO will come from data taken by the NCD array. The flux obtained from NCD data can be used to constrain the number of NC events expected in the PMT data, resulting in a more accurate measurement of the CC and ES fluxes.

# Chapter 9

# Conclusions

Results from the first two phases of the Sudbury Neutrino Observatory (SNO) experiment proved that the discrepancy between the measured and predicted flux of neutrinos produced by the Sun is explained by flavour changing neutrino transformation. At the time of writing, the analysis of the final phase of data, in which an independent measurement of the total neutrino flux, using purpose built Neutral Current Detectors (NCDs), is in progress. These results will be combined with those obtained in the first two phases to determine the neutrino mixing parameter ($\theta_{12}$) and difference in squared masses $\Delta m^2_{12}$ more accurately.

In SNO strict limits on radioactivity were imposed as naturally occurring thorium ($^{232}$Th) and uranium ($^{238}$U) chain nuclei produce gamma rays that have sufficient energy to break apart the deuterium nucleus, producing a neutron. A neutron produced in this way is indistinguishable from one produced by a Neutral Current interaction and is thus an irreducible background. To produce an accurate measurement of the neutrino flux, a good understanding and measurement of radioactivity in the detector was crucial.

As discussed in this thesis, the probability of detecting a neutron produced by photodisintegration is strongly dependent upon the location and type of parent radioactivity. Therefore, the background levels must be determined separately. The addition of the NCDs to the $D_2O$ region introduced new sources of background into the detector. The radioactivity contained in the NCD bulk could not be assessed using the standard *ex-situ* assay methods. Based on the isotropy only fitting methods used in the $D_2O$ and salt phases, a 2D (radius+isotropy) maximum likelihood fitting method was used to separate radioactivity in the heavy water ($D_2O$) from that in the NCDs. The development and testing of this method by the author is described in Chapter 4. Concentrations of $^{232}$Th and $^{238}$U in the PSUP $H_2O$ were obtained using an isotropy only method written by the author.

An independent measurement of Th chain activity in $D_2O$ and PSUP $H_2O$ was made

using the chemical assay technique described in Chapter 5. Filters loaded with Hydrous Titanium Oxide (HTiO) were used to extract radium (Ra) and thorium (Th) from the detector water. Radium was eluted from the filters using 15 $l$ of 0.1 mol/$l$ HCl which was concentrated to a volume of a few ml. This concentrated solution was added to 42 g of liquid scintillator and the sample was counted using beta-alpha coincidence counters. The secondary concentration technique was revised from that used in phases I and II to be less sensitive to trace impurities. This was used in all NCD phase assays with no significant problems. As a result in this phase, the HTiO and MnOx $D_2O$ assay results were merged to produce a single *ex-situ* result.

A number of unphysical PSUP $H_2O$ assay results were attributed to fluctuations in the $H_2O$ elution rig backgrounds. Additional systematic errors were assigned by the author to affected assays and the results agreed well with MnOx assays and *in-situ* results. This allowed merging of the HTiO and MnOx results to produce a single *ex-situ* number. To improve the statistical and fitting error, a revised analysis method was developed by the author. This method removed accidental coincidences from the data, allowing the full signal region to be analysed. The analysis and interpretation of these results is presented in Chapter 5.

The concentrations of $^{232}$Th and $^{238}$U in the $D_2O$ obtained from this work were in good agreement with measured values from the *ex-situ* assay techniques. The deduced amounts of $^{232}$Th and $^{238}$U impurities in the NCD bulk were also in good agreement with both pre-deployment radioassays and alpha coincidence measurements made using the NCD datastream. Agreement between the *in-situ* results and independent results demonstrated that radioactive backgrounds in the NCD phase were well understood and accurately determined. As the three independent measurements of the $D_2O$ Th and two independent measurements of the $D_2O$ U chain activities were in good agreement, the *ex-situ* and *in-situ* results were merged in Chapter 5 to produce a single Th and single U concentration for the $D_2O$ region. Monte Carlo simulations were used to convert the concentration of each background class into an equivalent number of neutrons produced per day and these numbers will be used by the signal extraction group to derive the neutrino flux. The resultant error was equivalent to 2.5% of the NC flux and hence was not a significant error.

The beta-alpha counting system used to count the samples produced by the HTiO assay method was becoming increasingly prone to failure due to its age and design. A new system was designed and built at Oxford and its testing, commissioning and calibration, which were carried out by the author, are described in Chapter 6. These low radioactivity $^{238}$Th and $^{226}$Ra source tests showed that the initial system was too sensitive to noise on the input pulse, making it difficult to separate signal from background events. Smoothing the

pulse between the PMT output and input to the electronics system solved the problem. Following this modification, the system was successfully used for a number of assays towards the end of SNO data taking. The results from these assays agreed with previous measurements that used the old counting system. The efficiency of this new counting system was found to be slightly higher when compared with the old system. Several other particle physics experiments are now using sets of these counters, including SNO+ and Daya Bay.

During the NCD phase, a significant amount of surface contamination was found on one of the NCDs. The significance of this contamination was highlighted by the author and it was demonstrated that any uncertainty in its composition would lead to an unacceptably high systematic error, approximately equal to the total background uncertainty in previous phases of the SNO experiment. A chemical method, using acid elution to remove surface radioactive deposits, was developed by the author to measure its composition. The eluate, containing radioactive deposits removed from the NCD, was then concentrated and mixed with liquid scintillator. The resulting solution was counted using beta-alpha coincidence counters, giving a measure of the activity plated on the NCD surface. The measured activity agreed with results from an independent alpha counting method. Combination of these results reduced a potentially damaging $\sim 7\%$ systematic error on the expected Neutral Current flux to an error of less than 1%.

If the NCD hotspots had remained undetected, the $\sim$7% higher Neutral Current flux would have probably agreed at the 1 sigma level with the values obtained from the salt and $D_2O$ phases. However, such a result could have brought into question the reliability of previous results from the SNO experiment. The work in this thesis has demonstrated that the low energy backgrounds in the NCD phase of the Sudbury Neutrino Observatory have been measured accurately and understood.

Finally, a study by the author using a full Monte Carlo simulation of the SNO detector demonstrated that it will not be possible to extract a more accurate NC flux measurement using only PMT data in the NCD phase. This is as a result of the NCDs capturing the majority of neutrons, leading to high statistical errors on PMT measurements. The most accurate measurement of the NCD phase NC flux will be from the NCD data. The NC flux measured by the NCDs will be used to constrain the NC flux in the PMT fit to the data. Such a constraint will lead to an improved measurement of the CC and ES fluxes.

The SNO experiment has proved the neutrino flavour changing hypothesis by comparison of measurements of the electron neutrino flux (CC reaction) and the total neutrino flux (NC reaction), providing further evidence that neutrinos have mass. The previous phases of the SNO experiment have found no sign of spectral distortions or day-night

effects. The $\Delta m^2_{12}$ and $\theta_{12}$ values are such that the effects predicted by the MSW theory were too small to be seen. More accurate measurements of the low energy CC spectrum from the $D_2O$ and salt phases are in progress. Such measurements may not reveal spectral distortions but they will yield the lowest energy measurement of the $^8$B CC spectrum to date.

As the solar oscillation parameters depend on the small but possibly finite mixing angle $\theta_{13}$, more accurate solar measurements could provide better limits on this third mixing angle. A combined analysis of the results from SNO phases I, II and III together with other neutrino experiments will produce very accurate values of the solar neutrino mixing parameters and will provide a fitting conclusion to the Sudbury Neutrino Observatory experiment.

# Appendix A

# Neutral Current induced backgrounds in salt

During the salt phase, there was a small probability that a neutral current event could produce a background to itself. In the salt phase, neutrons were most likely to capture on $^{35}$Cl as its largest neutron capture cross-section was far larger than that of deuterium. Neutron capture on $^{35}$Cl creates an 8.58 MeV excited state of $^{36}$Cl which decays to its ground state by gamma emission via one or more of its 75 excited states. The neutrino interaction was then detected via Compton scattering of these gammas. However, if the gammas emitted from $^{36}$Cl decays had certain energy characteristics, there was a small probability that two events could have been detected from one incident neutrino interaction. A double event could occur if the gamma cascade contained one gamma that had sufficient energy to photodisintegrate a deuteron i.e. an energy greater than 2.225 MeV and at least one other gamma capable of producing Čerenkov light above the detector energy threshold. The neutron produced by photodisintegration could then capture on $^{35}$Cl producing another gamma cascade. This cascade would only be visible if it produced Čerenkov light above the energy threshold of the detector. This type of event is shown schematically in Figure A.1. Double events may be identified by two important characteristics. First, they originate from the same source event and hence the same source vertex. Second, the two detected events are separated by the average time it takes for the neutron to capture on a $^{35}$Cl nucleus, approximately 5 ms. Five double type events were observed in the salt phase neutrino data set [23]. At the time, it was unclear as to what had caused these events and it was suggested that this interaction was the cause. To estimate the expected number of double events in the salt data set, Neutral Current (NC) Monte Carlo data, produced using SNOMAN, were analysed using the standard neutrino analysis cuts [23].

Events that satisfied the standard neutrino analysis cuts had their universal time, event ID and source vertex position recorded. This data was then analysed to find any

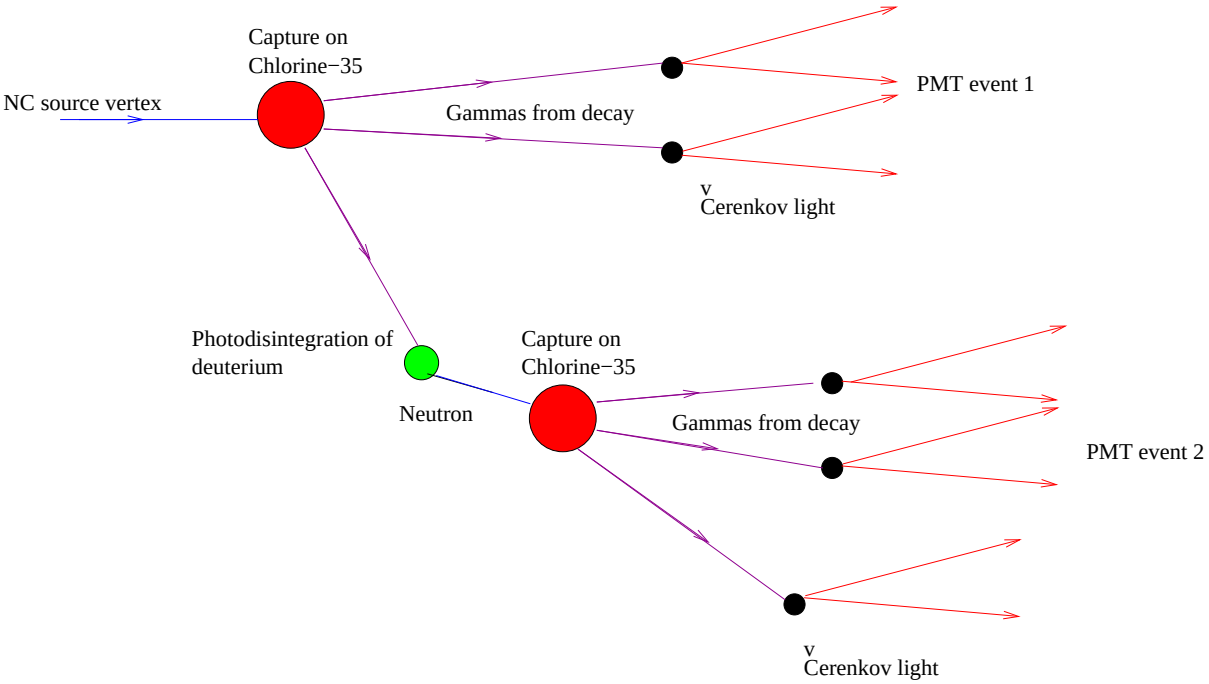


Figure A.1: A schematic representation of a double event.

consecutive events that originated from the same source vertex and occurred within 50 ms of each other. Any two events that passed these cuts were classed as a double event. The analysis of the salt neutral current Monte Carlo data set found 13 doubles in 267,617 neutral current events.

## A.1 Theoretical estimate

To check the results of the Monte Carlo analysis, a theoretical estimate was made using the following probabilities

- neutron capture on $^{36}$Cl $\approx 90\%$
- detection efficiency $\approx 48$ %
- photodisintegration
- correct decay characteristics of $^{36}$Cl

The neutron capture and detector efficiency were determined using Monte Carlo simulations and calibration data. Determination of the probability of photodisintegration will be discussed followed by that of $^{36}$Cl decay.

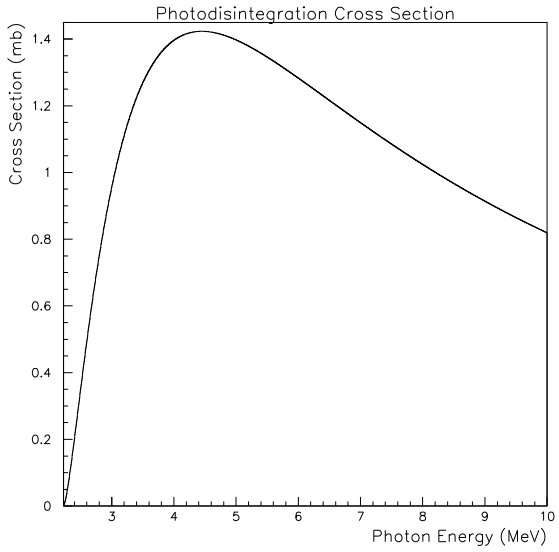


Figure A.2: Energy dependence of photodisintegration cross section. Taken from [91]. This analysis is concerned with the region of 2.2 to approximately 5 MeV where the cross section, and hence probability, is heavily dependent upon energy.

### A.1.1 The probability of photodisintegration

The probability of photodisintegration is directly proportional to the cross section of the process. Figure A.2 shows that in the energy range of interest, i.e. around 2-4 MeV, the cross section is strongly dependent upon energy. Therefore, in this calculation, the probability of photodisintegration is calculated for a given energy using the following formula

$$P_{photo} = \frac{\sigma_{photo}}{\sigma_{total}}$$

where $\sigma_{photo}$ is the photodisintegration cross section and $\sigma_{total}$ is the total cross section for all photon processes in heavy water. The total cross section was calculated from the following formula

$$\sigma_{total} = \frac{M_r \times \mathrm{MAC}}{N_A}$$

where $M_r$ is the relative molecular mass of the medium through which the gamma is propagating, MAC is the mass attenuation coefficient of the medium, and $N_A$ is Avogadro's number. The values of the mass attenuation coefficient were taken from [92]. This allowed the probability to be calculated for each energy.

The 8.58 MeV excited state of $^{36}$Cl produced an average of 2.5 gammas per decay, indicating that the majority of decays emitted 2 or 3 gammas. The decay scheme in

| Number of gammas | Probability of decay % |
|---|---|
| 2 | 1.12 |
| 2 | 5.26 |
| 2 | 2.01 |
| 3 | 0.256 |
| 3 | 0.189 |
| 3 | 0.159 |

Table A.1: Principle decay modes for 2 and 3 gamma decays involved in this calculation.

SNOMAN [41] was in the form of an upper diagonal 75 by 75 matrix of cumulative branching probabilities.

To be detected, the $^{36}$Cl decay must produce one gamma capable of photodisintegrating the deuteron and at least one other gamma that can produce a Čerenkov light signal above the detector threshold. An initial inspection of the decay scheme found that at least 63.3% of all decays [41] from the excited $^{36}$Cl state would not satisfy these conditions and would not therefore, be able to produce a double event.

The probability that a particular decay occurred was estimated using the branching fractions from the $^{36}$Cl decay scheme. The prominent decay modes for both 2 and 3 gamma decays involved in this calculation and their branching probabilities are given in Table A.1.

As the resolution of the detector was finite, there was a small chance that signals just below the energy threshold could be detected in the analysis. This effect was estimated using Nitrogen-16 calibration data from the salt phase. The design of the $^{16}$N source was such that only the 6.13 MeV gamma was released. This gamma Compton scattered, producing electrons with a range of energies. On average, a 6.01 MeV gamma produced a $5.03 \pm 0.02$ MeV kinetic energy electron [87], but there was a chance that a more or less energetic electron was produced. The number of events in the $^{16}$N data above certain energy thresholds were counted and compared to the total number of events. To relate the information obtained from the $^{16}$N data to the gammas from the $^{36}$Cl cascade, a number of other factors must be considered. First, the kinetic energy of an electron created via Compton scattering was on average, 1 MeV less than the energy of the gamma that produced it. Therefore, multiple gammas lose about 1 MeV each. Second, the width of the energy distribution was proportional to $\sqrt{E}$. Therefore, as the energy of the $^{16}$N peak was not equal to that of $^{36}$Cl, a further correction was required. Considering these two factors, the position on the $^{16}$N spectra corresponding to the energy of the gamma

emitted by the $^{36}$Cl decay, relative to the peak value was given by

$$\text{Position} = (T_{thresh} - T_e)\left(\frac{T_{thresh}}{T_e}\right)^{\frac{1}{2}} \tag{A.1}$$

where $T_{thresh}$ is the threshold kinetic energy (5.5 MeV) and $T_e$ is the kinetic energy of the electron in MeV, given by the following formula

$$T_e(\text{MeV}) = \left(\Sigma_n E_{\gamma_n}\right) - 0.5n$$

where $n$ is the number of gammas released by the decay excluding the photodisintegrating gamma and $E_{\gamma_n}$ is the energy of each gamma. By using (A.1), the position on the $^{16}$N spectra was related to the energy of the gammas produced by the $^{36}$Cl decay and the probability of that decay causing a signal in the detector obtained.

The probability that a particular decay occurred, caused a photodisintegration and produced a signal above threshold was calculated for 2 and 3 gamma decays, with branching probabilities greater than $10^{-4}$. This probability, for two and three gamma decays, $P_{decay}$, was calculated to be $P_{decay} = 8.98 \times 10^{-5}$. This was then combined with the detector and neutron capture efficiencies to give an estimate of the number of doubles, which was estimated to be 10 double events in 267, 617 Neutral Current events. This was in good, but not complete, agreement with the number calculated from the Monte Carlo data. As mentioned previously, the $^{36}$Cl decay scheme is very complicated and it was not possible to perform a calculation that included all decay modes. Approximately, 88 decay modes out of a possible 459 were considered in this estimation. The remaining 371 modes, had branching probabilities ranging from $10^{-5}$ to $10^{-11}$. Taking a typical branching probability to be $10^{-5}$, estimating the probability that the decay created a Čerenkov photon above the energy threshold, a photon that produced a photodisintegration to be $1 \times 10^{-3}$ and using the previously stated detector efficiency and neutron capture probability, the number of doubles expected from the remaining 371 decays* was approximately 2.28. Therefore, although significant in number, it is unlikely that these modes would have contributed more than 3 doubles to the theoretical estimate, due to the extremely small probabilities of detection and photodisintegration. Thus, the high number of these decay modes was, in fact, unlikely to contribute more than a few doubles to the estimate. However, it is thought that these modes would account for the discrepancy observed between the value obtained by this method and that derived using Monte Carlo, as the Monte Carlo used all of the decay modes. Therefore, the theoretical estimate should be taken as a lower limit on the expected number of doubles.

*Each decay has more than one possible way of creating a double event. It is estimated that each decay has four possible ways of creating a double.

An upper limit on the expected number of double events could be found by assuming that the major contribution arose from $^{36}$Cl decays with branching fractions greater than $10^{-4}$. The total probability for these decays was 18.17%. The probability of photodisintegration was assumed to be close to the average value of $\frac{1}{400}$ and the detector resolution was taken to be close to its average value of $\approx 50\%$. The calculation was not performed on a decay by decay basis and, as such, these probabilities were thought to be an overestimate for the majority of decays. Therefore, this calculation would produce an upper estimate and it was found to be 26 double events.

The theoretical calculation predicted that the number of double events should lie between 10 and 26 events for a data set of 217,617 NC events. A comparison of the Monte Carlo and theoretical calculation is given in Section 3.2.2.

# Appendix B

# NCD names and numbers

| NCD name | String number | NCD name | String number |
|---|---|---|---|
| I1 | 36 | J1 | 35 |
| I2 | 30 | J2 | 32 |
| I3 | 20 | J3 | 26 |
| I4 | 29 | J4 | 23 |
| I5 | 19 | J5 | 16 |
| I6 | 10 | J6 | 13 |
| I7 | 3 | J7 | 6 |
| I8 | 9 | J8 | 4 |
| K1 | 37 | M1 | 38 |
| K2 | 31 | M2 | 33 |
| K3 | 28 | M3 | 27 |
| K4 | 21 | M4 | 22 |
| K5 | 18 | M5 | 17 |
| K6 | 11 | M6 | 12 |
| K7 | 8 | M7 | 7 |
| K8 | 2 | M8 | 1 |
| L1 | 34 | N1 | 39 |
| L2 | 5 | N2 | 25 |
| L3 | 15 | N3 | 14 |
| L4 | 24 | N4 | 0 |

Table B.1: Name and numbering convention for NCDs

# Appendix C

# The Oxford Elution Rig

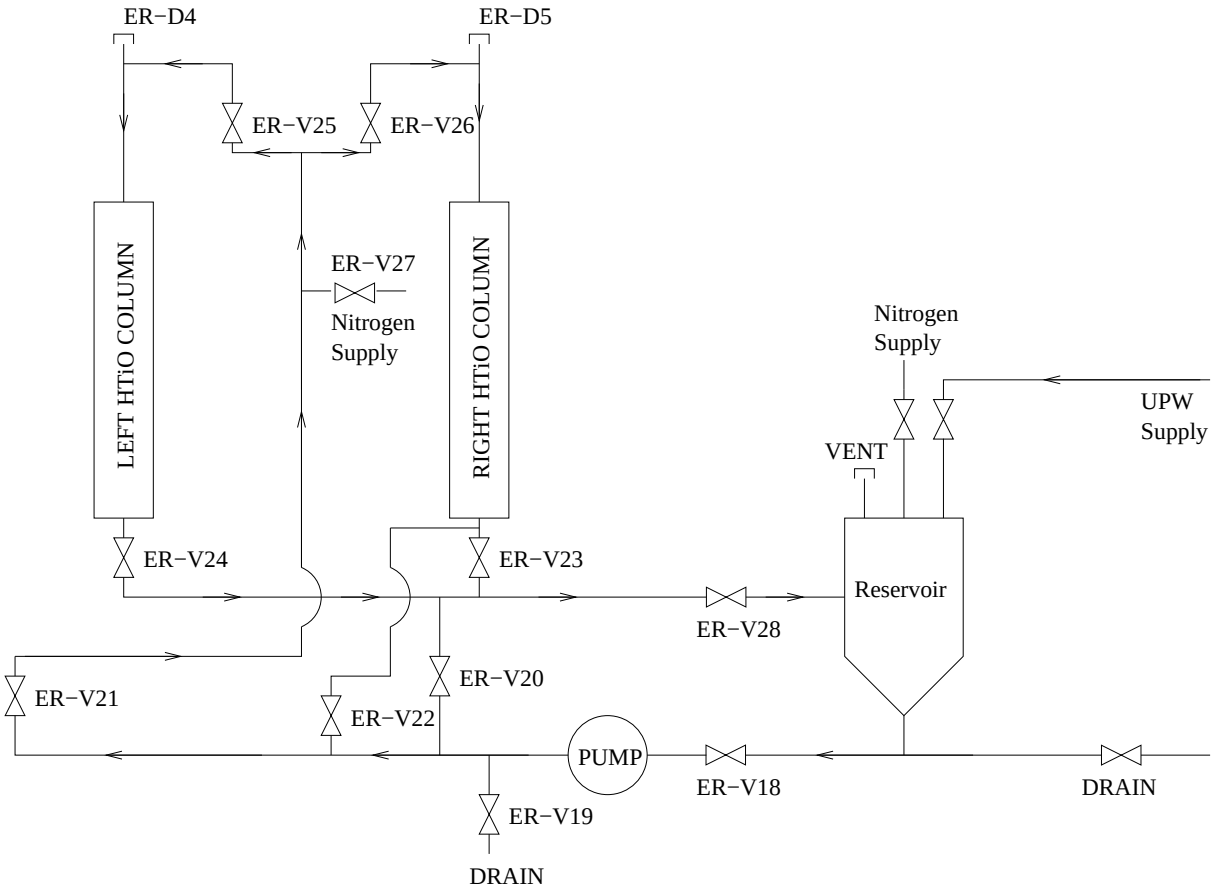


Figure C.1: A schematic diagram of the Oxford elution rig. ER-V is a shorthand for Elution Rig Valve and ER-D is shorthand for Elution Rig Drain. The arrows show the direction of flow during elution.

# Bibliography


[1] W. Pauli. *Physics Today*, **31**, 27.

[2] J. Chadwick. *Proceedings of the Royal Society of London. Series A.*, **136**, 830 (1932) 692–708.

[3] E. Fermi. *Zeitshrift fur Physik*, **88** (1934) 161–177.

[4] F. Reines and C.L. Cowan Jr. *Phys. Rev.*, **92** (1953) 830–831.

[5] F. Reines and C.L. Cowan Jr. *Nature*, **178** (1956) 446–449.

[6] M. Goldhaber *et. al. Phys. Rev.*, **109** (1958) 1015–1017.

[7] J.N. Bahcall, M.H. Pinsonneault and S. Basu. *Astrophys. J.*, **555**, 990.

[8] J.N. Bahcall, A.M. Serenelli and S. Basu. *Astrophys. J.*, **621** (2005) L85–L88.

[9] K. Zuber. "Neutrino Physics" (2004). Institute of Physics Publishing.

[10] J.N. Bahcall and M.H. Pinsonneault. *Phys. Rev. Lett.*, **92**, 12 (2004) 121301.

[11] R. Davis Jr *et. al. Phys. Rev. Lett.*, **20** (1968) 1205–1209.

[12] B.T. Cleveland *et. al. Astrophys. J.*, **496** (1998) 505.

[13] S. Fukuda *et. al. Phys. Rev. Lett.*, **86** (2001) 5651–5655.

[14] J.N. Abdurashitov *et. al. Phys. Lett. B*, **328** (1994) 234–248.

[15] P. Anselmann *et. al. Phys. Lett. B*, **285** (1992) 376–389.

[16] P. Aliani *et. al. Nuc. Phys. B*, **634** (2002) 393–409.

[17] V. Gribov and B. Pontecorvo. *Phys. Lett.*, **28B** (1969) 493–496.

[18] M. Apollonio *et. al. Eur. Phys. J.*, **C27** (2003) 331–374.

[19] L. Wolfenstein. *Phys. Rev.*, **D17** (1978) 2369.

[20] S.P. Mikheyev and A. Yu. Smirnov. *Sov. J. Nucl. Phys.*, **42** (1985) 913.

[21] The SNO Collaboration. *Phys. Rev. Lett.*, **87** (2001) 071301.

[22] The SNO Collaboration. *Phys. Rev. Lett.*, **92** (2004) 181301.

[23] The SNO Collaboration. *Phys. Rev. C*, **72** (2005) 055502.

[24] K. Eguchi *et. al. Phys. Rev. Lett.*, **90** (2003) 193.

[25] J.A. Dunmore. "Separation of CC and NC events at the Sudbury Neutrino Observatory" (2004). DPhil thesis, University of Oxford.

[26] The Super-Kamiokande Collaboration. *Phys. Rev. Lett.*, **81** (1998) 1562.

[27] The Borexino Collaboration. *Phys. Lett. B*, **658** (2008) 101–108.

[28] M.H. Ahn *et. al. Phys. Rev. D*, **74**.

[29] D.G. Michael *et. al. Phys. Rev. Lett.*, **97**.

[30] A.A. Aguilar-Arevalo *et. al. Phys. Rev. D*, **74**.

[31] W-M. Yao *et al. J. Phys. G*, **33**.

[32] The SNO Collaboration. *Nucl. Instrum. Meth.*, **A449** (2000) 172–207.

[33] G. t'Hooft. *Phys. Lett. B*, **37** (1971) 195.

[34] J.R.N. Cameron. "The Photomultiplier Tube Calibration of the Sudbury Neutrino Observatory" (2001). DPhil thesis, Univeristy of Oxford.

[35] The SNO Collaboration. "Sudbury Neutrino Observatory Proposal" (1987). SNO Internal Report, SNO-STR-87-12.

[36] G. Doucas *et al. Nucl. Instrum. Meth.*, **A370** (1996) 579–596.

[37] J.F. Armsbaugh *et al. Nucl. Instrum. Meth.*, **A579** (2007) 1054–1080.

[38] G.A. Cox *et al. IEEE Trans. Nucl. Sci.*, **51** (2004) 2227.

[39] Rick Norman *et al.* "$^{241}$Am-$^{9}$Be Source for Neutron and $\gamma$-Ray Calibrations of SNO" (2002). SNO Internal Report.

[40] SNO NCD analysts. "SNO NCD Phase Analysis Unidoc" (2008). SNO Internal Report.

[41] The SNO Collaboration. "SNOMAN User Manual" (2005). SNO Internal Report.

[42] I. Blevis *et al. Nucl. Instrum. Meth.*, **A517** (2004) 139–153.

[43] T.C. Andersen *et al. Nucl. Instrum. Meth.*, **A501** (2003) 399–417.

[44] N.K. McCauley. "Producing a Background Free Data Set for Measurement of the Charge Current Flux and Day-Night Asymmetry at the Sudbury Neutrino Observatory" (2001). DPhil thesis, University of Oxford.

[45] NCD Phase Data Cleaning Group. "Data Cleaning in the NCD Phase" (2005). SNO Internal Report.

[46] J. A. Formaggio. "An Analysis of High Multiplicity Events for the Extended Salt Data" (2004). SNO Internal Report.

[47] C.J. Sims. "Background determination in the Salt Phase of the Sudbury Neutrino Observatory Experiment" (2005). DPhil thesis, University of Oxford.

[48] S.R. McGee *et al.* "Limit on Neutron Production from Activity on NCD Outer Surfaces" (2008). SNO Internal Report.

[49] N.E.Holden and D.C.Hoffman. *Pure Applied Chemistry*, **72** (2000) 1525–1562.

[50] J. Goon. "Measurement of External Čerenkov Tails in the NCD phase" (2006). SNO Internal Report.

[51] G.A. McGregor. "The Measurement of the Neutral Current Interaction at the Sudbury Neutrino Observatory" (2002). DPhil Thesis University of Oxford.

[52] E.D. Earle *et al.* "A collection of notes on acrylic radioactivity" (1990). SNO Technical Report, SNO-STR-90-00.

[53] L.C. Stonehill. "Deployment and Background Characterization of the Sudbury Neutrino Observatory Neutral Current Detectors" (2005). PhD Thesis, University of Washington.

[54] X. Chen. "Monte Carlo Simulations and Analysis of Backgrounds in the Sudbury Neutrino Observatory" (1992). DPhil thesis, University of Oxford.

[55] A.W.P. Poon. "NCD Hotspots" (2005). SNO Internal Report.

[56] K. Rielage *et. al.* "Measurements of the activity and composition of the K5 and K2 hotspots" (2007). SNO Internal Report.

[57] R.F. MacLellan. "RSP for the NCD phase" (2007). SNO Internal Report.

[58] J. Secrest. "Energy systematics for phase 3" (2007). SNO Internal Report.

[59] G.A. McGregor. "Beta Alpha data aquisition software" (2000). SNO Internal Report.

[60] A.W.P. Poon. "Private Communication" (2007).

[61] ROOT documentation. "TFractionFitter" (2007). Http://root.cern.ch/root/html/TFractionFitter.html.

[62] J.C. Loach. "Private Communication" (2007).

[63] P-L. Drouin. "Comparison of Vertex Accuracies for the FTN Fitter: Old and New LRPB Banks" (2007). SNO Internal Report.

[64] B. Aharmim. "Private Communication" (2008).

[65] P.M. Thornewell. "$^3$He Neutral Current Detectors for the Sudbury Neutrino Observatory" (1997). DPhil Thesis, University of Oxford.

[66] N. Tolich. "Observing the NCD hotspot with the NCD array" (2006). SNO Internal Report.

[67] R.G.H. Robertson (2007). Private communication.

[68] H.S. Wan Chan Tseung. "Private Communication" (2007).

[69] C. Kraus, J. Farine and J. Goon. "Private Communication" (2006).

[70] B.T. Cleveland. "Private Communication" (2007).

[71] A.W.P. Poon. "PD Neutrons from Radioactivity" (2003). SNO Internal Report.

[72] T.C. Andersen *et al. Nucl. Instrum. Meth.*, **A501** (2003) 386.

[73] B. Aharmim *et al.* "High sensitivity measurement of $^{224}$Ra and $^{226}$Ra in water with an improved hydrous titanium oxide technique at the Sudbury Neutrino Observatory" (2008). ArXiv:0803.4162v1[nucl-ex].

[74] K.H. Howard. "Ion Exchange Properties of Hydrous Titanium Oxide" (1994). Honor School of Natural Science: Chemistry Part II thesis, University of Oxford.

[75] R.K. Taplin. "The Use of Photomultipliers in SNO" (1994). DPhil thesis, University of Oxford.

[76] H. Heron. "Techniques to Measure the NC background in the SNO Experiment" (1998). DPhil thesis, University of Oxford.

[77] N.J. Keen. *J. British Nuclear Energy Society*, **7** (1968) 178.

[78] X. Dai *et. al.* "Problems on the HTiO assays in the salt phase" (2003). SNO Internal Report.

[79] B. Aharmim. "Ex-situ lifetime weighted average of $^{224}$Ra concentration in the AV during the NCD phase of the SNO experiment" (2008). SNO Internal Report.

[80] X. Dai and N.A. Jelley. "Systematic uncertainties in HTiO radium assays in salt phase" (2003). SNO Internal Report.

[81] G. Knoll. "Radiation Detection and Measurement". Wiley (1979).

[82] C. Dodson. "Introduction to Alpha/Beta Discrimination". Beckman Bulletin, 7894 B.

[83] H.M. O'Keeffe, N.A. Jelley and S.J.M. Peeters. "The new Oxford Beta-Alpha Counting System User Manual" (2007). SNO Internal Report.

[84] H.M. O'Keeffe. "Ideas on NCD Hotspot Composition" (2006). SNO Internal Report.

[85] A. Newman. *Analytical Chemistry*, **68** (1996) 46A–51A.

[86] A.P. Ferraris. "Radiogenic Background Suppression in a Heavy Water Solar Neutrino Detector" (1992). DPhil Thesis, University of Oxford.

[87] J.R. Wilson. "A Measurement of the $^{8}$B Solar Neutrino Energy Spectrum at the Sudbury Neutrino Observatory" (2004). DPhil Thesis, University of Oxford.

[88] J.C. Loach. "DPhil Thesis, University of Oxford" (2008). Awaiting submission.

[89] H.M. O'Keeffe. "Cherenkov Tails in the $D_2O$ Region" (2008). SNO Internal Report.

[90] J. Formaggio. "Other Neutron Backgrounds" (2008). SNO Internal Report.

[91] M.J. Lyon. "Neutron Transport in the Sudbury Neutrino Detector" (1996). DPhil Thesis, University of Oxford.

[92] C. Kanchanawarin. "Photon Mass Attenuation Coefficient of Heavy Water from 1 MeV to 20 MeV" (1997). Long Vacation Project University of Oxford.